Università degli Studi di Ferrara

INTERNATIONAL DOCTORAL COURSE IN
"EARTH AND MARINE SCIENCES (EMAS)"

CYCLE XXXII

COORDINATOR Prof. COLTORTI MASSIMO

MULTIPORE ZEOLITES FOR ENVIRONMENTAL AND CATALYTIC APPLICATIONS: A STRUCTURAL FINGERPRINT OF "MOLECULAR TRAFFIC CONTROLLERS"

Scientific/Disciplinary Sector (SDS) GEO/06

Supervisor
Prof.ssa Martucci Annalisa

Candidate
Dott.ssa Beltrami Giada

Co-Supervisor
Dr. Ardit Matteo

Years 2016/2019

CONTENTS

CHAPTER 1. Introduction and aim of the thesis……... 1

CHAPTER 2. Zeolites: relation between structure and properties…… 9

2.1. Generalities about structure and crystal chemistry……... 9

2.2. Insights on catalytic properties……..... 11

2.3 Insights on cation-exchange properties…… 13

2.4. Insights on sorption properties…… 14

CHAPTER 3. Materials…….. 19

3.1. Medium pores zeolites…… 19

3.1.1. ZSM-5 (MFI)…… 19

3.1.2. Ferrierite (FER)……...…….. 21

3.2. Large pores zeolites……. 22

3.2.1. L (LTL)……. 22

3.2.2. Mordenite (MOR)……...…….. 23

3.2.3. Omega (MAZ)…….. 24

CHAPTER 4. Zeolites characterization: experimental techniques and data process…. 27

4.1 Synchrotron X-ray powder diffraction…….. 28

4.2 Neutron powder diffraction……... 29

4.3 Extended X-ray absorption fine structure (EXAFS)……..... 30

4.4 Rietveld method…… 31

4.5 Computational modeling…….. 32

CHAPTER 5. Experimental…… 35

SYSTEM 1. Thermal activation of templated ZSM-5 zeolites: an *in situ* synchrotron X-ray powder diffraction study…….. 35

SYSTEM 2. Structural characterization of acidic ZSM-5 zeolites through *in situ* synchrotron X-ray powder diffraction..... 47

SYSTEM 3. L-lysine adsorption in ZSM-5 zeolites: a synchrotron X-ray powder diffraction study…… 59

SYSTEM 4. Structural characterization of acidic L and its precursor by neutron powder diffraction…….. 71

SYSTEM 5. Temperature-induced structural modifications in acidic L zeolite: an *in situ* synchrotron X-ray powder diffraction study……. 81

SYSTEM 6. L-lysine adsorption in L zeolite: a combined synchrotron X-ray and neutron powder diffraction study……... 93

SYSTEM 7. Thermal activation of NH_4 precursor of acidic omega zeolite: a neutron and *in situ* synchrotron X-ray powder diffraction combined study……. 103

SYSTEM 8. Insights on Ga-zeolite catalysts: X-ray powder diffraction and absorption spectroscopy characterization at ambient conditions…. 117

CHAPTER 6. Conclusions……..... 133

Bibliography…… 139

Appendix 1……. 155

Appendix 2……. 185

Appendix 3……. 223

Appendix 4……. 233

Appendix 5……. 241

Appendix 6……. 245

Appendix 7……. 251

Appendix 8…… 257

CHAPTER 1. Introduction and aim of the thesis

Zeolites are amongst the most widely investigated and topical crystalline inorganic microporous solids due to the variable chemical composition of the framework as well as tunable pore size and architecture. These features make them very suitable for a wide range of applications in fields where the host-guest chemistry defines the final behaviour of the system (Van Speybroeck et al., 2015; Roth et al., 2014).

Nowadays, the applications spectrum of zeolite properties has been extended to cutting-edge technological uses, such as stabilization of nanoscale forms of matter and the separation of reaction spaces in electron transfer processes (Bein and Mintova, 2005). Beyond these advanced applications, zeolites play an important role in sustainable processes, such as the field of renewable energy and environmental remediation. In the field of renewable energy, these materials are principally studied for biomass conversion, fuel cells, thermal energy storage, CO_2 sequestration and conversion. Besides, zeolites for environmental remediation processes are mainly used for out-door air quality monitoring, water and wastewater purification from heavy metals and organic compounds of different nature, *etc.* (Li et al., 2017 and references therein). In addition, zeolites are growing their importance in both medical and biotechnological fields. In particular, from a medical point of view, they are considered well performing materials for the improvement of nutrition status and immunity of farm animals and organism detoxication of both humans and animals. Beyond that, biotechnologies investigate zeolites for construction of biosensors, detection of biomarkers, controlled drugs and gene delivery, tissue engineering, biomaterial coating and separation of cells and biomolecules (Bacakova et al., 2018).

Separation of biomolecules involves processes like purification and fractionation of proteins, aminoacids, nuclei acids, *etc*. Biomolecules as amino acids, in particular α-aminoacids, are fundamental for the human body because represent the main building units of proteins. According to their type, number and sequential bond order, aminoacids can originate different type of proteins. Among the 22 aminoacids, which are usually of biological interest, only several of them can be synthesized by the human body; whereas some others, defined essential aminoacids, have to be food supplied. Phenylalanine, threonine, tryptophan, methionine, lysine, leucine, isoleucine, histidine and valine are the 8 essential aminoacids.

Based on the previous statements, it emerges the important role played by aminoacids in the field of industries where they are usually employed as supplements to stock feed and to improve the quality of proteins in food technology (Munsch et al., 2001). Since their efficiency in these fields is strongly related to their purity level, separation and purification

are crucial tasks (Meng et al., 2004; Munsch et al., 2001). Commonly these two objectives are reached by means of classical procedures such as chromatographic and electrophoresis methods, (Poinsot et al., 2010; Zheng et al., 2003) using organic resins (Anasthas et al., 2001), silica particles (Saikia, 2008), carbon nanotubes (Ganji, 2009), magnetic silica nanoparticles (Cheng et al., 2006), as well as gold (Liedberg, et al., 1985) and copper (Poinsot et al., 2010; Zheng et al., 2003; Ihs et al., 1990). Only more recently, adsorption from solutions into molecular sieves, such as zeolites Y, ZSM-5, β (Wijntje et al., 2007; Krohn and Tsapatsis, 2005; Titus et al., 2003; Munsch et al., 2001), and mesoporous materials (Lacasta et al., 2011, Gao et al., 2008) is becoming increasingly widespread in separation and purification processes. This because porous materials allow reducing the loss of desired products that usually occurs during the adsorption/desorption cycles constituting these processes.

Zeolites are considered well performing in this field due to their high surface area, high specific capacity, adsorption selectivity and mechanical, biological, chemical and thermal stability. High thermal stability is required since loaded zeolites are usually regenerated through thermal treatment, a low cost process that does not affect the original adsorption properties (*e.g.*, Rodeghero et al., 2017a; Rodeghero et al., 2017b; Sarti et al., 2017; Martucci et al., 2015; Leardini et al., 2014).

Based on the pores dimension, zeolites are classified as small, medium, large and extra-large types. According to Flanigen et al. (2001), *small pores* zeolites are those with channels defined by 8-membered rings (8R) with free diameter ranging from 3.5 and 4.5 Å. *Medium pores* refers to 10-membered ring (10R) channels with free dimensions in the range 4.5 - 6 Å. *Large pores* consists of zeolites defined by 12-membered rings (12R) with free diameters ranging from 6 to 8 Å. Finally, the *extra-large pores* category is characterized by 14 or larger membered-rings (14+R) pore openings (Casci, 1994; Davis et al., 1989; Newsam, 1986). Primo and Garcia (2014) report that along with the dimension of the pores, the geometry of the channels is of primary importance in determining the intracrystalline diffusion coefficient of the molecules. Indeed, the diffusion in monodirectional zeolites (like zeolite L or mordenite) is more difficult than in bi- and tri-directional zeolites (such as ferrierite, ZSM-5 or omega). In the case of 1-dimensional channel systems, the molecules diffusion can be hindered by blocking effects. On the contrary, the diffusion in open 3-dimensional zeolites is easier because of the possibility of accessing cavities through independent windows (Primo and Garcia, 2014). As a consequence, different pores systems with a well-defined structure make zeolites excellent shape selective materials. Besides, the hydrophobic or hydrophilic nature of this class of

materials is fundamental in determining the zeolites sorption properties towards specific organic compounds from gas phases or water solutions.

Zeolites used as sorbent media for α-aminoacids adsorption usually belong to the classes of medium and large pores, thus providing a large pore volume. To ensure the α-aminoacids adsorption from water solutions and prevent from possible competitive behaviours, the zeolite has to be selected based on the affinity between the sorbent and α-aminoacids. The possibility of the molecules to be adsorbed within the pores strongly depends on their net charge, which can vary from positive/neutral to negative in water solutions (Wu and McMahon, 2008), as well as on occurring host-guest interactions. X-ray and neutron powder diffraction from high-flux sources are excellent tools to obtain detailed information about the structural features of the host-guest compounds as well as to investigate the nature of sorbent-sorbate interactions, which have a fundamental role in stabilizing the molecule within the pores after the adsorption.

Although all the new fields of applications, since the 1960s catalysis for petrochemical industries remains the field in which zeolites are more exploited due to their high potential in promoting catalytic reactions. Indeed, the presence of acid sites, the insertion of tri- or tetravalent heteroatoms in framework positions (Szostak, 1992), and of extraframework charge-compensating cations (*e.g.*, Guzzinati et al., 2018) confers them enhanced catalytic properties. In particular, the possibility to modify both type and location of extraframework cations and incorporate framework heteroatoms, allows modifying structure and properties of acid sites, and in turns both selectivity and catalytic activity of zeolites (Shamzhy et al., 2019).

With respect to *small pores*, which are principally used for catalytic processes involving small molecules such as NOx exhaust removal and methanol conversion to light olefins, large and medium pores zeolites have always been preferred in petrochemical applications. Indeed, channels of high dimensions as well as the presence of additional supercages made large pores zeolites suitable for large-scale processes involving catalytic reactions like fluid catalytic cracking of oil (FCC) for gasoline production and transalkylation for upgrading of platform molecules in the refinery processes. Besides, medium pores zeolites found widespread use as hydrocracking catalysts in processes that require higher shape-selectivity towards organic compounds, such as olefin isomerization, refinery dewaxing or xylene isomerization and ethylbenzene synthesis (Dusselier and Davis, 2018 and references therein).

Ga-exchanged zeolites are of particular interest since represent a breakthrough in two important fields of catalytic processes, such as aromatization of lower alkenes (Cyclar

process) and isomerization of alkylaromatics (Fricke et al., 2000). The most exploited Ga-exchanged catalyst is the ZSM-5 zeolite, and most of the recent literature is focused on the performances of this material towards the compounds aromatization, such as 1-hexene (Fang et al., 2017), acetic acid in a methane environment (Wang et al., 2017), and propane (Liu et al., 2015).

Besides, the Ga-exchanged family of zeolites possesses also suitable catalytic properties for disproportionation and alkylation of aromatics (Ausavasukhi et al., 2009; Bhan and Nicholas Delgass, 2008a; Fricke et al., 2000; Kanazirev et al., 1991). They are also considered well-performing in the field of environmental catalysis for the removal of NOx from gas streams of exhaust engine and the conversion of biomass into biofuels and bio-based chemicals (Shamzhy et al., 2019; Fricke et al., 2000; Yogo et al., 1992).

The main advantage of cation-exchanged zeolites, here in particular Ga-zeolites, is offered by the possibility of having Ga^{+3} in both framework and non-framework positions, thus allowing to enhance the Brønsted acidity once in the framework and simultaneously provide Lewis acidity when located at the extraframework sites (Fricke et al., 2000).

Ga-zeolite catalysts can be obtained through hydrothermal crystallization in presence of a suitable template agent or by means of post synthesis treatments, such as galliation, recrystallization, wet impregnation, chemical vapour deposition (CVD), and ion exchange (Uslamin et al., 2019; Fricke et al., 2000).

Althought hydrothermal synthesis was considered the best experimental procedure to guarantee the incorporation of Ga^{+3} cations in both framework and extraframework positions, it has been reported that post-synthesis methods, such as impregnation or ion exchange, are equally effective in introducing Ga^{+3} at tetrahedral sites through isomorphous substitution (Klik et al., 1997 and references therein).

Strong acidity is the most determining property for well-performing zeolitic catalysts because of the key role of Brønsted acid sites population, distribution and strength in catalytic reactions.

Brønsted acidity can be generated by means of ion exchange processes, firstly introducing NH_4^+ ions in the pores, and then heating the zeolite to desorb NH_3 molecules to promote the H^+ ions settlement (Chester and Derouane, 2009). Less frequently, through thermal degradation of the organic structuring agent in case of alkylammonium-templated zeolites, when synthesis is carried out without alkaline ions. The originated bridging $^{[IV]}$[Si(OH)Al] stabilize adsorbed species through van der Waals interactions and it accounts for an enhanced reaction selectivity (van Santen and Kramer, 1995). In catalytic reactions, the thermal stability is the main requirement to ensure the catalysts long-term durability, thus

preventing from possible deactivation processes, and allow regeneration through thermal treatment. Indeed, it is common knowledge that catalytic reactions are usually performed at high temperature, usually between 300 and 600 °C, as well as the thermal regeneration.

Based on this, an accurate determination at the atomic scale of Brønsted acid sites distribution, population, strength, and stability is required to understand mechanisms that are the basis of catalytic reactions (Lukyanov et al., 2014; Liu et al., 2011; Bhan and Iglesia, 2008b; Nash et al., 2008). Neutron powder diffraction is the most efficient experimental method to probe the location of Brønsted acid sites because of the strong interactions between neutrons and deuterium nuclei that accentuate the diffracted intensities. Besides, the knowledge of the catalyst structural response to the heating process is fundamental in the design of well-performing zeolite catalysts. *In situ* synchrotron powder diffraction is the ideal technique to obtain a continuous picture of the structural response of zeolites upon heating (Cruciani, 2006). The *real time* monitoring of the variations of tetrahedral bond distances and intertetrahedral angles upon dehydration and expulsion of ammonium ions and template molecules as a function of temperature provides insights on the formation of zeolites acid form.

Since in literature medium and large pore zeolites are considered the most performing catalytic and sorbent materials, in this thesis five zeolites belonging to those classes were selected. In particular, those most commonly employed and investigated in both catalytic large-scale processes and adsorption studies for environmental remediation or biotechnological applications were chosen, respectively: ZSM-5 (MFI) and ferrierite (FER) as representative of the *medium pores*, whereas L (LTL), mordenite (MOR) and omega (MAZ) for the *large pores*.

Since its discovery and synthesis, ZSM-5 zeolite is the most common employed catalyst in petrochemical industries. Besides, its use as sorbent material in the field of environmental remediation processes and more innovative applications is still increasing. Beyond the ZSM-5, ferrierite, mordenite and omega zeolites are catalytically performing as well, each of that in a different and specific large-scale process. Besides the catalytic applications, sorptive properties of these zeolites are mainly investigated for water depollution from emerging contaminants (*i.e.*, mordenite and ferrierite) and adsorption of gases from air (*i.e.*, omega). Finally, the interest towards the L zeolite in the field of cutting-edge applications, such as the development of optical devices is continuously growing. Further detailed information on the newest applications of each zeolite studied are available in Chapter 3 - Materials.

Samples object of this thesis were provided in different forms and investigated by using different experimental approach. For several of them the emphasis was posed on their catalytic properties; besides, for others, the attention was focused on their adsorption capacity towards organic molecules, such as amino acids.

The experimental results are reported in Chapter 5 (*Experimental*) that was divided into different sections devoted to the presentation of a specific zeolitic system. In general, subparagraphs of *Experimental* chapters are *samples*, *data collection* and *refinement strategy*, respectively. When carried out, the procedures used for the samples preparation are also described. Then, it follows the presentation of data obtained through the experimental approach used.

Among the 8 systems here presented, only the *System 8 - Insights on Ga-zeolite catalysts: X-ray powder diffraction and absorption spectroscopy characterization at ambient conditions*, was already published on an international peer-reviewed scientific journal and the title given to the system corresponds to that of the publication; only few variations in the order of the text were applied (Beltrami et al., 2019).

Below are reported the 8 systems investigated and the main goals would be achieved.

System 1: four samples of TPA^+ templated ZSM-5, characterized by different Si/Al ratios, were investigated through *in situ* synchrotron X-ray powder diffraction to follow the progressive catalyst activation. Indeed, along with the monitoring of the structural features evolution upon heating, the continuous data collection allowed to determine the temperature of the template decomposition, hence the temperature of the catalyst activation.

System 2: four samples of protonated ZSM-5, with different Si/Al ratios, were investigated through *in situ* synchrotron X-ray powder diffraction to determine structural changes undergoing at high temperature, which can give insights about distribution and number of Brønsted acid sites.

System 3: two of the ZSM-5 samples investigated in the previous system were selected to study their adsorption properties towards the L-lysine aminoacid. Room temperature synchrotron X-ray powder diffraction was used to characterize the sorbent structure after the amino acid adsorption, quantify the compound adsorbed (*i.e.*, along with adsorption studies), probe the host-guest interactions and study the influence of zeolite pore size and structure on the amino acid selectivity.

System 4: a sample of L zeolite in its as-synthesized, precursor and acidic form was characterized through neutron powder diffraction to determine the amount of the aluminium in framework positions and its distribution between the tetrahedral sites as well

as concentration and location of Brønsted acid sites. Besides, the structural characterization of the acidic L zeolite was supported by a computational modeling.

System 5: the same acidic L zeolite was investigated through *in situ* synchrotron X-ray powder diffraction to study the dehydration process and its structural behaviour upon thermal treatment, thus allowing making hypothesis on the distribution of Lewis acid sites.

System 6: the as-synthesized L zeolite was characterized through synchrotron and neutron powder diffraction after the L-lysine adsorption to highlight the structural features of the host and guest compounds, the amount of amino acid adsorbed (*i.e.*, by performing also adsorption studies) as well as to investigate the nature of sorbent/sorbate interactions.

System 7: the zeolite omega in its NH_4-form was investigated through *in situ* synchrotron X-ray powder diffraction to study the thermal behaviour upon heating, continuously monitoring the evolution of the material induced by calcination of the ammonium ions. The information gained, which provides indications about the activation process, was then combined with the structural characterization of the calcined and deuterated omega via neutron powder diffraction. This multidisciplinary approach by non-conventional sources can exhaustively highlight both activation and formation of acidic sites as well as determine the number and location of Brønsted sites in the calcined D-omega.

System 8: Ga-exchanged L, mordenite and ferrierite were investigated combining X-ray powder diffraction from laboratory source, X-ray absorption spectroscopy and adsorption studies. The multidisciplinary approach allowed to investigate the cation-exchange properties of the three zeolites, to characterize the zeolites structure at ambient conditions, locate and quantify gallium cations in framework and non-framework positions, determine the presence of water molecules completing the extraframework Ga^{+3} coordination and highlight host-guest interactions.

CHAPTER 2. Zeolites: relation between structure and properties

The strong relation occurring among structural features, chemical composition and exploitable properties of zeolites is widely argued in the first chapter of the *Introduction to zeolite science and practice* (McCusker and Baerlocher, 2001). The authors underline that the most known properties (*i.e.*, sorption capacity, catalytic activity, shape selectivity and ion exchange) strongly depend on their unique microporous structure and their chemical composition. The pores system built on cavities and/or channel, whose shape and size depends on the framework types as well as on the different arrangement and volume of the building units, makes zeolites outstanding molecular sieves and shape selective catalysts. Besides, the variable chemical composition of the zeolites framework affects properties such as hydrophobicity and/or hydrophilicity as well as the acidic character (*i.e.*, concentration and nature of catalytic active sites).

Therefore, considering the role that both structural and chemical features have in determining the specific properties of zeolites, the deep knowledge of framework types and structures (*i.e.*, defined as the connectivity of the tetrahedrally coordinated atoms and the arrangement of framework types, respectively) and crystal chemistry of zeolites is mandatory to control and optimize their unique properties.

2.1. Generalities about structure and crystal chemistry

The three-dimensional framework of the zeolites is built on Primary Building Units (PBUs) (Baerlocher et al., 2007; Meier and Olson, 1968), which consist of TO_4 corner-sharing tetrahedra. According to the CNMMN (*i.e.*, Commission on New Minerals and Mineral Names) (Coombs et al., 1998) definition, it is allowed the presence of not shared apical framework oxygen atoms when saturated by H (thus forming OH groups) or substituted by F atoms.

Based on the PBUs arrangement, different framework types that describe the disposition of the tetrahedra in the highest possible symmetry (topological symmetry) can be obtained.

Besides the PBUs, the zeolite framework is also described in terms of Secondary Building Units (SBUs), which are structural units constituted by a variable number of PBUs that repeat regularly to build the zeolite framework (Baerlocher et al., 2007; Meier and Olson, 1968). Up to now, 23 different types of SBUs are known.

Starting from the same SBU, according to the different space distribution, numerous structural types can be obtained. Indeed, the connection between the SBUs determines the formation of different chains (from that connection arises the formation of infinite layers) (Gottardi and Galli, 1985) and polyhedra (when closed, defined as *cages*, such as cancrinite,

sodalite, gmelinite cages, *etc*.; Tsitsishvili et al., 1992), also known as Composite Building Units that connected each other form the infinitely extended frameworks.

Independently from the structural type, the zeolites framework is defined as a tridimensional network built on interconnected cavities (*i.e*., finites or ideally infinites) with opening dimensions lower than 20 Å; these dimensions make zeolites microporous materials.

However, different structural types present different pores systems, characterized by different dimensions, geometry and path (*e.g*., straight, sinusoidal). In general, the channel dimensions, which control the access of the molecules within the zeolite framework, are defined in terms of rings diameter. The number of tetrahedra that delimit the ring determines the diameter width, therefore, the higher the tetrahedra number, the higher the ring dimensions.

Based on this, four different categories of zeolites can be highlighted (Flanigen, 2001): 1) small pores, 2) medium pores, 3) large pores and 4) extra-large pores. Small pores are defined by 8MR with mean dimensions of 4 Å, medium pores by 10MR with free diameter of 5.5 Å, large pores by the presence of 12MR with a free diameter of 7.5 Å whereas, extra-large pores are characterized by 14 or larger membered-rings, such as SSZ-53, ITQ-44, ITQ-43 and ITQ-37 whose pores dimension is defined by 14, 18, 28 and 30MRs, respectively (Bellussi et al., 2013 and references therein).

Based on the way membered-ring channels are interconnected among them, zeolites can be characterized by mono- bi- or three-dimensional channels system.

The extraframework species hosted in the zeolite channels are usually polar molecules (*e.g*., H_2O), *n*-valent cations and/or organic compounds. The immobilization of these species occurs through weak hydrogen bonds with framework oxygen atoms. The content of water and extraframework cations that can be hosted strongly depends on the chemical composition, in particular on the Si/Al ratio. This ratio ranges from 1 to 7 for natural zeolites and from 1 to infinite for synthetic ones. The lowest Si/Al threshold ratio is defined by the Loewenstein rule (Loewenstein, 1954), which claims that the occurrence of two Al^{+3} coordinated tetrahedra bonded each other by sharing apical oxygens is unfeasible.

When Si/Al=1 (50% Si^{+4} and 50% Al^{+3}), silicon and aluminium tetrahedra alternate regularly, thus meaning that each [SiO_4] tetrahedron is bonded to four [AlO_4] tetrahedra and *vice versa*. The ordered alternation of silicon and aluminium within the zeolite framework leads to clearly identify the sites in which Si^{+4} and Al^{+3} are located. On the contrary, in presence of Si/Al >1, the exact localization of the two cations becomes more difficult, up to unfeasible, because of the coexistence of different scenarios in which the [SiO_4] are bonded with different number of [AlO_4] and [SiO_4] tetrahedra.

Variations in Si/Al ratios also affect some of the zeolites fundamental properties, such as thermal stability, hydrophobic or hydrophilic character and ion-exchange capacity. In particular, the thermal stability increases up to 1300 °C for higher Si/Al ratio as well as the hydrophobic behaviour. On the contrary, the ion exchange capacity is lower for zeolites with high Si/Al ratio (Flanigen, 2001).

Although commonly the T site is occupied by Si^{+4} and Al^{+3}, other tetrahedral cations, such as P, B, Ge, Ga, *etc*. can be incorporated in the zeolite framework, demonstrating the possibility to extend the family of zeolites to a wide number of materials with variable chemical composition (Gatta and Lotti, 2019; McCusker and Baerlocher, 2001).

In general, when cations hosted at the center of the tetrahedron are Si^{+4} and/or Al^{+3}, the mean tetrahedral T-O bond distances are equal to 1.61 and 1.72 Å for Si-O and Al-O, respectively. Besides, the mean amplitude of the O-T-O and T-O-T angles are 109.4° (Liebau, 1985) and 154° (Wragg et al., 2008), respectively.

For the synthetic zeolites, defined as aluminosilicates with an open framework, the following general formula given by the CNMMN, can be assumed:

$$\boldsymbol{M_x N_y [T'_p T''_q O_{2(p+q+\ldots)-\varepsilon} (OH)_{2\varepsilon}]^* nQ,}$$

where: *M* is an exchangable cation, such as Na, Ca, K; *N* non-metal ions, like organic template; T'_p and T''_q represent the cations in tetrahedral coordination (usually Si, Al, P, Ga, Ge, *etc*) and Q the adsorbed molecules (*e.g*., H_2O).

2.2 Insights on catalytic properties

Zeolites in catalytic processes are considered well performing due to their high adsorption selectivity, which allows controlling the access of the molecules to the active catalytic sites. The shape selectivity property strongly depends on the zeolites structure; indeed, the presence of channels with different path and shape (*e.g*., sinusoidal or straight channels) and pore of different dimensions can limit or enhance the diffusion of the molecule, thus determining unique selectivity effects. Therefore, the access to the framework voids is allowed only to molecules characterized by shapes and sizes adapt to the framework topology selected. During the catalytic reaction, the zeolites selectivity can be expressed into three different scenarios.

The selectivity can be towards: 1) the reagent (I mechanism), when zeolites act as molecular sieve towards reagent compounds allowing the access to that with shape and dimensions compatible with the pore system; 2) the product (II mechanism), when the diffusion throughout the pores is allowed only to the reaction products; 3) the transition state (III

mechanism), meaning that among the different possible reactions, only those involving transition states (*i.e.* the most hindered species occurring in the reaction pathway) sterically compatible with the size and the shape of the pore close to the active site are allowed, while the other are inhibited (Moshoeshoe et al., 2017; Sugi and Ajayan, 2015).

Besides the imposition given by the zeolites crystal structure, the second factor that mainly affects the catalytic activity of the zeolites is the acidity, in turn deriving from the presence of trivalent metal ions in the framework. The acid sites are classified according to the model of Brønsted and Lewis (Figure 2.1). The first general discrimination is based on their different nature: Brønsted sites can donate protons, whereas Lewis sites can accept nonbonding electrons, hence are electron-pair acceptors.

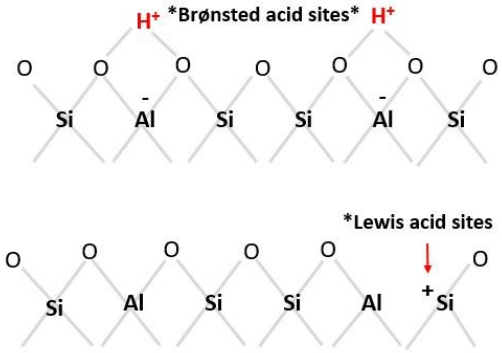

Figure 2.1. Representation of Brønsted and Lewis acid sites.

However, the determination of their position, acid strength (*i.e.*, defined as deprotonation energy, DPE, which is referred to the energy required for the separation of a proton from its conjugate anion (Jones and Iglesia, 2015)), concentration, accessibility and interaction with adsorbed molecules is fundamental to determine the level of catalytic activity of the zeolite. According to the model mentioned before, Brønsted acid sites (*i.e.*, BASs) are described as protons (H^+) positioned on framework oxygen atoms that determine the formation of bridging hydroxyl groups (Si-OH-Al), whereas Lewis sites (*i.e.*, LASs) are recognized as tri-coordinated framework or extraframework aluminium that can accept electron-pairs. The 3-fold coordinated aluminium, which is the source of the Lewis acidity, is obtained through the zeolite calcination (*i.e.*, Lewis sites originate between 550-600 °C) or steaming. Although at high temperature zeolites can possess simultaneously BASs and LASs, the Lewis acidity is prevalently related to acid zeolites obtained through dealumination processes (Chester and Derouane, 2009).

The number of Brønsted and Lewis acid sites strongly depends on the Si/Al ratio: the higher the Si/Al ratio (*i.e.*, the lower the aluminium content), the higher proton crowding within zeolite pores (*e.g.*, Yu et al., 2019). On the contrary, as reported by Sastre et al., (2000), to

evaluate the acidity it must be taken into account the remarkable contribute given by the short- and long-range interactions of the acid sites with the surrounding atom species.

For industrial applications employing zeolites as acid catalysts, especially for that related to the acid-catalyzed reactions of cracking, alkylation, isomerization, *etc*. of hydrocarbons, the presence of hydroxyl Si-OH-Al groups is the main requirement. The main method to form Brønsted acid sites in zeolites is the exchange of the extraframework charge-compensating cations by ammonium ions and subsequent thermal treatment (T > 300 °C) with elimination of ammonia and formation of the Si-OH-Al groups (Hunger et al., 2010; Rabo and Schoonover, 2001). In the case of alkylammonium-templated silica-richer zeolites, thermal degradation of the organic structuring agent directly provides the Si-OH-Al sites upon elimination of more or less complex organic fragments (*e.g*., Bourgeat-Lami et al., 1992).

In both cases, the thermal treatment is used to activate the zeolites and obtain the acid form. Based on what reported so far, it is easy to understand that to locate with high accuracy the acid sites within zeolite micropores and to investigate the structure–activity relationship is of paramount importance for elucidating the mechanism of zeolite-catalyzed reactions and their kinetics. Indeed, an accurate determination at the atomic scale of both acid sites distribution and stability is required to better investigate the zeolites catalytic behaviour, to improve their use as catalysts as well as to understand processes occurring during the zeolites activation.

2.3 Insights on cation-exchange properties

Due to their excellent cation exchange behaviour, zeolites are usually employed as ion exchangers for purification of water and wastewater from heavy metal ions and determination of soils fertility. This property arises from the isomorphous substitution of silicon by aluminum in tetrahedral coordination that determines a framework negative charge, which has to be counterbalanced introducing cations within cavities and/or channels. The cation-exchange process is defined as a reversible cations interexchange between two different *media*. One of the two, the exchanger, is not soluble in the medium within that the exchange occurs.

The reaction can be summarized as follows:

$$Z_A\, B_{(z)}^{Z_B^+} + Z_B\, A_{(s)}^{Z_A^+} <=> Z_A\, B_{(s)}^{Z_B^+} + Z_B\, A_{(z)}^{Z_A^+}$$

where, z_A and z_B are the A and B exchangeable cations and *z* and *s* are the coefficients referring to zeolite and aqueous solution. The reaction proceeds until the equilibrium is

achieved. The number of extraframework cations hosted depends on the amount of negative charge given by the framework aluminium. In a monocationic solution, the zeolite will contain exclusively the type of cation present in the solution whereas, in presence of polycationic solutions, the zeolite will select that more adapt to its chemical properties and structural features. Indeed, the cation exchange capacity (CEC, expressed *meq/g*) does not depend only on the zeolite chemical composition (*i.e.*, the aluminium content), but also on the crystal structure and the accessibility and distribution of extraframework exchange sites. Additional factors governing the exchange behaviour are the zeolite framework electrostatic field strength, nature and charge density of cations, composition and pH of contacting solution and finally, the operating conditions (Moshoeshoe et al., 2017 and references therein; Perego et al., 2013).

2.4 Insights on sorption properties

The use of zeolites as sorbent materials requires the knowledge of the differences existing between physical and chemical adsorption processes (physisorption and chemisorption, respectively). In general, adsorption processes are defined as a transfer phenomenon of molecules from a gas or fluid bulk (adsorbate) to the surface of liquid or solid phase (adsorbent).

In the case of the physisorption process (*i.e.*, also known as surface adsorption) the phenomenon is due to the presence of unbalanced valence forces of atoms at the surface that attract molecular species. The retention of the molecules once in contact with the solid surface is determined by weak intermolecular interactions, such as dipole-dipole and Van Der Waals forces, involving interaction energies in the order of few KJ/mol (ΔH=20-40 KJ/mol). Due to the weak interactions between the adsorbent and the adsorbate, the physisorption is significant at low temperatures (Figure 2.2), occurs with rapid kinetics, it is a reversible process, not site-specific. Furthermore, in these conditions, the adsorbate on the solid surface can dispose as monolayer or multilayer.

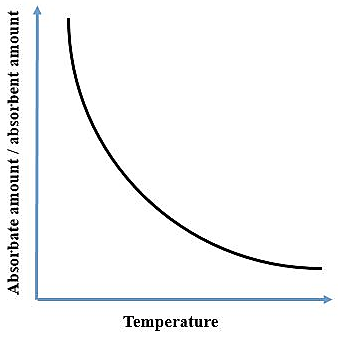

Figure 2.2. Relation between physisorption and temperature.

The chemisorption involves stronger chemical interactions or chemical bonds, such as covalent bonds, which are characterized by higher enthalpy of adsorption (ΔH=200-400 KJ/mol). The process can take place in a wide range of temperature up to a threshold T (°C) above that the adsorption becomes less efficient (Figure 2.3).

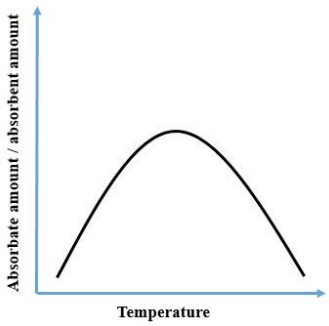

Figure 2.3. Relation between chemisorption and temperature.

It occurs with slower kinetics; it is irreversible and highly site specific. Furthermore, it allows the formation of monolayer of adsorbate on the adsorbent (Kralik, 2014 and references therein). As concerns zeolites, the adsorption is not exclusively related to the surface of the material but also to the uniform distribution of the molecules throughout the bulk. However, the chemisorption can occur exclusively when the adsorbed compounds have dimensions similar to that of the pores, thus allowing establishing favourable host-guest interactions. Otherwise, whether the dimensions of the molecule are not compatible with that of the channels, due to its steric hindrance, the creation of such bonds cannot be enabled, thus preventing from irreversible adsorptions.

Usually the adsorption is limited at the equilibrium conditions and the base mechanism can be rationalized in four different steps:

1) transfer of the adsorbate from the gas or fluid bulk to the surface film which covers the adsorbent particles;

2) the adsorbate passes through the surface film;

3) from the adsorbent particles is transferred within the adsorbent material though the pore system;

4) the adsorbate within the pores establishes interactions with the inner surface of the adsorbent.

The theoretical adsorption capacity (C_s) can be calculated by using the Eq.1:

$$C_s = M_{(adsorbate)}/M_{(adsorbent)} \quad (1)$$

where *M*=mass (kg).

In order to design efficient adsorption systems, adsorption isotherms are used to determine the affinity of the adsorbent and the C_s adsorption capacity. They are based on the relation, at a given temperature, between the amount of solute adsorbed (*i.e.*, for adsorbent unit, q_e) and the concentration of the solute in solution. When the adsorption process is favourable, q_e increases whether C increases although without displaying a linear trend (Figure 2.4).

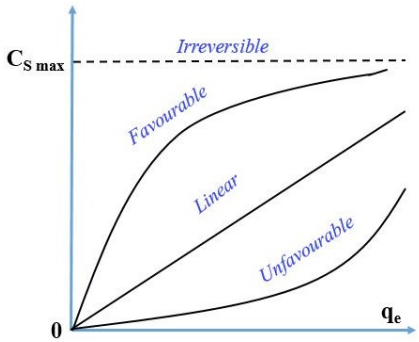

Figure 2.4. Relation between C_s and q_e: adsorption conditions.

Depending on the monolayer or multilayer disposition of the adsorbate molecules, on the favourable or unfavourable conditions and the state of the phases involved (*i.e.*, solid, liquid or gaseous), different experimental adsorption isotherms can be used, such as Langmuir, Henry, Tempkin and Freundlich., *etc*. (Saadi et al., 2015).

Furthermore, each adsorption process has to be subjected to the analysis of the adsorption kinetics in order to understand the applicability of the sorbent material towards the compound selected. The kinetics of the sorption processes can be described through different mechanisms. Therefore, a variety of kinetic models can be employed to describe solid/solution adsorption systems: the most used are pseudo first-order (PFO), pseudo second-order (PSO) and Elovich models. Among these equations, PFO e PSO are the most employed in modeling adsorption of cations onto microporous materials. The instantaneous rate of reaction depends on the adsorbate concentration in the solid phase at time t, and on the square of the adsorbate concentration in PFO and PSO, respectively (Moshoeshoe et al., 2017 and references therein). In general, the PFO and PSO models represent the relationship between the adsorbate in solution and the occupations of the adsorbent active sites in the adsorption process. Specifically, the PFO model describes a few occupations of the adsorbent active sites, while the PSO model represents most occupations of the adsorbent

active sites. The latter model describes a system in which the adsorbent is abundant with active sites. Consequently, the adsorption onto the active sites is the main mechanism and rate-controlling step of the adsorption processes.

The efficiency of zeolites as sorbent media depends on several factor. In principle, on the surface area, intended as the portion of the total area involved in the adsorption process: the higher the surface area, the higher the sorption capacity. Although as general rule it can be valid, it must be take into account further parameters, such as the pH, since the adsorption capacity towards organic substances changes in function of the basicity or the acidity of the solution in which the adsorption process is performed. The temperature is another variable playing a fundamental role: adsorption processes are enhanced at low temperature whereas high temperatures tend to promote exothermic reactions that inhibit the zeolite sorption capacity.

Further important factors are related to the chemical properties of the solute and its solubility; indeed, for example to favour the adsorption of inorganic compounds are required solutes in neutral or ionic form, whereas in presence of organic compounds it is fundamental to consider their solubility. Besides, also the solute structure is determinant; indeed, when the competition is between molecules with similar dimensions, some are favoured due to their structure. This is the case of aromatic compounds that, although have similar dimensions of the aliphatic, are preferentially adsorbed in presence of both the compounds due to their structural features. However, whether the aim is to favour the adsorption of the organic compounds (*i.e.*, in the case of adsorption processes from water solution) than that water, organophylic as well as hydrophobic zeolites have always to be preferred (*e.g.*, Rodeghero et al., 2019; Pasti et al., 2018; Pasti et al., 2016; Martucci et al., 2015).

CHAPTER 3. Materials

In the next paragraphs are presented the structural features and the main applications of all the zeolite samples investigated in this thesis. As introduced in the first chapter, the attention was focused on medium and large-pores zeolites. As *medium pores*, were selected ZSM-5 and ferrierite. Besides, L, mordenite and omega were selected as representative of *large pores*.

3.1. Medium pores zeolites

3.1.1. ZSM-5 (MFI)

ZSM-5, the synthetic counterpart of the mutinaite mineral, $[Na_{2.76}K_{0.11}Mg_{0.21}Ca_{3.78}][Al_{11.20}Si_{84.91}]\bullet 60H_2O$ (Vezzalini et al., 1997), is characterized by a MFI framework topology and a 3-dimensional channel system. It belongs to the so-called pentasil zeolite family (Olson et al., 1981; Kokotailo et al., 1978) and its ideal chemical formula is $[Na_n][Al_nSi_{96-n}\ O_{192}]\bullet(H_2O)_{16}$ n<27 (Baerlocher and McCusker, 2017). The structure is built on the intersection of two set of tubular channels, both defined by 10-membered ring openings: the straight channel (SC channel), parallel to the [010] direction and the sinusoidal channel (ZZ channel), parallel to the [100] direction. Free diameter of SC and ZZ channels are 5.3 × 5.6 Å and 5.1 × 5.5 Å, respectively.

The topological symmetry of the as-synthesized ZSM-5 (*i.e.*, intended as ZSM-5 with tetrapropylammonium template molecule within the channel system) is the orthorhombic *Pnma* (*i.e.*, lattice parameters at ambient conditions are equal to *a*=20.022(2) *b*=9.899(2) and *c*=13.383(1) Å), with 12 crystallographically independent tetrahedral sites in the unit cell (van Koningsveld et al., 1987) (Figure 3.1).

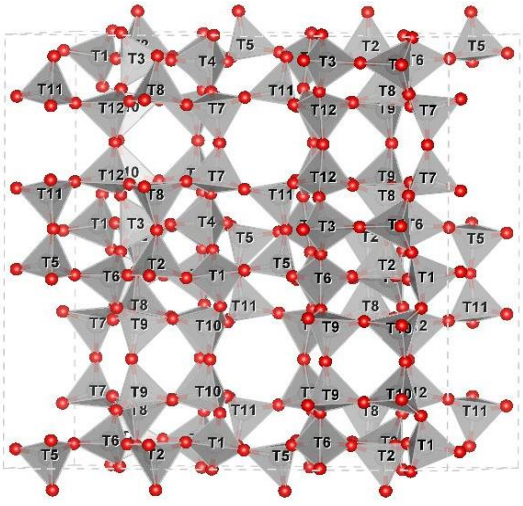

Figure 3.1. Distribution of the 12 tetrahedral sites in the ZSM-5 zeolite.

When the TPA^+ ions are burned off by calcining the as-synthesized form, typically at 500 – 550 °C, the symmetry of the ZSM-5 zeolite can be unchanged or lowered to the monoclinic (s.g. $P2_1/n$) on the basis of the Si/Al ratio, hence the Al^{+3} content.

Whether the crystal structure of ZSM-5 is lowered to the monoclinic space group, at high temperature the structure will be affected by a polymorphic displacive phase transition from the monoclinic $P2_1/n$ to the orthorhombic *Pnma*, $Pn2_1a$ or $P2_12_12_1$ space groups (*i.e.*, m→o) (Kamiya et al., 2013; Nishi et al., 2005; Reck et al., 1996; Van Koningsveld et al., 1996; Klein et al., 1994; Van Koningsveld et al., 1989a;). The m→o phase transition is induced by several factors, such as type and amount of sorbate molecules, when present in zeolite channels, and chemical composition. Indeed, the amount of framework Al^{+3} has a fundamental role in determining the m→o transition temperature; the latter usually decreases as a function of the Al^{+3} content increasing.

The nature of this m→o phase transition has been recently investigated through the analysis of the spontaneous strain variation by Ardit et al. (2015, 2018) on a high-silica ZSM-5 hydrophobic zeolite (Si/Al ratio = 140). H^+-ZSM-5 can be ascribed to a ferroelastic material, which presents a polymorphic phase transition (from the ferroelastic monoclinic to the paraelastic orthorhombic phase) with tricritical character (Ardit et al., 2015). Analyses on the thermodynamic properties of the m→o phase transition, probing that temperature of transition and its thermodynamic features strongly depend on the Si/Al ratio as well as the different nature of organic compounds encapsulated and the host-guest interactions (Ardit et al., 2018).

Concerning the applications, the interplay between structural features, excellent sorptive and catalytic properties, made the ZSM-5 the most exploited zeolite in industrial processes. Since the last three decades, it recovers a fundamental role as catalyst (*i.e.*, in both hydrogen and cation-exchanged form) in many catalytic reactions concerning the petroleum refining, such as the most known Fluid Catalytic Cracking (*e.g.*, Degnan et al., 2000). Besides, in the field of petrochemicals, it is mainly used for xylene isomerization, toluene disproportionation (*e.g.*, Uguina et al., 1991), methanol to propylene (MTP) (*e.g.*, Rostamizadeh et al., 2015), to gasoline (MTG) (*e.g.*, Biorgen et al., 2008) and to olefin (MTO) (*e.g.*, Zhang et al., 2011) conversion. Very recently, a cation-exchanged ZSM-5 was successfully employed in the field of the selective catalytic reduction (SCR) of N_2O by CO, thus demonstrating the high potential of the catalyst also in the abatement of greenhouse gas (You et al., 2020). Besides, as reported by Liu et al. (2020), ZSM-5 is showing excellent performances also in the field of biomass conversion, where it is investigated as catalyst for the conversion of lignocellulosic biomass into bio-oil through fast pyrolysis.

The ZSM-5 zeolite is also considered a competitive material in terms of adsorption properties. Indeed, its structural features make this zeolite a promising adsorbent for several types of organic compounds considered harmful contaminant of water and wastewater, such as chlorinated volatile organic compounds (Martucci et al., 2015), toluene (Rodeghero et al., 2016), 1,2-dichloroethane (Martucci et al., 2015) and antibiotics (Blasioli et al., 2014).

3.1.2. Ferrierite (FER)

Ferrierite is a pentasil zeolite characterized by a FER framework topology and a 2-dimensional channel system (Baerlocher and McCusker, 2017). The ideal chemical formula is $[Mg_{0.5}Na,K,Ca_{0.5}][Al_6Si_{30}O_{72}]\bullet 20H_2O$. It crystallizes in the orthorhombic *Pnnm* and *Immm* or the monoclinic $P2_1/n$ space groups, according to the different chemical composition (*i.e.*, Mg-, K- and Na-ferrierite, respectively) (Alberti et al., 1987; Gramlich-Meier et al., 1985).

Cell parameters at ambient conditions are a=18.02(1), b=14.20(1) and c=7.54(1) Å. The framework is built on the intersection of 10-membered and 8-membered ring channels (10 and 8MR) running parallel to the [001] and [010] crystallographic directions, respectively. Free diameter of 10MR and 8MR channels range from 4.2×5.4 Å and 3.5×4.8 Å, respectively (Vaughan, 1966). 10MR alternating along the *b* direction with the so-called ferrierite cages (*i.e.*, indicated as $[5^8 6^6 8^2]$ cages), structural units originated by the intersection of 8MR and 6MR channels. The zeolite framework is composed by four indipendent tetrahedral sites (*i.e.*, T1, T2, T3 and T4); T2, T3 and T4 build the 10MR channel; besides, along with the T1, T2 and T4 are shared, thus forming the 8MR (Figure 3.2).

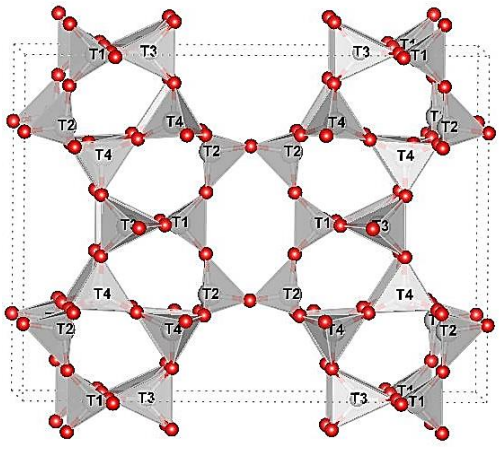

Figure 3.2. Distribution of T1, T2, T3 and T4 tetrahedral sites in the ferrierite zeolite; projection along the [001] direction.

The ferrierite zeolite finds a widespread use in the field of catalysis and environmental remediation. Concerning its use as catalyst, the ferrierite in the hydrogen form is preferred for isomerization of n-butene to isobutene (Xu et al., 1995). Besides, the cation-exchanged

forms (*e.g.*, Co- Ag-ferrierite) are considered suitable for the Selective Catalyst Reduction (SCR) of nitrogen oxides (Ciambelli et al., 2008a; Ciambelli et al., 2008b). More recently, excellent results were also obtained employing ferrierite in the production of olefins from both naphtha and naphtha-related compounds cracking (Bastiani et al., 2013 and references therein). Concerning the environmental remediation processes, Martucci et al., (2014) reported the excellent sorptive properties of this zeolite towards the methyl-tert-butyl-ether (MTBE, an octane-enhancing fuel additive), considered a hazardous water pollutant.

3.2. Large pores zeolites

3.2.1. L (LTL)

L zeolite is a large pore material characterized by LTL framework topology, hexagonal symmetry (*i.e.*, *P*6/*mmm* space group) and monodimensional channel system. It is the synthetic counterpart of the perlialite mineral (Artioli et al., 1990) and the ideal chemical formula is $(K_6Na_3)[Al_9Si_{27}O_{72}]\bullet 21H_2O$ (Baerlocher and McCusker, 2017).

The unit cell dimensions determined at ambient condition are a=18.40(4) Å and c=7.52(3) Å. The framework crystal structure, solved for the first time by Barrer and Villiger, (1969a), is built on columns of cancrinite cages stacked with double 6-membered rings (D6R) along the *c* axis. The 4-rings in these columns are cross-linked to form continuous 12-ring channels (12MR) running parallel to the *c*-direction (*i.e.*, maximum diameter of the channel = 7.1 Å) and separated each other by elliptical 8-membered ring channels. Two independent tetrahedral sites determine the arrangement of the framework: T1 defines the 12MR channel and part of the cancrinite cage, whereas the T2 is shared between the cancrinite cage and the D6R (Figure 3.3).

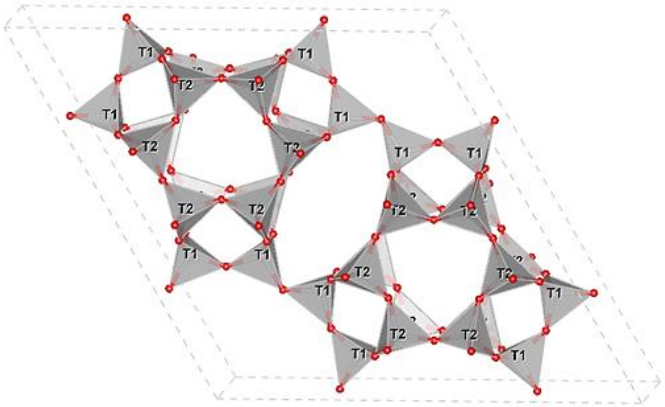

Figure 3.3. Distribution of T1, T2 tetrahedral sites in the L zeolite; projection along the [001] direction.

Due to the one-dimensional geometry of its channels, L zeolite is of great interest in the hydrocarbon conversion catalysis and the development of novel optical devices, such as

luminescent probes, lenses, special mirrors, filters, polarisers, grids, optical storage devices, windows, artificial antenna systems, effect pigments and luminescent concentrators (Zaarour et al., 2019; Yao et al., 2019; Gigli et al., 2018a; Woodtli et al., 2018; Gartzia-Rivero et al., 2017; Tabacchi et al., 2015; Cucinotta et al., 2014; Calzaferri, 2012; Fois et al., 2012; Calzaferri et al., 2003). Lanthanide-exchanged L zeolite can be also widely applied in medical imaging as carriers for paramagnetic Gd^{+3} ions that operate as a contrast promoter in magnetic resonance imaging (MRI) (Li and Li, 2018).

3.2.2. Mordenite (MOR)

Mordenite zeolite is characterized by a MOR framework topology and a 1-dimensional channel system (Baerlocher and McCusker, 2017). The ideal chemical formula is $[Na_2K_2Ca)_4][Al_8Si_{40}O_{96}]\bullet 28H_2O$, although the chemical composition of mordenite is moderately variable and Ca and K are the dominant cations (Deer et al., 2004). The crystal structure was determined for the first time by Maier (1961) studying a natural sample exchanged with sodium (Meier, 1961). Thereafter, many cation-exchanged mordenites were refined, such as Ca- and K-MOR (Mortier, 1976). The structure consists on the combination of single 6-ring sheets linked by single 4-rings. The 1-dimensional channel is defined by 12-membered rings running parallel to the [001] direction interconnected along the [010] direction through 8MR side pockets. Each side pocket links the 12MR through distorted 8MR, which runs parallel to the [001]. This configuration gives rise to two sets of channels running along the [001] direction: compressed 8MR and large 12MR channels.

The topological symmetry of the mordenite is orthorhombic *Cmcm* (Csicsery, 1976), whereas the real symmetry is reduced to $Cmc2_1$ in natural mordenites (Alberti, 1986). The latter space group allows to avoid a straight T-O-T angle, constraining the O8 framework oxygen atom on the inversion center. The framework is built on four indipendent tetrahedral sites and further ten sites, which are attributed to oxygen atoms (Figure 3.4). Cell parameters of synthetic mordenite at ambient conditions are a=18.26(1) Å, b=20.53(1) Å and c=7.54(1) Å.

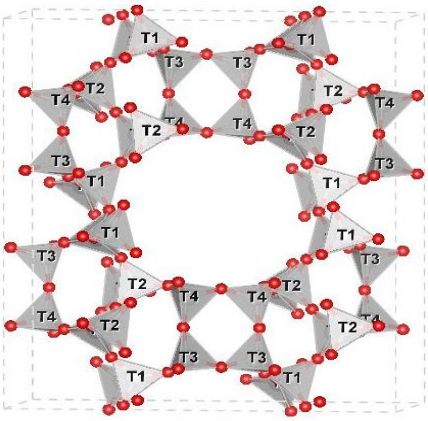

Figure 3.4. Distribution of T1, T2, T3 and T4 tetrahedral sites in the mordenite zeolite; projection along the [001] direction.

Mordenite zeolite, depending on its pore dimensions (*i.e.*, small and large port), is widely used as catalyst, in particular for cracking, (hydro-) isomerization and alkylation reactions in the petrochemical industries (Ban et al., 2010). Besides, in literature it is reported that mordenite acts also as excellent sorbent material for the removal of hydrocarbons and halogenated compounds, chlorinated volatile organic compounds (VOCs) and sulfonamide antibiotics from water. In particular, Arletti et al., (2012) evidenced the high affinity of mordenite towards both MTBE (as also reported by Anderson, 2000) and toluene organic molecules. Besides, Martucci and co-authors highlighted the high sorption capacity towards the 1,2-dichloroethane (DCE) compound (Martucci et al., 2012), the sulfachloropyridazine (Martucci et al., 2013) and the sulfamethoxazole (Blasioli et al., 2014) antibiotics. More sophisticated applications concern the photochemistry: in this field zeolites can be employed as microlasers, optical switches or artificial antenna systems (Simoncic et al., 2004 and references therein). These applications are based on host-guest systems built on photochromic and luminescent dyes intercalated into zeolites. According to Simoncic et al., (2004), mordenite represents a potential host material for the incorporation of dyes.

3.2.3. Omega (MAZ)

Omega is the name given by Union Carbide to a large-pore zeolite also claimed by Mobil as ZSM-4 (Flanigen, 1968). The structure of zeolite omega, whose ideal chemical formula is $(Na_2,K_2,Ca,Mg)_5$ $[Al_{10}Si_{26}O_{72}]\bullet(H_2O)_{28}$, was proposed for the first time by Barrer and Villiger, based on X-ray powder data poorly fitted with the measured intensities (Barrer, and Villiger, 1969b). The exact crystal structure of zeolite omega was determined by Martucci et al., (2003), who confirmed that the zeolite omega presents the MAZ framework topology as the natural analogue mazzite. High-resolution powder diffraction pattern revealed the absence of *hh*2*hl* diffractions with *l*=odd, thus indicating clearly that the exact space group

was $P6_3/mmc$ and not $P6_3/mmm$, as supposed by Barrer and Villiger (1969b), and lattice parameters at ambient conditions reported by the author are a=18.22(1) Å and c=7.63(1) Å. In both omega and mazzite zeolites the Building Unit is the open gmelinite cage, composed of 18 T atoms: three single-connected finite two-T4-ring ladders around a three-fold axis. Open gmelinite cages, related by pure translations, are connected along c by T4-rings (Figure 3.5(a)). Neighbouring gmelinite cages, related by a rotation of 60° around c accompanied by $a1/2c$ shift, are connected in the [001] plane through T5-rings. The lattice contains two crystallographically non-equivalent tetrahedral sites denoted as A (or T2) and B (or T1): sites A (24 per unit cell) in four-membered rings, and sites B (12 per unit cell) in six-membered rings (Figure 3.5(b)).

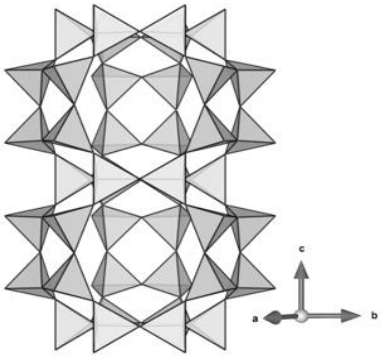

Figure 3.5(a). Gmelinite cages created by six chains connected -along c direction- through framework oxygen bridges.

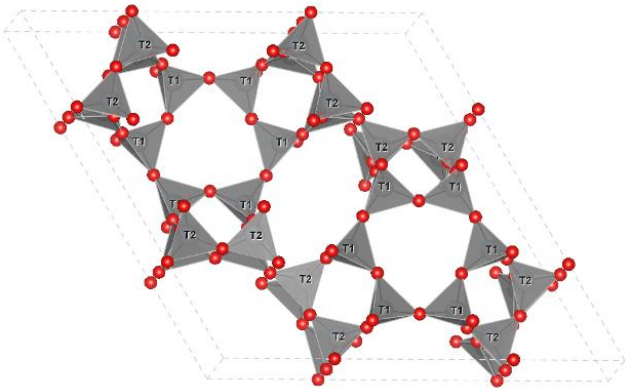

Figure 3.5(b). Distribution of T1, T2 tetrahedral sites in the omega zeolite; projection along the [001] direction.

Since the first synthesis experiments, zeolite omega was employed in the catalytic field for hydrocarbon cracking (Perrotta et al., 1978), hydrocracking (Cole et al., 1973), aromatic alkylation (Flanigen and Kellberg, 1980; Bowes and Wise, 1971), isomerization (Solinas et al., 1983), olefin hydration (Fajula et al., 1984) and toluene conversion (Mavrodinova et al., 1985). Besides, Cu-exchanged omega has recently revealed of being a promising catalyst for the selective conversion of methane to methanol (Knorpp et al., 2018). Only in the last two decades, the sorptive properties of zeolite omega were investigated for adsorption of gas, such as CH_4 and CO (Yamazaki et al., 2000) and more recently, for CO_2 capture and concentration from diluted emission sources (Terrab et al., 2016). The results obtained in this field make the omega zeolite an excellent porous solid for the air pollutant monitoring and the reversible capture of greenhouse gas.

CHAPTER 4. Zeolite characterization: experimental techniques and data process

As reported by Garino and co-authors (2014), the principal experimental techniques currently employed for the structural characterization take advantage of the elastic scattering, in particular diffraction methods (X-rays or neutrons), X-ray absorption spectroscopy (both EXAFS and XANES) and magnetic resonance spectroscopies (such as NMR and EPR). All of these techniques are considered powerful tools when the structure of a material has to be characterized. Besides, the possibility of using these experimental methods in a complementary way offers remarkable advantages, thus allowing to provide more detailed information on the materials structural features. Some of these techniques are applied through laboratory sources, but in several cases the use of synchrotron radiation is more advantageous because of the type of structural information it can provide. In general, X-rays provide information on the spatial distribution of the matter electron density, thus mapping the electron density around the atomic nuclei. Differently, neutrons, which are primarily scattered by atomic nuclei, give direct insights on the nuclear density (Garino et al., 2014).

In particular, the main advantageous prerogative of the third generation synchrotrons lies on the X-rays boost in brilliance (*i.e.*, parameter used to quantify the intensity of the synchrotron beam radiation) as well as on the wide variety of the experimental setups available, thus allowing to perform experiments otherwise difficult to reproduce in conventional laboratories. Indeed, the use of non-conventional sources and different external conditions (*e.g.*, temperature, pressure, presence of electric and magnetic fields, *etc*.) allows to directly monitor chemical and photochemical reactions, working catalysts, phase transitions, *etc*. (Garino et al., 2014; Bordiga et al., 2013; Grunwaldt et al., 2013; Frenkel et al., 2012).

Nowadays, the conventional crystallography can not only deal with materials affected by small deviations from the perfect periodic arrangement of atoms in the crystal lattice, but there is a relevant number of application fields which have to face with systems characterized by short-range order, hence totally or partially disordered structures (Egami and Billinge, 2012; Hodeau and Guinebretiere, 2007). As a consequence, provide additional detailed information also on short-range and partially ordered structures is of primary importance.

EXAFS spectroscopy is an elemental selective technique which can shed light on the local structural environment around the metal ion centres (D'Angelo and Spezia, 2012; Migliorati et al., 2011; Chillemi et al., 2002). The elemental selectivity represents an important advantage in the closer coordination environment of dispersed active sites and a

breakthrough for systems characterized by site-specific short-range order that does not allows the structural characterization through X-ray diffraction (Garino et al., 2014).

In this chapter the experimental techniques and the data process methods applied to study the materials selected for the project are presented. In most cases, non-conventional sources were employed but for the *System 8 -Insights on Ga-zeolite catalysts: X-ray powder diffraction and absorption spectroscopy characterization at ambient conditions*- where data collection was performed on the Bruker D8 Advance diffractometer at the University of Ferrara laboratories, X-ray powder diffraction experiments were carried out at the Elettra (Trieste, Italia), as well as XAS analysis (EXAFS region), and ESRF (Grenoble, France) synchrotrons. Besides, neutron diffraction analyses were performed at the Institut Laue-Langevin (Grenoble, France). All the collected synchrotron and neutron powder patterns were subjected to the same data analysis process, i.e. by means of structural refinements through the Rietveld method (see paragraph 4.4, *the Rietveld method*) using the GSAS-EXPGUI software (Toby, 2001; Larson and Von Dreele, 1994). Furthermore, in the case of the *System 4 - structural characterization of acidic L and its precursor by neutron powder diffraction*, the structural characterization performed on neutron data was combined by a computational modeling of the zeolite structure. A brief introduction of computational approaches used in zeolites modelling is reported in paragraph 4.5, *computational modeling*.

4.1 Synchrotron X-ray powder diffraction

According to Garino et al. (2014), synchrotron X-ray powder diffraction is the most exploited tool for the determination and characterization of crystal structures. The use of non-conventional X-ray sources is strongly increased in the last decades thanks to the enhancement of the X-ray beam intensity, the introduction of area detectors and specific systems for data collection at non-ambient conditions that allowed to extend the applicability of single-crystal and powder diffraction analysis (Garino et al., 2014). High brilliance, beam collimation and flexible monochromatic wavelength make considerably advantageous the use of non-conventional sources instead of the conventional laboratory diffractometers. Brilliance values in the order of 10^{21}–10^{22} photons s^{-1} mm^{-2} $mrad^{-2}$ 0.1% $bandwidth^{-1}$ are obtained using undulator insertion devices, whereas that of laboratory tubes range from 10^{9} photons s^{-1} mm^{-2} $mrad^{-2}$ 0.1% $bandwidth^{-1}$ (for stationary anode tubes) up to 10^{12} photons s^{-1} mm^{-2} $mrad^{-2}$ 0.1% $bandwidth^{-1}$ (for a rotating anode with micro-focusing) (Bilderback et al., 2005). The high brilliance of the synchrotron beam provides an enhanced experimental versatility depending on the possibility to insert on the incident and/or diffracted beam optical devices like monochromator, Soller slits or analyzer crystals to obtain powder

patterns of higher accuracy and precision hence, powder patterns of higher quality. Besides, the parallel beam allows to avoid the aberrations determined by the use of the conventional laboratory geometries, thus offering advantages in both peaks shape and intensity. Narrower peaks, more accurate peak positions and better signal-to-background ratio are fundamental prerequisites for accurate solution and characterization of crystal structures. As mentioned before, the high flexibility of the experimental set-up of the synchrotron facilities offers different advantages, such as performing of *in situ* experiments. The main interest towards *in situ* measurements arises from the possibility to investigate different processes undergoing at the atomic scale in real-time conditions. Indeed, fast data acquisitions (*i.e.*, time-resolved experiments) allows to record structural variations and phase transitions as well as to monitor continuously the kinetics of the dehydration processes or the chemical reactions upon heating, pressure or controlled humidity (Lo et al, 2018).

The degree of detail achievable coupled with the possibility to reproduce the real working conditions through *in situ* experiments, have made the X-ray powder diffraction as a fundamental technique for a deeper understating and by consequence has led to an improvement of the zeolites performances in catalysis, cation exchange and sorption processes throughout the years.

4.2 Neutron powder diffraction

Compared to the X-ray powder diffraction, the elastic neutron scattering (*i.e.*, neutron powder diffraction) has two main advantages: strong scattering length from light atoms and no variations of the *form factor* depending on the θ angle (*i.e.*, no decreasing of reflection intensities at high θ angle according to the senθ/λ). This is because, unlike the X-ray powder diffraction, neutrons are scattered from the nuclei of the atoms and their scattering power is independent from the atomic number, the momentum transfer Q and the θ angle. Since the neutron scattering depends on the properties of the nuclei, it offers the possibility to detect heavy as well as light atoms (*e.g.*, H, C and N), discriminate between neighbouring atoms (*i.e.*, with similar Z atomic number) and isotopes of the same atom (*e.g.*, hydrogen and deuterium) (Xinzhe, 2013).

Furthermore, since neutrons possess a magnetic moment are subjected to magnetic coherent scattering interaction with any other magnetic moment in matter, thus allowing the determination of the magnetic structure in coordination complexes and materials, using polarized neutron beams (Garino et al., 2014). Thermal neutrons employed in diffraction studies identify atomic nuclei as point-like objects, showing q-independent nuclear coherent scattering lengths b_c. Based on this, neutron diffraction is more performing than X-ray

diffraction in the collection of data in the high-q region although, in neutron diffraction experiments, the reflections amplitude at high 2θ values is dumped because of the thermal motion of the electron clouds that drag along the atomic nuclei (Garino et al., 2014; Borfecchia et al., 2013). As a consequence, neutron diffraction has become an important tool in the characterization of inorganic and organic materials for different application fields, such as natural minerals or synthetic analogues, pharmaceutical compounds, proteins, *etc*.

The contribution given by the neutron diffraction on microporous zeolites studies in the last years has been fundamental to improve the knowledge on their crystal chemistry. Indeed, in addition to powder or single-crystal X-ray diffraction, which is usually used for crystal structure determination and characterization, neutron diffraction is preferred in many cases since it can provide information not reachable with XRPD analysis. Among these, there is the possibility to evaluate the order of the tetrahedral sites discriminating between silicon and aluminium, to localize cations, organic compounds, water molecules as well as hydrogen bonds with high precision and accuracy and to determine position, geometry and amount of acid sites. All these aspects are essential to allow a better understanding of the relation occurring among zeolites structure, properties, chemistry and their catalytic or non-catalytic applications.

4.3 Extended X-ray absorption fine structure (EXAFS)

Garino et al., (2014) reports that, in the field of coordination chemistry, XAS technique (in particular in the EXAFS region), is the most obvious association between synchrotrons and structural characterization. The XAS method is based on the collection and analysis of the X-ray absorption coefficient μ(E) as a function of the energy E of incident X-rays. This allows to investigate the region immediately after an absorption edge (at energy E0: typically, up to 1000 eV after the edge), of the "absorber" atom, which is the atom which local environment is under investigation. When the "absorber" atom is surrounded by neighbour atoms, the spectrum is characterized by soft oscillations, modulating the monotonically decreasing atomic-like background μ0(E) (Garino et al., 2014).

Due to the necessity of a tunable high-flux X-ray source, the EXAFS technique can be applied only through synchrotron sources and usually hard X-rays are employed (from ~2 keV onwards). This spectral region includes the K-edges for the elements up to the second row of the transition elements, and the L-edges for the lanthanides.

The fitting of the EXAFS spectra based on a guess model structure enables the refinement of several parameters, such as: (1) the coordination number and type of atomic neighbours; (2) the average bond distances and (3) the Debye–Waller factors.

Due to the possibility of monitoring local geometry distortions, *in situ* red–ox reactions and site reactivity, this technique in the last decades has become widely used. Furthermore, it can provide important information for that cases-study where a local and element-selective structural probe is needed, thus becoming complementary to the X-ray diffraction methods (Garino et al., 2014 and references therein).

4.4 Rietveld method

The Rietveld method, whose name arises from the scientist who introduced it for the first time applying the procedure on neutron data (Rietveld, 1969), is recognized as the unique data processing method for structural analysis of powder polycrystalline materials. Only more recently the procedure was applied on X-ray powder diffraction data to derive crystal structure information because of complexity of modelling peak shape whose contribute arises not only from the Gaussian terms.

It is based on the Whole Powder Profile Fitting (WPPF) approach that considers each data point (2θ step) as an observation and takes into account the entire powder pattern profile, thus leading to obtain the maximum number of information from the least-square refinement of background, profile and structure (*i.e.*, lattice parameters, atomic coordinates, occupancy factor and atomic displacement parameters). The aim is to reach the best fit between observed and calculated patterns (*i.e.*, starting structural model that must be a reasonable approximation of the investigated structure) through the modelling of intensities of each i^{th} point at a given 2θ step.

As mentioned just above, the procedure is based on the least-square minimization. The quantity minimized is the residual S_y, given by Eq.1:

$$S_y = \sum_{i=1}^{N} Wi(y_{obs-i} - y_{calc-i})^2 \quad (1)$$

where: W_i (weight assigned to each step intensity)= $1/Yobs - i$; $Y_{obs\text{-}i}$ and $Y_{calc\text{-}i}$ are observed and calculated intensity at the i^{th} step, respectively; the sum is relative to all the measured data points along the 2θ range investigated.

$Y_{obs\text{-}i}$, is usually given by the contribution of several Bragg reflections at one 2θ point, besides calculated intensities ($Y_{calc\text{-}i}$) are obtained from the $|F_k|^2$.

The $|F_k|^2$ is calculated from the structural model, summing contributions of neighbouring Bragg reflections and background, Eq.2:

$$Y_{calc-i} = s \sum_K L_k |F_k|^2 \phi(2\theta_{obs-i} - 2\theta_k) P_k A + Y_{bi} \quad (2)$$

where: s=scale factor; K=hkl index for a Bragg reflection; L_k=Lorentz polarization and multiplicity factors; ϕ=profile shape function (*i.e.*, combines effects of instrumental contributions and sample features); P_k=preferred orientation function; A=adsorption function; F_k=structure factor for the K^{th} Bragg reflection; Y_{bi}=background intensity at the i^{th} step (depending on several factors, such as detector noise, fluorescence from the sample and scattering of X-ray from air) (Young, 1995).

4.5 Computational modeling

Computational approaches used in zeolite modeling may be categorized into two families: I) classical force-field techniques – basically, Monte Carlo (MC) and molecular dynamics (MD) approaches; II) quantum mechanical methodologies (*i.e.*, "ab initio" or "first principles").

Methods belonging to the first family model interatomic interactions by effective potentials. An example is classical molecular dynamics (MD), which describes atomic motion via empirical force fields; the physical properties of the system are then computed by averaging over the atomic configurations collected along a trajectory (Allen and Tildesley, 1987).

The second class of methodologies describes the electronic structure quantum-mechanically, *i.e.* via the time independent Schrödinger equation for the electronic wavefunction, or by Density Functional Theory (DFT). In DFT the system's energy is a unique functional of the electronic density. Since the exact form of the functional is unknown, approximated expressions are adopted (Parr and Yang, 1989).

Complex chemical systems require both a quantum treatment of the electronic structure and a description of the atomic motion. These requirements are fulfilled by first principles molecular dynamics (FPMD), originally proposed by Car and Parrinello, 1985 (Marx and Hutter, 2009; Remler and Madden, 1990; Car and Parrinello, 1985). FPMD performs the time evolution of a system with first-principles accuracy, because the forces on nuclei at each MD time step derive from a quantum mechanical description of the electrons. The electronic structure is mostly treated with DFT (Marx and Hutter 2009). The Car-Parrinello scheme for FPMD defines a fictitious dynamical system in which the potential energy surface depends on both the nuclear and the electronic degrees of freedom (Car and Parrinello 1985). The electronic wavefunction coefficients are propagated in time as

classical degrees of freedom, and their dynamics generates at each time step the correct adiabatic electronic configuration corresponding to the new ionic positions. Hence, if at the beginning of the simulation the electronic orbitals correspond to the ground state, they will follow the motion of nuclei adiabatically, and remain in that state as the nuclear configuration evolves in time. The dynamical parameters (fictitious electronic mass and time step) have to be chosen so that the transfer of energy between ions and electrons is kept very small during the simulation (Remler and Madden 1990). This condition is satisfied in systems with a large energy gap, such as zeolites.

The approach requires the definition of a simulation cell, to which periodic boundary conditions are applied. In applications to zeolites, this implies the capability of describing the full crystal from first principles, thus reproducing the flexibility properties of the framework – which are especially important in governing the response of zeolites to an applied pressure, or the penetration and diffusion of guest species in zeolite pores. It is generally convenient to held the cell parameters fixed at the values experimentally determined at such pressure conditions (where available), which are known to be very accurate. Importantly, no constraints – either symmetry restraints or "frozen" nuclear positions - are normally imposed to the atoms in the simulation cell, which are thus left free to move according to their own potential energy surface determined by the interatomic interactions.

CHAPTER 5. Experimental

As introduced in Chapter 1 – Introduction, in this chapter are presented the experimental data obtained on the 8 zeolitic systems selected for the thesis. Each system is divided in different sections, which encompass I) the description of the *Samples* investigated and their chemical properties, in some cases II) the procedures used for the samples preparation, III) the experimental approach used for the *Data collection*, IV) the *Refinement strategy* applied for Rietveld structural refinements and V) the experimental results obtained through the data processing.

SYSTEM 1

THERMAL ACTIVATION OF TEMPLATED ZSM-5 ZEOLITES: AN *IN SITU* SYNCHROTRON X-RAY POWDER DIFFRACTION STUDY

Samples. ZSM-5 zeolite samples (MFI topology, 3-dimensional channels system) were synthesized at different Si/Al ratio starting from the following molar composition:

$$0.1Na_2O - 0.08TPABr - 1SiO_2 - xAl_2O_3 - 20H_2O$$

where the molar amount of Al_2O_3 was varied in the range $0.005<x<0.033$, according to the expected Si/Al molar ratio in the gel, namely: 15, 25, 50 and 100. The synthesis gel was prepared (Migliori et al., 2014) by adding 2.66 g of sodium hydroxide (97%, Carlo Erba Reagenti) to 119.40 mL of distilled water. Aluminum hydroxide (98%, Fluka) was solubilized into the basic solution and 7.10 g of tetrapropylammonium bromide (98%, Fluka) and the solution added to the gel. The addition of 19.95 g of precipitated silica (100 %, Merck) in the batch was followed by 2 h stirring at room temperature. Crystallization was carried out at 175 °C PTFE-lined stainless steel static autoclave (Volume 0.150 l). After 96 h of crystallization, the solid phase was filtered, washed with distilled water and dried at 100 °C overnight. The bulk Si/Al molar ratio was determined via atomic absorption spectroscopy by using GBC 932 instrument (Catizzone et al., 2019); data are summarized in Table 5.1.1.

Table 5.1.1.
Labels, gel and bulk Si/Al ratio of templated ZSM-5 samples.

Sample label	Gel Si/Al ratio [mol/mol]	Bulk Si/Al ratio [mol/mol]
423_AS-ZSM-5	15	21
425_AS-ZSM-5	25	30
422_AS-ZSM-5	50	51
424_AS-ZSM-5	100	84

Data collection. Powder patterns in function of temperature were collected at the MCX Beamline of the Elettra Synchrotron Light Source (Trieste, Italy) on a 4-circle Huber diffractometer with a 3D translation stage. The diffractometer was equipped with a Si(111) double crystal monochromator and a high-count rate fast scintillator detector preceded by a pair of slits with vertical aperture of 200 and 300 μm. Each of the four samples was loaded into an axially spinning quartz capillary (Ø=0.5 mm) previously mounted on a goniometric head. The sample temperature was varied and monitored by means of the gas blower available at the beamline. Experimental conditions for each investigated temperature were λ=0.82700(1) Å, 2θ angular range=3-35°, step size=0.005° 2θ, counting time=1 second per step. X-ray powder diffraction patterns were recorded every 100 °C from room temperature to 800 °C in air with a heating rate of 5 °C min^{-1}.

Refinement strategy. Since no symmetry variation was highlighted within the investigated temperature range, the ZSM-5 structure at each temperature was refined starting from the structure model of the topological ZSM-5 structure (orthorhombic, *Pnma* space group) of Van Koningsveld et al., (1987). Peak profiles were modelled through a pseudo-Voigt function with the peak cut-off set to 0.05% of the peak maximum, by means of two Gaussian terms (θ-independent GW, tan-θ dependent GV, respectively), and two Lorentzian broadening coefficients ($\cos\theta^{-1}$- and tanθ-dependent, LX and LY, respectively) plus an asymmetry contribution (*asym*) and two terms to reproduce the anisotropic contributions of the Lorentzian broadening (*ptec* and *stec*). Besides 26 shifted Chebyshev polynomial coefficients to fit the background and a shift contribution (*shft*) to account for the sample displacement, the refinements included cell parameters, atomic coordinates, and Atomic Displacement Parameters (ADPs, U_{iso}). During the refinement of the framework atomic coordinates, a set of soft constraints was applied to tetrahedral T–O and O–O bond distances (1.60 and 2.60 Å, respectively, with σ=0.04 Å). The restraint weight (F) was progressively lowered in the last refinement cycles. The Atomic Displacement Parameters were constrained in order to have the same value for the same atomic species. Tetrapropylammonium organic structure-directing agent (TPA^+) atomic coordinates were derived from residuals of electron density calculated by mean of the Difference Fourier maps. On the contrary, no residuals attributable to H and Na atoms were detected due to the low scattering length of the former and the high disorder of the latter. In order to retain the TPA^+ molecule geometry, extraframework atomic coordinates were refined imposing soft constraints on N-C (*i.e.,* 1.48 and 2.48 Å, σ=0.04 Å) and C-C (*i.e.*, 1.42 and 2.70 Å, σ=0.04 Å) bond distances. Furthermore, fraction as well as ADPs for both N and C atoms of the

TPA^+ molecule were constrained to vary equally. TPA^+ atomic coordinates obtained from the room temperature refinements were imposed to be equal for all the four ZSM-5 zeolites. Details about data collection and R-values agreement indices are reported in Table 5.1.2. Framework atomic coordinates, fraction and Atomic Displacement Parameters of 423, 425, 422 and 424_AS-ZSM-5 at room temperature are reported in Appendix 1, Tables A, B, C and D, respectively. Atomic coordinates, fraction and Atomic Displacement Parameters of extraframework TPA^+ at room temperature are reported in Table E. Framework atomic coordinates, fraction and Atomic Displacement Parameters of 423_AS-ZSM-5 at selected temperature of 200, 400, 600 and 800 °C are reported in Table F, G, H and I, respectively. For 425_AS-ZSM-5 are reported in Table J, K, L and M, respectively. For 422_AS-ZSM-5 are reported in Table N, O, P and Q, respectively. For 424_AS-ZSM-5 are reported in Table R, S, T and U, respectively.

Table 5.1.2.
Details of data collection at room temperature and R-values agreement indices.

Parameter	423_AS-ZSM-5 (Si/Al 21)	425_AS-ZSM-5 (Si/Al 30)	422_AS-ZSM-5 (Si/Al 51)	424_AS-ZSM-5 (Si/Al 84)
Wavelength (Å)	0.82700(1)	0.82700(1)	0.82700(1)	0.82700(1)
Refined 2θ (°) range	3-35	3-35	3-35	3-35
N_{data}	6399	6399	6399	6399
N_{var}	156	156	156	156
R_{wp} (%)	21.62	15.59	13.98	18.77
R_p (%)	16.06	11.86	10.42	13.99
R_F^2 (%)	10.24	12.83	12.42	10.21

$R_p=\sum[Y_{io}-Y_{ic}]/\sum Y_{io}$; $R_{wp}=[\sum wi(Y_{io}-Y_{ic})^{\wedge}2/\sum wiY_{io}^2]^{\wedge}0.5$; $R_F^2=\sum|F_o^2-F_c^2|/|F_o^2|$

Results and discussion of room temperature structural refinements. Full profile Rietveld refinements allowed the structural characterization (*i.e.*, unit cell parameters, atomic bond distances and angles, location and quantification of extraframework template and water molecules) of the as-synthesized ZSM-5 zeolites under investigation. The crystal structure of ZSM-5 synthesized in the presence of tetrapropylammonium (TPA^+) ions has been studied by several authors in the orthorhombic space group *Pnma*. According to their chemistry, characterized by a gradual increase of the Si/Al ratio, variations are observed by comparing the lattice parameters of AS-ZSM-5 at room temperature. An inspection of Table 5.1.3 reveals slight differences along all the three *a*, *b* and *c*-axes of the four samples under investigation; as a consequence, variations in the unit cell volume are recorded: in general, it ranges from 5356.7 to 5370.9 $Å^3$. Besides the AS-ZSM-5 samples, in Table 5.1.3 are reported the unit-cell parameters corresponding to some MFI-TPA^+ systems for the $0<n<4$ (molecules/unit cell) pore-fillings. In all the selected zeolites, the space group is always orthorhombic *Pnma*, with 12 independent tetrahedral sites in the unit cell.

Table 5.1.3.
Unit cell parameters of templated ZSM-5 zeolites at room temperature.

	423_AS-ZSM-5	425_AS-ZSM-5	422_AS-ZSM-5	424_AS-ZSM-5	Lermer et al., 1985	Yokomori and Idaka, 1999	Chao et al., 1986	Olson et al., 1981	Price et al., 1982	Van Koningsveld et al., 1987
Space Group	*Pnma*	*Pnma*	*Pnma*	*Pnma*	*Pnma*	*Pnma*	*Pnma*	*Pnma*	*Pnma*	*Pnma*
Z	8	8	8	8	8	8	8	8	8	8
a (Å)	20.048(4)	20.044(4)	20.062(3)	20.049(1)	20.092	20.072	20.100	20.07	20.044	20.022
b (Å)	19.966(4)	19.939(4)	19.945(3)	19.933(1)	19.952	19.937	19.959	19.92	19.918	19.899
c (Å)	13.418(2)	13.411(3)	13.413(2)	13.404(1)	13.414	13.414	13.409	13.42	13.395	13.383
V (Å^3)	5370.9(2)	5359.8(2)	5367.0(4)	5356.7(7)	5377.4	5367.9	5379.4	5365.2	5347.8	5332.0
Si/Al	21	30	51	84	11.9	23	25	86	86.3	299

Figure 5.1.1 points out the relation occurring between unit cell volumes and Si/Al ratios. Indeed, in particular for Si/Al ratios lower than 25, it is highlighted that the higher the Si/Al ratio, the lower the unit cell volume. Although the trend appears less marked because of the Chao et al., 1986, 422_AS-ZSM-5 and Olson et al., 1981 out of trend points, the antithetical behaviour of the two parameters is showed also by Si/Al ratio >25.

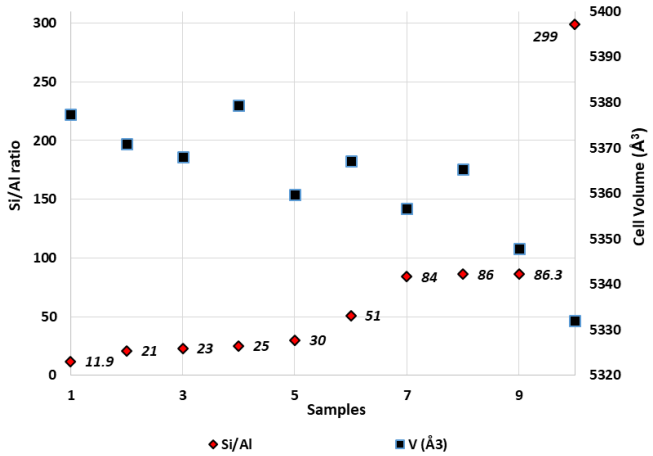

Si/Al=11.9 → Lermer et al., 1985;
Si/Al=21 → 423_AS-ZSM-5;
Si/Al=23 → Yokomori and Idaka, 1999;
Si/Al=25 → Chao et al., 1986;
Si/Al=30 → 425_AS-ZSM-5;
Si/Al=51 → 422_AS-ZSM-5;
Si/Al=84 → 424_AS-ZSM-5;
Si/Al=86 → Olson et al., 1981;
Si/Al=86.3 → Price et al., 1982;
Si/Al=299 → Van Koningsveld et al., 1987.

Figure 5.1.1. Unit cell volumes as a function of Si/Al ratios.
Sample labels are here referred to Si/Al ratios.

As far as concerns the ZSM-5 used in this work, T-O distances and O-T-O angles obtained from structural Rietveld refinements range from 1.586(5) to 1.598(1) Å and from 108 to 110°, respectively, in all the samples. On the contrary, intertetrahedral T-O-T bond angles appear more heterogeneous, thus revealing the irregular geometry of the channels since room temperature. The intertetrahedral angles of the four AS-ZSM-5 range from 140 to 173° and the differences of the same angle among the samples is always lower than 10°. Tetrahedral bond distances and T-O-T angles at room temperature are reported in Appendix 1, Table V, W, X and Y for 423, 425, 422 and 424_ AS-ZSM-5, respectively). Besides, in Appendix 1, Figure A, are represented some of the T-O-T angles of the four AS-ZSM-5 zeolites.

In order to quantify the distortion from a channel with an ideal circular section, it is possible to calculate the ellipticity parameter, ε, defined as the ratio between the longest and the shortest O-O bond distances that define the minimum and the maximum channel diameters. Data reported in Table 5.1.4 point out that, for all the investigated samples, both SC and ZZ-A channels are quite distorted (*i.e.*, the ellipticity values depart from ε=1, which identifies a circular shape), while ZZ-B appears more regular. No particular trends depending on the Si/Al ratio are highlighted. The Crystallographic Free Area (C.F.A., $Å^2$, π*(channel mean radius)^2, sensu Baerlocher (Baerlocher et al., 2007) calculated on each as-synthesized zeolite reveals slight differences among channels: the lowest and the highest areal dimensions being found for ZZ-A and ZZ-B sinusoidal channels, respectively.

Table 5.1.4.
Ellipticity and Crystallographic Free Area parameters at room temperature.

Parameter	Channel	423_AS-ZSM-5	425_AS-ZSM-5	422_AS-ZSM-5	424_AS-ZSM-5
Ellipticity (ε)	**SC**	1.082	1.104	1.084	1.080
	ZZ-A	1.086	1.085	1.078	1.083
	ZZ-B	1.037	1.045	1.050	1.040
Crystallographic Free Area (C.F.A., $Å^2$)	**SC**	23.56	23.61	23.65	23.60
	ZZ-A	22.95	22.90	22.84	22.79
	ZZ-B	24.30	24.22	24.03	24.02

According to Van Koningsveld et al. (1987), residuals of electron density calculated by mean of Difference Fourier maps suggest that the tetrapropylammonium ion (TPA^+) is located at the intersection of the sinusoidal and the straight channels. Due to the presence of the mirror plane *m*, the TPA^+ molecule can statistically assume two different orientations, which depend on the distribution of the four propyl-groups around the central nitrogen (Figure 5.1.2). Rietveld refinements of the atomic occupancy indicate that all the investigated AS-ZSM-5 samples contain four molecules per unit cell of TPA^+ molecules (*i.e.*, the maximum theoretical number of TPA^+ molecules that can be found within the zeolite channels (Fejes et al., 1998)).

Besides, no additional and reasonable residuals of electron density were obtained from the Fourier maps calculation, thus suggesting that no co-adsorbed water molecules are present within the zeolite framework.

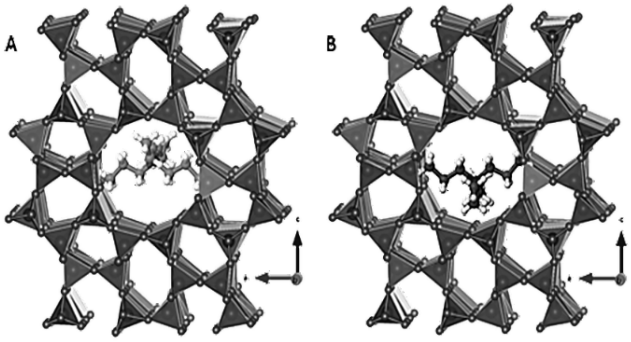

Figure 5.1.2. Polyhedral representation of the ZSM-5 structure along the [010] direction. Tetrapropylammonium ion (TPA^+) is located at the intersection of straight and sinusoidal channels. A and B refer to the possible orientations.

Results and discussion of high temperature structural refinements. Information on the kinetics of TPA^+ decomposition as well as structural variations due to the extraframework content release, and the resulting framework rearrangement, can be determined through an *in situ* X-ray diffraction data collection. Cascade plots in Figure 5.1.3 show the evolution of the investigated AS-ZSM-5 samples in the range between room temperature and 800 °C. No evidence of crystallinity loss is observed up to 800 °C, thus indicating the substantial high thermal stability of all as-synthesized ZSM-5 samples. Temperature increase induces variations in both peak positions and intensities for all the investigated samples. Specifically, up to about 300 °C, peaks move to lower 2θ angles, whereas at higher temperatures a peaks shifting toward higher 2θ angles is observed. This means that, a lattice expansion up to about 300 °C is followed by a unit-cell contraction up to 800 °C. According to Cruciani (2006), a lattice contraction can be related to the progressive removal of organic molecules through the calcination process. Further indications on the decomposition process can be inferred from the peak intensity variations (mainly related to changes in structural parameters) upon heating and will be discussed in the next section.

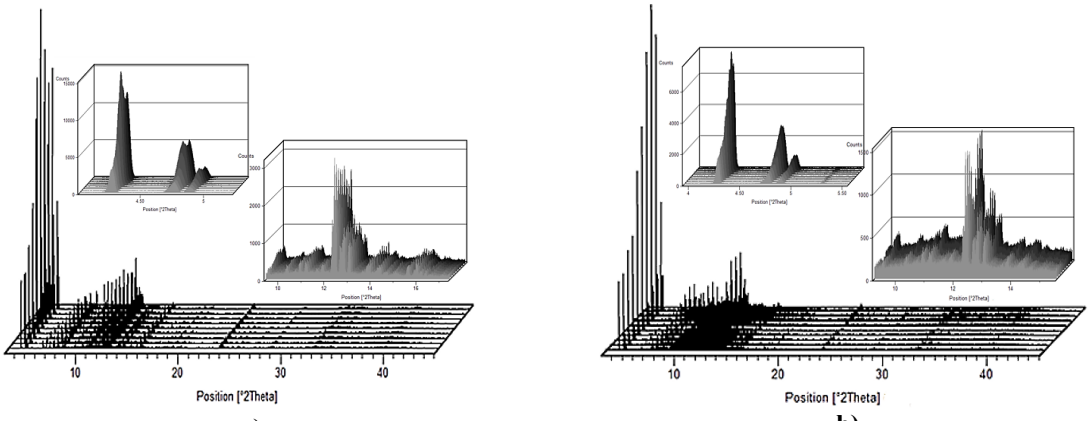

a) **b)**

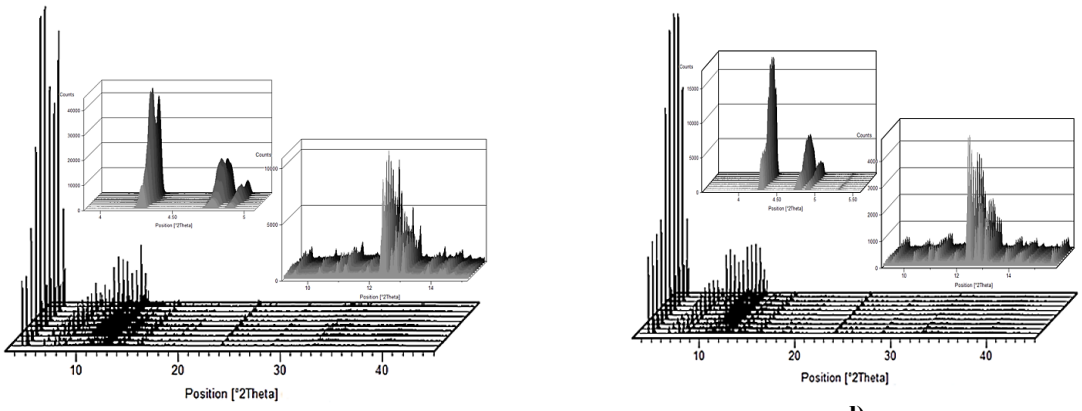

c) d)

Figure 5.1.3. Cascade plots of a) 423, b) 425, c) 422 and d) 424_AS-ZSM-5 zeolites (detail of 4-5 and 10-15° 2θ angles).

The variation of the unit-cell parameters as a function of temperature (normalized to their value at room temperature) is reported in Figure 5.1.4. Two distinct trends based on their evolution were rationalized for the couple of samples 423-425 and 422-424, respectively. These differences could derive by the different chemistry of the samples under investigation (*i.e.*, different Si/Al ratios). Indeed, as already reported by Sen et al. (2006), the concentration of Al^{+3} ions in orthorhombic H[Al]ZSM-5 zeolites has been ascribed as a crucial parameter to identify their different thermal behaviour. As far as concerns 423 and 425_AS-ZSM-5, the expansion registered along the first temperature steps (up to 300 °C) has an anisotropic character, indeed it is firstly driven by the gradual increase of the *a* parameter, whereas *b* and *c* remain almost constant or slightly decrease. From 300 to 800 °C, lattice parameters undergo to a progressive reduction with a similar rate, as suggested by the similar curves slope. Although *c* parameter of sample 423_AS-ZSM-5 slightly increases between 700 and 800 °C, no variations in volume trend are detected, indeed the progressive contraction of the unit cell continues up to the end of the thermal treatment, as with the 425_AS-ZSM-5. Although similar behaviour are highlighted in 422 and 424_AS-ZSM-5 as well, differences in curves slope lead to a general different temperature–dependent cell parameters evolution. From room temperature to 300 °C, *a* and *b* parameters of both samples are characterized by an antithetical trend, which foresees the increase and the reduction of *a* and *b*-axes, respectively. In the same thermal range, *c* parameter increases and decreases for 422 and 424_AS-ZSM-5, respectively. Between 300 and 700 °C, cell parameters undergo to a progressive reduction without a costant rate. Noteworthy is the abrupt slope change of all curves between 300 and 400 °C that highlights the non-gradual character of the contraction. From 700 °C a new lattice parameters increase is noticed in both AS-ZSM-5. The volume reduction shown by samples 423-425 is more gradual than that highlighted by samples 422 and 424, which is characterized by an abrupt

slope change between 200 and 300 °C and becomes smoother from 400 °C. From 700 and 800 °C, the latter samples are characterized by a cell volume expansion; on the contrary, cell volumes of the former continue to decrease. The total volume contraction calculated along all the thermal range is about 0.87, 0.89, 0.75 and 0.71 % for 423, 425, 422 and 424_AS-ZSM-5 samples, respectively, thus highlighting that: the lower the Al^{+3} content, the lower the cell volume contraction.

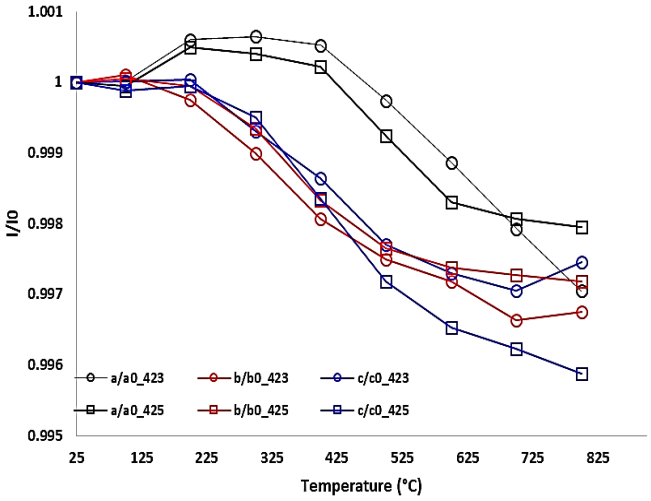

a)

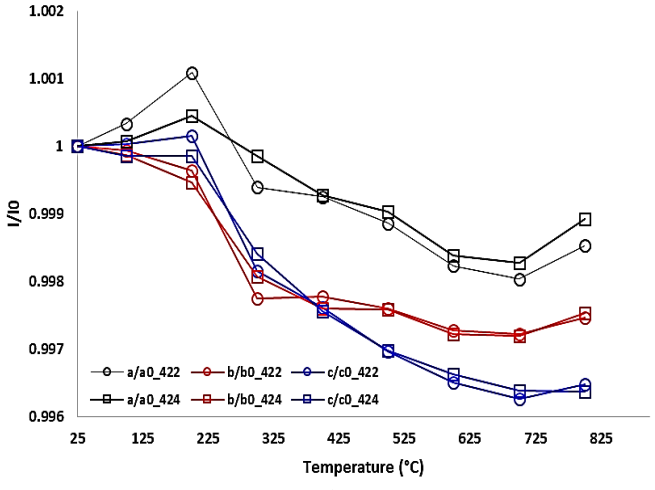

b)

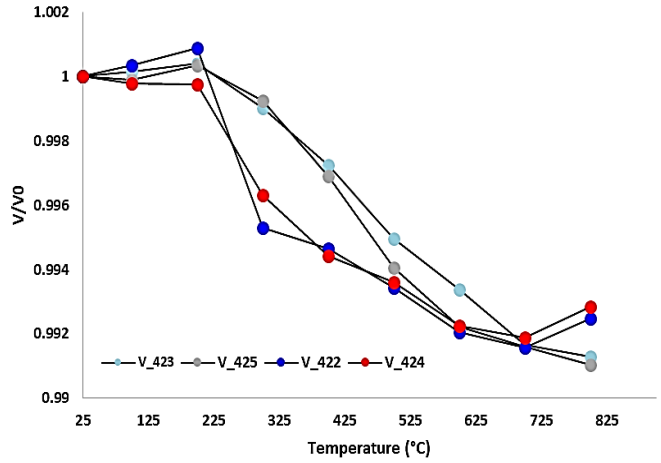

c)

Figure 5.1.4. Lattice parameters evolution at high temperature; a) 423 and 425_AS-ZSM-5, b) 422 and 424_AS-ZSM-5, c) volume of all the four AS-ZSM-5 samples.

Figure 5.1.5 shows the variation of the TPA^+ content as a function of temperature. Refined occupancies highlight that the template molecule sites remain unchanged up to 200 °C in all AS-ZSM-5 zeolites. Indeed, the TPA^+ degradation process starts between 200 and 300 °C and it is completed at 400 °C, when all the sites are completely empty. The degradation temperature of the TPA^+ helps to understand the lattice parameters evolution upon heating. Indeed, the unit-cell volume contraction observed above 200 °C can be attributed to the progressive release of the template molecule.

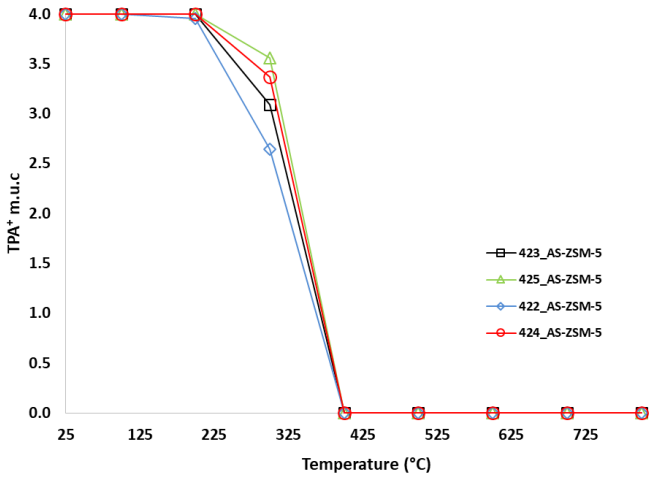

Figure 5.1.5. Extraframework TPA^+ molecules evolution at high temperature.

The polyhedral arrangement in zeolite structures bestows a high framework flexibility. This is testified by the evolution upon heating of T-O distances and T-O-T angles, which show slight variations along all the thermal range investigated, thus suggesting that the zeolites framework does not undergo to relevant structural distortions. T-O distances and T-O-T

angles at selected temperature of 200, 400, 600 and 800 °C are reported in Appendix 1, Table V, W, X and Y for 423, 425, 422 and 424_AS-ZSM-5 , respectively.

This is confirmed also by the analysis of the ellipticity parameter of the zeolite channels. While the ellipticity of ZZ-B channels is almost constant for all the samples throughout the whole temperature range (*i.e.*, ε fluctuates around 1.4), the heating process induced variation in the shape of both ZZ-A and SC channels (Figure 5.1.6(a), (b), (c) and (d)). In particular, two antithetic trends can be recognized: an increase in the ellipticity of channel ZZ-A (evidence of a progressive departure from the circular shape) is associated with a lowering in the ellipticity (regularization) of the SC channel. Albeit some non-homogeneous variations due to the TPA^+ depletion at the earlier heating stages (*i.e.*, between 200 and 300 °C) can be observed for samples 423 and 422_AS-ZSM-5s, the 10MR channel of all the investigated samples tends to become more regular, though a circular shape is never reached.

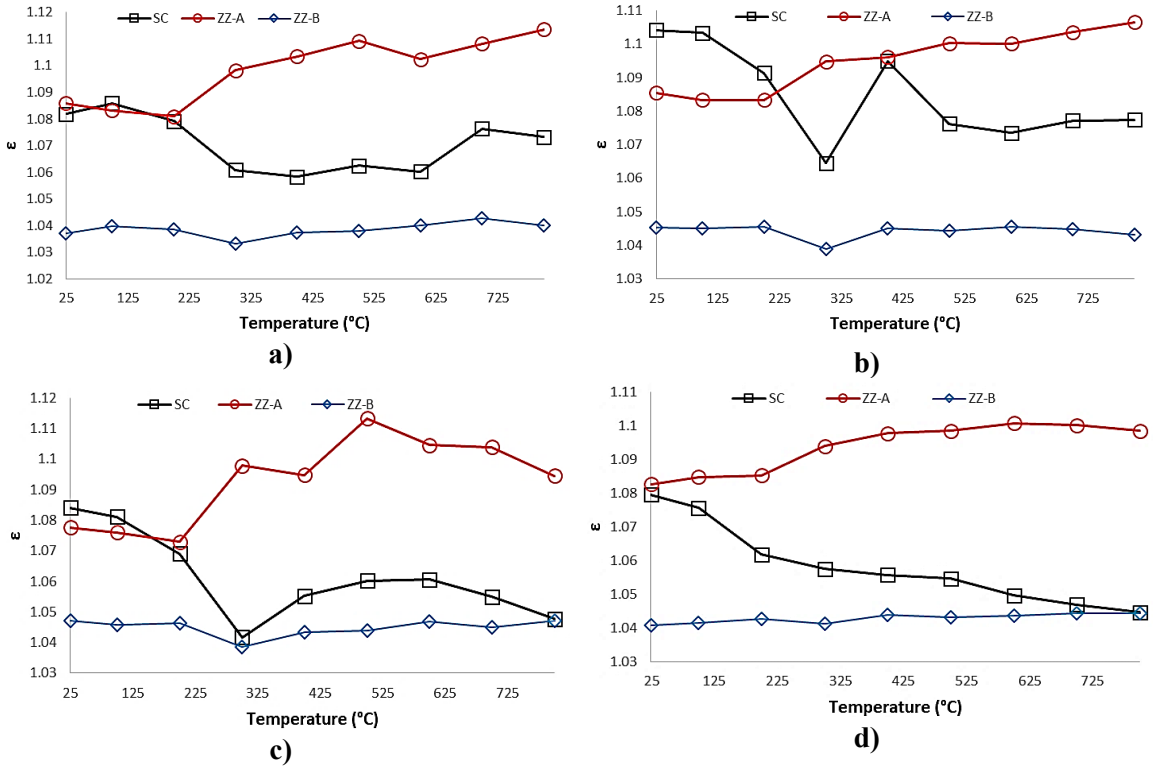

Figure 5.1.6. Ellipticity evolution at high temperature of (a) 423_AS-ZSM-5, (b) 425_AS-ZSM-5, (c) 422_AS-ZSM-5 and (d) 424_AS-ZSM-5.

The thermal treatment also induced slight variations in the CFA of AS-ZSM-5 zeolites (Appendix 1, Figure B1, B2, B3 and B4 for 423, 425, 422 and 424_AS-ZSM-5, respectively). Evidences of a pore diameter reduction on heating can be inferred by the lowering of CFA values for both SC and ZZ-A channels. On the contrary, the effect of the heating process is less pronounced on the ZZ-B channel.

Final consideration. The detailed structural analysis carried out on the four templated ZSM-5 samples by means of *in situ* synchrotron X-ray powder diffraction confirmed the high efficiency of thermal treatment in activating as-synthesized zeolites. Besides, the continuous monitoring of the structural features evolution upon heating confirmed the high ZSM-5 framework flexibility: indeed, the zeolite did not show relevant structural distortions that could affect its possible use after thermal activation. This structural behaviour points out the high thermal stability of the templated ZSM-5 zeolites, a fundamental property for ZSM-5 acid catalysts employed in catalytic processes.

SYSTEM 2

STRUCTURAL CHARACTERIZATION OF ACIDIC ZSM-5 ZEOLITES THROUGH *IN SITU* SYNCHROTRON X-RAY POWDER DIFFRACTION

Samples. Samples used in this work are four synthetic protonated H^+-ZSM-5 zeolites (*i.e.*, MFI topology, 3-dimensional channels system) characterized by different Si/Al ratios. All the samples were synthesized (and provided) by the research group of the Department of Chemical and Environmental Engineering of the University of Calabria (Rende, CS) using a common synthesis procedure. Differences on Si/Al ratios arise from the different amount of Al_2O_3 used in the starting gel molar composition (Frusteri, et al., 2016). Sample labels along with the corresponding Si/Al ratios and the Al^{+3} content are reported in Table 5.2.1.

Table 5.2.1.
Label, bulk Si/Al ratio and Al^{+3} content of each H^+-ZSM-5 sample.

Sample label	Bulk Si/Al ratio [mol/mol]	Al content (apfu), *n*
H^+-ZSM-5_15	15	6.19
H^+-ZSM-5_20	20	4.57
H^+-ZSM-5_37	37	2.53
H^+-ZSM-5_69	69	1.37

Data collection. *In situ* high temperature diffraction patterns were collected at the MCX (Material Characterization by X-ray Diffraction) beamline of the Elettra Synchrotron Light Source (Trieste, Italy) on a 4-circle Huber diffractometer with a 3D translation stage. The diffractometer was equipped with a Si(111) double crystal monochromator and a high-count rate fast scintillator detector preceded by a pair of slits with vertical aperture of 200 and 300 μm. Powder samples were placed into a quartz spinning capillary (Ø = 0.5 mm), previously mounted on a goniometric head, which rotated along the axis of the diffractometer. X-ray diffraction patterns were recorded from room to a maximum temperature of 800 °C according to the following experimental conditions: each 100 °C with a heating rate of 5 °C min^{-1}, fixed wavelength of 0.82700(1) Å (photon energy of 15 keV) in the 3–35° 2θ range, with a step size of 0.005° 2θ and an exposure time of 1 second per step.

Refinement strategy. Room temperature diffraction data of H^+-ZSM-5 with Si/Al ratio equal to 20, 37 and 69 respectively, were refined in the monoclinic crystal system (space group $P2_1/n$), starting from the structural model reported by van Koningsveld et al., (1990), whereas the sample with the Si/Al ratio=15 was refined in the orthorhombic *Pnma* symmetry starting from the atomic coordinates of van Koningsveld et al., (1987).
At higher temperature (*i.e.,* between 100 and 800 °C), all the structural refinements were carried out in the orthorhombic crystal system (space group *Pnma*). In all the refinements,

peak profiles were modelled through a pseudo-Voigt function with the peak cut-off set to 0.01% of the peak maximum, by means of three Gaussian terms (θ-independent *GW*, $\tan^2$-θ and tan-θ dependent *GU* and *GV*, respectively), the Lorentzian $\cos\theta^{-1}$-dependent *LX* coefficient and an asymmetry (*asym*) contribution. The experimental background was fitted through 28 shifted Chebyshev polynomial coefficients. Refinements included also lattice parameters, framework atomic coordinates and Atomic Displacement Parameters (ADPs, U_{iso}). Soft constraints were applied to the tetrahedral T–O and O–O bond distances (1.60 and 2.60 Å, respectively, with σ = 0.04 Å). The restraint weight (F) was progressively lowered in the last refinement cycles until atomic coordinates were allowed to vary almost freely. Furthermore, the U_{iso} parameters of tetrahedral sites and framework oxygen atoms were constrained in order to have the same value for the same atomic species. R-values agreement indices are reported in Table 5.2.2.

Framework atomic coordinates, fraction and Atomic Displacement Parameters of H^+-ZSM-5_15, H^+-ZSM-5_20, H^+-ZSM-5_37 and H^+-ZSM-5_69 at room temperature are reported in Appendix 2, Table A, B, C and D, respectively. Framework atomic coordinates, fraction and Atomic Displacement Parameters at selected temperature of 200, 400, 600 and 800 °C for H^+-ZSM-5_15 are reported in Appendix 2, Table E, F, G and H, respectively; for H^+-ZSM-5_20 in Table I, J, K and L, respectively; for H^+-ZSM-5_37 in Table M, N, O and P, respectively; for H^+-ZSM-5_69 in Table Q, R, S and T, respectively.

Table 5.2.2.
Lattice parameters, details of data collection and R-values agreement indices at room temperature.

Parameter	H^+-ZSM-5_15	H^+-ZSM-5_20	H^+-ZSM-5_37	H^+-ZSM-5 69
Space Group	*Pnma*	$P2_1/n$	$P2_1/n$	$P2_1/n$
***a* (Å)**	20.1464(11)	19.9413(9)	19.9119(11)	19.9108(5)
***b* (Å)**	19.9434(10)	20.1503(8)	20.1321(11)	20.1319(4)
***c* (Å)**	13.4168(9)	13.4167(6)	13.3952(8)	13.3943(4)
***V* (Å^3)**	5390.7(5)	5391.0(4)	5369.5(5)	5368.7(2)
β (°)	90	90.354(4)	90.477(2)	90.499(1)
Wavelength (Å)	0.82700(1)	0.82700(1)	0.82700(1)	0.82700(1)
2θ (°) range	3-35	3-35	3-35	3-35
N_{data}	6399	6399	6399	6399
N_{var}	117	256	256	256
R_{wp} (%)	12.88	13.23	13.84	9.45
R_p (%)	9.28	9.98	10.99	7.36
R_F (%)	9.48	8.08	8.2	4.72
R_F^2 (%)	10.58	13.00	12.01	7.23

$R_p=\sum[Y_{io}-Y_{ic}]/\sum Y_{_io}$; $R_{wp}=[\sum wi(Y_{io}-Y_{ic})^{\wedge}2/\sum wiY_{io}^2]^{\wedge}0.5$; $R_F^2=\sum|F_o^2-F_c^2|/|F_o^2|$

Results and discussion of room temperature structural refinements. The peak indexing of the collected powder diffraction pattern at room temperature evidences that in the H^+-ZSM-5_15 the characteristic doublets of peaks of the monoclinic polymorph are not fully resolved (*i.e.*, 311, -313 and 313), and only a broadening of the 8-14 2θ range can be appreciated (Figure 5.2.1). Additionally, when the powder pattern was in the $P2_1/n$ space group, the β angle of the monoclinic phase became very close to 90° and the R-values agreement indices increase (*i.e.*, R_{wp}=18.69 %, R_p=14.43 %, R_F=18.70 % and R_F^2=23.12 %), consequently Rietveld refinements of H^+-ZSM-5_15 sample was performed in the orthorhombic *Pnma* space group. This last is characterized by the presence of 12 independent tetrahedral sites and 26 framework oxygen atoms per unit-cell. On the contrary, powder diffraction patterns of H^+-ZSM-5 with higher Si/Al ratio (H^+-ZSM-5_20, 37 and 69) revealed a monoclinic symmetry (space group $P2_1/n$) with 24 independent sites and 48 framework oxygen atoms.

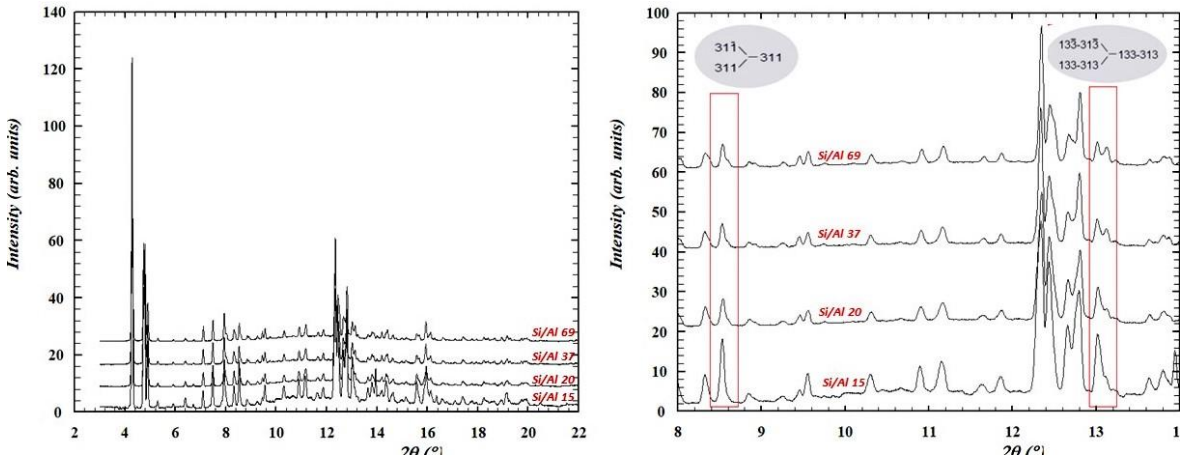

Figure 5.2.1. Powders diffraction patterns of all ZSM-5 samples in the complete investigated 2θ range (left) and in the 8.0-14.0 2θ (right) range, respectively. The characteristic doublet of peaks of the monoclinic phase at room temperature becomes large and broad single peak for the sample H^+-ZSM-5_15, characteristic of the orthorhombic polymorph.

The lattice parameters and unit-cell volumes obtained through full profile Rietveld refinements of the investigated ZSM-5 samples are listed in Table 5.2.2. Considering that the procedure used for the zeolite activation is common to all the samples under investigation, structural differences are exclusively dependent to their chemical composition (*i.e.*, to the different aluminium content). Indeed, the Si/Al ratio plays a key role in the formation of zeolite framework defectivities and, consequently, in their structural features. Indeed, as highlighted in the case of H^+-ZSM-5 single-crystals, high content of aluminium within the zeolite framework cause internal stresses that mainly affect the orientation of the ZSM-5 twin domains. This reflects into the β angle variation that changes from 90° (in the

orthorhombic symmetry) to wider values in function of higher Si/Al ratios, thus determining increasing degrees of “monoclinicity” (Van Koningsveld., 1989b). In Figure 5.2.2 the variation of the normalized lattice parameters, *a*, *b*, and *c* (Figure 5.2.2(a)), that of the *β* angle (Figure 5.2.2(b)), and that of the unit-cell volume, *V* (Figure 5.2.2(c)) is plotted as a function of the Si/Al ratio increasing. To allow the unit cell comparison among all the four samples, *a* and *b* axis of the H^+-ZSM-5_15 were plotted in the graph 5.2.2(a) using the *Pmnb* setting of the *Pnma* orthorhombic space group.

As a matter of fact, both normalized *a* and *c* lattice parameters decrease with a similar rate of variation as a function of the Si/Al ratio, while the unit-cell *b*-axis is the less affected by the different chemical composition. Indeed, Figure 5.2.2(b) clearly highlights a close relationship between the aluminium amount and the monoclinic degree ("monoclinicity") of activated ZSM-5 zeolites, with the *β* angle ranging from 90 to 90.49°.

A general framework on the H^+-ZSM-5 chemical-dependence is shown in Figure 5.2.2(c) where a evident volumetric drop occurs at the Si/Al ratio increasing. This volumetric change is mainly due to the Si^{+4} for Al^{+3} replacement at the tetrahedral site of the zeolite framework (the ionic radius of four-fold coordinated Al^{+3} and Si^{+4} are equal to 0.39 Å and 0.26 Å, respectively (Shannon, 1976)).

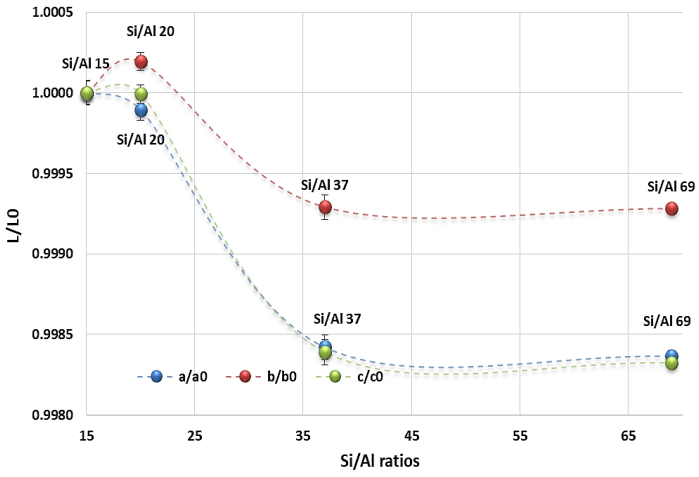

a)

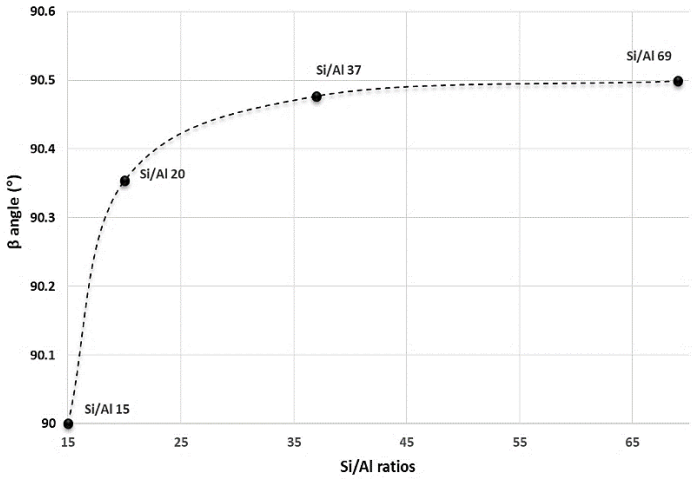

b)

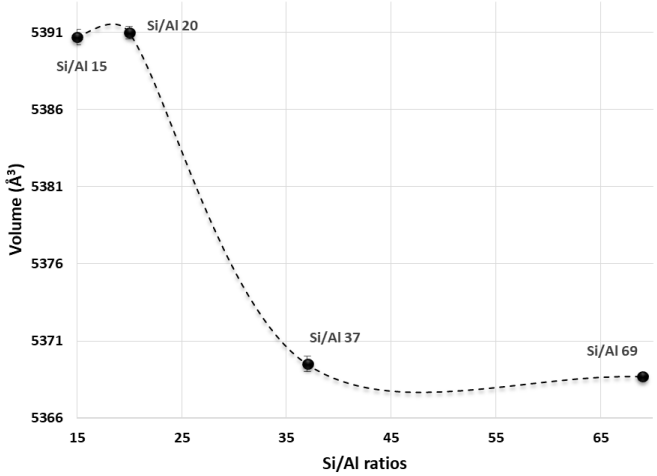

c)

Figure 5.2.2. Lattice parameters (*a*, *b*, *c* unit-cell axes (a), *β* angle (b) and unit-cell volume (c) of the four investigated H^+-ZSM-5 zeolite samples as a function of the Si/Al ratio at room temperature. Dashed lines are a reader's guide. Error bars are within the symbol size.

All the H^+-ZSM-5 samples here investigated are characterized by a regular framework geometry, with mean tetrahedral bond distances <T–O> ranging from 1.591 and 1.593 Å. Concerning the channels shape and dimension, the values obtained from the calculation of the ellipticity (ε) and the Crystallographic Free Area (C.F.A) parameters (Table 5.2.3) indicate that the Si/Al ratio affects also the channels opening. Indeed, the presence of slight differences in both straight and sinusoidal channels among the four samples suggests that their geometry is already slightly distorted at ambient conditions. This is directly related to the presence of wide T-O-T intertetrahedral angles that affect the whole framework geometry. For the orthorhombic ZSM-5 the widest angles are the T3-O3-T4, T8-O12-T12, T5-O14-T11, T1-O16-T4, which are equal to 167.7(6)°, 168.8(6)°, 162.2(5)° and 174.1(6)°, respectively. Besides, for the monoclinic samples some of the largest are the T8-O12-T12 (171.1(1)°, 172.6(8)° and 172.6(1)° for H^+-ZSM-5_20, 37 and 69,

respectively), the T1-O16-T16 (178.6(7)°, 173.5(5)° and 174.4(1)° for H^+-ZSM-5_20, 37 and 69, respectively) and the T6-O19-T15 (172.9(6)°, 172.4(5)° and 171.0(1)° for H^+-ZSM-5_20, 37 and 69, respectively). The list of T-O bond distances and T-O-T angles at room temperature is reported in Appendix 2, Table U for the orthorhombic H^+-ZSM-5_15 and V for the H^+-ZSM-5_20, 37 and 69.

Table 5.2.3.
O-O distances and C.F.A of straight (SC), ZZ-A and ZZ-B channels for the four H^+-ZSM-5 samples.

	Free diameter (Å)								
ZZA	**O28-O1**	**O27-O2**	**O20-O15**	**O24-O26**	**O41-46**	**Mean O-O (Å)**	**Radius (Å)**	**C.F.A. (Å²)**	**ε**
SAR 20	5.426	5.447	5.688	5.341	5.794	5.5392	2.7696	24.09	1.08
SAR 37	5.453	5.443	5.688	5.313	5.808	5.541	2.7705	24.10	1.09
SAR 69	5.405	5.476	5.651	5.301	5.835	5.5336	2.7668	24.04	1.1
SAR 15	**O18-O17**	**O18-O17**	**O4-O5**	**O4-O5**	**O25-O23**	**Mean O-O (Å)**	**Radius (Å)**	**C.F.A. (Å²)**	**ε**
	5.272	5.272	5.325	5.325	5.864	5.411	2.705	22.98	1.11
ZZB	**O31-O4**	**O30-O5**	**O44-O43**	**O25-O23**	**O18-O17**	**Mean O-O (Å)**	**Radius (Å)**	**C.F.A. (Å²)**	**ε**
SAR 20	5.233	5.491	5.44	5.853	5.146	5.4326	2.7163	23.17	1.13
SAR 37	5.163	5.549	5.498	5.498	5.061	5.3538	2.6769	22.50	1.09
SAR 69	5.145	5.587	5.483	5.822	5.071	5.4216	2.7108	23.07	1.14
SAR 15	**O1-O2**	**O1-O2**	**O15-O20**	**O15-O20**	**O24-O26**	**Mean O-O (Å)**	**Radius (Å)**	**C.F.A. (Å²)**	**ε**
	5.451	5.451	5.746	5.746	5.368	5.552	2.776	24.20	1.07
SC	**O47-O48**	**O31-O37**	**O44-O46**	**O8-O2**	**O7-O1**	**Mean O-O (Å)**	**Radius (Å)**	**C.F.A. (Å²)**	**ε**
SAR 20	5.425	5.512	5.561	5.399	5.491	5.477	2.738	23.55	1.03
SAR 37	5.438	5.517	5.929	5.379	5.436	5.539	2.769	24.09	1.10
SAR 69	5.444	5.554	5.629	5.407	5.409	5.488	2.744	23.65	1.04
	O1-O7	**O2-O8**	**O5-O11**	**O18-O20**	**O21-O22**	**Mean O-O (Å)**	**Radius (Å)**	**C.F.A. (Å²)**	**ε**
SAR 15	5.642	5.440	5.621	5.839	5.518	5.511	2.755	23.84	1.07

Results and discussion of high temperature structural refinements. Inspection of powder diffraction patterns collected at high temperature (*i.e.*, from 100 to 800 °C, each 100 °C) reveals that the samples with the higher Si/Al ratio (H^+-ZSM-5_20, 37 and 69) underwent to a monoclinic to orthorhombic phase transition for temperatures below 100 °C. All the characteristic doublets of peaks identified for the monoclinic polymorphs merged into single peaks (Figure 5.2.3(a) and (b)) and, consequently, all Rietveld refinements at temperature ≥ 100 °C were carried out in the orthorhombic *Pnma* space group.

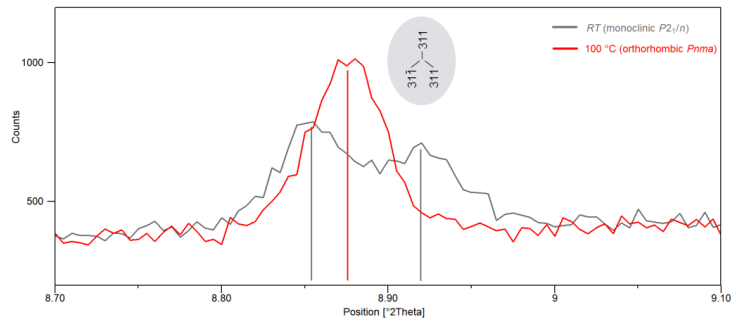

a)

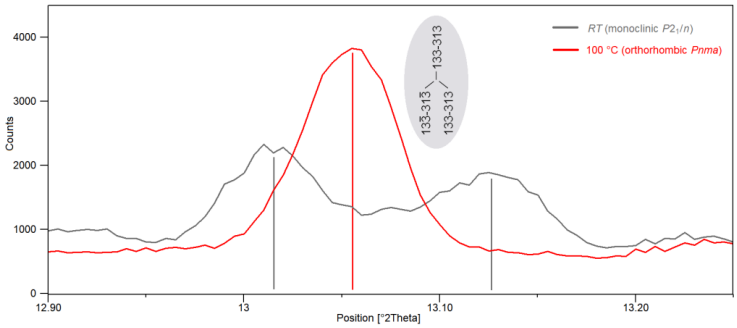

b)

Figure 5.2.3. Example of peak merging (the characteristic doublet of peaks of the monoclinic phase at room temperature becomes a single peak at high temperature, characteristic of the orthorhombic polymorph) for the sample H^+-ZSM-5_69 in the 8.70-9.10° 2θ (a) and in the 12.90-13.25° 2θ (b) ranges, respectively.

The evolution of the powder patterns upon heating is reported in Figure 5.2.4 (*i.e.*, details of high temperature patterns in the 3-10° 2θ and 10-20° of 2θ ranges, respectively). Within the investigated temperature range, no evidences of crystallinity loss are observed, thus confirming the high thermal stability usually exhibited by ZSM-5 zeolites.

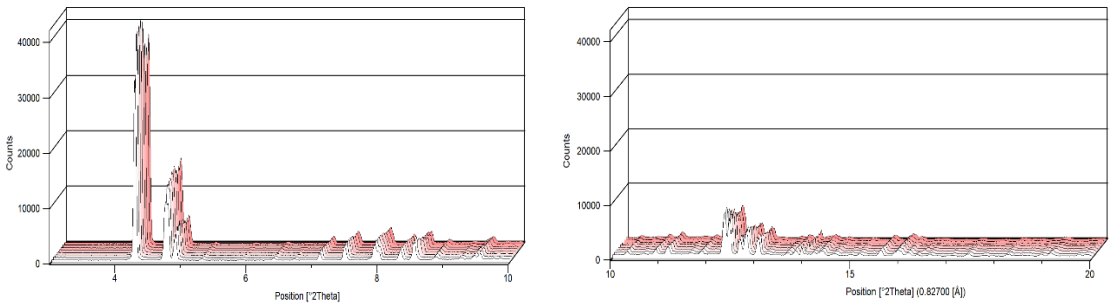

a) **b)**

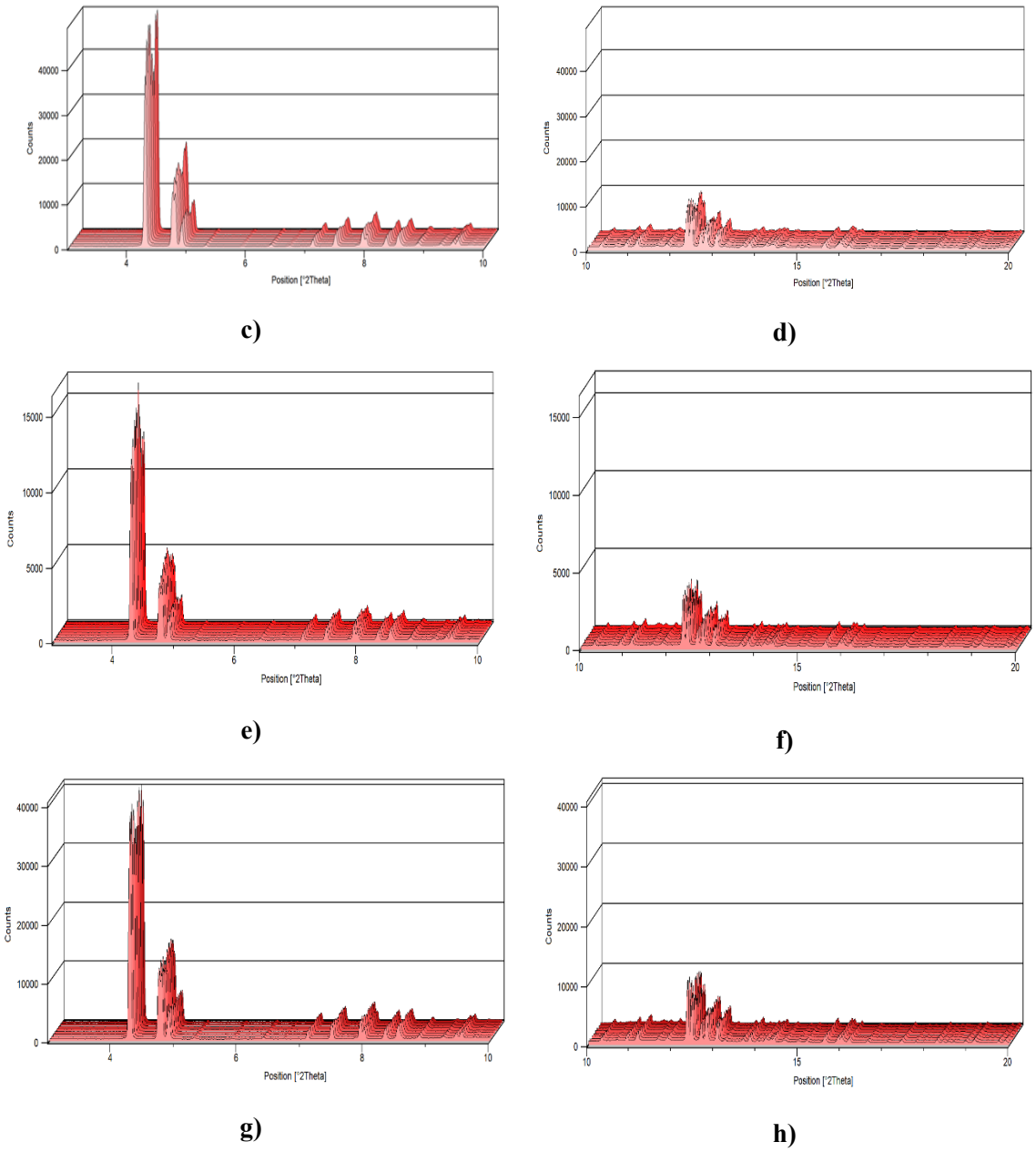

Figure 5.2.4. X-ray powder diffraction patterns collected at high temperature (details of low and high 2θ angles) for samples H^+-ZSM-5_15- (*a*,*b*), H^+-ZSM-5_20 (*c*,*d*), H^+-ZSM-5_37 (*e*,*f*) and H^+-ZSM-5_69 (*g*,*h*).

A comparison of the high temperature evolution of the normalized lattice parameters for the H^+-ZSM-5 samples is reported in Figure 5.2.5. Despite a remarkable difference in their crystal chemistry (with a Si↔Al substitution that varies from 1.4 to 6.2 apfu, Table 5.2.1), all the investigated zeolite samples show a common lattice parameters evolution on temperature. As a matter of fact, after a minimal variation of the lattice parameters between 100 and 200 °C, a common lattice shortening is observed along the crystallographic unit-cell axes. Up to the maximum investigated temperature, the average lattice shortening for all the H^+-ZSM-5 under comparison is equal to 0.3, 0.1, and 0.15% for *a*, *b*, and *c* unit-cell parameters, respectively, thus indicating an anisotropic answer to the thermal treatment.

Noteworthy is the behaviour of the H^+-ZSM-5_69 between 400 and 500 °C along all the directions, where no changes in lattice parameters are observed.

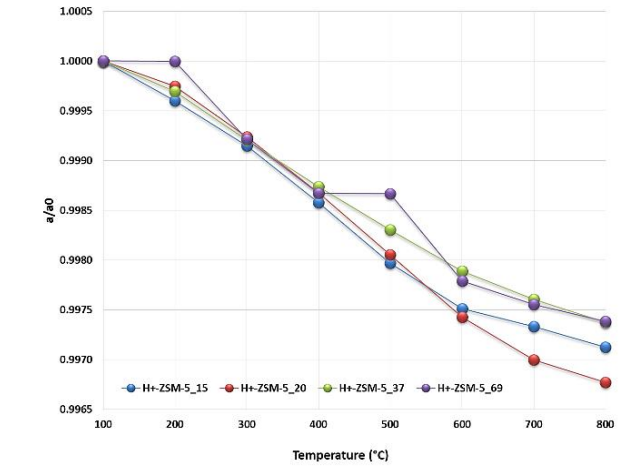

a)

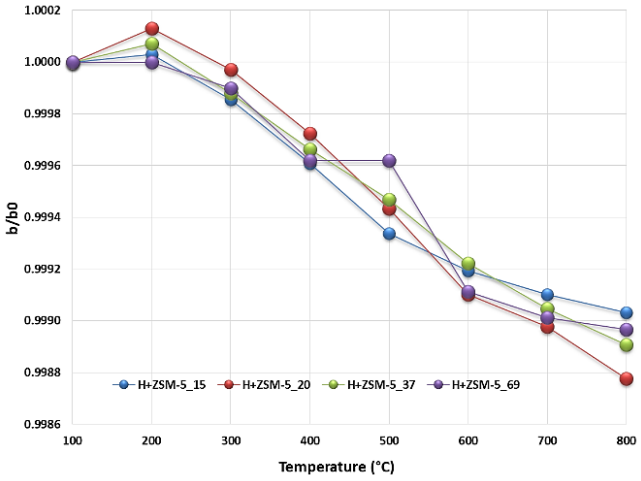

b)

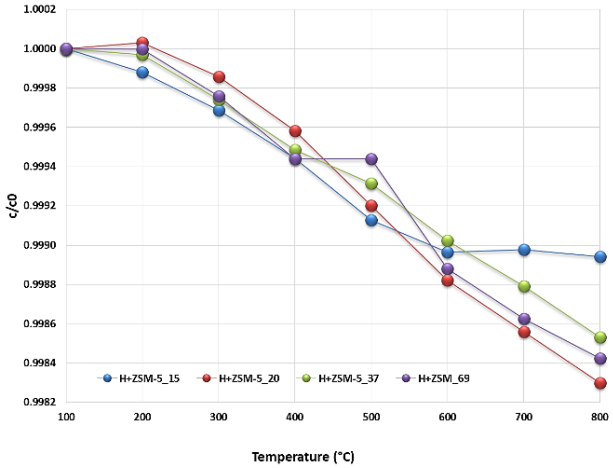

c)

Figure 5.2.5. Temperature dependence evolution of the normalized lattice parameters ((a) *a*/*a*0, (b) *b*/*b*0 and (c) *c*/*c*0) for the H^+-ZSM-5 samples under investigation.

Besides to reproduce all the features previously described for the lattice parameters, the contraction of the unit-cell volume upon heating (Figure 5.2.6) is ascribable to the so-called Negative Thermal Expansion (NTE) phenomenon, which arises from *the cooperative or supramolecular structural mechanisms that prevails over the positive thermal expansion of interatomic bonds* (Arletti et al., 2019).

The mean volumetric reduction (δV) calculated on the normalized values is equal to 0.5%, with the exception of the sample H^+-ZSM-5_20 which shows a slightly higher variation (*i.e.*, $\delta V = 0.6\%$).

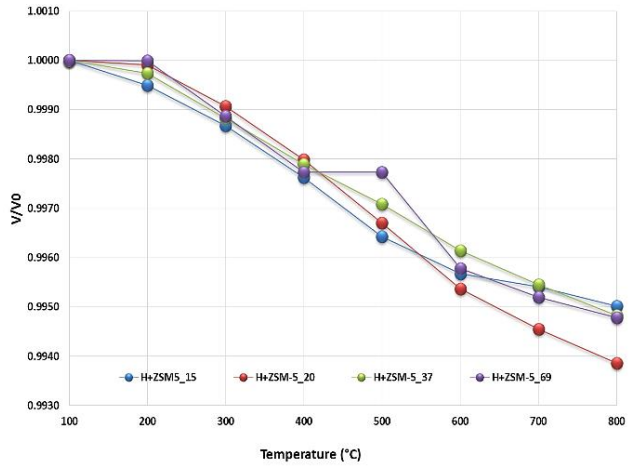

Figure 5.2.6. Evolution of the unit cell volume upon heating of the H^+-ZSM-5 samples under investigation.

In order to describe in a thermodynamic way, the observed NTE phenomenon, it was rationalized through the Fei polynomial function (Fei, 1995), as implemented in EosFit7c (Angel et al., 2014), Eq.1:

$$\alpha = \alpha_0 + \alpha_1 T + \alpha_2 T^{-2} \ (T\text{=Kelvin}) \qquad (1)$$

where the mean thermal expansion coefficient α is expressed in K^{-1}, while constants α_0, α_1,and α_2, are expressed in K^{-1}, K^{-2}, and K, respectively. Values obtained applying the Eq.1 on each ZSM-5 sample are reported in Table 5.2.4.

Table 5.2.4.
Values of Constants in the previous equation (with $\alpha_0 \times 10^{-5}$, $\alpha_1 \times 10^{-8}$, and α_2 in K^{-1}, K^{-2}, and K, respectively) obtained from fits. $\alpha_{(200\text{-}800)}$ ($\times 10^{-6}$ in K^{-1}) is the mean thermal expansion coefficient between 200 and 800 °C.

	H^+-ZSM-5_15	H^+-ZSM-5_20	H^+-ZSM-5_37	H^+-ZSM-5_69 *
V_0	5373.46(25)	5370.76(34)	5373.46(25)	5368.52(19)
α_0	-2.1(6)	-6.1(9)	-2.1(6)	-4.08(5)
α_1	1.3(5)	4.5(9)	1.3(5)	3.30(4)
α_2	1.4(9)	7.9(9)	1.40(9)	3.35(7)
$\alpha_{V(200\text{-}800)}$	-8.21	-10.08	-8.21	-8.67

* the data at 500 °C was an outlier not considered in the calculation of the polynomial regression.

Although the mean volumetric thermal expansion coefficients calculated between 200 and 800 °C for the investigated samples are quite similar, they are higher than those reported for other zeolites with MFI framework topology. In details, a $\alpha_{V(150–600)}$ of $–6.43 \times 10^{-6}$ K^{-1} has been reported for a H^+-ZSM-5 with a Si/Al ratio of 140 (Ardit et a., 2015), while a $\alpha_{V(150–600)}$ of $–7.60 \times 10^{-6}$ K^{-1} for a sample of silicalite (*i.e.*, Al → 0 (Bhange and Ramaswamy, 2006)). In Figure 5.2.7 is reported the evolution of the Atomic Displacements Parameters for the cations hosted at the tetrahedral sites between 100 and 800 °C for all the H^+-ZSM-5 samples. As reported in the section *Refinement strategy*, ADPs were constrained to be isotropic and to change equally for the 12 tetrahedral sites in the unit-cell. ADPs undergo a continuous increase up to the investigated maximum temperature. Since no extraframework species are present within the zeolite pores system, ADPs evolution on temperature has to be exclusively ascribed to the atomic thermal motion.

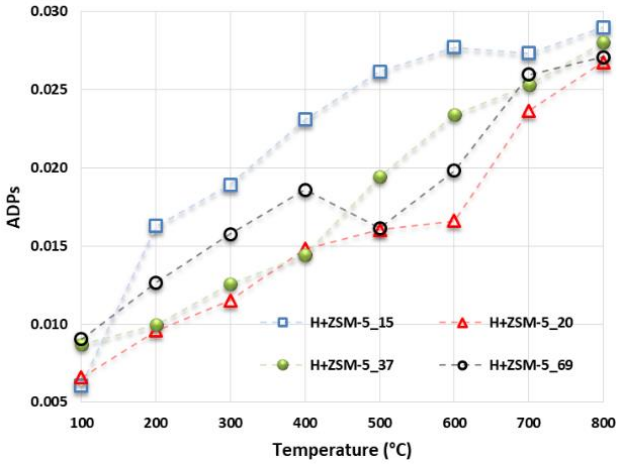

Figure 5.2.7. Evolution of ADPs parameters upon heating.

Although it could be reasonable to attribute the ADPs increase to a structural disorder increasing, no direct experimental evidences can be inferred through X-ray powder diffraction about the T–O–T bonds breaking, and the formation of Lewis acid sites (Milanesio et al., 2003). Indeed, the refined T-O bond distances and T-O-T angles at high temperature (reported in Appendix 2 at 200, 400, 600 and 800 °C for each sample; Table W, X, Y and Z for H^+-ZSM-5_15, H^+-ZSM-5_20, H^+-ZSM-5_37 and H^+-ZSM-5_69, respectively) confirms the high stability and flexibility of the selected catalysts.

Not significant variations were then detected in the evolution of the ellipticity parameter. Indeed, both sinusoidal (ZZ-A and ZZ-B) and straight channels (Figure 5.2.8) do not show evident variations in shape and geometry between 100 and 800 °C, thus probing that the zeolitic framework does not undergo to relevant distortions up to the end of the thermal treatment. More specifically, the evolution of the sinusoidal channels (*i.e.*, for both entrance

and exit) appears more regular than that the straight one. Additionally, the ellipticity progressively increases from 100 to 800 °C for all the samples analysed, although with a slight rate. Besides, the samples with the lowest Si/Al ratios are characterized by straight channels evolving with similar trends: the ellipticity progressively increase (*i.e.*, 500 °C point has not to be taken into account) up to 800 °C, unlike the samples with the highest Si/Al ratios.

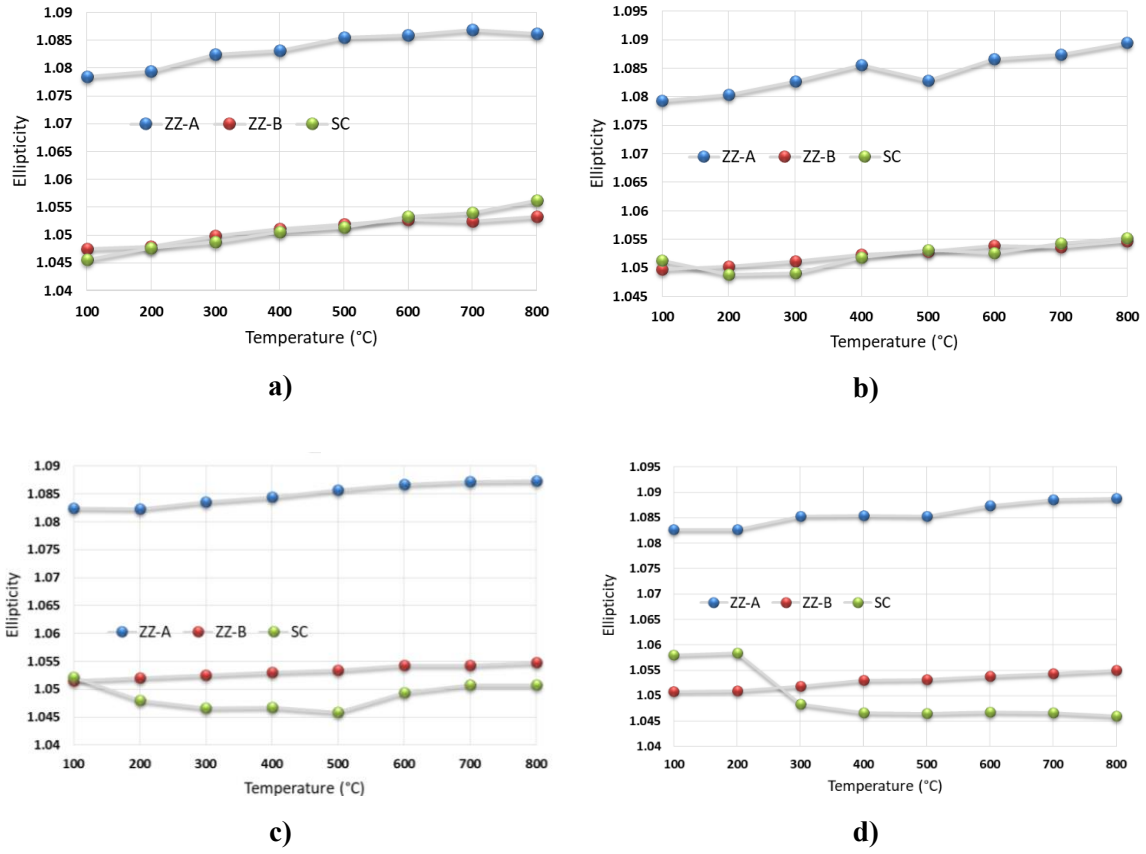

Figure 5.2.8. Evolution of the ellipticity parameter upon heating for the four H^+-ZSM-5 samples. (a) H^+-ZSM-15; (b) H^+-ZSM-20, (c) H^+-ZSM-37 and (d) H^+-ZSM-69.

Final consideration. The *in situ* synchrotron X-ray powder diffraction performed on ZSM-5 zeolites in their protonated form allowed obtaining important structural information of the most common exploited acid catalysts. Indeed, the knowledge of the structural answer of the catalysts under operating conditions is a fundamental task to prevent from unexpected phenomena limiting the catalyst activity. The results here reported confirmed that the ZSM-5 zeolites maintain unchanged their crystallinity up to the end of the thermal treatment without significantly changing their initial structural features, thus allowing to guarantee their full efficiency whether employed as acid catalysts.

SYSTEM 3

L-LYSINE ADSORPTION IN ZSM-5 ZEOLITES: A SYNCHROTRON X-RAY POWDER DIFFRACTION STUDY

Samples. The two samples of ZSM-5 zeolite were synthesized by sol-gel technique and provided by the Department of Chemical and Environmental Engineering of the University of Calabria (Rende, CS) (Frusteri et al., 2016) in their H^+ form. They were characterized by Si/Al ratios of 37 and 15 (*i.e.*, samples here labelled ZSM-$5_{(37)}$ and ZSM-$5_{(15)}$, respectively). L-lysine amino acid ((2S)-2,6-Diaminohexanoic acid, Lys) was provided by Sigma-Aldrich (Steinheim, Germany), with a purity of 99.8%. L-lysine chemical structure and its properties are shown in Table 5.3.1.

Table 5.3.1.
Properties and structure of L-lysine amino acid.

Name	***L-Lysine***
Chemical formula	$C_6H_{14}N_2O_2$
Molar mass	146.19 g·mol^{-1}
pK_a	3.12 (at 0 °C)
3D structure (https://pubchem.ncbi.nml.nih.gov/compound/Lysine)	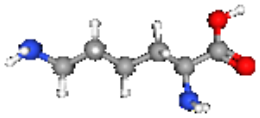

Adsorption experiments. Adsorption experiments were performed at the Department of Chemical and Pharmaceutical Sciences of the University of Ferrara. The adsorption was determined by using aqueous solutions of L-Lysine (Lys) at different initial concentrations (5, 10, 20, 50, 70, 100, 150 and 200 mg L^{-1}), placed in contact with ZSM-5 zeolites with a solid/liquid ratio of 1:1 (mg/mL). The suspensions were kept at ~ 25 °C under stirring during the contact time at pH 5.5, obtained by adding small volume of 0.1 M H_3PO_4. The contact time was of 18 h, longer than the equilibration time determined by kinetics experiments to assure equilibrium conditions. To determine the adsorption kinetics, the Lys uptake was measured starting from solutions at concentration of 50, 75, 100 mg L, after contact time equal to 1, 2, 5, 10, 20, 30, 45, 60 120 min. All batch experiments were carried out in duplicate. An Agilent Technologies Capillary Electrophoresis series 7100 system (Santa Clara, CA, USA) was employed to quantify Lys in the solution before and after the contact with zeolites. The Capillary Electrophoresis system was equipped with diode array detection (DAD). For separations, extended light path (bubble cell) bare fused-silica capillaries (red G1600-61232 I.D.: 50 μm, total length: 64.5 cm, effective length: 56

cm, bubble factor: 3) obtained from Agilent Technologies (Santa Clara, CA, USA) were employed.

Hydrodynamic injection of the solutions was performed at a pressure of 10 mbar applied for 30 seconds. The detection wavelength of the CE system was 200 nm. Positive polarity (15 kV) was applied at the capillary inlet for the duration of separation. The running buffer was obtained by a 50 mM solution of Na_2HPO_4 in MilliQ water, at pH 5.5 adjusted by adding H_3PO_4.The pH of the electrolyte was measured using an AMEL pHmeter (Milano, Italy). Before use, the capillary was pretreated through sequential flushing with 1M NaOH for 5 minutes, 0.1M NaOH for 5 minutes and MilliQ (Millipore, Bedford, MA, USA) grade water for 15 minutes. The capillary was also rinsed with water for 3 minutes, 0.1M NaOH for 2 minutes, water for 3 minutes, and running buffer for 5 minutes between each run.

The amount of Lys adsorbed at equilibrium, q_e (mg g^{-1}), was calculated from the mass balance equation, Eq.1:

$$q_e = \frac{(C_i - C_e)V}{M} \quad (1)$$

where C_i and C_e (mg L^{-1}) are the liquid-phase concentrations of Lys in the reference solution and at equilibrium respectively; V (L) is the volume of the solution and M (g) is the mass of dry zeolite used. Samples of saturated zeolite with Lys were used for structural investigations. ZSM-$5_{(37)}$ and ZSM-$5_{(15)}$ (0.5 g) were suspended with stirring in 500 ml of an aqueous solution of Lys at pH 5.5 at 298 K for 24 h. The zeolite was recovered by filtration, washed with 200 mL of MilliQ water and dried in oven at 300 K overnight.

Data collection. Room temperature synchrotron data were collected at the MCX Beamline of the Elettra Synchrotron Light Source (Trieste, Italy) on a 4-circle Huber diffractometer with a 3D translation stage. The diffractometer was equipped with a Si(111) double crystal monochromator and a high-count rate fast scintillator detector preceded by a pair of slits with vertical aperture of 200 and 300 μm. ZSM-$5_{(37)}$ and ZSM-$5_{(15)}$ samples were loaded into an axially spinning borosilicate capillary (Ø=0.5 mm) and all powder patterns were collected at room temperature (λ=0.82700(1) Å, in the 3-36° 2θ range, with 0.006 ° 2θ step size).

Thermogravimetric (TG) and thermodifferential (DTA) curves were obtained through the simultaneous TG/DTA thermogravimetric balance after L-lysine adsorption on both ZSM-$5_{(37)}$ and ZSM-$5_{(15)}$ samples. Thermal analyses were performed from room temperature to 900 °C, with a heating rate of 10 °C/min in costant flux of air conditions.

Refinement strategy. Full profile Rietveld refinements were performed in the $P2_1/n$ monoclinic space group for both ZSM-$5_{(37)}$ and ZSM-$5_{(15)}$. Framework atoms coordinates of

Van Koningsveld et al., (1990) were selected as starting model for unit cell and structural parameters determination. Peaks profile was modelled through the Pseudo-Voigt function with 0.01% cut-off peak intensity. Refined profile coefficients were the Gaussian θ-indipendent *GW*, $\tan^2\theta$-dependent *GU*, Lorentian $\tan\theta$-dependent LY terms and the peak *asymmetry* and *stec* parameters. The instrumental background was fitted by a Chebyschev polynomial function with 18 coefficients. Scale factor and 2θ zero shift were also accurately refined. For both structural refinements, equal soft constraints were initially imposed on tetrahedral distances (T-O=1.60 Å and O-O=2.60 Å, σ=0.04) and completely removed in the last refinement cycles. Extraframework molecules were firstly detected with the Difference Fourier Maps and L-lysine bond distances were refined after the imposition of soft constraints: C-C and C-N =1.40 Å and C-O =1.35 Å (*i.e.*, σ=0.04). The geometry of the molecule was then completed and optimized through the EXPO2014 software and the optimize geometry tool (*i.e.*, the tool allows to obtain accurate molecular structures applying different levels of theory: molecular mechanics, semi-empirical methods, Hartree-Fock methods and density functional theory (DFT)) (Altomare et al., 2013; http://www.ba.ic.cnr.it/softwareic/expo/geometry-optimization) to obtain reasonable bond lengths and angles and provide a reasonable structural model for the extraframework L-lysine sites. The resulting structure was then refined again together with the GSAS program until the geometry of the organic was reasonable and the structural model showed the best agreement with the experimental data. Their atomic coordinates were then fixed in the final cycles of Rietveld refinement of both ZSM-5 samples, in order to reduce the number of refined parameters. Finally, framework atomic coordinates and Atomic Displacement Parameters (ADPs, U_{iso}) were refined, constraining equivalent U_{iso} for Si^{+4} and O^{-2}. The final fit of both Rietveld refinements is given in Figure 5.3.1.

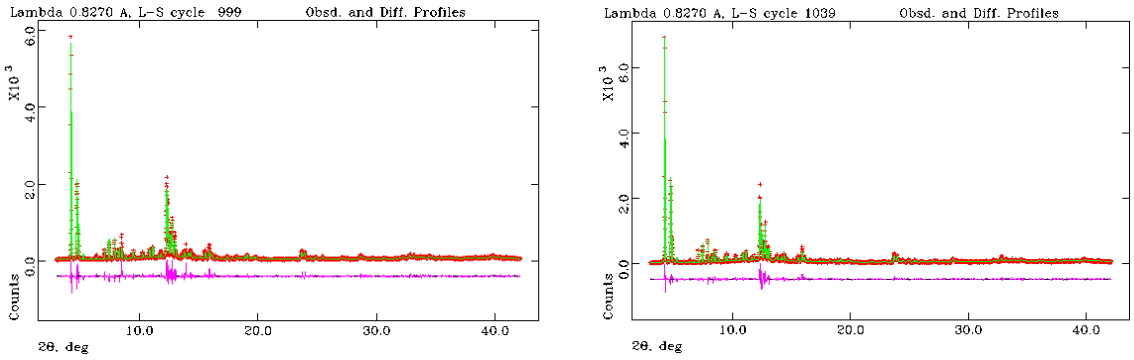

Figure 5.3.1. Final Rietveld fit of synchrotron X-ray powder diffraction patterns of ZSM-5 zeolites loaded with L-lysine. (a) ZSM-$5_{(15)}$, (b) ZSM-$5_{(37)}$, crosses represent observed data, the solid line is the calculated pattern, and the difference profile and allowed reflection positions are shown beneath.

Details about data collection and R-values agreement indices are reported in Table 5.3.2. Framework atomic coordinates, fraction and Atomic Displacement Parameters of ZSM-5$_{(37)}$ and ZSM-5$_{(15)}$ are available in Appendix 3, Tables A and B, respectively. Extraframework atomic coordinates, fraction and Atomic Displacement Parameters are given in Appendix 3, Table C. T-O bond distances and T-O-T angles of both ZSM-5 samples are reported in Appendix 3, Table D.

Table 5.3.2.
Details of data collection and R-values agreement indices.

Parameter	ZSM-5$_{(37)}$	ZSM-5$_{(15)}$
Wavelength (Å)	0.82700(1)	0.82700(1)
Refined 2θ (°) range	3-36	3-36
N_{data}	6522	6522
N_{var}	316	316
R_{wp} (%)	14.19	16.82
R_p (%)	11.03	12.58
R_F^2 (%)	9.92	8.39

$R_p=\sum[Y_{io}-Y_{ic}]/\sum Y_{_io}$; $R_{wp}=[\sum wi(Y_{io}-Y_{ic})^{\wedge}2/\sum wiY_{io}^2]^{\wedge}0.5$; $R_F^2=\sum|F_o^2-F_c^2|/|F_o^2|$

Effect of pH on sorption capacity. The effect of pH on the adsorption of Lys onto ZSM-5 was investigated in the 4-8 pH range obtained by adding small volume of 0.1 M H_3PO_4. This range was selected in order to avoid partial dissolution or degradation of zeolite in acidic and basic aqueous media. The Lys distribution diagram (Figure 5.3.2) highlights that in the 4-8 pH range the Lys is mainly in its protonated form.

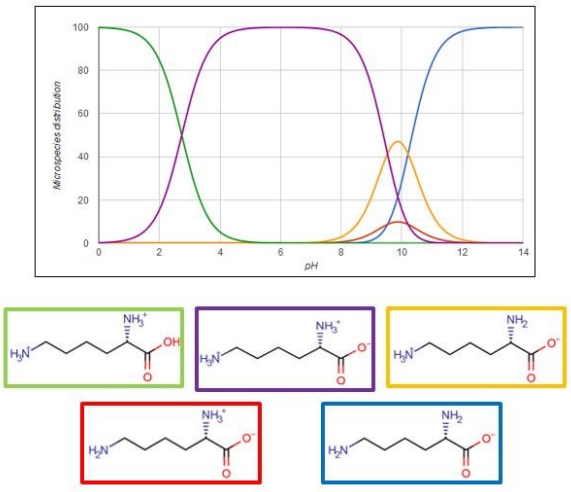

Figure 5.3.2. Lys distribution diagram (images taken from https://chemicalize.com/app/calculation/lysine website).

Therefore, in such pH interval, adsorption should not be influenced by pH (Krohn and Tsapatsis, 2005). However, it has been reported by Munsch et al., (2001) that adsorption of lysine on ZSM-5 zeolite having a SAR equal to 25 increases with the pH. The data gathered from adsorption experiments at pH equal to 4, 5.5 and 8 do not show a significant difference

in the Lys uptake (Figure 5.3.3). Therefore, the interaction responsible for the adsorption between Lys and both the adsorbents are mainly driven by the ionic form of the amino acid than from specific hydrophobic interactions involving amino acid lateral chain group. In these experiments, a contact time of 24 h was employed to reach the equilibrium conditions.

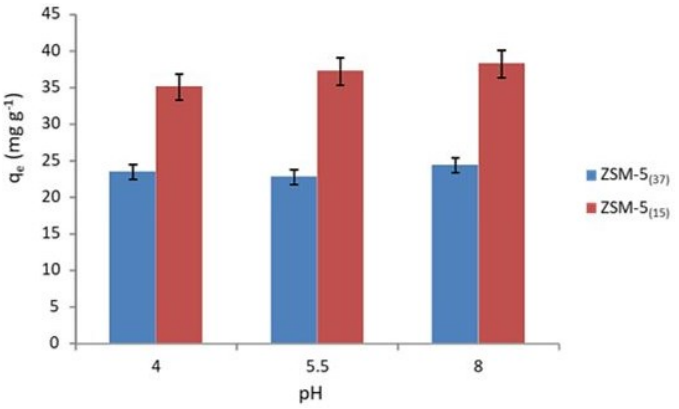

Figure 5.3.3. Adsorbed quantity on ZSM-5 zeolites obtained from Lys solution of initial concentration equal to 50 mg L^{-1}.

Kinetics experiments. To gain insight on the equilibrium time and the kinetics of the adsorption process, the Lys uptake vs. time was measured. Figure 5.3.4 shows that adsorption equilibrium is reached in about 60 minutes. Similar behaviour has been observed for the ZSM-5$_{(37)}$, hence for both the zeolites.

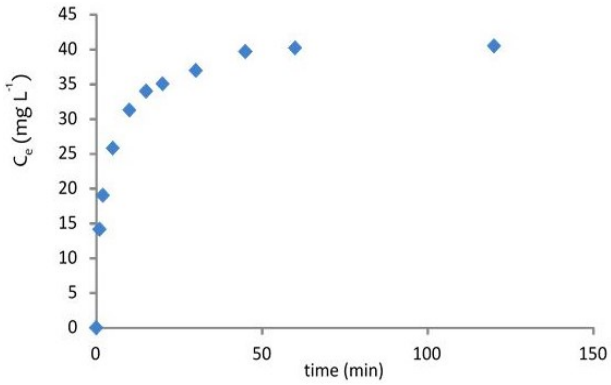

Figure 5.3.4. Uptake of Lys on ZSM-5$_{(15)}$ *vs*. time.

The experimental data were modelled by using the pseudo first-order (PFO) equation, given by Eq.2:

$$q_t = q_e[1 - \exp(-k_1 t)] \quad (2)$$

where q_t, is the adsorbed quantity per unit mass after a contact time t and k_1 is the pseudo first-order kinetic constant.

In addition, a pseudo second-order (PSO) relationships, Eq.3:

$$q_t = \frac{k_2\ q_e^2\ t}{1+k_2\ q_e\ t} \quad (3)$$

where k_2 is the pseudo second-order kinetic constant.

The parameters obtained by nonlinear fitting regression are reported in Table 5.3.3 and 5.3.4.

Table 5.3.3.
Parameters obtained by non-linear fitting of the uptake data using a PFO model. The error is given as confidence interval at 95% of probability.

Samples	k_1 (min^{-1})	q_e (mg L^{-1})	R^2
ZSM-5$_{(15)}$	0.29 ± 0.11	37 ± 3	0.9464
ZSM-5$_{(37)}$	0.21 ± 0.12	20.0 ± 0.4	0.9264

Table 5.3.4.
Parameters obtained by non-linear fitting of the uptake data using a PSO model. The error is given as confidence interval at 95% of probability.

Samples	k_2 (g mg^{-1} min^{-1})	q_e (mg L^{-1})	R^2
ZSM-5$_{(15)}$	0.010 ± 0.003	41.0 ± 2.1	0.9905
ZSM-5$_{(37)}$	0.00720 ± 0.00052	23.0 ± 2.3	0.9887

It has been reported in the literature (Simonin, 2016) that the goodness of fitting is not a criteria sufficient to assess the mechanism underlying the adsorption process. However as suggested by Simonin (2016), the reliability of the fitted parameters could be employed to select the kinetic model. From the comparison of data in Table 5.3.3 and 5.3.4, it can be observed that the kinetic constant evaluated by PSO are more precise than those obtained by PFO, thus suggesting the rate-limiting step is the adsorption into the zeolites pores.

Adsorption results. The quantity adsorbed from solution at different initial concentrations has been measured at constant temperature. The experimental data are reported in Figure 5.3.5(a) and (b) for ZSM-5$_{(15)}$ and ZSM-5$_{(37)}$, respectively. For both zeolites, the data indicate that shape of isotherm curves is convex, showing a favourable adsorption for Lys.

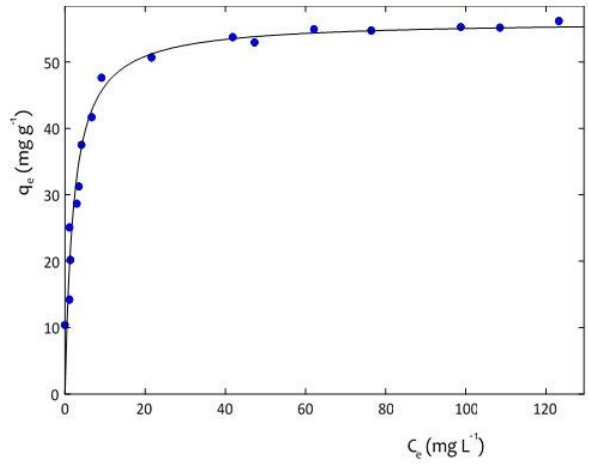

a)

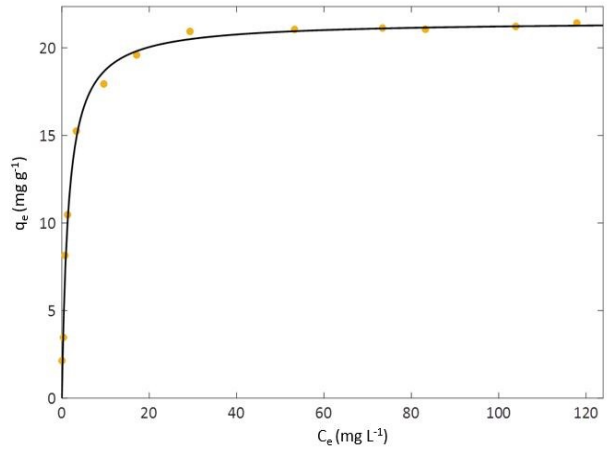

b)

Figure 5.3.5. Adsorption of Lys on (a) ZSM-$5_{(15)}$ and (b) ZSM-$5_{(37)}$.

Data were fitted through a Langmuir model, Eq.4:

$$q_e = \frac{q_s\ b\ C_e}{1\ b\ C_e} \tag{4}$$

where q_s is the saturation capacity of the zeolite and b is the binding constant. The model has been already employed to model the adsorption of amino acids onto ZSM-5 (Titus et al., 2003).

In Table 5.3.5 the binding constants and saturation capacities for the adsorption of Lys on both ZSM-5 zeolites are reported.

Table 5.3.5.
Binding constants and saturation capacities for the adsorption of Lys. The error is given as confidence interval at 95% of probability.

Samples	q_{max} (mg/g)	*B* (L/mg)	R^2
ZSM-5$_{(15)}$	56.2 ± 2.7	0.60 ± 0.23	0.9633
ZSM-5$_{(37)}$	21.5 ± 1.2	0.40 ± 0.14	0.9827

The parameters in Table 5.3.5 indicate that both saturation capacity and binding constant are larger for ZSM-$5_{(15)}$ with respect to ZSM-$5_{(37)}$. These differences seem to be due to the

different chemical composition of the two zeolites and in particular to the different SAR ratio. This result can be explained on the basis of a higher hydrophilicity of ZSM-$5_{(15)}$ that can positively affect the adsorption of the cationic form of Lys. In addition, the observed behaviour is in agreement with those reported by Krohn and Tsapatsis, (2005).

Results and discussion of structural refinements. The comparison of powders patterns collected before and after the L-lysine adsorption (Figure 5.3.6), showed that although the separation between the angular positions of the -313 and 313 reflections of the monoclinic phase is not well appreciated, the β angle refined is sufficiently wide to suggest the monoclinic symmetry of both systems (β=90.505(3)° and 90.517(2)° in ZSM-$5_{(15)}$ and ZSM-$5_{(37)}$, respectively).

On the whole, the refined lattice parameters highlighted only slight differences between the two loaded-samples (a=19.9111(5) Å, b=20.1324(5) Å, c=13.3944(4) Å, V=5369.02(25) Å^3 for ZSM-$5_{(15)}$; a=19.9075(5) Å, b=20.1316(4) Å, c=13.3905(3) Å, V=5366.29(22) Å^3, for ZSM-$5_{(37)}$, respectively).

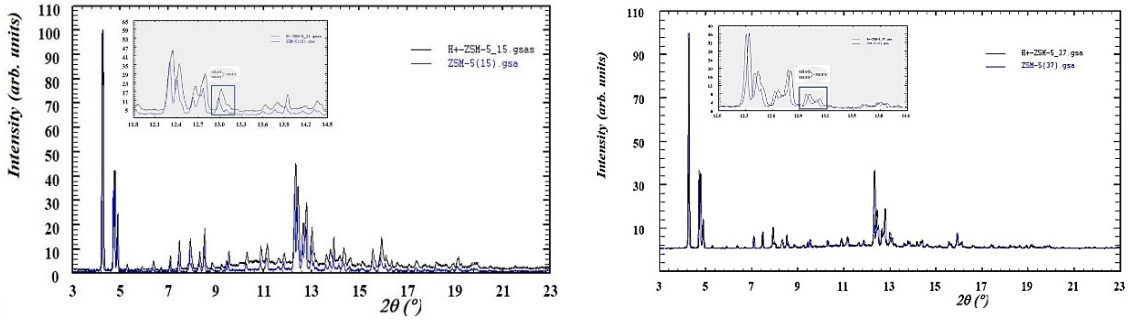

Figure 5.3.6. Comparison between X-ray powder patterns before and after the L-lysine adsorption. (a) H^+-ZSM-5_15 and ZSM-$5_{(15)}$; (b) H^+-ZSM-5_37 and ZSM-$5_{(37)}$.

The analysis of the Difference Fourier maps revealed the presence of two adsorption sites attributed to the L-lysine in both systems analysed. The first one is located at the intersection of the sinusoidal and the straight channel (site A), whereas the second one within the sinusoidal channel (site B). The carbon atoms defining the side chain of the guest molecule lie on the [100] and on the [010] directions for the site A and B, respectively. The refinement of the occupancies showed that the two sites are partially occupied in both systems. On a whole, 4.8 and 6.7 wt% of L-lysine was detected within the ZSM-$5_{(37)}$ and ZSM-$5_{(15)}$, respectively (equal to ~1.9 and 2.8 molecules of L-lysine per unit cell). Besides, in both systems, one additional residual of electron density was highlighted by the Difference Fourier maps and then attributed to coadsorbed water molecules (*i.e.*, labelled W1, fractional coordinates equal to: x/a=1/2, y/b=1/2 and z/c=0.0). The distribution of extraframework

molecules in both ZSM-$5_{(37)}$ and ZSM-$5_{(15)}$ is shown in Figure 5.3.7(a) and (b). On the basis of the refined occupancies, 0.2 and 0.07 wt% of coadsorbed water molecules were calculated for ZSM-$5_{(37)}$ and ZSM-$5_{(15)}$, respectively. As reported by Titus et al., (2003), the presence of extremely low content of water with respect to the amino acid is due to the higher affinity of the zeolite towards the solutes organic molecule.

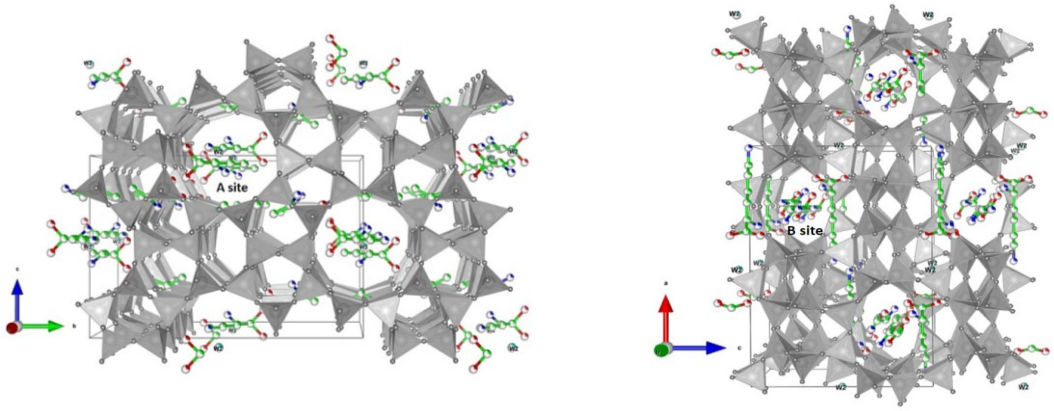

Figure 5.3.7. Distribution of extraframework sites. (a) Site A observed along the [100] direction. (b) Site B observed along the [010] direction.

The bond distances analysis confirmed the presence of strong host-guest and guest-guest interactions. Specifically, the L-lysine molecules appear bonded each other as well as to the framework oxygen atoms and water molecules, as testified by bond lengths reported in Table 5.3.6. The interactions with framework oxygens guarantee the immobilization of the guest molecule within the zeolite channel system. On the contrary, no interactions between water molecules and framework oxygen atoms were highlighted.

Table 5.3.6.
Bond distances between extraframework molecules and/or framework oxygen atoms.

Distances (Å)	ZSM-$5_{(37)}$	ZSM-$5_{(15)}$
C98a-O20	2.90(3)	2.92(1)
C98a-O28	3.18(2)	3.14(1)
C99a-O31	2.74(4)	2.70(1)
C99a-O44	2.88(4)	2.91(2)
C101b-O18	2.86(1)	2.93(2)
C101b-O25	2.93(2)	2.97(3)
Na1-O31	2.80(1)	2.76(1)
Na1-O45	2.73(1)	2.68(2)
Oa1-O27	2.85(5)	2.87(3)
Oa1-O28	2.48(2)	2.48(1)
Oa1-W1	2.34(2)	2.36(3)
Oa2-O20	2.33(1)	2.32(1)
Oa2-O28	2.88(3)	2.83(2)
Oa2-Ob1	2.96(2)	2.98(1)
Oa2-Ob2	2.14(2)	2.12(1)
Nb1-O15	2.98(2)	2.96(3)
Nb1-O41	2.44(1)	2.47(1)
Ob1-O26	2.75(2)	2.87(3)
Nb2-O18	2.24(1)	2.27(3)
Nb2-O35	2.78(5)	2.74(4)
Nb2-O44	2.88(2)	2.85(3)

Furthermore, the analysis of the ellipticity parameter (*i.e.*, ε, defined as the ratio of the larger and the smaller O-O free diameter) confirmed that both sinusoidal and straights channels retain a circular shape after the L-lysine adsorption, as testified by the following values: 1) SC channel: ε=1.05 - ZZ channel entrance and exit: ε=1.07 and 1.03 for ZSM-$5_{(37)}$; 2) SC channel: ε=1.05 - ZZ channel entrance and exit: 1.07 and 1.04 for ZSM-$5_{(15)}$.

Refined extraframework occupancies resulted in good agreement with thermal curves (Figure 5.3.8(a) and (b)), which register between 100 and 900 °C a total weight loss of ~4.2 and 6.6 wt% for ZSM-$5_{(37)}$ and ZSM-$5_{(15)}$, respectively. The mass reduction observed in this thermal range is driven by the H_2O molecules desorption and the L-lysine decomposition. Along the same thermal range, the DTA curve of both samples showed the presence of two exothermic peaks between 300 and 700 °C reasonably ascribable to L-lysine oxidation/combustion processes since both measurements were performed in flux of air. The mass loss observed from room temperature to 100 °C, almost equal for both ZSM-$5_{(37)}$ and ZSM-$5_{(15)}$ samples (~2 wt%), is attributed to the release of surface adsorbed water, as suggested by the first intense endothermic peak of the DTA curve.

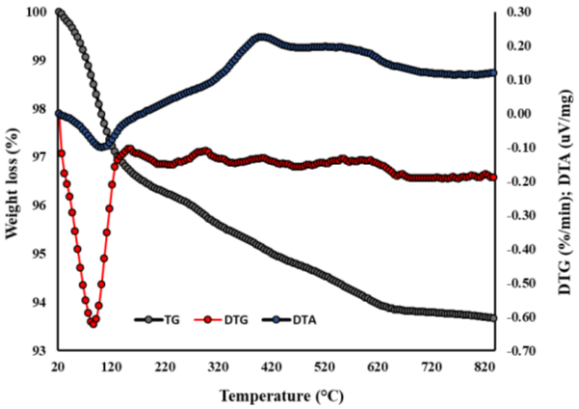

a)

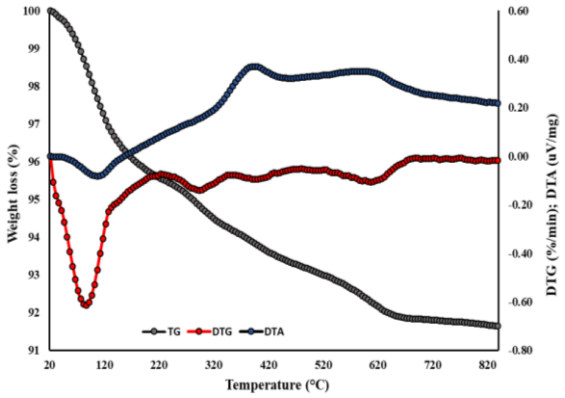

b)

Figure 5.3.8. Thermal analysis of ZSM-$5_{(37)}$ (a) and ZSM-$5_{(15)}$ (b). In grey and red circles the total weight loss curve (TG) and its first derivative (DTG), respectively; in blue the differential thermal analysis (DTA) curve.

Final consideration. The multitechnical approach used to study the sorption capacity of ZSM-5 zeolites towards the L-lysine aminoacid allowed to probe the efficiency of both samples in encapsulating the organic molecule. Indeed, both ZSM-5 showed of being selective for the L-lysine, thus indicating that co-adsorbed water molecules do not act as competitors in the adsorption processes, although the different degree of hydrophilicity of the two samples. The results gained suggest that ZSM-5 is a performing sorbent material for the L-lysine compound and its use in separation and/or purification processes of this molecule could provide excellent results reducing the product loss that usually occurs during adsorption and desorption processes.

SYSTEM 4

STRUCTURAL CHARACTERIZATION OF ACIDIC L AND ITS PRECURSOR BY NEUTRON POWDER DIFFRACTION

Samples. The sample used in this investigation is a synthetic commercial L zeolite in its K form, provided by Tosoh Corporation (code 500KOA, namely L-LTL from now). The SiO_2/Al_2O_3 ratio (SAR) is equal to 6.1. The Na_2O and K_2O contents are 0.25 and 16.8 wt%, respectively. The surface area (BET) is 290 m^2/g. The L-LTL form was exchanged with 1 M ND_4NO_3 aqueous solution for ≈140 h at room temperature in order to obtain the acidic precursor (ND_4-LTL). Subsequently, the sample was filtered and heated under vacuum for 24 h at 600 °C to remove ND_3, then washed with D_2O and dried overnight at 96 °C (D-LTL).

Data collection. LTL, ND_4-LTL and D-LTL samples were packed in an argon-flushed glove-bag into a vanadium container sealed with a rubber gasket and six screws to ensure humidity-free transport to the neutron source. Neutron data were collected at low temperature (-270.9 °C) at the high-resolution two-axis powder diffraction beamline D2B (wavelength = 2.3984(1) Å, 4.0 –150° 2θ range) of the Institut Max Von Laue-Paul Langevin (ILL, Grenoble).

The TG/DTA thermogravimetric balance was employed to perform both thermogravimetric (TG) and differential thermal analysis (DTA) on L zeolite before the exchange process. The measurements were performed in conditions of constant flux of air using a heating rate of 10 °C/min, from room temperature to 900 °C.

Refinement strategy. Rietveld structure refinements were performed in the hexagonal *P*6/*mmm* space group. For all structural refinements, Bragg peak profiles were modelled using a pseudo-Voigt function with a 0.01% cut-off of the peak intensity. The background curve was fitted using 20 shifted Chebyschev polynomial coefficients. Others refined parameters were: 2θ-zero shift, scale factor, unit-cell parameters, atomic coordinates, occupancy factors and Atomic Displacement Parameters (ADPs, U_{iso}) for both framework and extraframework atoms. Soft constraints were initially imposed to T-O (*i.e.*, 1.68 Å and 0.04 Å tolerance value), and D-O (*i.e.*, 1.00 Å and 0.04 Å tolerance value) bond distances and then relaxed in last refinement cycles. The location of protons and extraframework species was carried out by a combination of least squares and Difference Fourier map techniques. Specifically, the possible location of protons was derived from residuals of electron density calculated by mean of delta Fourier maps. In a successive step, the fractional atomic coordinated of the previously localized protons were refined through

least squares refinement cycles. Details of data collection and R-values agreement indices are reported in Table 5.4.1.

Table 5.4.1.
Details of data collection and R-values agreement indices of L-LTL, ND_4-LTL and D-LTL samples.

Parameter	L-LTL	ND_4-LTL	D-LTL
Wavelength (Å)	2.3984(1)	2.3984(1)	2.3984(1)
2θ (°) range	4.0-150	4.0-150	4.0-150
N_{obs}	311	311	311
N_{var}	69	60	63
R_{wp} (%)	7.10	5.96	5.46
R_p (%)	5.29	3.34	4.16
R_F^2 (%)	9.78	15.75	19.66

$R_p = \sum[Y_{io} - Y_{ic}]/\sum Y_{io}$; $R_{wp} = [\sum wi(Y_{io} - Y_{ic})^2/\sum wiY_{io}^2]^{0.5}$; $R_F^2 = \sum |F_o^2 - F_c^2|/|F_o^2|$

Atomic coordinates, fraction and Atomic Displacement Parameters of framework and extraframework atoms of L-LTL, ND_4-LTL and D-LTL samples are listed in Appendix 4, Table A, B and C, respectively. The final Rietveld fit of the L-LTL is reported in Figure 5.4.1.

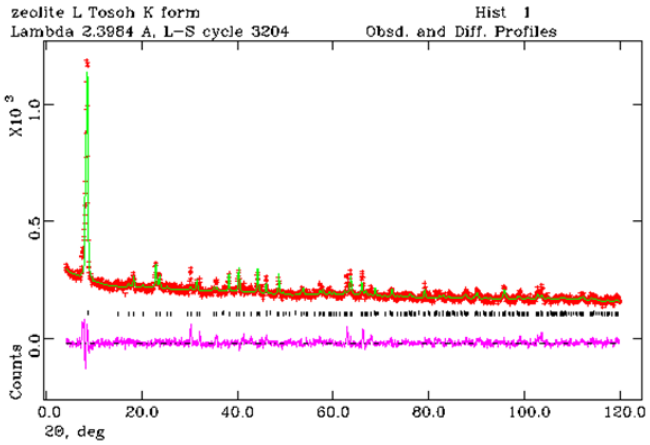

Figure 5.4.1. Final Rietveld fit of the L-LTL system. The experimentally observed data are indicated in red, the calculated pattern in green, and the pink curve is the weighted difference between the calculated and observed patterns.

D-LTL modeling. Computational modeling of D-LTL sample was performed by the research group of the Department of Science and High Technology of University of Insubria (Como). All the simulations performed on the D-LTL sample were carried out with the CPMD (Car Parrinello Molecular Dynamics) code (www.cpmd.org). It is a program package based on the DFT scheme, plane wave basis sets and periodic boundary conditions, which allows for the FPMD simulation of systems up to a few hundreds of atoms in the simulation cell. FPMD simulations, due to their high computational cost, are limited to elapsed times of the order of tens of ps.

Results and discussion of L-LTL structural refinement. The L-LTL crystal structure was refined by the Rietveld method in the *P*6/*mmm* space group, starting from the structural model reported by Barrer and Villiger, (1969a). According to Newsam (1987), the refined bond lengths suggested that the (Si, Al) distribution is not random (<T1−O>=1.640 Å; <T2−O>=1.654 Å), and indicated that Al is preferentially located at the T2 site (Appendix 4, Table D). The enrichment of Al at T2 site was corroborated by the refined tetrahedral occupancies, also confirming that neutron diffraction is an excellent tool for the differentiation of Si and Al atoms due to their different scattering lengths (b(Al)=3.449 x 10^{-15} m, b(Si)=4.149 x 10^{-15} m) (Sears, 1992).

As already reported by Gigli et al. (2013), the KA site is empty and all K ions are hosted in KB, KC and KD sites, respectively (Figure 5.4.2(a) and (b) and Appendix 4, Table D). On the whole, 10.0 K ions are detected by means of the refined occupancies.

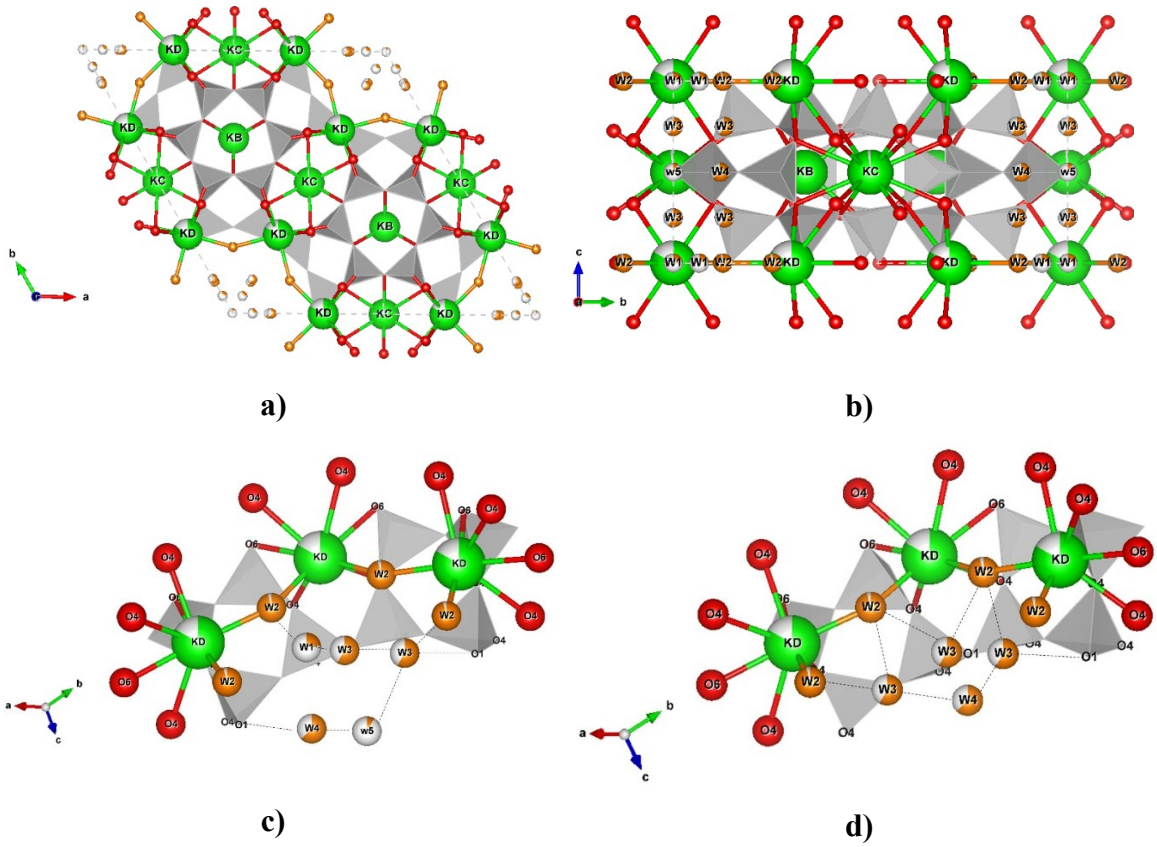

Figure 5.4.2. Projection along the *c*- (a) and *a*-axis (b) of L-LTL at room temperature. (c) and (d) Red: framework oxygens. Orange: water sites; green: K sites + clusters.

Eighteen water molecules per unit cell (corresponding to ≈11.3 wt%) spread over five partially occupied extraframework sites have been detected through Rietveld structural refinements. They are all located in the main channel thus forming a succession of clusters with partial regularity, hydrogen-bonded to O1 framework oxygen atom (O1-W3=3.22(1) and O1-W4=2.80(1), respectively) (Figure 5.4.2(c) and (d) and Appendix 4, Table D).

Their arrangement is slightly different to that reported by Lee et al., (2007) and Gigli et al., (2013) due to the different degrees of the overall hydration upon non-framework cation substitution. The total number of water molecules - as calculated from the refined occupancies of all W sites - well agrees with the weight loss registered by the thermal analysis (*i.e.*, ≈11.5 wt%, from room temperature to 900 °C; Figure 5.4.3).

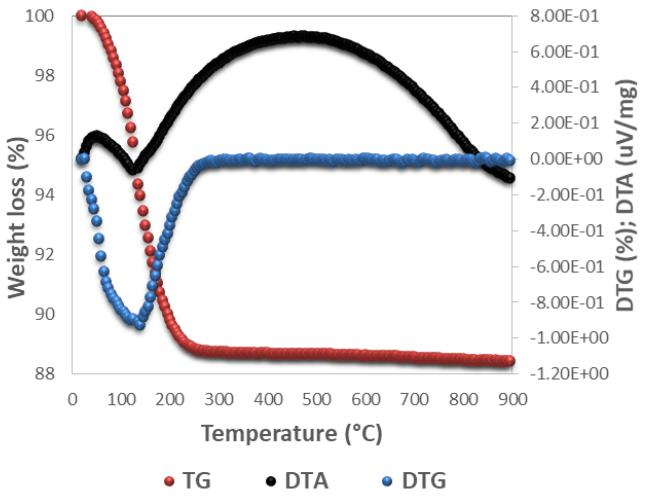

Figure 5.4.3. Thermal analysis of L-LTL sample from room temperature to 900°C. In red and blue circles the total weight loss curve (TG) and its first derivative (DTG), respectively; in black the differential thermal analysis (DTA) curve.

Results and discussion of ND_4-LTL structural refinement. After ND_4-exchange, no evidence of symmetry changes was found, consequently the same *P6/mmm* space group as in L-LTL was adopted for this structure refinement. Framework atoms of L-LTL provided the starting structural model for determining the structure of ND_4-LTL sample. Rietveld refinement indicated a small but significant increase in unit-cell parameters with respect to the as-synthesized zeolite (L-LTL: $a=b=18.3746(11)$ Å, $c=7.5270(6)$ Å, $V=2200.84(25)$ Å^3; ND_4-LTL: $a=b=18.4202(10)$ Å, $c=7.5402(5)$ Å, $V=2215.67(23)$ Å^3) in agreement with other NH_4-exchanged zeolites (Gualtieri and Passaglia, 2006; Armbruster et al., 2000; Gualtieri, 2000; Martucci et al., 2000a; Meneghinello et al., 2000; Alberti et al., 1999; Sani et al., 1999). Along with the lattice parameters, also the mean T-O bond distances underwent a remarkable lengthening with respect to those of L-LTL sample (*i.e.*, <T1-O>=1.674 Å and <T2-O>=1.705 Å for ND_4-LTL, while <T1-O>=1.640 Å and <T2-O>=1.654 Å for L-LTL, respectively) (Appendix 4, Table D). Furthermore, the mean T-O-T angles changed from 141.8° (for L-LTL sample) to 148.2° (for ND_4-LTL sample). Worth noting, the very wide T1-O2-T1 angle (~164°) in the 12-membered ring channel, one of the widest angles found to date in zeolites, as well as the remarkably narrow T2-O5-T2 angle (~129°) (Martucci et al., 2003; Rinaldi et al., 1975; Galli et al., 1974). It is well known that wide T-O-T angles

are expected to generate strong acidity in protonic zeolites (Rabo and Gajda, 1990), thus providing a rationale for the presence of very strong Brønsted sites. At the same time, the narrowing of T2-O5-T2 angle can be explained with the interaction of framework oxygen O5 with a new extraframework site located in the 8-membered ring (N1 in Figure 5.4.4(a) and (b) and Appendix 4, Table D). This was assigned to ND_4-species hydrogen-bonded to the framework (N1-O5=2.84(1) Å) and which are responsible for the strong distortion of the 8MR. Three other extraframework sites were assigned to ND_4 (N2, N3 and N4, respectively). One of this (N2) is weakly hydrogen-bonded to O6 framework oxygens (N2-O6=3.20(1) Å), thus forming O6-N2-N3-N4-N4-N3-N2-O6 oligomers. The residual extra-framework K cations (4 a.u.c.) occupy the KB site and are six-fold coordinated to the O3 framework oxygen atom (KB-O3=3.18(1) [x6] Å) (Appendix 4, table D).

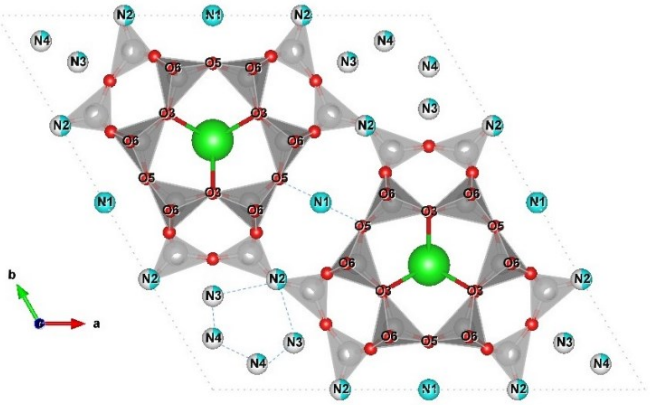

a)

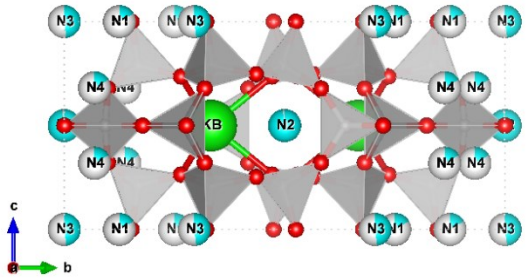

b)

Figure 5.4.4. Projection along the *c* (a) and *a* (b) axes of ND_4-LTL. Red: framework oxygens. Light blue: nitrogen sites; green: K sites.

Results and discussion of D-LTL structural refinement. From the structure refinement of the acidic L zeolite investigated in this work, two Brønsted acid sites were identified (Appendix 4, Table C). The first one, D1, faces the framework oxygen O5 pointing toward the center of the 8-membered ring channel (D1-O5=1.09(3) Å); the second one, D2, located in proximity of the framework oxygen O1 (D2-O1=1.19(6) Å) pointing toward the 10-membered ring channel running parallel the *c*-axis (Figure 5.4.5(a) and (b)). On the whole, about 7.7 acid sites were located in the unit-cell, corresponding to 58 and 14% for

D1 and D2, respectively. These values fit very well with theoretical concentration expected on the basis of the aluminum content, thus indicating that D-LTL reached its maximum concentration of Brønsted sites. Refinement of individual Atomic Displacement Parameters of Brønsted acid sites highlights a wider mobility of D2 with respect to D1 (Appendix 4, Table C), in very good agreement with the simulations discussed in the next section. The structure refinement of D-LTL (a=18.3737(11) Å, c=7.5273(6) Å, V=2200.73(26) Å^3) has shown that in addition to the two D1 and D2 Brønsted acid sites, two other partially occupied extra framework sites are present (W1, and W2, respectively). Due to a prolonged calcination performed at high temperature (*i.e.*, 24 h under vacuum at 600 °C), the presence of residual ND_4 groups as well as of extraframework Al atoms have to be excluded.

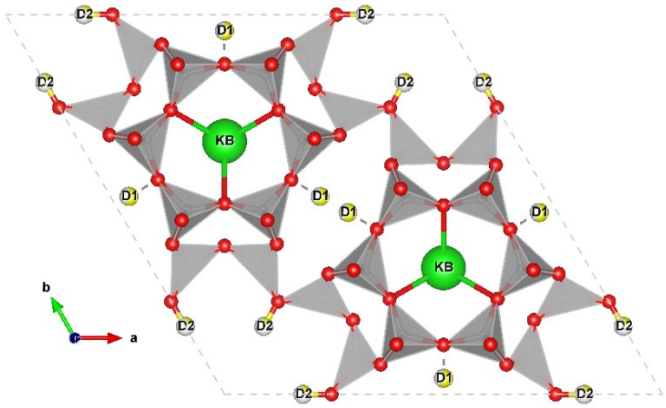

a)

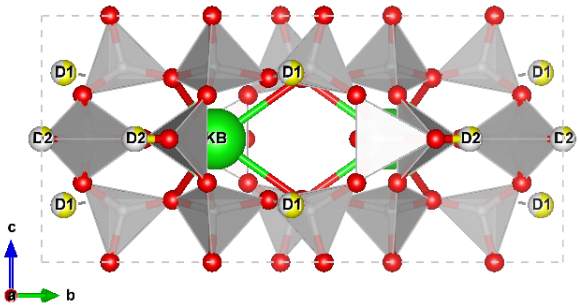

b)

Figure 5.4.5. Projection along the *c* (a) and *a* (b) axes of D-LTL. Red: framework oxygens. Yellow: deuterium sites; green: K sites.

At the same time, the hypothesis of dealumination of the framework can also be disregarded on the basis of Difference Fourier maps that exclude the occurrence of any residuals of electron density that can be inferred to oxygen atoms coordinated to Al^{+3}. Consequently, these extra framework sites are assigned to water molecules, as already observed in acidic ferrierite (Alberti and Martucci, 2010; Martucci et al., 1999), mordenite (Martucci et al., 2000b) and heulandite (Martucci et al., 2009), respectively. W1 site is 4-fold coordinated and bonded to the O5 framework oxygens (W1-O5=2.71(1) [x4] Å), and 4-fold coordinated

to D1 (W1-D1=2.09(1) [x4] Å), respectively (Figure 5.4.6). As far the W2 site is concerned, its position revealed interactions with both O4 (W2-O4=3.20(1) Å [x4]) and O6 framework oxygens (W2-O6=3.07(1) Å [x2]) (Appendix 4, Table D). On the basis of their occupancies, Rietveld refinement revealed ~4 water molecules per unit-cell corresponding to ~3.0 wt%.

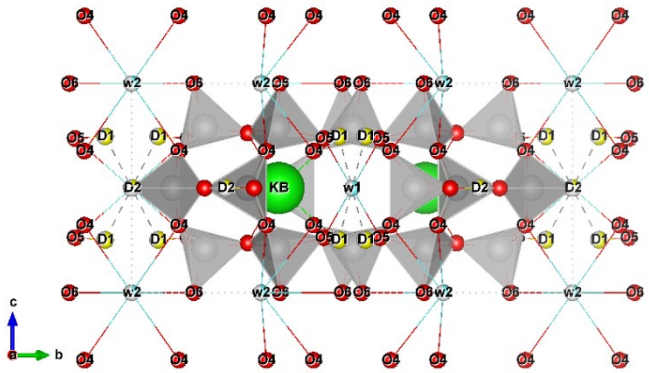

Figure 5.4.6. Interactions between deuterium sites and framework oxygen atoms. Projection along the *a* axis of D-LTL. Red: framework oxygens. Yellow: deuterium sites; green: K sites.

Results of D-LTL modeling. The first-principles simulations of zeolites have a long history (*e.g.* Tabacchi, 2018). In the case of L zeolite, due to its relevance in many fields, simulations ranging from modelling of dyes adsorption and room temperature dynamical behaviour (Gigli et al., 2018a; Gigli et al., 2018b; Tabacchi et al., 2016; Tabacchi et al., 2015; Gigli et al., 2014; Fois et al., 2013; Zhou et al., 2013; Fois et al., 2012; Fois et al., 2010) to the organization of water in its channels were performed. In the present case, were adopted the experimentally determined unit cell parameters. Also, the stoichiometry of the simulated system was as close as possible to the experimental one. The model system consists of two unit cells along the crystallographic *c* axis. The adopted framework stoichiometry, $[Al_{18}Si_{54}O_{144}]$ with an Al/Si ratio of 0.3333, allows for a total extraframework compensating charge of +18|e|. Such charges were compensated by 4 potassium cations and by 14 deuterons. The Al atoms were distributed in the T1 and T2 sites according to a ratio 1:2. Al-O-Al bridges were not present. The K atoms were positioned in the KB positions (see below). The D atoms were initially positioned in the D1 and D2 sites in a 1:6 ratio. Following a well-established procedure, after 5 ps equilibration, averages were gathered on a production run of 12 ps. Periodic boundary conditions were applied to the hexagonal cell, however no symmetry constraint was imposed on the atoms. In order to have a more direct comparison with data from diffraction studies, average crystallographic coordinates were obtained from the first-principles trajectory by adopting the following scheme: each average atomic set of cartesian coordinates was folded to the crystallographic one. Each folded set of coordinates was replicated according to the symmetry operations of the *P6/mmm* space

group. The final averaged crystallographic coordinates were obtained by folding back to the asymmetric unit positions and averaging (Appendix 4, Table E).

Furthermore, are presented the results where the last step of the above described scheme was not performed (as shown in Figure 5.4.7), thus allowing to gather a visual estimation of the atomic thermal motions (Trudu et al., 2019; Arletti et al., 2017).

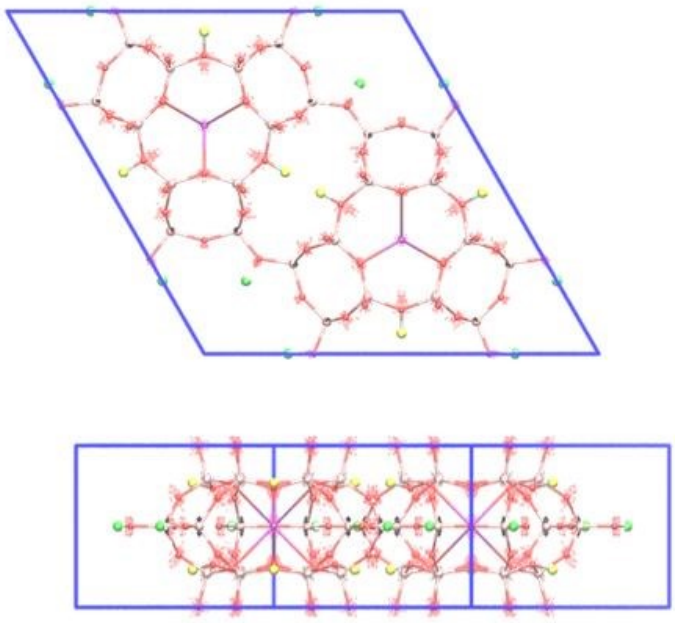

Figure 5.4.7. Two projections of the dry D-LTL zeolite structure showing the graphical comparison of diffraction determined structure (ball-and-stick representation) with the results of the first-principles calculations (dots representation). Experimental D1 and D2 atomic positions are represented as yellow and green spheres, respectively.

The results of the 300 K first-principles molecular dynamics simulation indicate that all Si, Al, K and O atoms oscillate around their average positions. On the other hand, all deuterons show an interesting behavior: due to the fact that they are involved in just one chemical bond (the O-D one) they have much more degrees of freedom and therefore a substantially higher mobility with respect *e.g.*, to framework atoms, all involved in T-O-T bridges. In addition K cations, which are caged in the KB position and coordinated to 6 framework oxygens each, are more constrained than D atoms. As a consequence, the spatial range explored by the D atoms along the dynamics – graphically represented by the white dots in Figure 5.4.7. - is far greater in comparison to all the other atoms of the zeolite. Interestingly, D1 atoms behave quite differently from D2 ones, as described below.

In Figure 5.4.7, the average structure of the simulated dry D-LTL is compared with the experimentally detected one, indicating that the modelling reproduces quite well the experimental structure. As an added value, modelling results highlight for the first time the above-mentioned high mobility of both D atoms associated to the D1 and D2 crystallographic positions. In particular, simulations evidence a large mobility of D2

deuteron in line with the high thermal factor associated to such atomic position (Appendix 4, Table C). On the other hand, the D1 atom is split in two positions. This implies a quite different thermal behavior of the two deuteron atomic positions: whereas D1 shows a behaviour typical of static disorder, D2 is characterized by a significant dynamical disorder.

Final consideration. The neutron diffraction technique associated to the computational modeling provided here insights on the aluminium distribution within the framework sites and on the location and amount of Brønsted acid sites within zeolite micropores through a detailed structural analysis of as-synthesized, precursor and acid L zeolites. The information gained on L zeolite here investigated represent a step forward on the knowledge of its acidic properties that along with the peculiar structural features, make this zeolite an excellent catalyst for hydrocarbon conversion.

SYSTEM 5

TEMPERATURE-INDUCED STRUCTURAL MODIFICATIONS IN ACIDIC L ZEOLITE: AN *IN SITU* SYNCHROTRON X-RAY POWDER DIFFRACTION STUDY

Samples. L sample used in this work is a synthetic commercial L zeolite, purchased from Tosoh (code 500KOA), with a SiO_2/Al_2O_3 ratio equal to 6.1. The Na_2O and K_2O contents are 0.25 and 16.8 wt%, respectively. The surface area (BET) is 290 m^2/g. The sample was exchanged with 1 M NH_4NO_3 aqueous solution for ≈140 h, then calcined at 600 °C for 6 h and dried overnight at 96 °C to obtain the acid form (*i.e.*, sample here labelled H-LTL).

Data collection. *In situ* time-resolved XRPD experiments were performed at the European Synchrotron Radiation Facility (ESRF, Grenoble), at the ID22 beamline, using a fixed wavelength of 0.400031(1) Å (photon energy of 31 keV) and an X-ray transfocator with parabolic cylindrical Al lenses. Using this method, along with the aid of a monochromator, the presence of harmonics up to five orders of magnitude has been suppressed (Polikarpov et al., 2014). The sample was placed into a spinning capillary rotating along the axis of the diffractometer and scanned in a continuous mode. High-resolution diffraction patterns were collected in parallel by means of nine scintillation detectors. Once diffracted, the highly energetic incident X-ray beam was directed through nine Si(111) analyzer crystals (Hodeau et al., 1998). The collected patterns were then normalized and combined in a subsequent data-reduction step to produce the equivalent step scan (Wright et al., 2003). X-ray diffraction patterns were recorded from room temperature to 810 °C, every 10 °C in air, in the 0.5–25.0° 2θ range. Figure 5.5.1 illustrates the good quality of the data through a magnification of the collected XRPD patterns in the (a) 1.3-1.6°, (b) 2.35-4.75° and (c) 4.75-9.0° 2θ regions from room temperature to 810 °C. The change in the intensity was pronounced in all 2θ range suggesting that water desorption was not the only process involved as confirmed by the refinement of the framework atoms.

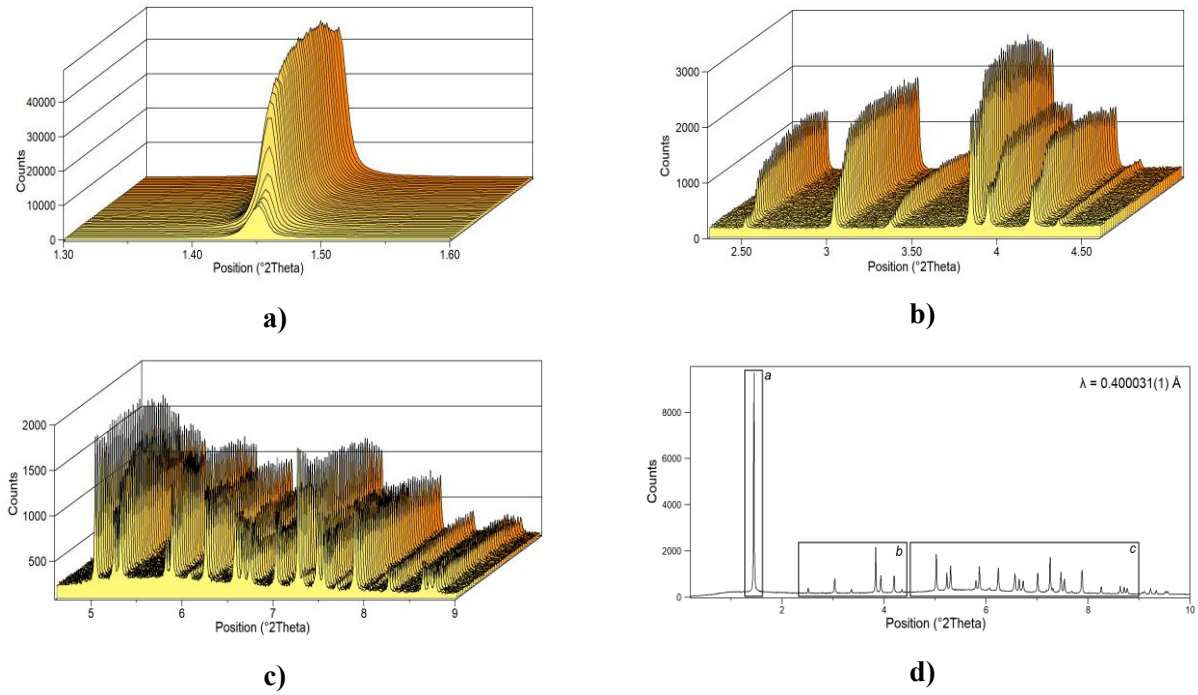

Figure 5.5.1. Cascade plots; (d) the whole powder pattern and the three 2θ ranges highlighted: (a) 1.3-1.6°, (b) 2.35-4.75°, (c) 4.75-9.0°.

Refinement strategy. Rietveld structure refinements of H-LTL were carried out in the *P*6/*mmm* space group, starting from the atomic coordinates of the acidic D-LTL zeolite determined in chapter 5, *System 4*. The strategy adopted for the room temperature data refinement was maintained unchanged in the whole thermal range investigated. The Bragg peak profile of the collected patterns was modelled using a pseudo-Voigt function with a cut-off of the peak intensity set to 0.01%. The background curve was fitted using a Chebyschev polynomial function with 20 coefficients. Refined parameters were: 2θ-zero shift, scale factor, unit-cell parameters, atomic coordinates, fraction, and thermal displacement parameters for both framework and extraframework atoms. The framework refinement was done by fixing the Si and Al occupancy to 0.70 and 0.30 and 0.78 and 0.22 for the tetrahedral T1 and T2 sites, respectively, according to the refined site occupancies from neutron diffraction (chapter 5, *System 4*). During the refinement of the framework atomic coordinates, a set of soft constraints was applied to the tetrahedral T–O bond distances (*i.e.*, 1.68 Å with σ=0.04 Å). The restraint weight (F) was progressively lowered in the last refinement cycles. The Atomic Displacement Parameters (ADPs, U_{iso}) were constrained in order to have the same value for the same atomic species. Besides, evidence of the possible location of extraframework species was derived from residuals of electron density calculated by mean of difference Fourier maps associated with a least square refinement of the atomic coordinates. Details of data collection and R-values agreement indices at 30, 190, 550 and 810 °C are reported in Table 5.5.1. For the same

temperature values, atomic coordinates, fraction and Atomic Displacement Parameters are reported in Appendix 5, Table A, B, C and D. Final Rietveld fits are shown in Figure 5.5.2(a), (b), (c) and (d).

Table 5.5.1.
Lattice parameters, details of data collection and R-values agreement indices.

Parameter	30 °C	190 °C	550 °C	810 °C
Space group	*P6/mmm*	*P6/mmm*	*P6/mmm*	*P6/mmm*
***a* (Å)**	18.2700(3)	18.2670(1)	18.2960(4)	18.2430(2)
***c* (Å)**	7.5650(1)	7.5564(3)	7.5501(3)	7.5201(4)
V (Å^3)	2186.87(7)	2183.68(4)	2188.75(8)	2167.46(7)
Wavelength (Å)	0.400031(1)	0.400031(1)	0.400031(1)	0.400031(1)
2*θ* (°) range	0.5-25	0.5-25	0.5-25	0.5-25
N_{data}	8149	8149	8149	8149
N_{var}	65	61	51	51
R_{wp} (%)	8.48	10.64	11.18	12.12
R_p (%)	6.46	7.53	8.26	8.65
R_F^2 (%)	24.57	19.91	25.37	29.39
R_F (%)	10.12	13.15	23.6	27.8

$R_p=\sum[Y_{io}-Y_{ic}]/\sum Y_{io}$; $R_{wp}=[\sum wi(Y_{io}-Y_{ic})^{\wedge 2}/\sum wiY_{io}^2]^{\wedge 0.5}$; $R_F^2=\sum|F_o^2-F_c^2|/|F_o^2|$

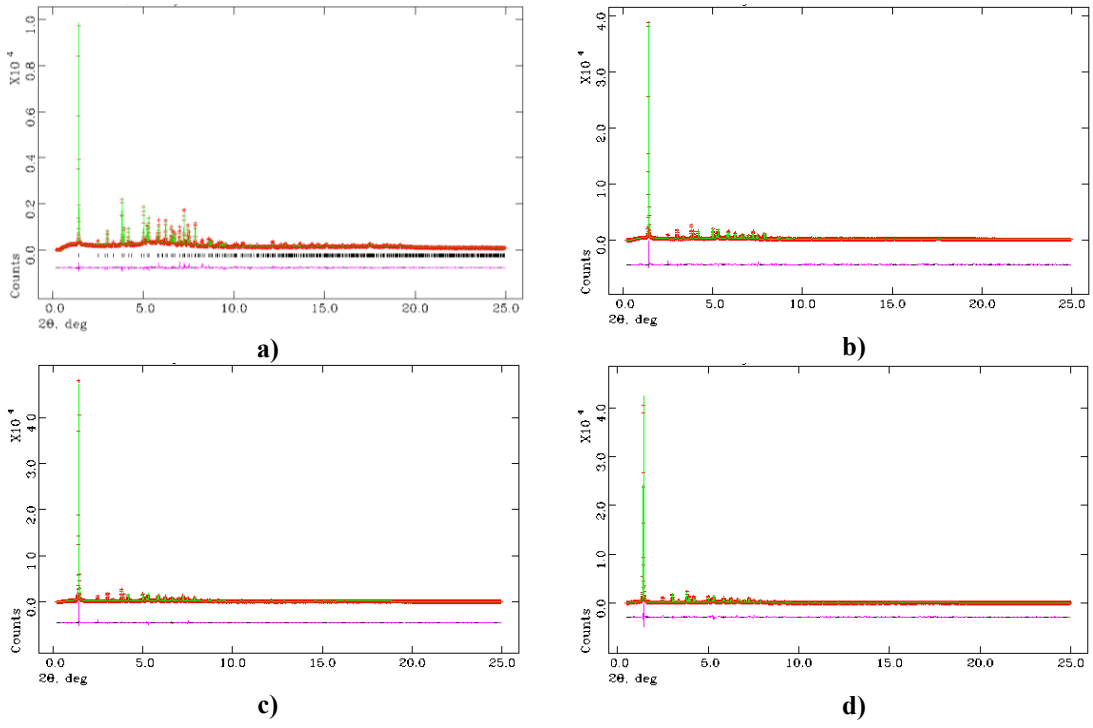

Figure 5.5.2. Final Rietveld fits at room temperature (a), 190 (b), 550 (c) and 810 °C (d). The experimentally observed data are indicated in red, the calculated pattern in green, and the pink curve is the weighted difference between the calculated and observed patterns.

Results and discussion of room temperature structural refinement. The structure refinement of the zeolite H-LTL (unit-cell parameters *a*=18.2700(3) Å, *c*=7.5650(1) Å and *V*=2186.87(7) Å^3) reveals that the mean <T-O> distances are 1.625 and 1.638 Å for T1 and T2, respectively. Besides, T-O-T angles fluctuate between 128.2(8)° and 167.8(8)° for

T2-O5-T2 and T1-O2-T1 angles, respectively (<T-O-T>=144.6°) (Appendix 5, Table E). The analysis of delta Fourier maps revealed that, after NH_4-ion exchange and calcination, KA, KC and KD sites are empty and all K ions are hosted in KB (Figure 5.5.3(a) and (b)). On the whole, 4.0 K ions are detected by means of the refined occupancies with respect to 10.0 in the as-synthesized material (chapter 5, *system 4*, L-LTL sample). K^+-bearing site is located at the center of the cancrinite cage, and is six-fold coordinated to O3 framework oxygens (KB-O3= 2.96(1) [x6] Å). Four other partially occupied extra-framework sites are also identified within the 12MR channel and assigned to water molecules (W1, W2, W3, and W4, respectively). This suggests that, although a prolonged calcination at high temperature (*i.e.*, 24 h at 600 °C, under vacuum conditions) has been performed in order to obtain the acidic H-LTL zeolite, a rehydration process has occurred anyway. This phenomenon was already observed in many other zeolites, such as acidic ferrierite (Alberti and Martucci, 2010; Martucci et al., 1999), mordenite (Martucci et al., 2000b), and heulandite (Martucci et al., 2009). On the whole, ~15.5 water molecules per unit-cell were determined through the refinement of the atomic site occupancy.

The analysis of the bond distances between framework oxygen atoms and water molecules and among water molecules, reveals the occurrence of a succession of water W1-W2-W2-W3-W4 oligomers (W1-W2=2.52(1) and 3.15(1) Å, W2-W2=2.52(1) and 3.21(1) Å, W2-W3=3.08(1) Å, W3-W4=2.60(1) Å) hydrogen bonded to O1 and O6 framework oxygen atoms (O1-W1=3.16(1), W4-O6=3.18(1), respectively).

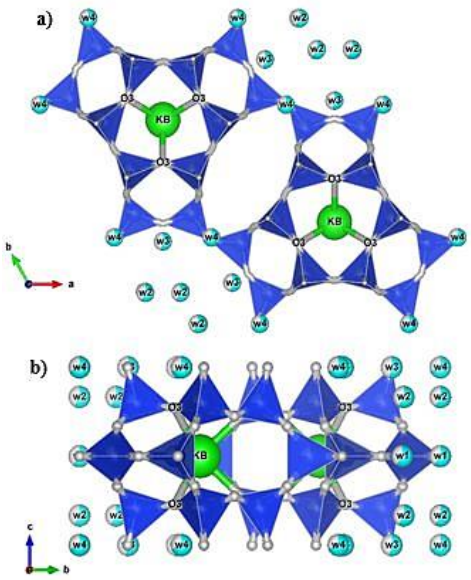

Figure 5.5.3. (a, b) Zeolite H-LTL extraframework distribution at room temperature: KB centred at the cancrinite cage, and water molecules W1, W2, W3, and W4 within the 12MR channel.

Lattice parameters, thermal expansion and water content variation upon heating. Figure 5.5.4 (and Table 5.5.1. for selected temperature of 30, 190, 550 and 810 °C) reports the evolution of the unit cell parameters normalized for their value at room temperature (*i.e.*, V/V_0, a/a_0, c/c_0), up to 810 °C.

According to the thermal ranges identified for the cell parameters, the volumetric thermal expansion has been calculated through the Fei polynomial function (Fei, 1995), as implemented in EosFit7c (Angel et al., 2014), by means of the Eq.1:

$$\alpha = \alpha_0 + \alpha_1 T + \alpha_2 T^{-2} \ (T \text{ in K}) \qquad (1)$$

where the mean thermal expansion coefficient α is expressed in K^{-1}, while α_0, α_1,and α_2, constants determined from fits to the experimental data, are expressed in K^{-1},K^{-2}, and K, respectively. Values of the constants derived by applying equation to the unit cell volume, along with the mean thermal expansion coefficient, for the H-LTL zeolite in the four thermal ranges are reported in Table 5.5.2.

Table 5.5.2.
Values of α_0, α_1,and α_2 constants in Eq. 1 (with $\alpha_0 \times 10^{-5}$, $\alpha_1 \times 10^{-8}$, and α_2 in K^{-1}, K^{-2}, and K, respectively) obtained from fits to the unit-cell volume. α ($\times 10^{-6}$ in K^{-1}) is the mean thermal expansion coefficient calculated within the four identified thermal ranges, $T_1 - T_4$.

Thermal ranges	T_1 **30–90 °C**	T_2 **90–190 °C**	T_3 **190–550 °C**	T_4 **550–790 °C**
V_0	N.R.*	2181.76(6)	2184.01(9)	2188.22(29)
α_0	N.R.	11.86(1.05)	1.82(18)	23.92(1.97)
α_1	N.R.	-26.58(2.54)	-1.87(28)	-27.66(2.08)
α_2	N.R.	N.R.	N.R.	N.R.
α	0	7.42	6.09	-23.15

*N.R. = Not Refined and fixed to 0.

A detailed inspection of the H-LTL zeolite response at the temperature increase reveals that from room temperature to 90 °C (T_1 range) lattice parameters as well as unit cell volume are substantially unchanged (*i.e.*, the volumetric variation δV is negligible).

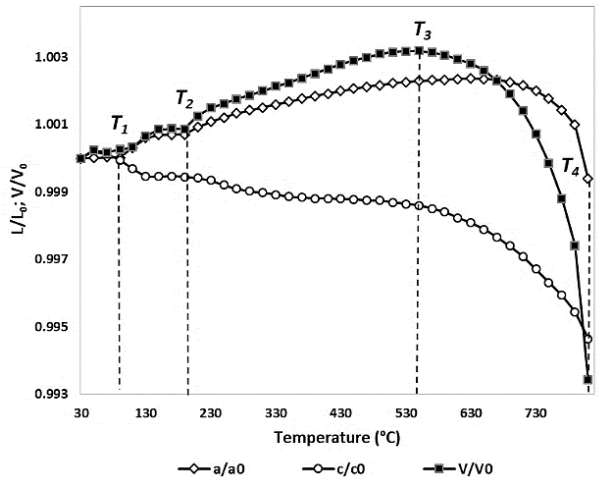

Figure 5.5.4. Evolution of lattice parameters upon heating. T_1, T_2, T_3 and T_4 indicate the four thermal ranges detected.

In the same thermal range, the distribution of the water molecules within the 12MR channel and their interactions with the framework oxygen atoms undergo to minimal variations. The first drop in the water molecules content is detected at ~ 90 °C, when 2.5 water molecules per unit cell are desorbed (Figure 5.5.5).

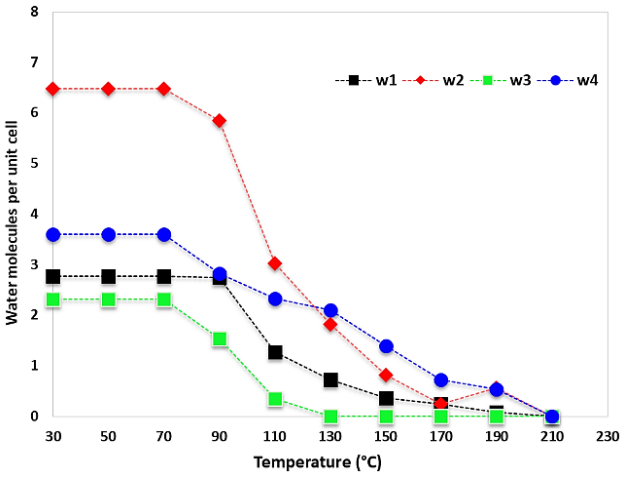

Figure 5.5.5. Evolution of water content upon heating.

From 90 to 190 °C (T_2-range), *a* and *c* lattice parameters show an anisotropic behaviour. While the *a*-axis increases, the *c*-axis undergoes a progressive contraction. Within the T_2-range, a volumetric expansion of 0.09% is recorded, and the progressive desorption of all the water molecules (~ 13 water molecules per unit-cell) takes place, leading the full dehydration at 210 °C (Figure 5.5.5). Water molecules at site W3 leave the framework first, reaching zero occupancy at ~130 °C. The emptying of the W3 site interrupts the continuity of water oligomers thus inducing disorder in the water positions and weakening the interactions with the framework oxygens. The water molecules at sites W1, W2, and W4 desorb simultaneously at ~190 °C. The dehydration process is associated to a volumetric

thermal expansion (in the T_2-range, α=7.4×10^{-6} K^{-1}) (Dosen and Marinkovic, 2019; Martucci et al., 2016; Wang et al., 2004) related to the progressive lengthening of the water framework oxygen distances.

From 190 to 550 °C (T_3-range), the previously highlighted lattice anisotropy becomes more pronounced. In the T_3-range, the zeolite structure along the *ab* plane shows a very high rate of expansion (δa=0.16%), while the *c*-axis contracts with a δc=-0.09%. These variations provoke, on the whole, a volumetric expansion δV=0.23% (α=6.1×10^{-6} K^{-1}).

Above this temperature (T_4-range), the marked contraction of *a*-axis (whole δa=-0.30%) is accompanied by a similar trend along the *c*-axis (δc=-0.39%) and consequently of the unit-cell volume (δa=-0.97% up to 810 °C). In this temperature range it is reasonable to assume that the zeolite is completely dehydrated (without H_2O, H_3O^+ and OH of both isolated vacancies or Brønsted acid sites), thus indicating negative thermal expansion (NTE) for this materials (negative mean thermal expansion coefficient α=-23.2×10−6 K^{-1}). This behaviour is very different from that reported by Gigli et al. (2013) for L zeolite with a Si/Al ~3.29, when heated from room temperature up to 814 °C. In this case, it undergoes a volumetric expansion from 140 °C until the maximum temperature reached, thus suggesting that the response to heating of L framework could be modulated by changing the framework composition and/or the nature, distribution and coordination environment of the cationic sites.

Structural variations upon heating. Rietveld refinements of the collected *in situ* powder diffraction data provide a continuous monitoring of the structural changes at high temperature, hence information about the effects of the dehydration process as well as the framework flexibility.

The behaviour of the tetrahedral bond distances with temperature highlights that the T2 site undergoes to a more relevant distortion than the T1 one (single bond distances T1-O and T2-O in figure 5.5.6(a) and (b) and Appendix 5, Table E for selected temperature of 30 and 190 °C, Table F for 550 and 810 °C). As can be observed in Figure 5.5.6(b), the expansion of the T2 site is mainly due to the progressive elongation of the T2-O5 distance, which shows an abrupt lightening from 530 to 810 °C, varying from 1.821(1) to 2.005(10) Å.

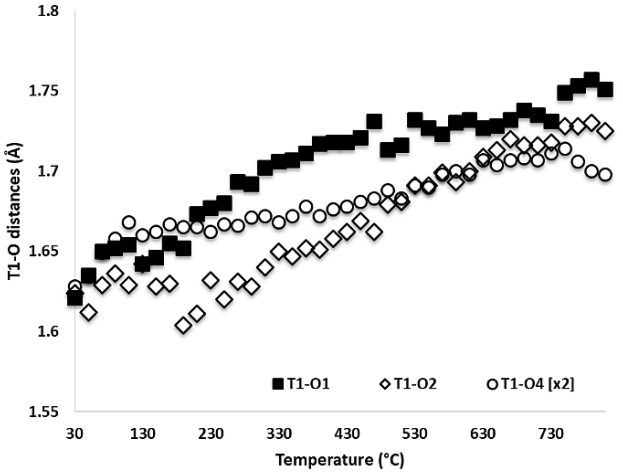

a)

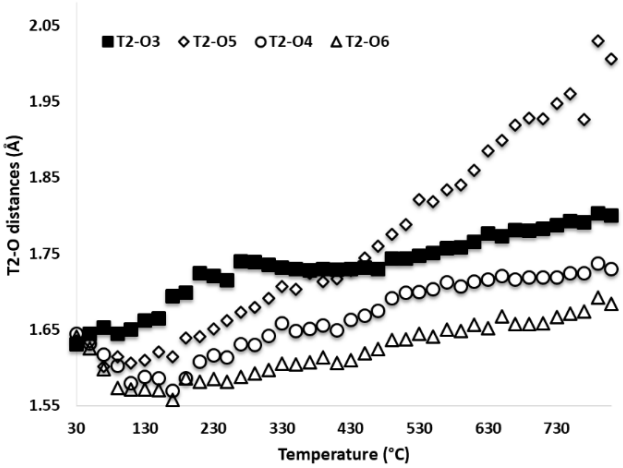

b)

Figure 5.5.6. Evolution of the (a) T1-O and the (b) T2-O bond distances upon heating.

The lightening of this distance is associated to the progressive widening of the O3-T2-O5 angle (from 109.4° at room temperature to 143.7° at 810 °C), and an anti-rotation (*i.e.*, along the *ab* plane) of the T2 polyhedron. Considering that neutron diffraction data of acidic L zeolite attesting the presence of a Brønsted acid site on O5 pointing towards the center of the 8MR (chapter 5, *system 4*), this phenomenon can reasonably be ascribed to the formation of a Lewis acid site on this framework oxygen atom upon heating. Similar structural X-ray diffraction evidences of the formation of Lewis sites were also reported for HY (Agostini et al., 2009), CoAPO (Martucci et al., 2005) and borosilicates (Leardini et al., 2013).

Simultaneously, the anti-rotation of the T2 polyhedron determines the progressive shrinkage of the T1-O4-T2 angles and it is associated to the co-rotation of the T1 site. The latter phenomenon is reflected in the T1-O1-T1 behaviour, which becomes larger up to temperatures similar to that of the dehydration (Figure 5.5.7).

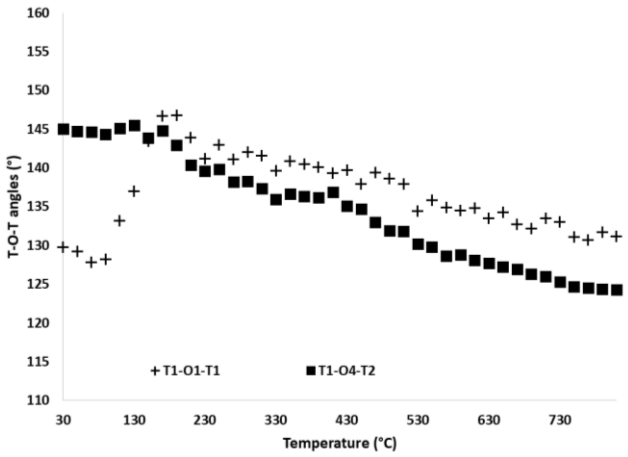

Figure 5.5.7. Evolution of the T1-O1-T1 and T1-O4-T2 angles upon heating

The structural modifications highlighted so far are also reflected in the geometry variations of the 6MR, 8MR as well as on the 12MR channel (Figures 5.5.8, 5.5.9 and 5.5.10, respectively). Noteworthy are the distortions occurring in the 6MR unit: the O5-O3 distance, which defines the ring boundary, tends to increase upon heating (Figure 5.5.8) due to the progressive migration of the O5 oxygen towards the center of the 8MR. The migration is testified by the continuous narrowing of the T2-O5-T2 angle upon heating (Figure 5.5.11).

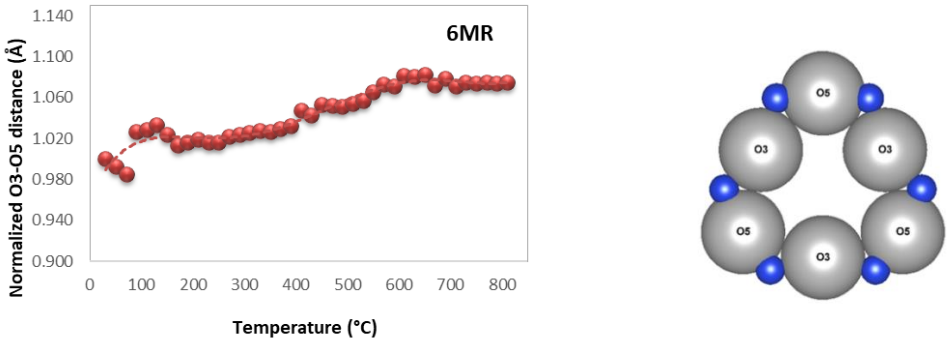

Figure 5.5.8. Evolution of the 6MR O-O distance upon heating. Line is reader's guide.

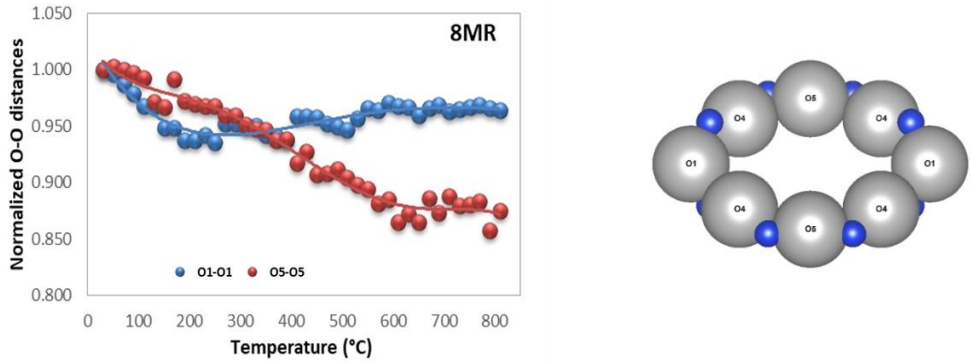

Figure 5.5.9. Evolution of the 8MR O-O distances upon heating. Lines are reader's guide.

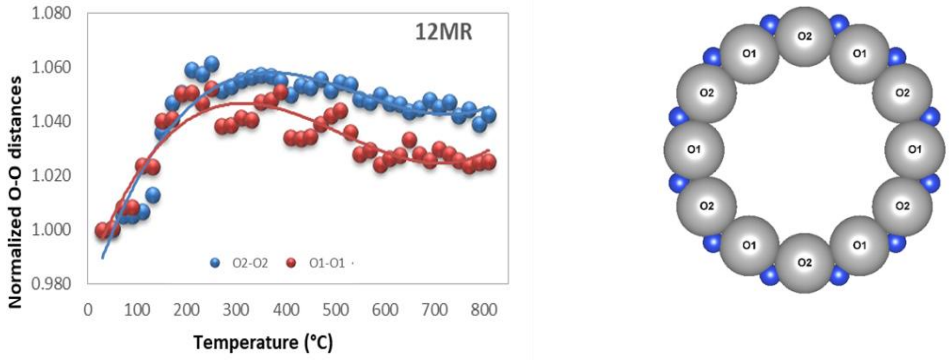

Figure 5.5.10. Evolution of the 12MR O-O distances upon heating. Lines are reader's guide.

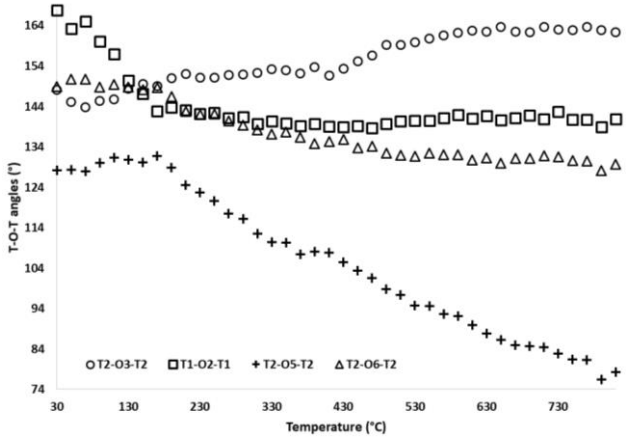

Figure 5.5.11. Evolution of T-O-T angles upon heating.

The response to heating of the zeolite framework at the selected temperature of 30, 350, 610 and 810 °C is reported in Figure 5.5.12(a), (b), (c) and (d), respectively, as representative of the structural distortions undergoing at high temperature.

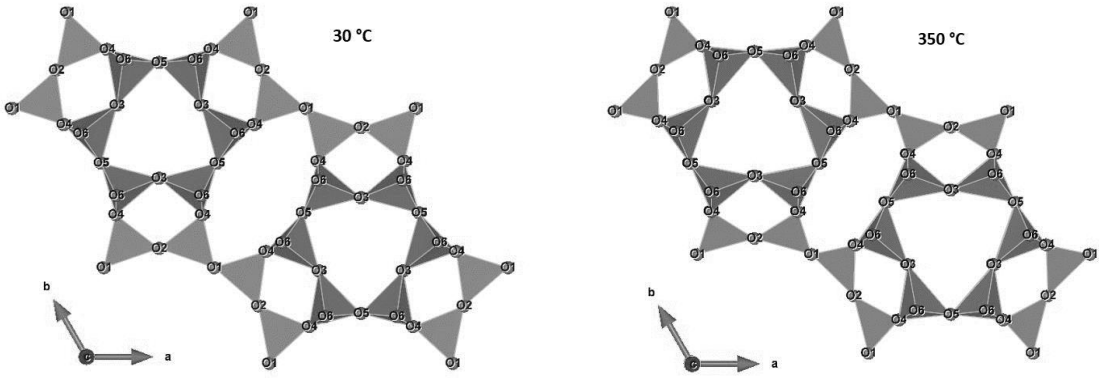

a) **b)**

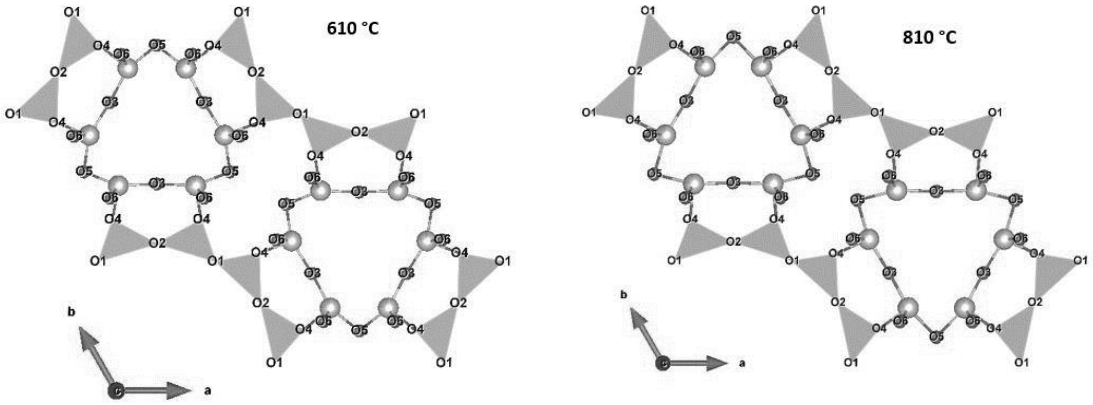

c) d)

Figure 5.5.12. Evolution of the structural features upon heating. (a) 30, (b) 350, (c) 610 and (d) 810 °C.

Final consideration. The *in situ* synchrotron X-ray powder diffraction performed on the H-LTL sample allowed to determine the thermal stability of the zeolite simulating the operating conditions of the catalysts. The structural information gathered by means of the continuous monitoring revealed that the crystallinity of the sample is maintained up to the end of the thermal treatment, although important structural variations occur. Noteworthy is the formation of a Lewis acid site on a framework oxygen atom upon heating, thus conferring to the material a further and fundamental catalytic property. Besides, this process determines a progressive rearrangement of the zeolite framework: the knowledge of these structural phenomena is of primary importance to predict the catalysts behaviour under operating conditions.

SYSTEM 6

L-LYSINE ADSORPTION IN L ZEOLITE: A COMBINED SYNCHROTRON X-RAY AND NEUTRON POWDER DIFFRACTION STUDY

Samples. The zeolite selected is a synthetic and commercial L zeolite purchased by Tosoh Corporation (HSZ-500KOA code) in its potassium form, with a Si_2O/Al_2O_3 equal to 6.1, Na_2O content of 0.25 wt% and surface area of 290 m^2/g. L-lysine (Lys) was provided by Sigma-Aldrich (Steinheim, Germany), with a purity of 99.8% in the hydrogen (L-lysine) and deuterated (d-L-lysine) forms, respectively.

Data collection. L zeolite loaded with L-lysine was characterized through room temperature X-ray powder diffraction at the MCX Beamline of the Elettra Synchrotron Light Source (Trieste, Italy) on a 4-circle Huber diffractometer with a 3D translation stage. The diffractometer was equipped with a Si(111) double crystal monochromator and a high-count rate fast scintillator detector preceded by a pair of slits with vertical aperture of 200 and 300 μm. The sample was loaded into an axially spinning borosilicate capillary (Ø=0.5 mm) and then collected at room temperature, using a fix wavelength equal to 0.82700(1) Å, in the 1.5-65° 2θ range.

On the same sample, thermogravimetric (TG) and thermodifferential (DTA) analysis were carried out in costant flux of air conditions by using the STA 409 PC LUXX® (Netzsch Gerätebau GmbH, Selb, Germany) simultaneous TG/DTA thermogravimetric balance from room temperature to 900 °C, with a heating rate of 10 °C/min.

L zeolite loaded with deuterated L-lysine was investigated through neutron diffraction at the D2B beamline at ILL (Grenoble, France) at low temperature (-269.15 °C), using a fix wavelength equal to 1.59432(1) Å, in the 4-146° 2θ range. The deuterated sample was analyzed once packed into a vanadium container sealed with a rubber gasket to ensure humidity-free transport to the neutron source.

Refinement strategy. Synchrotron and neutron refinements were performed in the hexagonal *P6/mmm* symmetry starting from the atomic coordinates of the L-LTL sample described in chapter 5, *System 4*. For both histograms, peaks profiles were modelled through the Pseudo-Voigt function with 0.05% cut-off peak intensity. Gaussian GW and GU as well as Lorentzian LX and *stec* parameter were the coefficients refined for the synchrotron pattern profile; whereas Gaussian GW, GU and GV, Lorentzian LX and the *asym* parameter that of neutron data (function type 3 and 2 for synchrotron and neutron data, respectively). The background was empirically fitted though the Chebyschev function with 18 coefficients. Besides, scale factor and 2θ zero shift were also accurately refined for both the histograms.

Soft constraints were initially imposed on tetrahedral (T-O=1.62 Å, σ=0.04) and organic molecule (C-C=1.54, C-O=1.43; C=O=1.25 and C-N=1.4 Å; σ=0.04) distances and completely removed in the last refinement cycles. Finally, atomic coordinates, fraction and Atomic Displacement Parameters (ADPs, U_{iso}) were refined, constraining equivalent ADPs for tetrahedral sites, framework oxygens and the sites of the organic molecule. Details about data collection and R-values agreement indices are reported in Table 5.6.1. Refined framework atomic coordinates, fraction and Atomic Displacement Parameters obtained by synchrotron and neutron refinements are available in Appendix 6, Table A and B, respectively. Atomic coordinates, fraction and Atomic Displacement Parameters of the extraframework molecules are reported in Appendix 6, Table C.

Table 5.6.1.
Details of synchrotron and neutron data collection and R-values agreement indices.

Parameters	Synchrotron X-ray diffraction	Neutron diffraction
Wavelength (Å)	0.82700(1) Å	1.59432(1) Å
2θ range (°)	1.5-65	4-146
N_{data}	10596	2917
N_{obs}	1068	891
R_{wp} (%)	9.8	2.96
R_p (%)	9.7	2.11
R_F^2 (%)	10.93	12.28

$R_p = \sum[Y_{io} - Y_{ic}]/\sum Y_{io}$; $R_{wp} = [\sum wi(Y_{io} - Y_{ic})^2/\sum wiY_{io}^2]^{0.5}$; $R_F^2 = \sum |F_o^2 - F_c^2|/|F_o^2|$

Adsorption experiments. Adsorption experiments were performed at the Department of Chemical and Pharmaceutical Sciences of the University of Ferrara. The adsorption was determined by using aqueous solutions of L-Lysine at different initial concentrations (in the 0.5-200 mg/L range), placed in contact with L zeolites with a solid/liquid ratio of 1:1 (mg/mL). The suspensions were kept at 25 °C under stirring during the contact time. The contact time was of 18 h, larger than the equilibration time determined by kinetics experiments. The pH was adjusted at 5.5 during adsorption by adding small volume of 0.1 M H_3PO_4.

To investigate the adsorption kinetics, the Lys uptake was measured starting from solution at concentration of 50, 75, 100 mg/L, after contact time equal to 1, 2, 5, 10, 20, 30, 45, 60 120 min. All batch experiments were carried out in triplicate. An Agilent Technologies Capillary Electrophoresis series 7100 system (Santa Clara, CA, USA) was employed to quantify Lys in the solution before and after the contact with zeolites. The CE system was equipped with diode array detection (DAD). For separations, extended light path (bubble cell) bare fused-silica capillaries (red G1600-61232 I.D.: 50 μm, total length: 64.5 cm,

effective length: 56 cm, bubble factor: 3) obtained from Agilent Technologies (Santa Clara, CA, USA) were employed.

Hydrodynamic injection of the solutions were performed at a pressure of 10 mbar applied for 30 seconds. The detection wavelength of the CE system was 200 nm. Positive polarity (15 kV) was applied at the capillary inlet for the duration of separation. The running buffer was obtained by a 50 mM solution of Na_2HPO_4 in MilliQ water, at pH 5.5 adjusted by adding H_3PO_4.The pH of the electrolyte was measured using an AMEL pHmeter (Milano, Italy). Before use, the capillary was pretreated through sequential flushing with 1 M NaOH for 5 minutes, 0.1 M NaOH for 5 minutes and MilliQ (Millipore, Bedford, MA, USA) grade water for 15 minutes. The capillary was also rinsed with water for 3 minutes, 0.1 M NaOH for 2 minutes, water for 3 minutes, and running buffer for 5 minutes between each run.

The amount of Lys adsorbed at equilibrium, qe (mg g^{-1}), was calculated from the mass balance equation, Eq.1:

$$q_e = \frac{(C_i - C_e)V}{m} \quad (1)$$

where C_i and C_e (mg L^{-1}) are the liquid-phase concentrations of Lys in the reference solution and at equilibrium respectively; V (L) is the volume of the solution and M (g) is the mass of dry zeolite used. Samples of saturated zeolite with Lys were used for structural investigations. Zeolite L (0.5 g) were suspended with stirring in 500 ml of an aqueous solution of Lys 500 mg/L, at pH 5.5 at 25 °C for 24 h (see *Adsorption Experiments*). The zeolite was recovered by filtration, washed with 200 mL of MilliQ water and dried in oven at 300 K overnight. A similar procedure was employed to prepare the samples saturated with deuterated Lys, in such a case deuterated Lys was dissolved in D_2O at concentration of 1000 mg/L.

Adsorption kinetics. The adsorbed quantity for unit mass of adsorbent was measured at different contact time, starting from Lys solution at three different initial concentrations (Table 5.6.2). Figure 5.6.1 shows that the adsorption process reaches equilibrium in roughly 1 h.

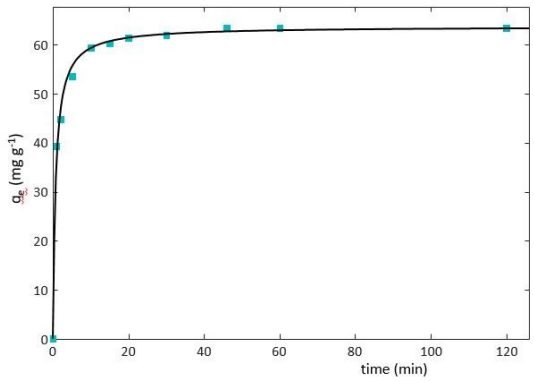

Figure 5.6.1. Uptake of Lys on L *vs*. time

To quantify the kinetic constant, a pseudo second order (PSO) model was employed to model the data. The PSO equation is given by Eq.2:

$$q_t = \frac{k_2\ q_e^2\ t}{1+k_2\ q_e\ t} \qquad (2)$$

where q_t, is the adsorbed quantity per unit mass of adsorbent after a contact time t and k_2 is the pseudo second order kinetic constant that was employed. PSO was chosen as kinetic model since it has been reported in the literature that it can better represent the kinetics of adsorption onto zeolites with respect to both neutral and cationic species (Table 5.6.2). Recently, it has also been shown for the adsorption of amino acids onto ZSM-5 that PSO shows a larger relative goodness of fitting with respect to pseudo first order kinetic model (chapter 5, *System 3*).

Table 5.6.2.
Parameters obtained by non-linear fitting of the uptake data on L zeolite using a PSO model. The error is given as confidence interval at 95% of probability.

C_i (mg/L)	k_2 (g/mg·min)	q_e (mg/L)	R^2
50	0.0340 ± 0.0064	41.0 ± 1.1	0.9962
75	0.0200 ± 0.0022	62.0 ± 1.3	0.9945
100	0.0120 ± 0.0068	67.0 ± 1.9	0.9877

The adsorption data (Figure 5.6.2) obtained at 25 °C were fitted to a Langmuir model, Eq.3:

$$q_e = \frac{q_s\ b\ C_e}{1 + b\ C_e} \qquad (3)$$

where q_s is the saturation capacity of the zeolite and b is the binding constant; the estimated parameters with the confidence limits calculated at 95% of probability are reported in Table 5.6.3.

Table 5.6.3.
Binding constants and saturation capacity for the adsorption of Lys. The error is given as confidence interval at 95% of probability.

	q_s (mg/g)	B (L/mg)	R^2
L	96.9 ± 4.1	0.097 ± 0.018	0.9913

The saturation capacity is about 97 mg/g, which correspond to 0.62 mmol/g, is higher than that reported for the adsorption of Lys on mesoporous siliceous materials (MCM-41). Therefore, L zeolite shows characteristics that make it a promising adsorbent for amino acids.

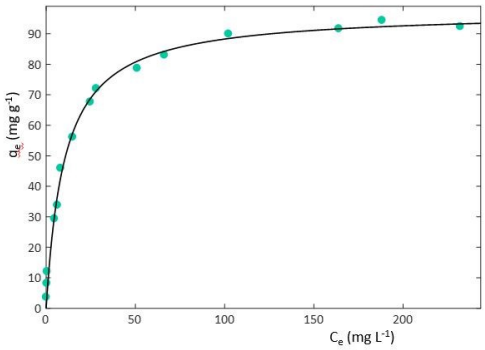

Figure 5.6.2. Adsorption isotherm of Lys on L zeolite.

Results and discussion of synchrotron and neutron structural refinements. As expected, synchrotron X-ray powder diffraction indicated that the zeolite loaded with the amino acid gives significantly higher quality of powder diffraction patterns than neutron diffraction, hence this material was chosen for the initial structural investigation. The diffractogram was indexed using the TREOR program that confirmed the hexagonal simmetry of the zeolite beyond the amino acid adsorption, as a consequence all the observed reflections in the X-ray pattern were indexed using the *P6/mmm* space group. Lattice parameters refined from synchrotron X-ray have been reported: $a=b$=18.4287(1) Å, c=7.5383(1) Å, V=2217.13(3) Å^3. When using neutron data on d-L-lysine, the unit cell parameters were $a=b$=18.4117(2) Å, c=7.5278(2) Å, V=2209.98(8) Å^3, respectively. The slight differences between them can be easily explained considering that neutron data have been collected at -269.15 °C, whereas synchrotron ones at ambient conditions. As far as concerns the tetrahedral bond distances (reported in Appendix 6, Table D), Rietveld refinement revealed that the <T2-O> is the longest (*i.e.*, 1.643 and 1.669 Å for <T1-O> and <T2-O>, respectively), thus indicating an enrichment of Al in the T2 site, in good agreement with what reported in chapter 5, *System 4*. Iterating the Rietveld cycles for synchrotron and neutron data using only silica framework model without an inclusion of the adsorbed guest molecule yields a fit to the diffraction patterns with residual values: R_{wp}=0.2189, R_p=0.1729 for X-ray and R_{wp}=0.2829, R_p=0.2138 for neutron, respectively.

At this stage, the Difference Fourier maps were generated on both synchrotron and neutron data to detect the extraframework species but no relevant differences between them were

highlighted. Only variations concerning the thermal motions of the organic molecules were detected, thus providing a good picture of the real location of them. Both structural models refined provides a potassium cation distribution similar to that reported by Gigli et al., (2013) and in chapter 5, *System 4*, L-LTL sample. K^+ ions are hosted in KB, KC and KD sites, located at the centre of the 6MR, 8MR and close to the edge of the 8MR, respectively. KB is six-fold coordinated by the O3 framework oxygen atoms (KB-O3=2.87(1) Å [x6]), KC four-fold coordinated by the O5 (KC-O5=2.69(1) Å [x4]) and KD seven-fold coordinated by the O4 (KD-O4=3.19(1) Å [x4]), the O6 (KD-O6=3.02(1) Å [x2]) and one coadsorbed water molecule (W1-KD=2.53(1) Å) (Figure 5.6.3(a) and (b)). Along with W1 site, another Fourier residual peak was attributed to co-adsorbed water molecules (W2 site), H-bonded to O1 and O2 framework oxygens (W2-O1=3.25(1) [x2], W2-O2=2.90(1) Å). Four others residuals peaks, lying on the *ab* plane, were located within the 12MR channel and their bond lengths and angles confirmed clearly their assignment to the L-lysine molecule (C1, C2, C3 and C4 sites, respectively). The difference Fourier map generated from neutron data exhibited more features than the X-ray one because deuterium has a large scattering cross section for neutrons, while hydrogen or deuterium scattering is insignificant for X-rays. Due to the hexagonal symmetry, the amino acid can statistically assume six different orientations, but its real symmetry (monoclinic $P2_1$) was lower than that of the zeolite framework.

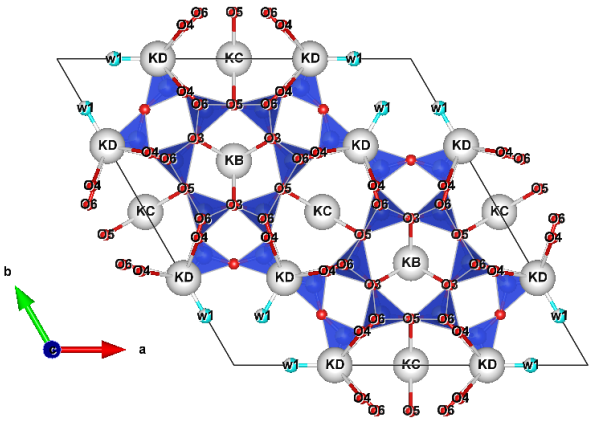

a)

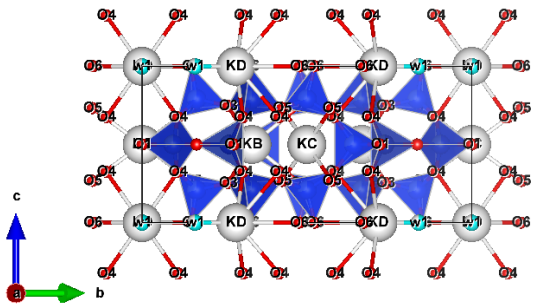

b)

Figure 5.6.3. Projection along *c*- (a) and *a*- (b) axis. Distribution and interactions of K sites.

Incorporating this model for the guest species into further Rietveld refinement cycles, the residual values in the Rietveld fit have been drastically decreased to R_{wp}=0.098, R_p=0.097 for X-ray and R_{wp}=0.0296, R_p=0.0211 for neutron data (Table 5.6.1). Final Rietveld fit of synchrotron and neutron data is given in Figure 5.6.4(a) and (b), respectively.

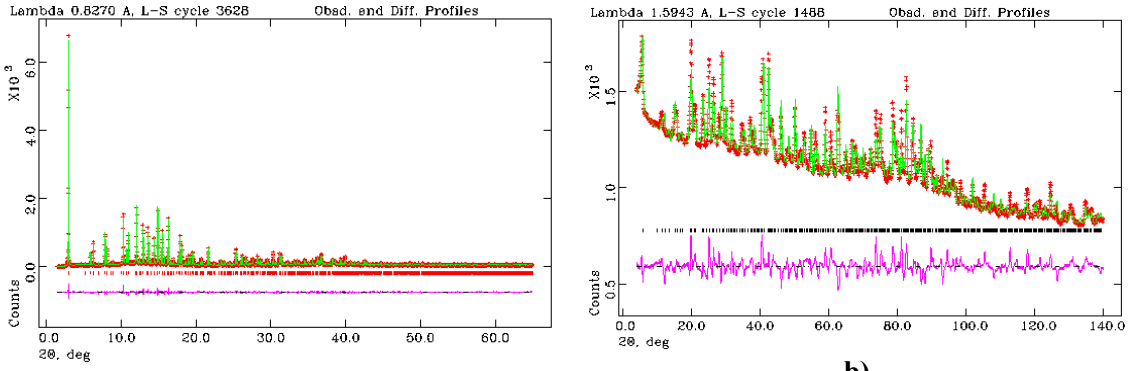

a) **b)**

Figure 5.6.4. (a) Final Rietveld fit of synchrotron X-ray powder diffraction pattern of L zeolite loaded with L-lysine. (b) Final Rietveld fit of neutron powder diffraction pattern of L zeolite loaded with d-L-lysine. Crosses represent observed data, the solid line is the calculated pattern and the difference profile and allowed reflection positions are shown beneath.

In the final refinements, X-ray and neutron data were weighted according to their statistical uncertainties, weighting for the framework interatomic distances were progressively reduced providing reasonable bond lengths, for both framework and extraframework sites. The refinement evidenced the occurrence of interactions between the guest molecules and the host zeolite framework. The carboxyl groups of the amino acid strongly interact (*e.g.*, H-bonds) with both water molecules, (C3-W1=2.37(1) Å, C3-W2=2.65(1) Å, C4-W2=3.11(1) Å, C1-W2=2.38(1) [x2] Å, C2-W1=2.88(1) and 2.20(1) Å, C2-W2=2.66(1) [x2] Å) and framework oxygen atoms (C4-O1=2.61(1), C4-O2=2.82(1) and C4-O4=2.76(1) Å). On the whole, the refinement of the occupancies led to calculate 8 water (Δw ~5.4 wt%) and 3.4 (Δw ~9.5 wt%) L-lysine molecules per unit cell, respectively. The total amount of the extraframework content determined through the Rietveld refinement (*i.e.*, Δw ~15 wt%) is in good agreement with the weight loss registered by the TG analysis between 120 and 900 °C (Figure 5.6.5). The first weight loss (~2 wt%), recorded at low temperature (*i.e.*, 20-120 °C), corresponds to the release of the surface H_2O molecules, not detectable through Rietveld powder refinement. Besides, the more relevant mass reduction (~14.8 wt%), registered between 120 and 900 °C, is due to desorption of the water molecules located within the zeolite framework as well as the degradation of the amino acid. The structural water desorption reasonably starts at 120 °C, as testified by the presence of the right shoulder of the negative DTG peak centred at 100 °C, whereas the L-lysine step decomposition begins at higher temperature (~200 °C) and continues up to the end of the thermal treatment. As

already reported for ZSM-5 zeolites loaded with the same amino acid (chapter 5, *Sytem 3*), the two exothermic peaks recorded by the DTA curve in the same thermal range are attributable to the oxidation and/or combustion of the compound that occurs upon heating.

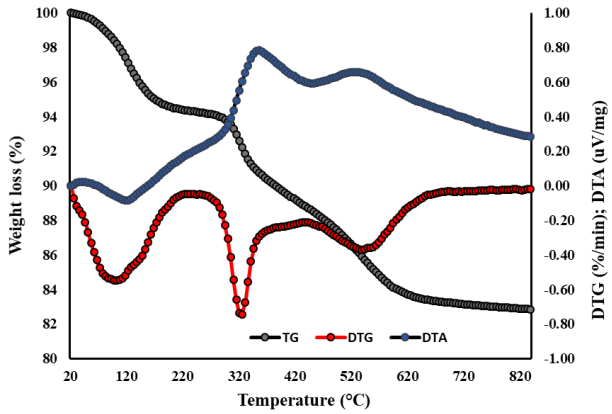

Figure 5.6.5. Thermal analysis: in grey and red circles the total weight loss curve (TG) and its first derivative (DTG), respectively; in blue the differential thermal analysis (DTA) curve.

The geometry optimization tool implemented in EXPO2014 (Altomare et al., 2013) was finally used to minimize the energy of the crystal structure as well calculate the position of the H/D atoms. The resulting optimized structure in the *P*1 space group (Appendix 6, Table E) was then used as input coordinates for GSAS and refined again together with the framework until the geometry of the L-lysine was reasonable described. In order to secure a stable refinement, the L-lysine molecule coordinates were fixed in the final cycles of Rietveld refinement thus limiting the number of refined Atomic Displacement Parameters. The geometry optimization confirms the amino acid site locations, reduces its orientations to two of the six of the hexagonal Rietveld model (Figure 5.6.6) and confirms the occurrence of strong interactions between L-lysine and framework oxygens and water molecules.

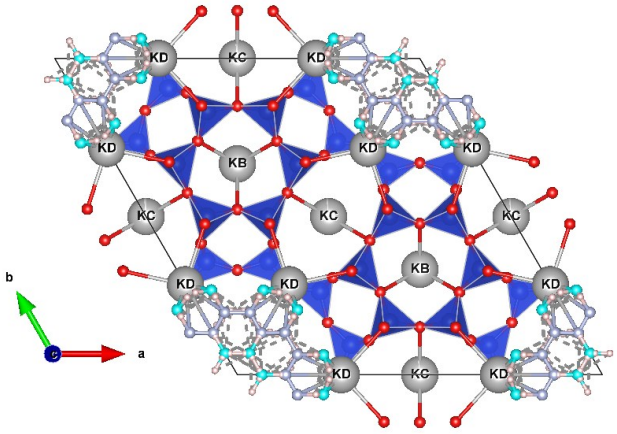

Figure 5.6.6. Projection along the *c* axis. Position and interactions of the l-lysine molecule.

Final consideration. Adsorption experiments, neutron and synchrotron X-ray powder diffraction associated to thermal analysis, were here applied for determining the sorption capacity of the acidic L zeolite towards the L-lysine aminoacid. Results gathered showed that the structural features, the channel system and the chemical properties of the host material favour the molecule adsorption process, although do not limit the diffusion of water molecules within the zeolite micropores. However, considering the total L-lysine content encapsulated and the host-guest interactions that stabilize the molecule within the pores, the L zeolite can be considered a proper sorbent material to operate in aminoacids fractionation.

SYSTEM 7

THERMAL ACTIVATION OF NH_4 PRECURSOR OF ACIDIC OMEGA ZEOLITE: A NEUTRON AND *IN SITU* SYNCHROTRON X-RAY POWDER DIFFRACTION COMBINED STUDY

Samples. The zeolite omega, with the MAZ framework topology, used in this work (composition $Na_{6.6}TMA_{1.8}(H_2O)_{22.2}[Al_{8.4}Si_{27.6}O_{72}]$) is the same sample previously characterized by Martucci et al., 2003. Its synthesis was carried out in a stirred stainless-steel autoclave at 105 °C starting from a synthesis batch with composition $0.48Na_2O/0.024TMA_2O/0.075Al_2O_3/SiO_2/26.6H_2O$ (Martucci et al., 2003). Na, Al, Si, C and N contents of the as-synthesized zeolite omega were determined by elemental analysis, which were carried out at the Service Central d'Analyse of the CNRS in Solaize, France. The as-synthesized sample was NH_4-ion exchanged three times at room temperature and three times at 90 °C. The exchanged form, labelled from now NH_4-omega (Scheme 5.7.1), had composition $Na_{2.4}TMA_{1.14}(NH_4)_{5.0}(H_2O)_{10.0}[Al_{8.4}Si_{27.6}O_{72}]$. The calcination of NH_4-omega to form H-omega is further described in the section on thermal ramp.

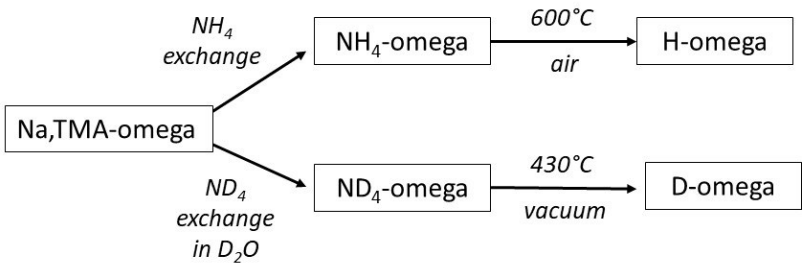

Scheme 5.7.1. Nomenclature of samples

The same $Na_{6.6}TMA_{1.8}(H_2O)_{22.2}[Al_{8.4}Si_{27.6}O_{72}]$ was exchanged twice at 25 °C upon 10 days in 2M ND_4Cl solution in D_2O to obtain an intermediate ND_4-exchanged form (ND_4-omega). After exchange, the sample was filtered and washed, then refilled in a glass ampoule and heated under vacuum for 24 h at 430 °C to remove D_2O and ND_3. The glass ampoule was sealed under vacuum to avoid contact with air and humidity. Finally, the heat-treated D-omega sample was repacked in an argon-flushed glove-bag from the ampoule into a vanadium container sealed with a rubber gasket and six screws to ensure humidity-free transport to the neutron source.

Data collection. NH_4-omega was characterized by *in situ* time-resolved X-ray powder diffraction. Analysis were carried out at the GILDA-BM8 beamline at the ESRF, Grenoble (France), using a wavelength of 0.68881(1) Å. The powder was loaded and packed in a quartz Lindemann capillary (i.d. 0.3 mm) and heated *in situ* using a hot air stream equipped with Eurotherm controller from room temperature to 940 °C, with a heating rate of 5 °C/min. The temperature was constantly monitored through a thermocouple placed at the heating gun opening. Analysis were carried out through the translating image plate (TIP) experimental setup and powder diffraction patterns were collected on the 4 mm slit-delimited portion of a 2D image plate with a 2.5 pixel/c of translating rate compared to the temperature increase (Norby, 1997). The sample-image plate distance obtained by the calibration procedure implemented in the FIT2D program was about 204.7 mm. A whole of 59 one-dimensional powder patterns were extracted from the image plate by integrating on the 5 °C-wide strips and with an integration step of 10 °C.

D-omega neutron data collection was carried out at the high-resolution two-axis powder diffraction beamline D2B of the Institut Max Von Laue-Paul Langevin (ILL) at -271.15 °C and with a wavelength of 2.3980(1) Å.

Thermogravimetric (TG, DTG) and differential thermal (DTA) analysis were performed on a Netzsch STA 409 PC LUXX® simultaneous TG/DTA apparatus from room temperature to 900 °C in costant flux of air conditions with a heating rate of 5 °C/min.

Refinement strategy. NH_4-omega structural refinements were performed starting from the framework atoms position reported in the PhD thesis of Parodi (Parodi, 2006-2008), which conducted a preliminary study on the NH_4-omega X-ray powder diffraction data here used for the *in situ* structural characterization. Since no evidences of temperature-dependent symmetry changes were observed, the starting $P6_3/mmc$ space group (No. 194) was maintained unchanged in all the temperature range investigated. Due to the progressive peak broadening, Rietveld refinements were allowed up to 785 °C; from this temperature up to the end of the thermal treatment only lattice parameters were determined through the LeBail method. All the data collected were refined using the same strategy: Bragg peak profiles were modelled by a pseudo-Voigt function with a 0.005% cut-off peak intensity; the instrumental background was empirically fitted using a Chebyschev first kind polynomial function with 22 coefficients; 2θ-Zero shift, scale factor and unit-cell parameters were also accurately refined. Soft constraints were initially imposed on T–O distances (*i.e.*, 1.65 Å bond distance and 0.02 Å tolerance value) and gradually released in last cycles. Lastly, atomic coordinates, fraction and Atomic Displacement Parameters (ADPs, U_{iso}) were refined. The Atomic Displacement Parameters were constrained to change equally for each

tetrahedral cation, framework oxygen atom and TMA molecules. Atomic coordinates, fraction and Atomic Displacement Parameters of framework and extraframework atoms at 30, 250, 430, 600 and 770 °C are reported in Appendix 7, Table A, B, C, D and E, respectively.

NH_4-omega framework atoms positions were used as starting model for neutron Rietveld refinement of D-omega. Bragg peak profile was modeled using a pseudo-Voigt function with a 0.01% cut-off of the peak intensity. The background curve was empirically fitted with a Chebyschev polynomial with 24 variable coefficients. 2θ-zero shift, scale factor and unit-cell parameters were also accurately refined. In final cycles, refined structural parameters were the following: atomic coordinates, occupancy factors and Atomic Displacement Parameters (one each for tetrahedral sites, framework oxygen atoms, organic template). Soft constraints were imposed on T-O (*i.e.*, 1.65 Å and 0.02 Å tolerance value), and D-O (*i.e.*, 1.00 Å and 0.04 Å tolerance value) distances and the same weight was used throughout the refinement. All the restraints were relaxed in last cycles, and both Si, Al and D atoms coordinates were allowed to refine independently.

Atomic coordinates, fraction and Atomic Displacement Parameters of D-omega zeolite framework and extraframework atoms are reported in Appendix 7, Table G.

Data collection details and R-values agreement indices at selected temperature of 30, 250, 430, 600 and 770 °C for NH_4-omega and at -271.15 °C for D-omega are reported in Table 5.7.1 and 5.7.2, respectively.

Table 5.7.1.
Lattice parameters, details of data collection and R-values agreement indices of NH_4-omega.

Parameter	30 °C	250 °C	430 °C	600 °C	770 °C
Space Group	$P6_3/mmc$	$P6_3/mmc$	$P6_3/mmc$	$P6_3/mmc$	$P6_3/mmc$
a (Å)	18.2481(9)	18.2126(8)	18.2164(7)	18.2084(4)	17.974(3)
c (Å)	7.6447(4)	7.6456(3)	7.6423(3)	7.6128(2)	7.529(1)
V (Å^3)	2204.58(19)	2196.18(16)	2196.23(15)	2185.84(10)	2106.9(6)
Wavelength	0.68881(1)	0.68881(1)	0.68881(1)	0.68881(1)	0.68881(1)
2θ (°) range	1.62-41.5	1.62-41.5	1.62-41.5	1.62-41.5	1.62-41.5
N_{data}	3959	3959	3959	3959	3959
N_{var}	66	63	60	53	48
R_{wp} (%)	6.51	6.43	6.72	6.29	10.02
R_p (%)	5.03	4.97	5.16	5.57	8.15
R_F^2(%)	8.35	9.84	10.73	9.86	13.49

$R_p = \Sigma[Y_{io} - Y_{ic}]/\Sigma Y_{io}$; $R_{wp} = [\Sigma w_i(Y_{io} - Y_{ic})^2/\Sigma w_i Y_{io}^2]^{0.5}$; $R^2_F = \Sigma|F_o^2 - F_c^2|/\Sigma|F_o^2|$

Table 5.7.2.
Lattice parameters, details of data collection and R-values agreement indices of D-omega.

Parameter	D-omega
Space Group	$P6_3/mmc$
a (Å)	18.2055(17) Å
c (Å)	7.5911(8) Å
V (Å^3)	2178.9(4) Å^3
Wavelength (Å)	2.3980(1) Å
2θ (°) range	6.35–158.30°
N_{obs}	2879
N_{var}	34
R_{wp}(%)	9.42
R_p(%)	4.45
R_F^2(%)	26

$R_p = \Sigma[Y_{io} - Y_{ic}]/\Sigma Y_{io}$; $R_{wp} = [\Sigma w_i(Y_{io} - Y_{ic})^2/\Sigma w_i Y_{io}^2]^{0.5}$; $R^2_F = \Sigma|F_o^2 - F_c^2|/\Sigma|F_o^2|$

Results and discussion of NH_4-omega room temperature structural refinement.

Full-profile Rietveld refinement allowed to determine both the extraframework species content and position after the ammonium-exchange. As reported by Martucci et al. (2003) in the as-synthesized zeolite omega, Na cations are distributed over two sites: most of Na is located at the centre of the 8-membered ring, (NaI site) and 8-fold coordinated to six framework oxygen atoms and two water molecules. Residual Na cations (NaII site) are located along the axis of the 12-ring channel, and are coordinated to nine H_2O molecules. TMA template, located within the gmelinite cage can statistically assume two different orientations.

After the NH_4-exchange only half of the original Na content was detected. On a whole, 2.48 Na ions per unit cell were calculated, rather than 6.6 Na ions determined in the as-synthesized zeolite omega (Martucci et al., 2003). Na cations detected are located in the NaI site where they maintain their 8-fold coordination to six framework oxygens and two water molecules (W1 site), thus forming Na-W1 chains (Martucci et al., 2003). Since the occupancy of 2.48 Na per cell is in excellent agreement with the chemical analysis, it was reasonable assuming that the NaII site cations had been completely exchanged with ammonium ions.

A nearby crystallographic site, located within the 12MR channel and labelled $NH_4(1)$, was attributed to ammonium ions and water molecules (Figure 5.7.1). This extraframework site was close to the W6 one in the as-synthesized omega. The $NH_4(1)$ site occupancy revealed the occurrence of about 5.97 molecules per unit cell (corresponding to ~4 wt%). As far as concerns TMA, slightly more than 1 molecule per unit cell (~3.8 wt%) was detected within the gmelinite cage, in fair agreement with chemical analysis. Based on the charge

compensation of the lattice anions corresponding to the aluminium content, only about 5 of the $NH_4(1)$ sites can host NH_4^+, the residual one being attributed to water molecules.

After NH_4-ion exchange, only W1 and W5 water sites of the as-synthesized omega (Martucci et al., 2003) were detected, whereas W4 and W6 resulted completely emptied. An amount of ~11 water molecules per unit cell (corresponding to ~7 wt%) were located in W1, W5 and $NH_4(1)$ sites. On the whole, the structural refinement suggests that the total content of volatile compounds is equal to ~15 wt%.

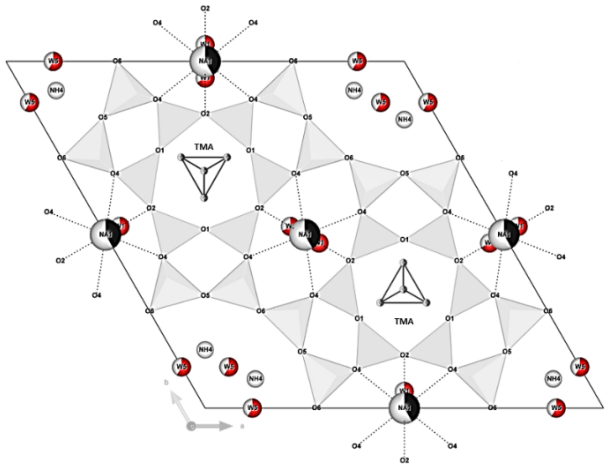

Figure 5.7.1. Extraframework sites (Na cations in black, NH_4 ions in white, H_2O in red and TMA molecules) distribution within NH_4-omega.

From a structural point of view, ammonium exchange induced a unit-cell volume increase (a=18.249(1) Å, c=7.645(1) Å, V=2204.5(1) Å^3) compared to the as-synthesized zeolite omega (a=18.215(1) Å, c=7.634(1) Å, V=2193.6(1) Å^3) (Martucci et al., 2003). An increase in cell parameters of zeolites with the exchange of sodium by ammonium was early observed for synthetic analogue of faujasite and was recently confirmed on Sasbach natural faujasite (Fantini et al., 2018; Kerr, 1989; Breck et al., 1969). Similar results were also obtained from NH_4-exchanged phillipsite (Gualtieri, 2000), barrerite (Alberti et al., 1999), chabasite (Gualtieri and Passaglia, 2006) and ferrierite (Martucci et al., 2014). NH_4 exchange did not cause relevant framework distortions: the average T-O distance is nearly unchanged in the ion-exchanged form (<T1-O>=1.641 Å and 1.637 Å; <T2-O>=1.645 and 1.619 Å in the as-synthesized and NH_4-exchanged omega, respectively) and the mean T-O-T angles are only slightly different (<T-O-T>=145.6° and 150.4° in the as-synthesized and NH_4-exchanged omega, respectively). Noteworthy is the wide 6-ring T1-O2-T1 angle (171.6°, Appendix 7, Table F) within the gmelinite cage, which is very similar to the dehydrated form of mazzite (172°) (Rinaldi et al., 1975) and similar to the value calculated in as-synthesized omega (176°) (Martucci et al., 2003) and sodium mazzite (171°) (Arletti et al., 2005).

Results and discussion of NH_4-omega high temperature structural refinements.

The powder patterns evolution at high temperature is reported in Figure 5.7.2. As already advanced in the *Refinement strategy* section, Rietveld refinements were performed up to 785 °C. Indeed, from 785 °C, the progressive peaks broadening, which highlights the loss of crystallinity, did not allow detailed structural analysis and only unit cell parameters were refined up to the end of the thermal treatment.

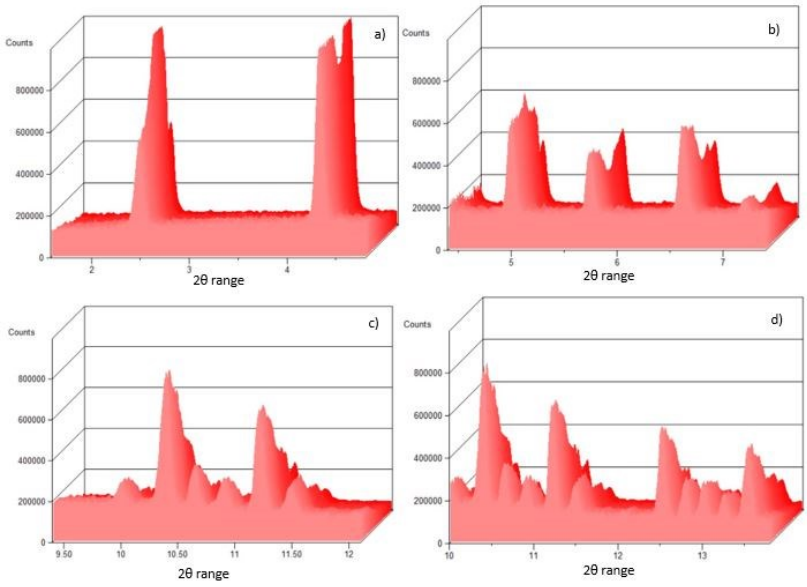

Figure 5.7.2. (a-b-c-d) powder patterns evolution at high temperature. Each image presents a 2θ angle detail (1.5-14° 2θ range).

The evolution of the lattice parameters upon heating is reported in Table 5.7.1 and in Figure 5.7.3. Based on the curve slope changes, the trend obtained can be rationalized in different *discrete* steps. From 50 to ~150 °C, the volume decrease registered (ΔV=0.35%) is reasonably due to the slight contraction occurring along the *a*-axis. Between ~150 and ~450 °C, the lattice parameters remain almost unchanged, whereas from this last temperature up to ~500 °C, a second step of volume decrease (ΔV=0.39%) arising from the simultaneous contraction of both *a* and *c*-axes occurs. Then, the volume remains unmodified up to ~600 °C (ΔV=0.01%), temperature at which starts a third step of volume contraction that continues up to 900 °C (ΔV=5.90%). Along this thermal range, noteworthy is the drop registered between 740 and 750 °C along both *a* and *c*-axes, reasonably related to the progressive loss of crystallinity of the zeolitic structure. In this case, the most relevant contribute to the volume contraction is given by the stronger decreasing of the *a* lattice parameter than the *c*-axis.

The unit cell variations can be related to both degradation and desorption of extraframework species (*i.e.*, NH_4 ions, H_2O molecules and template) upon heating. Occupancies of both

water molecules and NH_4 ions from XRD refining (Figure 5.7.4) remain constant up to 140 °C, thus suggesting that the weight loss registered in the TG curve (mass loss ~4 wt%) is ascribable to the release of surface adsorbed water molecules (Figure 5.7.5).

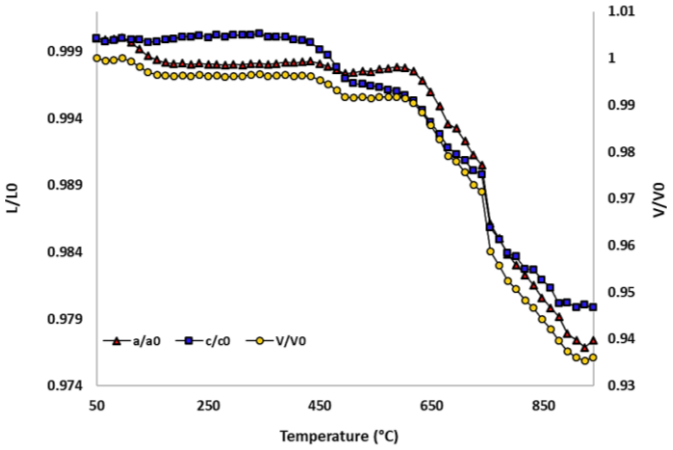

Figure 5.7.3. Temperature dependent variation of normalized unit cell parameters of NH_4-omega.

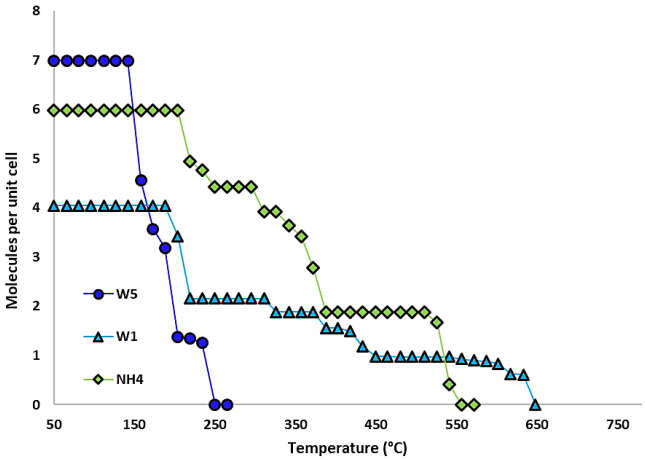

Figure 5.7.4. Temperature-dependent variation of water and NH_4 sites occupancy of NH_4-omega.

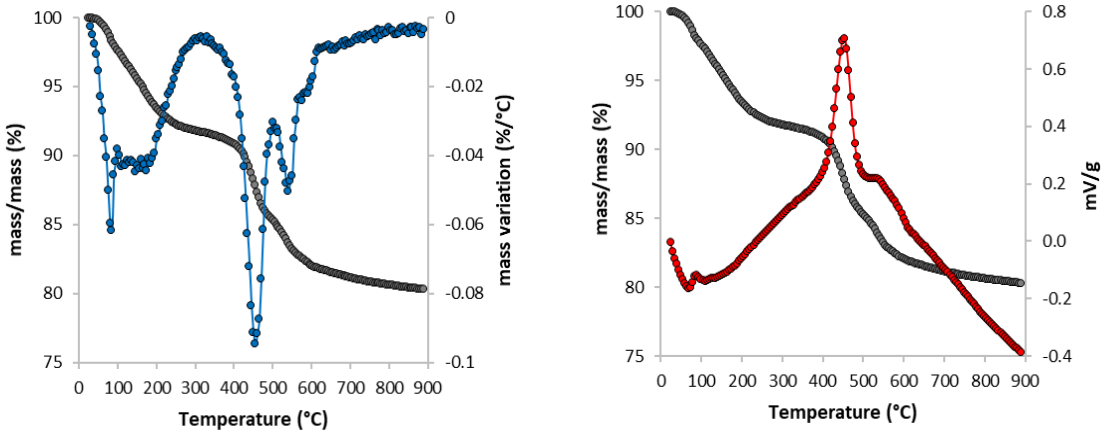

Figure 5.7.5. TG trace of NH_4-omega accompanied by DTG (lefthand) and DTA (righthand) curves.

The emptying of the W5 site (located in the main channel) starts at about 150 °C and is completed around 250 °C. On the other hand, desorption of W1 site (*i.e.*, located within the 8-ring channel) starts at 200 °C, due to the strong interaction with Na cations, which delays the start of dehydration and prevents the complete W1 desorption until 630 °C. As far as NH_4(1) site is concerned, 2 molecules per unit cell are desorbed between 200 and 300 °C, reasonably corresponding to the loss of the water present in the site. Only from 370 °C, the further loss of 2 molecules can be attributed to ammonium ions. The NH_4 desorption can be considered complete at about 540 °C.

TMA occupancy refinements (Figure 5.7.6) highlight that the template is significantly altered at relatively low temperature (about 150 °C), when the C2 site is emptied and the N site occupancy is reduced by about 30%. This phenomenon corresponds to the degradation of the organic template and is completed in the 480-600 °C temperature range, with the emptying of N and C1 sites.

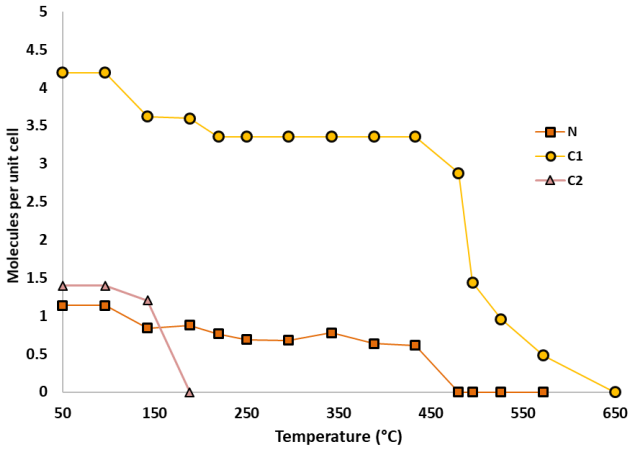

Figure 5.7.6. Temperature dependent variation of TMA sites occupancy of NH_4-omega.

At this stage of the thermal treatment we can infer that the complete elimination of the volatile products resulting from both NH_4 and template elimination corresponds to the formation of the acidic omega form (H-omega). The structural features of H-omega will be discussed in the next sections.

A good agreement between NH_4-omega refined occupancies and thermal analysis data was found. The endothermic weight loss of ~8%, observed at temperature lower than 300 °C, can be attributed to loss of water molecules and TMA degradation template. From 400 to 500 °C, the TG curve shows a sudden weight loss corresponding to the final steps of TMA and NH_4 degradation. The total weight loss registered is equal to 19.75% of the initial mass.

From a structural point of view, Rietveld refinements highlight the effect of desorption and degradation processes on the framework geometry distortions. Noteworthy is the progressive 8MR expansion (more circular shape upon heating) highlighted by O2-O2 and O5-O5 distances changes accompanied by a simultaneous narrowing of the 6MR (Figure 5.7.7(a)).

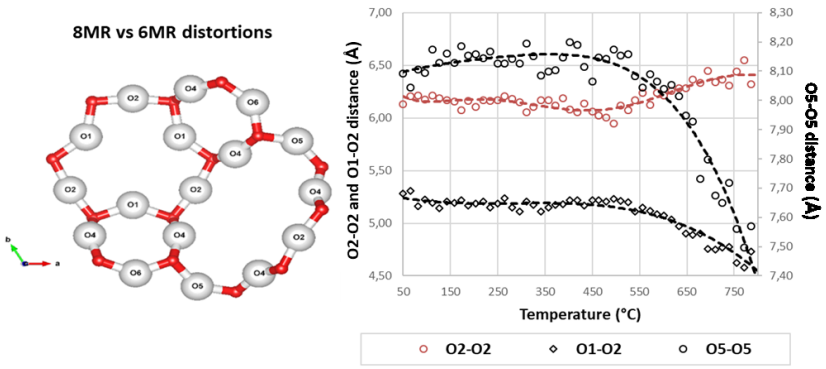

a)

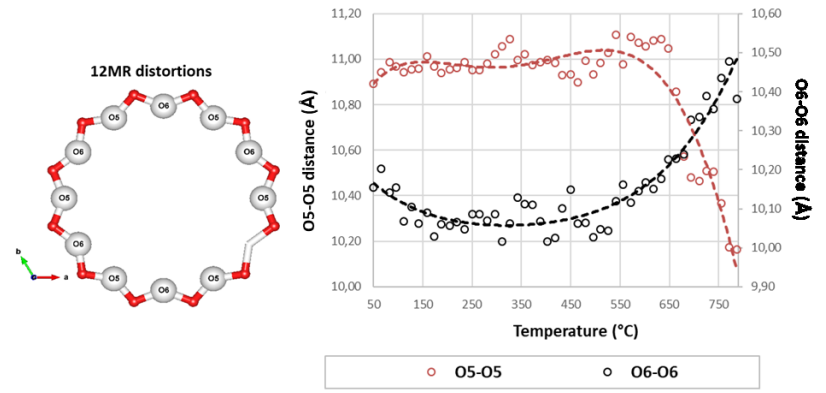

b)

Figure 5.7.7. Temperature-dependent variations of O-O distances in 8MR and 6MR (a) and in 12MR (b) in NH_4-omega. Dashed lines are reader's guide.

These structural distortions are especially significant in the temperature range 550-770 °C when zeolite calcination and dehydration are completed. They highlight a progressive shortening of the O1-O2 bond distance upon heating, from 5.26 at room temperature to 4.6 Å (Figure 5.7.7(a)). A minimal fraction of this temperature-induced deformation in 6MR will be retained in the acid omega at room temperature (O1-O2=5.16 Å).

A distortion mechanism involves also the 12MR channel, as testified by the analysis of O5-O5 and O6-O6 bond distances (Figure 5.7.7(b)). From 580 to 770 °C, an abrupt slope change is registered. The O5-O5 distance decreases suddenly whereas the O6-O6 increases, thus highlighting a progressive change in both shape and geometry of the 12MR channel. The T2-O5-T2 angle changes from ~139° at 30 °C and ~142° in H-omega to ~126° at 770°C. At the same time, the T2-O6-T2 angle varies from ~140° at 30°C and 142° in H-omega to 151° at 770 °C (Appendix 7, Table F). In order to understand the effects of template

decomposition and dehydration on the structural deformation, the results of neutron diffraction analysis are discussed below.

Results and discussion of neutron structural refinement. Lattice parameters obtained through Rietveld refinement highlighted that the D-omega unit cell (a=18.2055(17) Å, c=7.5911(8) Å, V=2178.9(4) Å^3) is significantly smaller than those refined for the NH_4-form at room temperature (a=18.2481(1) Å, c=7.6447(4) Å, V=2204.58(18) Å^3) but more similar to that of H-omega (a=18.2084(4) Å, c=7.6128(2) Å, V=2185.84(10) Å^3).
The analysis of Difference Fourier maps allowed to detect two Brønsted acid sites, labelled D1 and D2, respectively. The first was on the O5 framework oxygen atom, bridging two T2 tetrahedron cations, pointing towards the center of the 12MR channel. The second, which bridges two T1 sites, on the O2 framework oxygen, not far from the center of the 6MR (Figure 5.7.8). On a whole, ~3.9 atoms per unit cell of deuterium were obtained through the occupancy refinement: 2.25 arising from the D1 site, whereas 1.68 from the D2 one. Fourier maps revealed the presence of other extraframework sites, which were assigned to protonated amine as well as confirmed by the atomic coordinates and bond distances refinement. Although the amine was located in the same adsorption sites of the as synthesized and NH_4 omega, coordinates determined through the Rietveld refinement were different. Nitrogen (N site) was located at the center of the cage (x/a=1/3, y/b=2/3 and z/c=0.6042(4)), methyl group (C1 site) is positioned on the three-fold axis (x/a=0.2902(2), y/b=0.5803(6) and z/c=0.5514(3)) (Appendix 7, Table G). The amine molecule can statistically assume two different orientations (Figure 5.7.8).

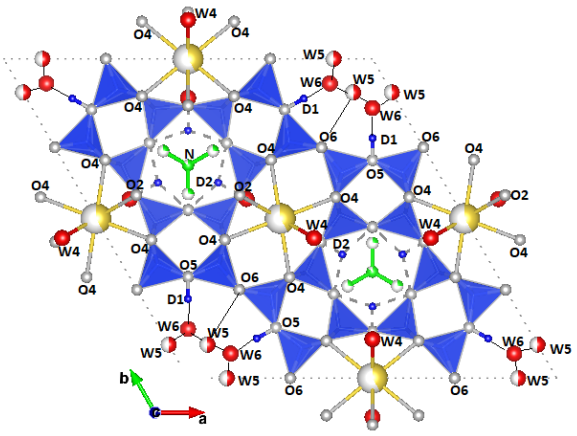

Figure 5.7.8. Proton (small blue circles) and water (small red circles) sites distribution within D-omega. Sodium cations are large yellow circles, protonated amines are small green circles.

The correct attribution of the residuals to the amine molecule was confirmed by thermogravimetric analysis (TG and DTA, Figure 5.7.9) of D-omega, which does not display the typical features of ND_3 loss.

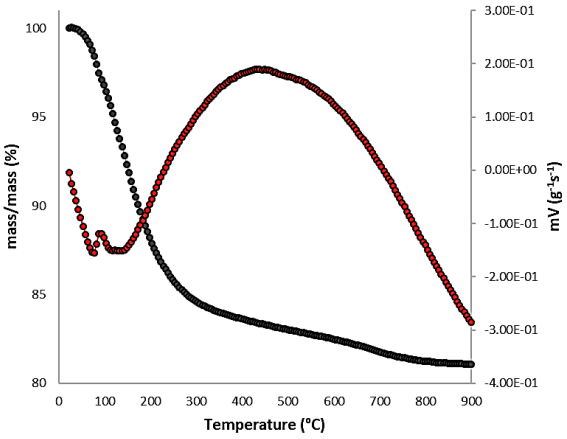

Figure 5.7.9. Thermal analysis of D-omega. In dark grey and red circles the total weight loss (TG) and the thermal differential analysis (DTA) curves, respectively.

Additionally, residual Na cations and H_2O molecules (sites labelled W4, W5 and W6) (Figure 5.7.8) were also detected by Difference Fourier maps. The NaI site, whose presence results from the incomplete ND_4^+ ion exchange, is located within the 8MR, as in the as-synthesized, NH_4 and H-omega. Bond distances highlight that the Na cation is 8-fold coordinated to two water molecules (NaI-W4=2.71(1) Å [x2]), four O4 (NaI-O4=2.99(1) Å [x4]) and two O2 framework oxygens atoms (NaI-O2=2.99(1)) (Figure 5.7.8). Besides, W5 and W6 water molecules are located within the 12MR channel whereas the W4, which interacts with the Na1 site, is placed within the 8MR.

Beyond the 3.9 atoms per unit cell of deuterium, refined occupancies allowed to calculate 2 organic molecules per unit cell and 2.46 Na ions, in good agreement with the Al^{3+}given by chemical analysis. Concerning the water content, 18 water molecules per unit cell (corresponding to the 12.4 wt% of the sample) were calculated. The total occupancy arising from the decomposition product of the TMA and water molecules (~14 wt%) is in good agreement with the thermal analysis (Figure 5.7.9), which records a weight loss of about 15.1% in the thermal range between 100 and 900 °C, due to the progressive dehydration and trimethylamine degradation.

The analysis of the bond distances (visible in Figure 5.7.10(a)) highlighted the presence of a ‘‘tube’’ of water molecules strongly interacting with D1 Brønsted site. The occurrence of protonated water clusters (O5-D1-W5-W6-W5-D1-O5) is increasingly very stable due to a large proton affinity of larger clusters (Vener et al., 2009).

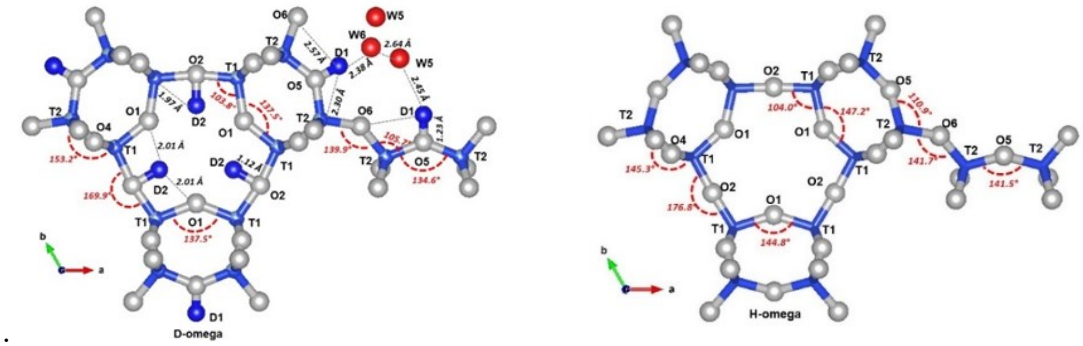

a) b)

Figure 5.7.10. Structural features and extraframework and/or framework interactions in D-omega (a) structural features of H-omega (b).

Their occurrence contributes also to both the T2-O5-T2 angle narrowing and the O5-D1 refined bond length. Convincing evidences for proton transfer (PT) from the Brønsted site to readsorbed H_2O molecules were also reported by ^1H MAS NMR measurements (Li et al., 2007; Batamack et al., 1993; Hunger et al., 1991) FTIR (Bordiga et al., 2005; Wakabayashi et al., 1996) as well as computational studies (Mihaleva et al., 2004; Demuth et al., 2001; Benco et al., 2000). Water clusters interacting with Brønsted acid sites was also reported by Martucci et al. (2009); Martucci et al. (2000b), Martucci et al. (1999) and Alberti and Martucci (2010) on the basis of neutron diffraction data.

Beyond that, Rietveld refinement highlights that the refined D1-O5 and D2-O2 bond distances are 1.12(1) and 1.23(1) Å, respectively, thus suggesting a lower acid strength in the shorter one (D1). In D-omega, the refined T-O-T angles at the protonated O2 and O5 oxygens decreases slightly with respect to the H-acid form (Appendix 7, Table F for H-omega at 600 °C; Table H and Figure 5.7.10(a) for D-omega). This results can be explained not only considering the different acquisition data (on powders *ex situ* dehydrated at a selected temperature and subsequently collected for D-omega, and on powders *in situ* time- and temperature-resolved powder diffraction collected far the equilibrium condition for H-omega, respectively) but also the combination of short- and long-range interactions affecting the acidity of the acid Brønsted sites.

Their occurrence causes proton-induced deformations, which are not limited to the T-O-T angle on the lattice anion site but are coupled with other bond angles contributing to the distortions of the D-omega framework. In particular, D2 site lies at 2.01(1) Å from O1 and the deformation is localized not only to T1-O2-T1, but also to the T1-O1-T1 bond angle, which participate in the easily deformable 8MR and 6MR, respectively. At the same time, D1 site lies at 2.57(1) Å from O6 and the distortions are shared with T2-O5-T2 bond angle,

participating in 12MR deformation. The overall effect is a contraction of both 12MR and 8MR pore openings and, consequently, an increase of the ellipticity. This process causes a flattening in the D6R unit - as indicated by the O1-O2 distance reduction - which justifies the unit-cell volume contraction in D-omega (Figure 5.7.11). A similar behaviour was also reported by Katada et al. (2009) for FAU, BEA, MFI, FER, MWW, and MOR structures. These results demonstrate the importance of topological constraints in the deformation paths of the zeolite framework.

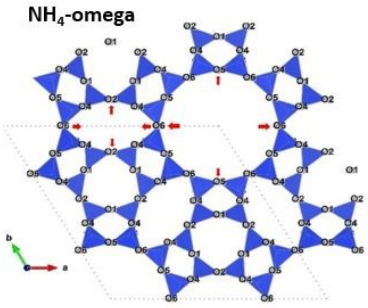

	12MR	
	NH_4-omega	D-omega
O5-O5	10.93 Å	10.72 Å
O6-O6	10.18 Å	10.10 Å
C.F.A	48.43 Å³	46.66 Å³
ε	1.00	1.08
	8MR	
O2-O2	6.14 Å	5.80 Å
O6-O6	8.06 Å	8.12 Å
O4-O4	5.73 Å	5.98 Å
C.F.A	12.21 Å³	12.14 Å³
	6MR	
O2-O1	5.26 Å	5.16 Å
	4MR	
O4-O4	3.90	3.64
O5-O5	3.62	3.92

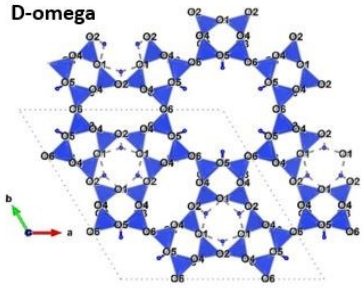

Figure 5.7.11. Differences in 12MR, 8MR, 6MR and 4MR dimensions between NH_4-omega and D-omega.

However, the structure also plays an important role in the determination of the acidity of a given zeolite and a given Brønsted site, as witnessed by the different acidity of sites with different geometry in the same zeolite at a given composition. It has been reported that in strongly acidic zeolites, such as H-ZSM-5 or mordenite, the T–O–T angles range between 137º-177º and 143º–180º, respectively. These values are wider with respect to those reported in less acidic materials like HY (138º–147º) (Kassab et al., 1998; Corma, 1995; Sauer, 1989). Indeed, it was early suggested that the Al-O-Si angle contributes to the definition of the acidity of a Brønsted site (Senchenya et al., 1986). However, further modelling of zeolite-like clusters indicated that the T-O-T angle has no significant influence on the level of acidity (Eichler et al., 1997). The difference of acid strength between different sites of the same zeolite has been earlier attributed to a property less local than the T-O-T angle, namely the size of the ring to which the acid site belongs. It was observed that the O-H stretching frequency of sites in 6- or 8MR underwent a bathochromic shift from the frequencies of sites in 10- or 12MR of a given zeolite (Jacobs and Mortier, 1982).

These findings support the conclusion of Sastre et al., (2000) that the geometry of Brønsted sites (elongation of the O-D bond and, consequently, the resulting acidity) is a combination

of short- and long-range interactions, which have all to be considered when attempting to calculate properties that contribute to the acidity of the site.

Final consideration. *In situ* synchrotron X-ray and neutron powder diffraction as well as thermal analysis were here fundamental to study the structural behaviour of the NH_4 precursor upon heating and the structural features of the omega zeolite in the acidic form. Besides, the experimental approach and the structural information gained allowed to deeply analyse the influence of zeolite structure and topology on the acidic properties. Considering the important rule recovered by the omega zeolite in the field of catalysis for petrochemical industries, this study represents an important step forward in the knowledge of the omega structural answer in operating conditions and its catalytic properties.

SYSTEM 8

INSIGHTS ON GA-ZEOLITE CATALYSTS: X-RAY POWDER DIFFRACTION AND ABSORPTION SPECTROSCOPY CHARACTERIZATION AT AMBIENT CONDITIONS

(Beltrami G., Chenet T., Pasti L., Gigli L., Pollastri S, Martucci A., 2019. Catalysis Today, *in press*, https://doi.org/10.1016/j.cattod.2019.09.016)

Samples. The synthetic L zeolite (HSZ-500KOA code) was provided by Tosoh Corporation in the K form (*i.e.*, SiO_2/Al_2O_3 ratio of 6.1, Na_2O content of 0.25 wt% and a surface area of about 290 m^2/g). MOR (CBV10A code) and FER (CP914C code) samples were purchased by Zeolyst International in Na^+ and ammonium forms, respectively. Mordenite was characterized by a SAR equal to 13, a Na_2O content of 6.5 wt% and a surface area of 425 m^2/g, ferrierite by a SAR equal to 20, Na_2O content lower than 0.05 wt% and surface area of 400 m^2g^{-1}.

Cation exchange. As-received L and MOR zeolites were exchanged with ammonium by the following procedure: 1 g of zeolite was stirred in 200 mL of 0.5 M solution of ammonium nitrate (>99%, Sigma Aldrich) in MilliQ water at 343 K for 24 h. The suspension was then filtered, by using a Nylon filter 0.22 μm (Sigma Aldrich) at room temperature and rinsed with 300 mL of MilliQ water. This procedure was repeated twice. The ammonium form of L and MOR and the as-received FER were heated in a furnace for five hours at ~ 600 °C in order to obtain the calcined form.

Wet impregnation. Cation exchange capacity was determined by using aqueous solutions of gallium nitrate ($Ga(NO_3)_3 \cdot xH_20$, Aldrich 99.9%) at different initial concentrations (5, 10, 20, 50, 70, 100, 150 and 200 mg L^{-1}), placed in contact with zeolites (L, FER and MOR) with a solid/liquid ratio of 1:1 (mg/mL). The suspensions were kept at ~70 °C under stirring during the contact time at pH 4.3, the pH was monitored during the contact and variation of 0.3 pH unit occur from the beginning to the end of the contact. All batch experiments were carried out in duplicate. The concentrations of Ga^{+3} in the solutions after the contact with zeolites and in the reference solutions obtained by keeping solutions in the same conditions of the adsorption experiments but without the addition of zeolites, were quantified by ICP-OES (Perkin-Elmer Optima 3100 XL) (axial view) equipped with a solid-state charge-coupled device detector (CCD), a peristaltic pump and a low-flow GemCone nebulizer coupled to a cyclonic spray chamber. Background correction was carried out using a two-points method. Analytical line 294.364 nm was selected for quantitative determination.

The amount of exchanged cations at equilibrium, qe (mg g^{-1}), was calculated from the mass balance equation, Eq.1:

$$q_e = \frac{(C_i - C_e)\,V}{M} \quad (1)$$

where C_i and C_e (mg L^{-1}) are the liquid-phase concentrations of Ga in the reference solution and at equilibrium respectively; V (L) is the volume of the solution and M (g) is the mass of dry zeolite used. Samples of saturated zeolite exchanged with Ga were used for structural and spectroscopic investigations. Calcined mordenite, ferrierite and L zeolites (0.5 g) were suspended with stirring in 500 ml of an aqueous solution of gallium nitrate ($Ga(NO_3)_3 \cdot xH_20$, Aldrich 99.9 %) at pH 4.2, 69.85 °C for 24 h. The zeolite was recovered by filtration, washed with 200 mL of MilliQ water and dried in oven at ~ 110 °C overnight.

Data collection. Powder patterns of the Ga-exchanged zeolites, here labelled Ga-L, Ga-MOR and Ga-FER, were collected on a Bruker D8 Advance diffractometer equipped with a Si/Li solid state detector (Sol-X). Measurements were performed at room temperature, using the Cu$K\alpha 1,\alpha 2$ wavelength, in a 3-100 ° 2θ range (*i.e.*, 0.01° 2θ step size).

Refinement strategy. Refinements were carried out in the hexagonal *P*6/*mmm* and the orthorhombic *Cmcm* and *Immm* space groups for Ga-L, Ga-MOR and Ga-FER systems, respectively. Details of data collection and R-values agreement indices are reported in Table 5.8.1 and below:

Ga-L. Peak profiles were modelled through the Pseudo-Voigt function with 0.1% cut-off peak intensity. The profile function selected was the number 2 and the coefficients refined were: Gaussian θ-indipendent *GW*, Lorentian $\cos\theta^{-1}$ and $\tan\theta$-dependent *LX* and *LY* terms, peak asymmetry and *ptec* parameters. The empirical background was fitted through the Chebyschev polynomial function and 18 coefficients.

Ga-MOR. Peak profiles were modelled through the Pseudo-Voigt function with 0.5% cut-off peak intensity. The profile function selected was the number 2 and the coefficients refined were: Gaussian θ-indipendent *GW*, $\tan^2\theta$-dependent *GU*, $\tan\theta$-dependent *GV* and Lorentian $\cos\theta^{-1}$ dependent *LX* terms, peak asymmetry and *ptec* parameters. The empirical background was fitted through the Chebyschev polynomial function and 26 coefficients.

Ga-FER. Peak profiles were modelled through the Pseudo-Voigt function with 0.1% cut-off peak intensity. The profile function selected was the number 2 and the coefficients refined were: Gaussian θ-indipendent *GW*, Lorentian $\cos\theta^{-1}$ and $\tan\theta$-dependent

LX and *LY* terms, peak asymmetry parameter, *ptec* and *stec*. The empirical background was fitted through the Chebyschev polynomial function and 15 coefficients.

For all the systems, scale factor and 2θ zero shift were also accurately refined. Besides, in all the structural refinements soft constraints were initially imposed on tetrahedral distances (σ=0.04Å) and completely removed in the last refinement cycles. Whereas, atomic coordinates, fraction and Atomic Displacement Parameters (ADPs, U_{iso}) were refined, constraining equivalent ADPs for tetrahedral sites and framework oxygen atoms of each system. Framework and extraframework atomic coordinates, fraction and Atomic Displacement Parameters of Ga-L, Ga-MOR and Ga-FER systems are reported in Appendix 8 (Table A, B and C, respectively).

Table 5.8.1.
Details of data collection and R-values agreement indices of Ga-L, Ga-MOR and Ga-FER systems.

Parameter	Ga-L	Ga-MOR	Ga-FER
	$Ga_{2.57}K_2((GaAlSi)_{36}O_{72}) \cdot 14H_2O$	$Ga_{1.16}Na_2((GaAlSi)_{48}O_{96}) \cdot 13H_2O$	$Ga_{1.3}((GaAlSI)_{36}O_{72}) \cdot 5H_2O$
Wavelength (Å)	1.54059	1.54059	1.54059
2θ (°) range	5.5-100	5.5-100	5.5-100
N_{data}	1339	1482	1564
N_{var}	56	76	64
R_{wp} (%)	14.45	13.35	14.59
R_p (%)	10.83	10.17	11.34
R_F^2 (%)	16.85	11.32	12.29

$R_p = \sum[Y_{io} - Y_{ic}]/\sum Y_{io}$; $R_{wp} = [\sum wi(Y_{io} - Y_{ic})^2/\sum wiY_{io}^2]^{0.5}$; $R_F^2 = \sum |F_o^2 - F_c^2|/|F_o^2|$

X-ray Absorption Spectroscopy. Ga K-edge XAS spectra were collected at the XAFS beamline (ELETTRA, Trieste, Italy) (Di Cicco et al., 2009) in transmission mode using fixed exit double crystal Si(111) monochromator. For all the samples, energy calibration was accomplished by collecting simultaneously a reference spectrum of a GaAs pellet placed in a second experimental chamber after the sample and after the I1 ionization chamber, with the position of the first inflection point taken at 10369.0 eV. All spectra were collected at room temperature and in vacuum conditions, with a variable energy step as a function of the energy: Large step (5 eV) in the first 200 eV of the spectrum, smaller step (0.2 eV) in the XANES region and a k-constant step of 0.03 $Å^{-1}$ (up to 1.8 eV) in the EXAFS region. For each sample, four spectra have been collected and merged in order to increase the signal to noise ratio; merged spectra were then normalized with respect to the high-energy side of the curve and EXAFS signals have been extracted using the Athena software (Ravel and Newville, 2005). The extracted EXAFS signals were then Fourier transformed using a Hanning window in the k range 3 – 15 $Å^{-1}$ and quantitative analysis were carried out using the Artemis software (Demeter 0.9.25 package) (Ravel and Newville, 2005; Newville,

2001). Structural model for the calculation of the theoretical paths were retrieved by Rietveld refinements of the XRPD data of Ga-FER, Ga-MOR, Ga-L. Along with the samples, the compound $Ga(NO_3)_3 \cdot xH_2O$ used for the sample preparation was also measured as reference for octahedral coordinated gallium.

Adsorption results. The Ga-exchanged samples were obtained by wet impregnation by placing in contact aqueous solution of gallium nitrate with the zeolites. During this process, the solution pH can affect the adsorption, since in very acidic media (pH <2) the stability of zeolite diminished and dissolution phenomena occur with change in crystallinity and in composition (dealumination) of the adsorbent material (Petushkov et al., 2010). On the other hand, gallium undergoes hydrolysis and polymerization in aqueous solution, with increasing pH. Starting from pH >2, a progressive formation of hydroxylated monomeric specie occurs and at slightly acid pH polymeric polycations are the dominant species. Therefore, a compromise pH value equal to 4 was selected for the experiments. The total quantity of gallium adsorbed from the solution at different concentrations were evaluated by atomic spectroscopy. In Figure 5.8.1(a), (b) and (c) are reported the adsorption isotherms, it can be seen that all the three zeolites show an L-Type isotherm, and L zeolite is characterized by a higher saturation capacity. The data were fitted by Langmuir and Tòth isotherm models given respectively by Eq.2 and 3:

$$q_e = \frac{q_s K_L c_e}{1+bC_e} \tag{2}$$

$$q_e = \frac{q_s K_T c_e}{(1+(bC_e)^{\nu})^{1/\nu}} \tag{3}$$

where, q_s is the saturation capacity and K_L and K_T the affinity constant for the Langmuir and the Tóth models, respectively; in Eq.3 ν represent the heterogeneity parameter.

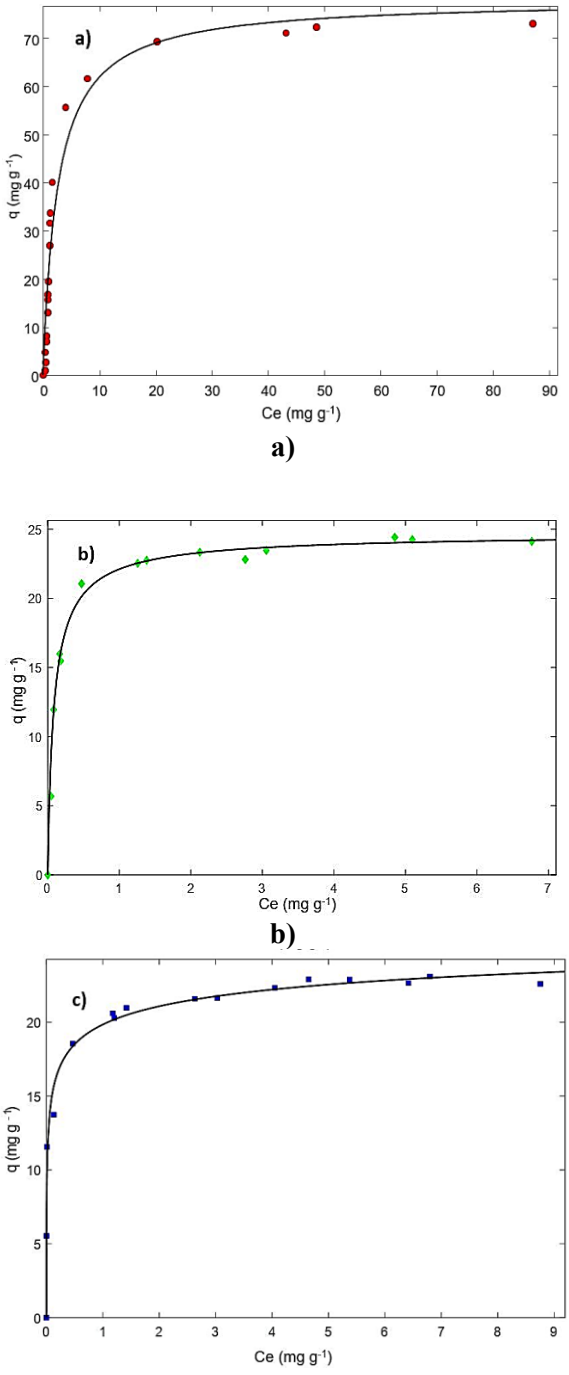

Figure 5.8.1. Adsorption of gallium on (a) L zeolite, (b) ferrierite and (c) mordenite.

The fitting results are reported in Table 5.8.2, the values in parenthesis indicate the confidence limits at 95% of probability. As can be seen from the coefficient of determination listed in this table, both the Langmuir and the Tóth models fit quite well the experimental data. In particular, for both L and FER, the heterogeneity parameter ν appearing in the Tóth isotherm (Table 5.8.2) is not significantly different from 1 and for ν=1 the Tóth isotherm corresponds to the Langmuir one. On the contrary, for MOR a ν value lower than 1 was found. The heterogeneity parameter is related to the width of the energy distribution

function, and lower values correspond to larger distribution and, therefore, to energetically heterogeneous sites on the surface.

Table 5.8.2.
Gallium cation exchange isotherm parameters. q_e (mg g^{-1}): exchanged concentration at equilibrium; C_e (mg dm^{-3}): concentration in the solution at equilibrium; K_L, K_T (dm^3 mg^{-1}): affinity constants for the Langmuir and the Tóth models, respectively; q_s (mg g^{-1}) cation exchange capacity; v heterogeneity parameter in the Tóth model (see text for further details). Confidence bounds at 95% of probability are reported in parenthesis.

Parameters	L	FER	MOR
q_s (mg g^{-1})	78.02 (70.71, 85.33)	24.52 (23.86, 25.17)	21.36 (20.07, 22.65)
K_L (dm^3 mg^{-1})	0.3841 (0.2723, 0.4959)	9.946 (8.329, 11.56)	34.9 (17.87, 51.9)
R^2	0.9505	0.9913	0.9328
q_s (mg g^{-1})	71.16 (65.61, 76.71)	24.76 (23.72, 25.8)	30.47 (21.88, 39.07)
K_T (dm^3 mg^{-1})	0.2788 (0.2191, 0.3385)	14.14 (7.92, 20.36)	38.4 (25.7 52.3)
v	0.83 (0.42, 1.24)	0.86 (0.64, 1.08)	0.2291 (0.1135, 0.3447)
R^2	0.9696	0.9954	0.9874

From the adsorption data therefore it seems that the adsorption onto MOR could involve sites of different energies. However, it should be mentioned that Langmuir isotherm has also been employed to describe the adsorption on multiple sites (Ardit et al., 2018); in such cases, it is supposed that their interactions energies are similar and they can be averaged to give a single averaged energy for all the sites. To gain more information on the involved site a structural investigation on the Ga-exchanged zeolites were carried out.

Results and discussion of Ga-L structural refinement. The Ga-L crystal structure was refined in the *P*6/*mmm* space group, starting from the atomic coordinates reported by Barrer and Villiger, H. (1969) (Barrer and Villiger, 1969a). The refined Ga-L lattice parameters are the following: *a*=*b*=18.2177(24) Å, *c*=7.5538(15) Å and V=2171.1(6) $Å^3$. According to Newsam (1987), the framework bond distances confirm the not random distribution of Al (and/or Ga) in the tetrahedral sites (Appendix 8, Table D). The T1-O bond lengths range from 1.630(4) and 1.668(3) Å (<T1-O>=1.650 Å); whereas the T2-O ranges from 1.639(6), Å and 1.846(1) Å (<T2-O>=1.722 Å). Compared with the mean <T-O> bond lengths refined for the L-LTL precursor (<T1-O>=1.640 Å and <T2-O>=1.654 Å, chapter 5, *system 4*), a lightening of both tetrahedral distances is highlighted. This result suggests the incorporation of gallium in both tetrahedral sites and a Ga-enrichment in the T2 one due to the longer average <T2-O> bond length. From a structural point of view, worth noting are the very narrow T-O-T angles centred on the O1 and O5 framework oxygen atoms (T1-O1-T1=112.6(5)° and T2-O5-T2=115.4(3)°, respectively), even if they are not the narrowest found in zeolites (Cruciani et al., 2003; Sani et al., 2002; Stuckenschmidt et al., 1996; Cannillo et al., 1966). The difference Fourier maps highlight the presence of six

extraframework sites, which were distributed among K^+ and Ga^{+3} cations, and water molecules (Figure 5.8.2(a) and (b)). The not-exchanged K^+ was localised at the centre of the 6MR (corresponding to the KB site in the L-LTL zeolite (chapter 5, *System 4*), within the cancrinite cage. Two extraframework sites were assigned to Ga^{+3} ions (*i.e.*, labelled Ga1 and Ga2, respectively) and were located not far from the centre of the 8MR (Ga1) and close to the edge of the 12MR channel (Ga2), respectively. The remaining three partially occupied sites were all positioned within the 12MR channel and were attributed to H_2O molecules (*i.e.*, W1, W2 and W3 sites, respectively).

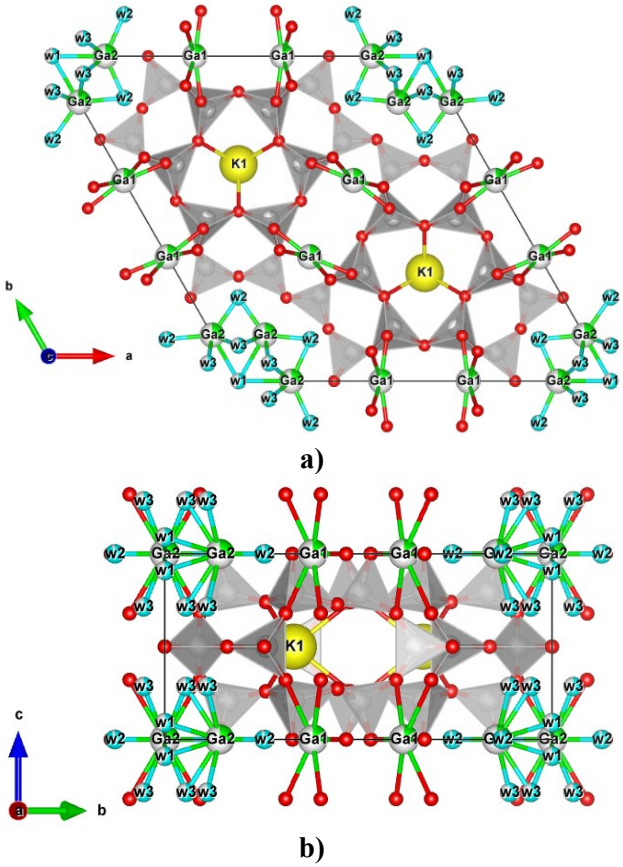

Figure 5.8.2. Extraframework content distribution of Ga-L system. Projection along *c*- (a) and *a*- (b) axis.

K^+ is six-fold coordinated to six framework oxygens, as suggested by the K1-O3=2.92(1) [x6] Å distance. Ga1 is six-fold coordinated to O4 and O6 framework oxygen atoms (Ga1-O4= 2.85(1) [x4] Å and Ga1-O6=2.21[x2] Å). The refined bond distances (Ga2-W1=2.67(1) [x2] Å, Ga2-W2= 2.23(1) [x2] Å and Ga2-W3=2.56(1) [x4] Å) and occupancies of W1, W2 and/or W3 water molecules indicate that Ga2 is four (with W1 and W2, or only W3) or six-fold coordinated (with W1 or W2 and W3) to water. Indeed, bond distances suggest also the presence of short W1-W3-W3 water oligomers developing along the [*001*] direction, as testified by the W1-W3=2.26(1) and W3-W3= 2.98(1) Å distances. On the whole, Rietveld refinement reveals the occurrence of ~14 water molecules, 2 K^+ and

2.57 atoms of Ga^{+3} per unit cell, respectively. The K and Ga content was consistently lower than the theoretical concentration calculated on the basis of the aluminium content of the L precursor. This discrepancy cannot be attributed to an underestimation of the cations sites, neither to an incomplete NH_4^+ ion exchange or dehydroxylation and/or dealumination during calcination, as well as residual NH_4^+ after calcination. Moreover, difference Fourier maps do not show any indication of extraframework sites attributable to NH_4^+ groups. The hypothesis of extraframework Al^{+3} atoms is also disregarded by the DF synthesis that does not show any maximum that can be interpreted as oxygen atoms coordinated to Al^{+3}. Hence, it is suggested that the lattice charge defects give rise to Brønsted acidic Si-OH-Ga bridging hydroxyl group, whose occurrence is confirmed by the lengthening of the T-O distance after Ga^{+3} incorporation. In chapter 5, *System 4* was demonstrated the presence of Brønsted acid sites through neutron powder diffraction on the acidic form of L zeolite. The first site (D1) was located on the framework oxygen O5, not far from the centre of the 8-ring of the cancrinite cage. The second (D2 site) on the framework oxygen O1, heading towards the centre of the 12 MR channel. On the whole, 7.7 Brønsted sites were recognized, in consistence with the tetrahedral aluminium content determined starting from the Si/Al ratio. In our refinement, the T-O distances involving the O5 and O1 framework oxygens were always among the largest of the tetrahedra (Appendix 8, Table D). At the same time, the attractive force of Brønsted acid sites could reasonably responsible of the very narrow T-O-T angles centred on the O1 and O5 framework oxygen atoms (T1-O1-T1=112.6(5)° and T2-O5-T2=115.4(3)°).

As reported by Fricke et al., (2000), the excess of gallium determines the formation of a segregate phase coexisting with the main zeolitic one. In this case, a phase of gallium hydroxide (GaO(OH)) was recognized through the qualitative analysis, which highlights the presence of some extra peaks (*i.e.*, [*101*], [*200*] and [*201*] *hkl* reflections at the 21.41 and 18.06 and 26.68° 2θ angles, respectively) not attributable to the L zeolite (Figure 5.8.3). The semi-quantitative analysis reveals the presence of 83 and 17 wt% of L zeolite and GaO(OH), respectively.

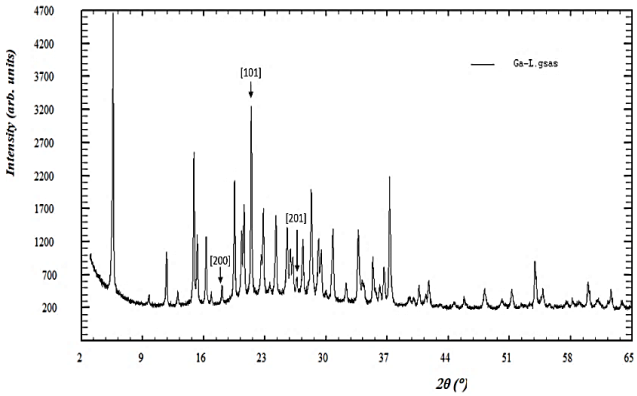

Figure 5.8.3. Powder diffraction pattern of Ga-L system.

Results and discussion of Ga-MOR structural refinement. The crystal structure of the Ga-exchanged mordenite was refined in the topological orthorhombic *Cmcm* symmetry, starting from the structural model of Alberti et al. (1986). After the Ga-exchange, lattice parameters highlight a slight reduction of the unit cell volume (Ga-MOR=2766.35(25) $Å^3$, Na-MOR=2781.58(25) $Å^3$) compared to that of the starting Na-MOR sample, due to the decrease of *b* and *c* parameters (Ga-MOR: *b*=20.3510(9) Å, *c*=7.4940(4) Å; Na-MOR: *b*=20.4447(10) Å, *c*= 7.5152(4) Å). On the contrary, along *a* direction, a small increase is observed (18.1387(9) Å and 18.1038(10) Å for Ga-MOR and Na-MOR, respectively). The comparison of the mean tetrahedral distances between the exchanged one (<T1-O>=1.662 Å, <T2-O>=1.654 Å, <T3-O>=1.658 Å, <T4-O>=1.657 Å) and the Na-form (<T1-O>=1.654 Å, <T2-O>=1.650 Å, <T3-O>=1.657 Å, <T4-O>=1.656 Å) does not reveal a preferential siting of gallium in framework position. On the contrary, intertetrahedral angles of the Ga-MOR are narrower than those of the starting material. Among them, noteworthy is the shrinkage of the T3-O9-T3 angle, which moves from 165.5(1)° in the Na-MOR to 151.9(1)° in the Ga-MOR (Appendix 8, Table E).

The analysis of the difference Fourier maps allows to detect the presence of extraframework sites assigned to residual Na^+ cations, Ga^{+3} and water molecules, respectively (Figure 5.8.4(a) and (b)). Not exchanged Na^+ (labelled Na2) is located within the 8MR in a six-fold coordination with O1 (Na2-O1=3.06 Å [x4]) and O6 (Na2-O6=3.01 Å [x2]) framework oxygen atoms. Gallium site (labelled Ga1) is positioned within the 12MR channel, along with all the three sites attributed to water molecules (W1, W2 and W3), which have a fundamental role in the completion of the gallium cation coordination.

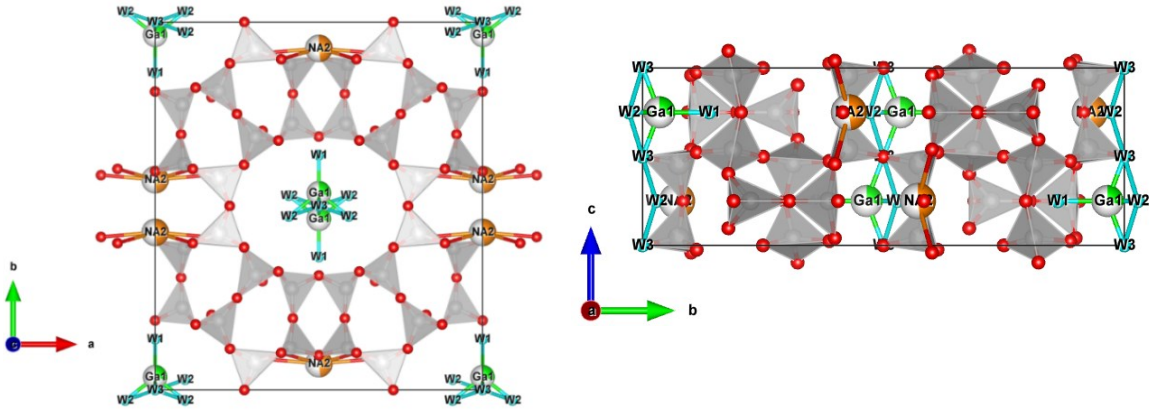

Figure 5.8.4. Extraframework content distribution of Ga-MOR system. Projection along *c*- (a) and *a*- (b) axis.

In this case, gallium is five-fold coordinated, as testified by the following bond distances: Ga1-W1=2.10(1) Å, Ga1-W2=2.09(1) Å [x2] and Ga1-W3=2.00(1) Å [x2]. Furthermore, W2 and W3 show to be hydrogen bonded each other (W2-W3=2.56(1) Å [x4]), thus forming short W2-W3 water oligomers running along the 12MR. No further residual of electron density, attributable to NH_4^+ groups, were detected through the difference Fourier maps, thus indicating that all the ammonium content has been substituted by Ga^{+3} and that the extraframework gallium quantified is the maximum exchangeable for the mordenite here studied. Concerning the amount of extraframework content, refined occupancies indicate the presence of 2 and 1.16 a.u.c of Na^+ and Ga^{+3} cations, respectively, along with 13 water molecules per unit cell. Na^+ and Ga^{+3} values obtained are lower than the theoretical concentration, hence also in this case the presence of Brønsted acidic Si-OH-Ga bridging hydroxyl group has to be supposed to counterbalance the framework charge defect. Martucci et al. (2000b) reports that the position of Brønsted acid sites does not strictly depends on the nature of the zeolite (natural or synthetic) and on its Si/Al ratio. Indeed, in all the three samples considered in that work (with Si/Al ratio equal to 5.5, 5.6 and 10, respectively), the four Brønsted acid sites detected were constantly located on the same framework oxygen atoms. The first, D1, was on framework oxygen O10 and headed towards the center of the 12-ring; the second, D2, was on the framework oxygen O6 and headed towards the side pocket; the third, D3, was on O5 and headed towards the center of the 12-ring; the last, D4, was on O9 and headed toward the center of the eight-ring. Hence, it is reasonable to assume the presence of charge compensator protons in these sites.

The comparison of powder patterns before and after gallium exchange shows the occurrence of [*301*] and [*200*] *hkl* reflections at the 33.64 and 18.09 ° 2θ angles, respectively. This

testifies the presence of the segregate gallium hydroxide phase arising from the gallium-exchange process (Figure 5.8.5). The semi-quantitative analysis reveals the presence of 74 and 26 wt% of mordenite and GaO(OH), respectively.

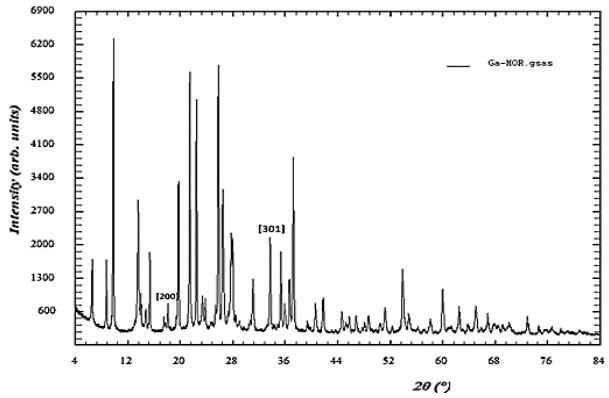

Figure 5.8.5. Powder pattern of Ga-MOR system.

Results and discussion of Ga-FER structural refinement. Due to the absence of *I*-centering forbidden peaks ($h+k+l=2n+1$ reflections), the Ga-FER crystal structure was refined in the *Immm* space group, starting from the atomic coordinates reported by Dalconi et al. (2003). From the analysis of the lattice parameters obtained through the Rietveld refinement, not noteworthy differences can be detected between the starting NH4-ferrierite (Martucci et al., 2014) and Ga-exchanged samples. Indeed, it is highlighted a very small reduction of the unit cell volume (NH4-FER=1978.6(1) Å^3, Ga-FER=1977.20(15) Å^3) principally attributable to the slight decrease of *a* and *b* parameters, whereas *c* remains almost unchanged (NH4-FER: *a*=18.8477(8) Å, *b*=14.1049(5) Å, *c*=7.4425(2) Å; Ga-FER: *a*=18.8394(10) Å, *b*=14.0885(6) Å, *c*=7.4494(2) Å). On the contrary, the comparison of framework bond distances and angles between them, suggests that the metal-exchange process has led to the incorporation of gallium within tetrahedral sites. After the Ga-exchange, <T-O> distances of the four tetrahedral sites appear homogeneously longer (Ga-FER: <T1-O>=1.651 Å, <T2-O>=1.654 Å, <T3-O>=1.653 Å and <T4-O>=1.635 Å; NH4-FER: <T1-O>=1.607 Å, <T2-O>=1.607 Å, <T3-O>=1.609 Å and <T4-O>=1.607 Å), whereas T-O-T angles result narrower than that of the precursor (Appendix 8, Table F), thus suggesting the presence of tetrahedral Ga^{+3} cations. Indeed, according to Fricke et al., (2000), structural modifications strongly depend on the concentration of gallium and on the degree of substitution achieved. The analysis of the difference Fourier maps reveals the presence of five partially occupied extraframework sites: three of them are occupied by water molecules (sites labelled W1, W2 and W3), the remaining by gallium cations (sites labelled Ga1 and Ga2). W1, W2 and Ga1 are located within the 10-membered ring, whereas W3 and Ga2

close to the edges of the 8-membered ring window, which defines the limits of the ferrierite cage (Figure 5.8.6(a) and (b)). As already observed in Ga-L system, no evidences of ammonium are highlighted by the Difference Fourier maps analysis, thus indicating that all the NH_4 content has been replaced by gallium after the exchange. Along with the ~5 water molecules per unit cell, the refinement of the extraframework Ga^{+3} occupancies highlighted the presence of 1.3 ions per unit cell, in good agreement with the amount of ammonium calculated in the precursor sample (~1.2 ions per unit cell; Martucci et al., 2014). The analysis of the extraframework bond lengths reveals the existence of strong interactions among water molecules and Ga^{+3} cations.

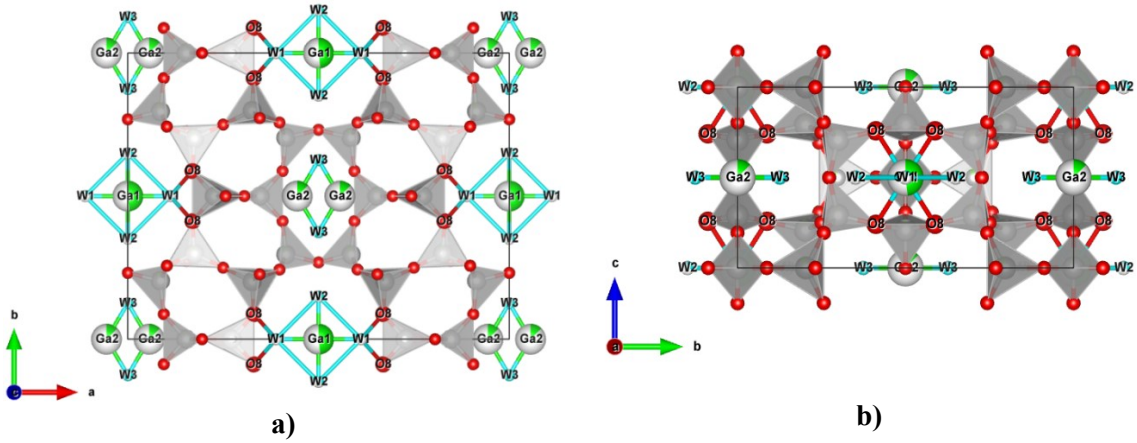

Figure 5.8.6. Extraframework content distribution of Ga-FER system: projection along *c*- (a) and *a*- (b) axis.

Distances refined indicate that Ga1 site is four-fold coordinated exclusively to water molecules (Ga1-W1=2.09(1) Å [x2] and Ga1-W2=2.09(1) Å [x2]). Besides, W1 and W2 interact between them thus creating W1-W2-W1 short oligomers (W1-W2=2.96(1) Å [x2], oriented parallel to the 10MR channel which are hydrogen bonded to the O8 framework oxygen atom (O8-W1= 2.53(1) Å [x4]). Ga2 site is coordinated by the W3 site, as testified by the Ga2-W3=2.06(1) Å [x2] distance. No other interactions between Ga2 and H_2O were detected and no additional reasonable electronic density residues to be attributed to water were recognized. Considering that, the four-fold coordination is the lowest for Ga^{+3} cations, the presence of some not detectable protons which complete the gallium coordination has to be assumed (Joshi and Thomson, 2005). Also in this case, the segregate phase of gallium hydroxide was recognized through the qualitative analysis. It has been highlighted by the occurrence of two extra reflections (*i.e.*, [*101*] and [*301*] *hkl* at the 21.41 and 33.61° 2θ angles, respectively) not attributable to the ferrierite and not present in the NH4-FER powder pattern (Figure 5.8.7). The semi-quantitative analysis reveals 96 and 4 wt% of ferrierite and GaO(OH), respectively.

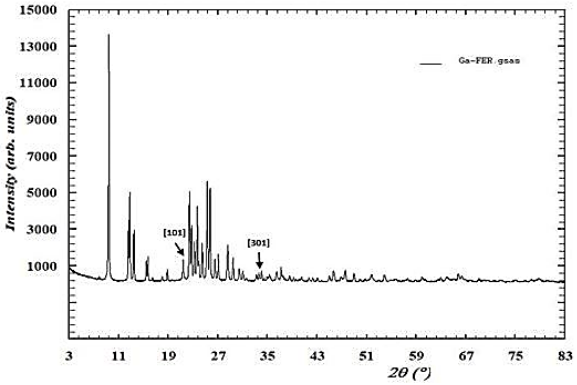

Figure 5.8.7. Powder pattern of Ga-FER system.

XAS results. Figure 5.8.8(a) shows the normalized spectra of all samples and $Ga(NO_3)_3 \bullet xH_2O$, whereas the corresponding $k^2\chi(k)$ experimental data are reported in Figure 5.8.8(b).

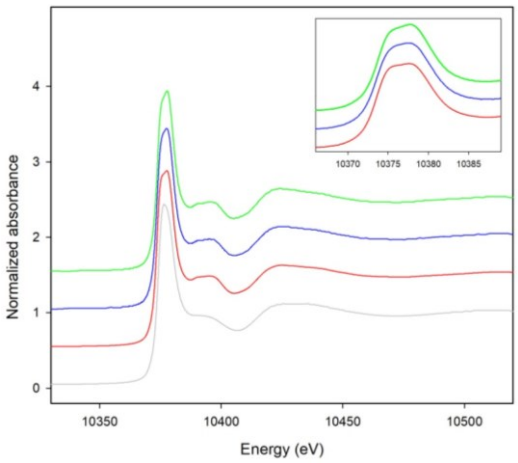

a)

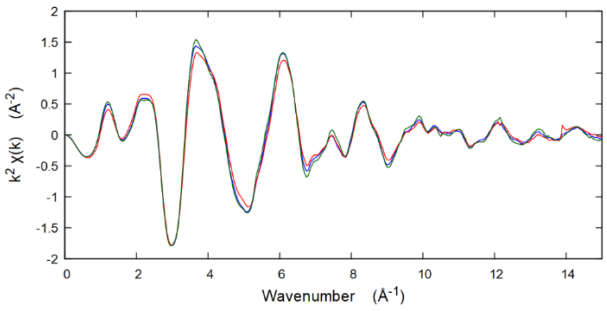

b)

Figure 5.8.8(a). Normalized spectra of Ga-MOR (green), Ga-FER (blue), Ga-L (red) and $Ga(NO_3)_3$ reference (grey). Small box on the top right is a zoom around the edge area. **(b)** $k^2\chi(k)$ experimental data of Ga-MOR (green), Ga-FER (blue) and Ga-L (red).

As can be seen in the zoom area of Figure 5.8.8(a), the two peaks in the white line of Ga-exchanged zeolites (at energies of 10375 and 10379 eV) are a preliminary indication of the fact that Ga is present in both tetrahedral and octahedral geometry, according to previous studies (Akatsuka et al., 2016; Nishi et al., 1998). The presence of Ga atoms in

non-equivalent crystallographic sites, due to the symmetry of the zeolites, together with the secondary phase GaO(OH) in various amount in all the samples (as evidenced by the XRPD data) complicated the EXAFS refinements, so we focused only on the first shell. First-shell contribution has been modelled using Ga–O bond distances coming from the Ga in tetrahedral sites of the zeolite (as the Ga atoms in extraframework sites have longer bond distances) and the octahedral Ga in GaO(OH) impurity (structural model taken from Li et al., 2003). This strategy has been adopted as Ga-O bond distances in tetrahedral and octahedral coordination are quite similar and partially overlapping (Gagné and Hawthorne, 2018), confirmed also by the quantitative EXAFS results on the first-shell, summarized in Table 5.8.3 (fits are shown in Figure 5.8.9(a), (b) and (c)).

Table 5.8.3.
EXAFS results on the first shell.

Sample	Shells	%	R	N	R(Å)[a]	S_0^2	R-	σ^2(Å^2)	ΔE_0(eV)
$Ga(NO_3)_3 \bullet xH_2O$			*			1.04 (8)	0.012	0.007 (1)	6 (1)
	Site1 - Ga – O_1	0.5		6	1.939(4)				
	Site2 - Ga – O_4	0.5		4	1.935 (4)				
	Site2 - Ga – O_5			2	1.961 (4)				
Fer						1.05 (5)	0.003	0.002 (2)	2 (2)
	Site1[b] - Ga – O	0.2 (1)*0.5		4	1.93 (1)				
	Site2[b] - Ga – O	0.2 (1)*0.5		3	1.91 (1)				
	Site2[b] - Ga – O			1	1.94 (1)				
	GaO(OH) contamination:		**					0.005 (1)	
	Ga – O_1	0.8 (1)		3	1.904 (6)				
	Ga – O_2			3	2.031 (6)				
Mor						1.05 (4)	0.003	0.001 (3)	3 (1)
	Site1[b] - Ga – O	0.15 (8)*0.5		4	1.96 (2)				
	Site2[b] - Ga – O	0.15 (8)*0.5		4	1.92 (2)				
	GaO(OH) contamination:		**					0.005 (2)	
	Ga – O_1	0.85 (8)		3	1.912 (8)				
	Ga – O_2			3	2.040 (8)				
L						1.05 (9)	0.004	0.001 (3)	3 (1)
	T1 - Ga – O_4	0.16 (4)*0.5		4	1.93 (2)				
	T2 - Ga – O_5	0.16 (4)*0.5		2	1.91 (2)				
	T2 - Ga – O_6			2	1.94 (2)				
	GaO(OH) contamination:		**					0.007 (2)	
	Ga – O_1	0.84 (4)		3	1.900 (3)				
	Ga – O_2			3	2.026 (3)				

[a]All the bond lengths values are in excellent agreement with the mean values reported by Gagné and Hawthorne (2018) for Ga^{+3} ion in both tetrahedral and octahedral coordination.
[b]These sites represent an average of the Ga atoms in tetrahedral coordination and did not refer to the real crystallographic sites.
*Hendsbee et al., 2009.
**Li et al., 2003.

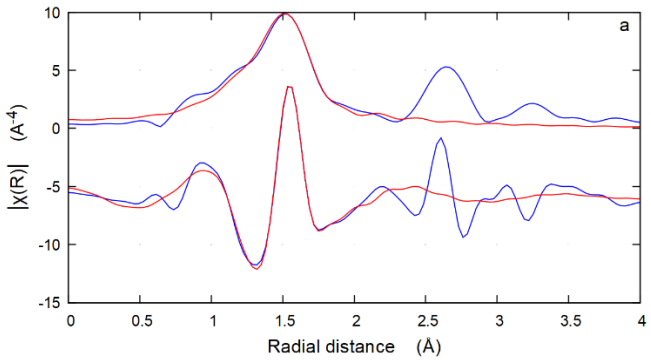

a)

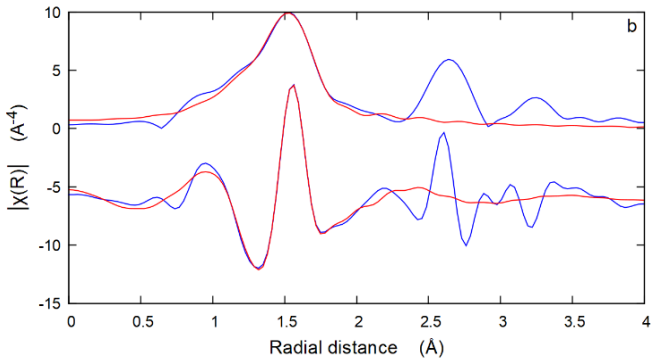

b)

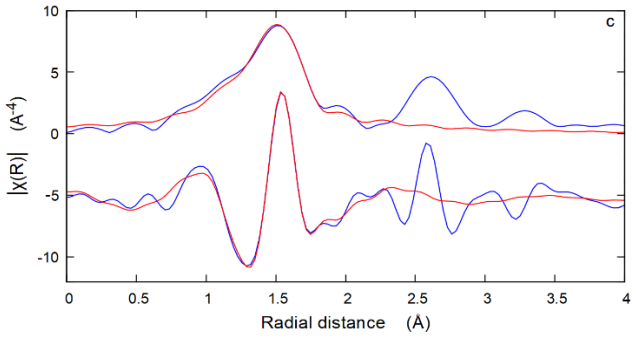

c)

Figure 5.8.9. The obtained EXAFS fit on the three samples: (a) Ga-FER; (b) Ga-MOR; (c) Ga-L.

The obtained average bond lengths are of 1.928 ±0.01, 1.937 ±0.02 and 1.925 ±0.02 A˚ for Ga-FER, Ga-MOR and Ga-L respectively; the refined value (1.04) of the amplitude factor S_0^2 on the $Ga(NO_3)_3 \bullet xH_2O$ reference compound is almost identical to that obtained for the zeolite samples. As can be seen in Table 5.8.3, the major contribution to the EXAFS signal is due to Ga in GaO(OH) impurity, being about 80% in all the samples; nevertheless, a good fit cannot be achieved without introducing also tetrahedral Ga contribution. This fact, together with the XANES information of the splitted peak of the white line (zoom area in Figure 5.8.8(a)), allows to confirm the presence of tetrahedral Ga and consequent incorporation into the zeolite framework.

Final consideration. A multidisciplinary approach built on adsorption experiments, X-ray powder diffraction and X-ray absorption spectroscopy, was here selected to investigate the cation-exchange capacity of L, mordenite and ferrierite zeolites. The information gained indicated that all the samples are characterized by high cation-exchange capacity since extraframework gallium cations were found within micropores of all the three zeolites. Interestingly, the post-synthesis treatment performed to obtain Ga-exchanged zeolites, led also to the incorporation of gallium at tetrahedral framework positions. This information is of primary importance considering the relevance of Ga-zeolite catalysts in aromatization of lower alkanes and isomerization of alkylaromatics. Indeed, having both framework and extraframework gallium cations determines the presence of both Brønsted and Lewis acidity, which play an important role in determining the efficiency of a zeolitic catalyst in catalytic reactions.

CHAPTER 6. Conclusions

In this work, the relations between structure and applications of the some of the most commonly employed zeolites characterized by different pore dimensions have been investigated. The efficiency of these microporous zeolites for particular catalytic or environmental applications has been described in terms of "*selective diffusion by "molecular traffic control" through the channels"*, but also in terms of "*the selective active-site population in certain crystallographic positions of these pores"* (Moliner et al., 2015). In particular, physical and chemical features of five zeolites (*i.e.,* ZSM-5 (MFI), ferrierite (FER), mordenite (MOR), L (LTL) and omega (MAZ)), as well as the host-guest interactions between zeolite frameworks and extra-framework species, were investigated by using different experimental approaches (*i.e.* XRD from both conventional and non-conventional sources, neutron diffraction, XAS spectroscopy). The selection of these systems can be explained since medium and large-pore zeolites containing specific building units, such as 5-1 (MOR, FER, MFI), cancrinite cages (LTL) or gmelinite cavities (MAZ), are competitive to consider their potential application in the industrial processes, such as catalysis in the petrochemical field (*e.g.*, fluid catalytic cracking, transalkylation, olefin isomerization, xylene isomerization and ethylbenzene synthesis) and fractionation or purification of biomolecules, such as amino acids, in biotechnological one. Besides, these materials are also competitive in terms of environmental remediation processes, since their topology, channel system and adsorption capacity make them excellent sorbent media for air quality monitoring, water and wastewater clean-up from pollutants.

The zeolites selected were firstly characterized in their as-synthesized forms and secondly upon thermal activation. The results here highlighted demonstrated that the presence of active sites in specific crystallographic positions favours the occurrence of host-guest interactions in open pores and most importantly, addresses the diffusion through the void volumes of these medium and large multipore zeolites. This last phenomenon is strongly controlled by the presence of specific positions of the framework charge defects with great interest in several commercial processes.

For each of them, the main outcomes are hereafter highlighted, before drawing a brief general conclusion.

In situ synchrotron powder diffraction allowed to monitor the progressive thermal activation of four TPA^+ templated ZSM-5 characterized by different Si/Al ratios *(System 1)*. Rietveld refinements of the room temperature data highlighted that all the samples contained the maximum amount allowed of tetrapropylammonium ion (4 TPA^+/u.c.) located at the

intersection of the sinusoidal and the straight channels. The analysis of the bond distances evidenced the lack of interactions between the TPA^+ and the framework oxygen atoms. Besides, the ellipticity parameters revealed that the geometry of the channels is slightly distorted since the beginning of the thermal treatment. The high temperature refinements confirmed the high thermal stability of all the four ZSM-5 samples, which remain crystalline up to the end of the thermal treatment (800 °C). The complete activation of ZSM-5 occurs between 300 and 400 °C, when the TPA^+ template is completely removed from the pores. The template burning does not cause relevant variations in framework geometry and channel shape, thus confirming the high flexibility of the MFI framework.

After TPA^+ decomposition and thermal activation, possible framework distortions affecting the thermal regeneration and the efficiency of the ZSM-5 zeolite could occur (*System 2*). The charge balance in ZSM-5 is reached by the formation of Brønsted acid sites, which are responsible of variations of the unit cell dimensions addressed mainly by T−O−T angles changes. Besides, these variations reveal that the achieved bonding geometries are affected by the initial Si/Al ratio. Furthermore, the T-O-T angles and the pore-sized geometries suggested a direct effect on the active-site distribution within the pores/cavities. This information allows to better understand the catalytic activities and selectivities for particular chemical processes.

The diffusion of guest molecules inside this excellent adsorbent material was then monitored by adsorption studies and synchrotron X-ray powder diffraction in order to investigate ZSM-5 sorption capacity and structural modifications driven by the L-lysine adsorption (*System 3*). Rietveld structural refinements revealed the adsorption of the amino acid in both the samples with different Si/Al ratio. The refinement of the amino acid occupancies revealed higher sorption capacity for the ZSM-5 with lower SAR ($ZSM\text{-}5_{(15)}$), whereas the amount of co-adsorbed water molecules calculated is negligible in both cases. Besides, the study of host-guest and guest-guest interactions evidenced that the L-lysine molecules are bonded to each other as well as to the framework oxygen atoms in both ZSM-5 samples. The extraframework content quantified was in good agreement with adsorption isotherms data and thermal analysis results. The bond distances analysis suggested that no relevant structural deformations occur after the L-lysine adsorption, so this system can be useful employed for sequestration of aminoacids.

As far as large pore L zeolite is concerned, Rietveld structural refinement performed on the neutron data collected on the as-synthesized, precursor and acid L zeolite allowed to determine with high accuracy position and concentration of Brønsted acid sites as well as amount and distribution of aluminium in framework positions (*System 4*). Firstly, the L-LTL

structural analysis allowed to determine the structural features of the starting material, through the determination of the potassium cations location and coordination numbers, the positioning and quantification of the water molecules and their interactions with framework oxygen atoms. These insights are fundamental for a better understanding of the activation process. The precursor of the acidic form was then prepared by ND_4^+ ion exchange and the presence of ammonium ions replacing two of the three cationic sites was detected by Rietveld neutron diffraction refinements. The calcination to produce the acid L zeolite induced remarkable effects on the framework geometry, associated to variations of the T1-O2-T1 and T2-O5-T2 angles and, as a consequence, distortions of the 8MR. The very wide angle changes provided a rational for the presence of Brønsted acid sites, one (D1) located on O5 and another (D2) located on O1. The Atomic Displacement Parameters of Brønsted acid sites highlighted a wider mobility of D2 with respect to D1, in very good agreement with the computational modeling. Besides, the number of charge-compensating protons is in good agreement with the total amount of Al^{+3} determined through the refinement of the tetrahedral occupancies.

In situ time-resolved powder diffraction allowed a careful investigation of the response to heating of acidic L zeolite (*System 5*). The crystallinity is maintained unchanged up the maximum temperature reached (810°C) but, notwithstanding this, thermal pathways suggested important deformations of the channel apertures. The latters are mainly due to the variation of the position of the O5 framework oxygen atom at temperature higher than 550 °C, thus suggesting the progressive conversions from Brønsted to Lewis site upon heating. The existence of Brønsted/Lewis acid synergy was supported by the occurrence of continuous changes in the channels system geometry as well as by a pronounced increase of specific tetrahedral distances, highlighting tetrahedral bond breaking and Lewis sites formation. Hence, *in situ* synchrotron X-ray diffraction data supported valid evidences of the high thermal stability of the acidic L zeolite as well as of the flexible behaviour of the framework during the Brønsted to Lewis acid sites formation. The Brønsted/Lewis acid synergy model presented here could be useful for studying the mechanism of numerous hydrocarbon reactions occurring in dealuminated zeolites.

Adsorption, synchrotron and neutron data allowed a careful examination of the as-synthesized L zeolite sorption capacity towards the L-lysine amino acid (*System 6*). The Rietveld refinement demonstrated the efficiency of the material in L-lysine embedding and confinement in zeolite cavities. The analysis of the host-guest interactions suggested that the aminoacid is stabilized within the zeolite framework through hydrogen bonds occurring between carboxyl groups of the L-lysine, water molecules and framework oxygen atoms.

The effects of the thermal activation in acidic zeolite was also deeply investigated in the large pore omega zeolite by a combined neutron and *in-situ* synchrotron X-ray powder diffraction analysis (*System 7*). Synchrotron Rietveld refinements allowed to monitor in real time conditions the evolution of structural features during the thermal activation of NH_4^+ precursor of the acidic omega zeolite as well as the effects of TMA and NH_4^+ degradation. The temperature increase is accompanied by relevant variations of the zeolite structural features, in particular about the T-O-T angles, which are addressed by the formation of Brønsted acid sites on the O5 and O2 framework oxygen atoms. Neutron Rietveld refinement highlights clearly the presence of two proton sites (D1 and D2, respectively) on both O5 and O2 framework oxygen atoms and pointing towards the centre of the 12MR and 6MR channels, respectively. The final framework geometry changes (in terms of both O-D and T-O-T angles) are localized not only to T1-O2-T1 and T2-O5-T2 bond angles, but are shared to the T1-O1-T1 bond angle, due to the strong interaction of D2 with O1. The neutron Rietveld refinement highlighted the presence of a ‘‘tube’’ of water molecules strongly interacting with D1 Brønsted site contributing to both the T2-O5-T2 angle narrowing and the O5-D1 refined bond length. All these results suggest that the geometry of Brønsted sites (elongation of the O-D bond and, consequently, the resulting acidity) is a combination of short- and long-range interactions.

Finally, the role of Lewis site was investigated in Ga-loaded zeolites due to their excellent performances in catalysis and newest applications concerning the removal of NOx from gas streams of exhaust engine and the conversion of biomass into biofuels and bio-based chemicals (*System 8*). Specifically, the investigation of the structural features of gallium-exchanged L, mordenite and ferrierite zeolites allowed to elucidate the nature of the gallium active sites combining X-ray powder diffraction, X-ray absorption spectroscopy and adsorption study. Rietveld structure refinements led to locate Ga^{+3} cations in framework and non-framework positions as well as determine the presence of water molecules completing the extraframework Ga^{+3} coordination. The presence of gallium in framework positions was firstly highlighted by the elongation of tetrahedral bond distances and narrowing of intertetrahedral T-O-T angles and then corroborated by XAS analysis, which shows that the average bond lengths derived from the analysis of the first-shell are longer than the <T-O> distances expected in presence of $Si^{4+}$and Al^{3+} as framework cations.

In conclusion, the results obtained in this work represent an effort for combining the structure microporous selection and utilization, starting from a deep investigation of their features, including chemical compositions, thermal stabilities, activation and behaviour in operative conditions. Neutron and synchrotron powder diffraction have been powerful tools for the

determination of cation-exchange capacity, thermal stability, adsorption properties and acidity, thus helping in designing and selecting the best microporous candidates in commercial applications. The rational selection of pore materials with the appropriate rigidity/flexibility offer a unique opportunity to combine the catalytic and adsorption properties of important zeolites in industrial applications.

Bibliography

Agostini G., Lamberti C., Palin L., Milanesio M., Danilina N., Xu B., Janousch M. and Van Bokhoven J.A., (2009). J. Am. Chem. Soc., 132(2), 667.

Akatsuka M., Yoshida T., Yamamoto N., Yamamoto M., Ogawa S. and Yagi S., (2016). J. Phys. Conf. Ser., 712(1), 012056.

Alberti A. and Martucci A., (2010). J. Phys. Chem. C, 114(17), 7767.

Alberti A., Martucci A., Sacerdoti M., Quartieri S., Vezzalini G., Ciambelli P. Rapacciuolo M., (1999). In M.M.J. Treacy, B.K. Marcus, M.E. Bisher, J.B. Higgins, Proc. 12th Int. Zeolite Conf., Materials Research Soc. Warrendale, Pennsylvania, 2345.

Alberti A. and Sabelli C., (1987). Z. Krist-Cryst. Mater., 178(1-4), 249.

Alberti A., Davoli P. and Vezzalini G., (1986). Z. Krist-Cryst. Mater., 175(1-4), 249.

Allen M. and Tildesley D., (1987). Computer simulation of liquids. Clarendon Press, Oxford.

Altomare A., Cuocci G., Giacovazzo C., Moliterni A., Rizzi R., Corriero N. and Falcicchio A., (2013). J. Appl. Crystallogr., 46, 1231.

Anasthas H.M. and Gaikar V.G., (2001). React. Funct. Polym., 47(1), 23.

Anderson M.A., (2000). Environ. Sci. Technol., 34, 725.

Angel R.J., Alvaro M. and Gonzalez-Platas J., (2014). Z. Krist-Cryst. Mater., 229(5), 405.

Ardit M., Martucci A., Pasti L., Rodeghero E., Beltrami G. and Cruciani G., (2018). J. Phys. Chem. C, 12(13), 7249.

Ardit M., Martucci A. and Cruciani G., (2015). J. Phys. Chem. C, 119(13), 7351.

Arletti R., Cruciani G. and Ferraris G., (2019). In: Gilmore C. J., Kaduk J. A. and Schenk H. (Eds.), International Tables for Crystallography H, chapter 7.14, Section 7.14.2, 886.

Arletti R., Fois E., Gigli L., Vezzalini G., Quartieri S. and Tabacchi G., (2017). Angew. Chem. Int. Edit., 56(8), 2105.

Arletti R., Martucci A., Alberti A., Pasti L., Nassi M. and Bagatin R., (2012). J. Solid State Chem., 194, 135.

Arletti R., Galli E., Vezzalini G., Wise W. S., (2005). Am. Mineral., 90(7), 1186.

Armbruster T., Stolz J. and Hennessy B., (2000). Z. Krist-Cryst. Mater., 215(5), 278.

Artioli G. and Kvick Å., (1990). Eur. J. Mineral., 749.

Ausavasukhi A., Sooknoi T. and Resasco D.E., (2009). J. Catal., 268(1) 68.

Bacakova L., Vandrovcova M., Kopova I. and Jirka I., (2018). Biomater. Sci., 6(5), 974.

Baerlocher C. and McCusker, L.B., (2017). Database of zeolite structures, http://www.izastructure.org/databases/.

Baerlocher C., McCusker L.B. and Olson D.H., (2007). Atlas of Zeolite Framework Types, 6th rev. ed., Elsevier, Amsterdam.

Ban S., van Laak A.N.C., Landers J., Neimark A.V., de Jongh P.E., de Jong K.P. and Vlugt T.J.H., (2010). J. Phys. Chem. C, 114(5), 2056.

Barrer R.M. and Villiger H., (1969a). Z. Krist-Cryst. Mater., 128(1-6), 352.

Barrer R.M., Villiger H., (1969b). J. Chem. Soc., Chem. Commun., 12, 659.

Bastiani R., Lam Y.L., Henriques C.A. and da Silva V.T., (2013). Fuel, 107, 680.

Batamack P., Dorémieux-Morin C., Vincent R. and Fraissard J., (1993). J. Phys. Chem., 97(38), 9779.

Bein T. and Mintova S., (2005). Stud. Surf. Sci. Catal., 157, 263.

Bellussi G., Carati A., Rizzo C. and Millini R., (2013). Catal. Sci. Technol., 3, 833.

Beltrami G., Chenet T., Pasti L., Gigli L., Pollastri S. and Martucci A., (2019). Catal. Today, *in press*, https://doi.org/10.1016/j.cattod.2019.09.016.

Benco Ľ., Demuth T., Hafner J. and Hutschka F., (2000). Chem. Phys. Lett., 324(5-6), 373.

Bhan A. and Nicholas Delgass W., (2008a). Cataly. Rev., 50(1), 19.

Bhan A. and Iglesia E.A, (2008b). Accounts Chem. Res., 41, 559.

Bhange D. and Ramaswamy V., (2006). Mater. Res. Bull., 41(7), 1392.

Bilderback D.H., Elleaume P. and Weckert E., (2005). J. Phys. B-At. Mol. Opt., 38, S773.

Biorgen M., Joensen F., Holm M.S., Olsbye U., Lillerud K-P. and Svelle S., (2008). Appl. Catal. A-Gen., 345, 43.

Blasioli S., Martucci A., Paul G., Gigli L., Cossi M., Johntson C.T., Marchese L. and Braschi I., (2014). J. Colloid Interf. Sci., 419, 148.

Bordiga S., Groppo E., Agostini G., van Bokhoven J.A. and Lamberti C., (2013). Chem. Rev, 113, 1736.

Bordiga S., Regli L., Lamberti C., Zecchina A., Bjørgen M. and Lillerud K.P., (2005). J. Phys. Chem. B, 109(16), 7724.

Borfecchia E., Gianolio D., Agostini G., Bordiga S. and Lamberti C., (2013). In: F. X. Llabrés I. Xamena, J. Gascón (Eds.), Metal Organic Frameworks as Heterogeneous Catalysts, RSC, Cambridge, 143.

Bourgeat-Lami E., Di Renzo F., Fajula F., Mutin P.H. and Des Courières T., (1992). J. Phys. Chem., 96, 3807.

Bowes E. and Wise J.J., (1971). US Pat. 3, 578.

Breck D.W. and Flanigen E.M., (1969). In R. Barrer (Ed.), Molecular Sieves, Society of Chemical Industry, 47.

Calzaferri G., (2012). Langmuir, 28 (15), 6216.

Calzaferri G., Huber S., Maas H. and Minkowski C., (2003). Angew. Chemie - Int. Ed., 42(32), 3732.

Cannillo E., Coda A. and Fagnani G., (1966). Acta Crystallogr., 20(2), 301.

Car R. and Parrinello M., (1985). Phys. Rev. Lett., 55, 2471.

Casci J.L., (1994). Stud. Surf. Sci. Catal., 85, 329.

Catizzone E., Migliori M., Purita A. and Giordano G., (2019). J. Energy Chem., 30, 162.

Chao K.J., Lin J.C., Wang Y. and Lee G.H., (1986). Zeolites, 6(1), 35.

Cheng S.L., Yan H.S. and Zhao C.Q., (2006). J. Chromatogr. A, 1108, 43.

Chester A.W. and Derouane E.G., (2009). Zeolite characterization and catalysis, New York, EUA, Springer, 360.

Chillemi G., D'Angelo P., Pavel N.V., Sanna N. and Barone V., (2002). J. Am. Chem. Soc., 124, 1968.

Ciambelli P., Sannino D., Palo E., Balboni E., Martucci A., Dalconi M.C. and Alberti A., (2008a). Stud. Surf. Sci. Catal., 174, 1039.

Ciambelli P., Sannino D., Palo E., Gargano G., Balboni E., Martucci A., Dalconi M.C. and Alberti A., (2008b). Il Nuovo Cimento, 123, 1583.

Cole J.F., Kouwenhoven H.W. (1973). In W. M. Uytterhoeven, J. B. Meier (Eds.), Molecular Sieves, Adv. Chem. Ser. 121, Am. Chem. Soc. Washington, 583.

Coombs D.S., Alberti A., Armbruster T., Artioli G., Colella C., Galli E., Grice J.D., Liebau F., Mandarino J.A., Minato H., Nickel E.H., Passaglia E., Peacor D.R., Quartieri S., Rinaldi S., Ross M., Sheppard R.A., Tillmanns E., (1998). Mineral. Mag, 62(4), 533.

Corma A., (1995). Chem. Rev., 95, 3559.

Cucinotta F., Guenet A., Bizzarri C., Mroz W., Botta C., Milian-Medina B., Gierschner J. and De Cola L., (2014). Chempluschem, 79(1), 45.

Cruciani G., (2006). J. Phys. Chem. Solids, 67(9-10), 1973.

Cruciani G., Martucci A. and Meneghini C., (2003). Eur. J. Mineral., 15(2), 257.

Csicsery S.M., (1976). Zeolites Chemistry and Catalysis. ACS Monograph 171, J. Am. Chem. Soc., Washington, D.C., 12, 695.

D'Angelo P. and Spezia R., (2012). Chem. Eur. J., 18, 11162.

Dalconi M.C, Alberti A., Cruciani G., Ciambelli P. and Fonda E., (2003). Micropor. Mesopor. Mat., 62(3), 191.

Davis M.E., Hathaway P.E. and Montes C., (1989). Zeolites, 9, 436.

Deer W.A., Howie R.A., Zussman, J., (2004). Rock-forming minerals. 4B: Framework silicates. Silica minerals, feldspathoids and the zeolites. Geo. Soc.

Degnan T.F., Chitnis J.K. and Schipper P.H., (2000). Micropor. Mesopor. Mat., 35-36, 245

Demuth T., Benco L., Hafner J. and Toulhoat H., (2001). J. Quantum Chem., 84(1), 110.

Di Cicco A., Aquilanti G., Minicucci M., Principi E., Novello N., Cognigni A. and Olivi L., (2009). J. Phys. Conf. Ser., 190(1) 012043.

Dosen A. and Marinkovic B.A., (2019). B. Mater. Sci., 42(3), 86.

Dusselier M. and Davis M.E., (2018). Chem. Rev., 118(11), 5265.

Dwyer J. and Jo'Malley P., (1988). Stu. Surf. Sci. Catal., 35, 5.

Egami T. and Billinge S.J.L., (2012). Underneath the Bragg Peaks: Structural Analysis of Complex Materials, Elsevier Science, Oxford.

Eichler U., Brandle M. and Sauer J., (1997). J. Phys. Chem. B, 101, 10035.

Fang Y., Su X., Bai X., Wu W., Wang G., Xiao L and Yu A., (2017). J. Energy Chem., 26(4), 768.

Fantini R., Arletti R., Pastero L., Quartieri S., Di Renzo F., Camara F. and Vezzalini G., (2018). Eur. J. Mineral., 30(3), 515.

Fajula F., Ibarra R., Figueras F. and Gueguen C., (1984). J. Catal., 89, 60.

Fei Y., (1995). In Mineral physics & crystallography: A handbook physical constants; Ahrens, T., Ed.; AGU: Washington, DC.

Fejes P., Nagy J.B., Halász J. and Oszkó A., (1998). Appl. Catal. A-Gen, 175(1-2), 89.

Flanigen E.M., (2001). Stud. Surf. Sci. Catal., 137, 11.

Flanigen E.M. and Kellberg E.R., (1980). U.S. Patent 4, 241, 036.

Flanigen E.M., (1968) Neth. Pat. 6, 710.

Fois E., Tabacchi G., Devaux A., Belser P., Brühwiler D. and Calzaferri G., (2013). Langmuir, 29(29), 9188..

Fois E., Tabacchi G. and Calzaferri G., (2012). J. Phys. Chem. C 116(31), 16784.

Fois E., Tabacchi G. and Calzaferri G., (2010). J. Phys. Chem. C, 114(23), 10572.

Frenkel A.I., Rodriguez J.A. and Chen J.G., (2012). ACS Catal., 2, 2269.

Fricke R., Kosslick H., Lischke G. and Richter M., (2000). Chem. Rev., 100(6), 2303.

Frusteri F., Bonura G., Cannilla C., Drago Ferrante G., Aloise A. Catizzone E., Migliori M. Giordano, G., (2016). Appl. Catal. B-Environ., 176-177, 522.

Gagné O.C. and Hawthorne F.C., (2018). Acta Crystallogr. B, 74(1), 63.

Galli E., Passaglia E., Pongiluppi D., Rinaldi R., (1974). Contrib. Mineral. Petr., 45(2), 99.

Ganji M.D., (2009). Diam. Relat. Mater., 18(4), 662.

Gao Q., Xu W.J., Xu Y., Wu D., Sun Y.H., Deng F. and Shen W., (2008). J. Phys. Chem. B, 112, 2261.

Garino C., Borfecchia E., Gobetto R., van Bokhoven J. A. and Lamberti C., (2014). Coordin. Chem. Rev., 277, 130.

Gartzia-Rivero L., Bañuelos J. and López-Arbeloa I., (2017). Materials (Basel), 10(5), 495.

Gatta G.D. and Lotti P. (2019). In Modified Clay and Zeolite Nanocomposite Materials, chapter 1, 1.

Gigli L., Arletti R., Tabacchi G., Fabbiani M., Vitillo J.G., Martra G., Devaux A., Miletto I., Quartieri S., Calzaferri G. and Fois E. (2018a). J. Phys. Chem. C, 122(6), 3401.

Gigli L., Arletti R., Fois E., Tabacchi G., Quartieri S., Dmitriev V. and Vezzalini G. (2018b). Crystals, 8(2), 79.

Gigli L., Arletti R., Tabacchi G., Fois E., Vitillo J. G., Martra G., Agostini G, Quartieri S. and Vezzalini G., (2014). J. Phys. Chem. C, 118(29), 15732.

Gigli L., Arletti R., Quartieri S., Di Renzo F. and Vezzalini G., (2013). Micropor. Mesopor. Mat., 177, 8.

Gottardi G. and Galli E., (1985) Natural Zeolites, Minerals and Rocks Series, Berlin, Heidelberg, New York, Tokyo: Springer-Verlag, 18, 49.

Gramlich-Meier R., Gramlich V. and Meier W.M., (1985). Am. Mineral., 70(5-6), 619.

Grau-Crespo R., Peralta A.G., Ruiz-Salvador A.R., Gomez A. and Lopez-Cordero R., (2000). Phys. Chem. Chem. Phys., 2, 5716.

Grunwaldt J.D., Wagner J.B. and Dunin-Borkowski R.E., (2013). ChemCatChem, 5, 62.

Gualtieri A.F. and Passaglia E., (2006). Eur. J. Mineral., 18(3), 351.

Gualtieri A.F., (2000). Acta Crystall. B-Stru., 56(4), 584.

Guzzinati R., Sarti E., Catani M., Costa V., Pagnoni A., Martucci A., Rodeghero E., Capitani D., Pietrantonio M., Cavazzini A. and Pasti L., (2018). ChemPhysChem, 19(17), 2208.

Hendsbee A.D., Pye C.C. and Masuda J.D., (2009). Acta Crystall., E65(8), i65.

Hodeau J. L. and Guinebretiere R., (2007). Appl. Phys. A-Mater., 89, 813.

Hodeau J.L., Bordet P., Anne M., Prat A., Fitch A.N., Dooryhee E., Vaughan G. and Freund, A.K., (1998). P. Soc. Photo-Opt. Ins., 3448, 353.

https://chemicalize.com/app/calculation/lysine.

https://pubchem.ncbi.nml.nih.gov/compound/Lysine, National Center for Biotechnology Information. PubChem Database, Lysine, CID=5962

http://www.ba.ic.cnr.it/softwareic/expo/geometry-optimization.

Hunger H., in Cejka J., Corma A., Zones S. (Eds.), (2010). Zeolites and Catalysis: Synthesis, Reactions and Applications; Wiley-VCH, Weinheim, 493.

Hunger M., Freude D. and Pfeifer H., (1991). J. Chem. Soc., Faraday Trans., 87(4), 657.

Ihs A., Liedberg B., Udval K., Törnkvist C., Bodö P. and Lundstörm I., (1990). J. Colloid Interf. Sci., 140, 192.

Jacobs P.A. and Mortier W.J., (1982). Zeolites, 2, 226.

Jones A.J. and Iglesia E., (2015). Acs Catal., 5(10), 5741.

Joshi Y.V. and Thomson K.T., (2005). Catal. Today, 105(1), 106.

Kamiya N., Oshiro T., Tan S., Nishi K. and Yokomori Y., (2013). Micropor. Mesopor. Mat., 169, 168.

Kamiya N., Iwama W., Kudo T., Nasuno T., Fujiyama S., Nishi K. and Yokomori Y., (2011). Acta Crystall. B-Stru., 67(6), 508.

Kanazirev V., Mavrodinova V., Kosova L. and Price G.L., (1991). Catal. Let., 9(1-2), 35.

Kassab E., Seiti K. and Allavena M., (1998). J. Phys. Chem. C, 92, 6705.

Katada N., Suzuki K., Noda T., Sastre G. and Niwa M., (2009). J. Phys. Chem. C, 113(44), 19208.

Kerr G.T., (1989). Zeolites, 9, 350.

Klein H., Fuess H., Ernst K. and Weitkamps J., (1994). Micropor. Mesopor. Mat., 3, 291.

Klik R., Bosacek V. and Kubelkova L., (1997). Zeolites, 19, 343.

Kokotailo G.T., Lawton S.L, Olson D.H. and Meier W.M., (1978). Nature, 272(5652), 272.

Kralik M., (2014). Chem. Pap., 68(12), 1625.

Krohn J.E. and Tsapatsis M., (2005). Langmuir, 21(19), 8743.

Lacasta S., Sebastian V., Casado C., Mayoral A., Romero P., Larrea A., Vispe E., Lopez-Ram-de-Viu P., Uriel S. and Coronas J., (2011). Chem. Mater., 23, 1280.

Larson A.C. and van Dreele R.B., (1994). GSAS-Generalized structure analysis system. Los Alamos National Laboratory Report LA-UR, 86-748, 1.

Leardini L., Martucci A., Braschi I., Blasioli S. and Quartieri S., (2014). Mineral. Mag., 78(5), 1141.

Leardini L., Martucci A., Alberti A. and Cruciani G., (2013). Micropor. Mesopor. Mat., 167, 117.

Lee Y., Kim S.J., Ahn D.C. and Shin N.S., (2007). Chem. Mater., 19(9), 2277.

Lermer H., Draeger M., Steffen J. and Unger K.K., (1985). Zeolites, 5(3), 131.

Li H. and Li P., (2018). Chem. Commun., 54(99), 13884.

Li Y., Li L. and Yu J., (2017). Chem, 3(6), 928.

Li S., Zheng A., Yongchao S., Zhang H., Chen L., Yang J., Ye C. and Deng F., (2007). J. Am. Chem. Soc., 129(36), 11161.

Li S.J., Zheng C. and Lobringn K.C., (2003). Z. Krist.-New Cryst. St., 218(JG), 11.

Liebau F., (1985). Structural Chemistry of Silicates: Structure, Bonding and Classification, Springer-Verlag, Berlin.

Liedberg B., Lundstörm I., Wu C.R. and Salaneck W.R., (1985). J. Colloid Interf. Sci., 108, 123.

Liu R., Rahman M.M., Sarker M., Chai M., Li C. and Cai J., (2020). Fuel Process. Technol., 201, 106319.

Liu R., Zhu H., WU Z., Qin Z., Fan W. and Wang J., (2015). J. Fuel Chem. Tech., 43(8), 961.

Liu D., Bhan A., Tsapastis M., Al Hashimi S., (2011). ACS Catal., 1(1), 7.

Lo B.T.W., Ye L. and Tsang S.C.E., (2018). Chem., 4(8), 1778.

Loewenstein W., (1954). Am. Minerl., 39, 92.

Lukyanov D.B., Vazhnova T., Cherkasov N., Casci J.L. and Birtill, J.J., (2014). J. Phys. Chem. C, 118(41), 23918.

Martucci A., Rodeghero E. and Cruciani G., (2016). Eur. J. Mineral., 28(1), 5.

Martucci A., Rodeghero E., Pasti L., Bosi V. and Cruciani G., (2015). Micropor. Mesopor. Mat., 215, 175.

Martucci A., Leardini L., Nassi M., Sarti E., Bagatin R. and Pasti L., (2014). Mineral. Mag., 78(5), 1161.

Martucci A., Cremonini M.A., Blasioli S., Gigli L., Gatti G., Marchese L. and Braschi I., (2013). Micropor. Mesopor. Mat., 170, 274.

Martucci A., Pasti L., Nassi M., Alberti A., Arletti R., Bagatin R., Vignola R. and Sticca R., (2012). Micropor. Mesopor. Mat., 151, 358.

Martucci A., Parodi I., Simoncic P., Armbruster T. and Alberti A., (2009). Micropor. Mesopor. Mat., 123(1-3), 15.

Martucci A., Alberti A., Cruciani G., Frache A., Marchese L. and Pastore H. O., (2005). J. Phys. Chem. B, 109(28), 13483.

Martucci A., Alberti A., Guzman-Castillo M. L., Di Renzo F. and Fajula F., (2003). Micropor. Mesopor. Mat., 63(1-3), 33.

Martucci A., Alberti A., Sacerdoti M., Vezzalini G., Ciambelli P. and Rapacciuolo M., (2000a). In Colella C., Mumpton F.A. (Eds.), Natural Zeolites for the Third Millenium, 45.

Martucci A., Cruciani G., Alberti A., Ritter C., Ciambelli P. and Rapacciuolo M., (2000b). Micropor. Mesopor. Mat., 35, 405.

Martucci A., Alberti A., Cruciani G., Radaelli P., Ciambelli P. and Rapacciulo M., (1999). Micropor. Mesopor. Mat., 30(1), 95.

Marx D. and Hutter J., (2009). Ab initio molecular dynamics: basic theory and advanced methods. Cambridge University Press.

Mavrodinova V., Minchev C., Penchev V. and Lechert H., (1985). Zeolites, 5(4), 217.

McCusker L.B. and Baerlocher C., (2001). In: van H. Bekkum, E. M. Flanigen, P. A. Jacobs, J. C. Jansen, Elsevier. Introduction to zeolite science and practice, chapter 3, 37.

Meier W.M., Olson D.H., (1968) Zeolite structures, Proc. Conf. on Molecular Sieves, Soc. Chem. Ind., London, 10.

Meier W.M., (1961). Z. Krist-Cryst. Mater., 115(1-6), 439.

Meneghinello E., Alberti A., Cruciani G., Sacerdoti M., Intyre G. M., Ciambelli P. and Rapacciuolo M.T., (2000). Eur. J. Mineral., 12(6), 1123.

Meng M., Stievano L., Lambert J.F., (2004). Langmuir, 20, 914.

Mentzen B.F. and Sacerdote-Peronnet M., (1993). Mater. Res. Bull., 28, 1017.

Migliorati V., Mancini G., Chillemi G., Zitolo A. and D'Angelo P., (2011). J. Phys. Chem. A, 115, 4798.

Migliori M., Catizzone E., Aloise A. and Giordano G., (2014). Ind. Eng. Chem. Res., 53(38), 14885.

Mihaleva V.V., Van Santen R.A. and Jansen A.P.J., (2004). J. Chem. Phys., 120(19), 9212.

Milanesio M., Artioli G., Gualtieri A.F., Palin L. and Lamberti C., (2003). J. Am. Chem. Soc., 125(47), 14549.

Moliner M., Martinez C. and Corma A., (2015). Angew. Chem. Int. Edit., 54(12), 3560.

Mortier W.J.J., Pluth J. and Smith J.V., (1976). Mater. Res. Bull., 11(1), 15.

Moshoeshoe M., Nadiye-Tabbiruka M.S. and Obuseng V., (2017). Am. J. Mater. Sci., 7(5), 196.

Munsch S., Hartmann M. and Ernst S., (2001). Chem. Commun., 19, 1978.

Nash M.J., Shough A.M., Fickel D.W., Doren D.J., Lobo R.F., (2008). J. Am. Chem. Soc., 130(8), 2460.

Newsam J.M., (1987). J. Chem. Soc., Chem. Commun., 2, 123.

Newsam J.M., (1986). Science, 231, 1093.

Newville M., (2001). J. Synchrotron Radiat., 8, 322.

Nishi K., Hidaka A. and Yokomori Y., (2005). Acta Crystall., 61(2), 160.

Nishi K., Shimizu K., Takamatsu M., Yoshida H., Satsuma A., Tanaka T., Yoshida S. and Hattori T., (1998). J. Phys. Chem. B, 102(50), 10190.

Norby P., (1997). J. Appl. Crystallogr., 30(1), 21.

Olson D.H., Kokotailo G.T., Lawton S.L. and Meier W.M., (1981). J. Phys. Chem., 85(15), 2238.

Parodi I., supervisor: Martucci A., (2006-2008). Structural characterization of zeolitic catalysts in non-ambient conditions by X-ray and neutron diffraction, PhD thesis.

Parr R.G. and Yang W., (1989). Density-functional theory of atoms and molecules. Oxford University Press, New York, Oxford.

Pasti L., Rodeghero E., Beltrami G., Ardit M., Sarti E., Chenet T., Stevanin C. and Martucci A., (2018). Minerals, 8, 80.

Pasti L., Rodeghero E., Sarti E., Bosi V., Cavazzini A., Bagatin R. and Martucci A., (2016). RSC Adv., 6(59), 54544.

Perego C., Bagatin R., Tagliabue M. and Vignola R. (2013). Micropor. Mesopor. Mat., 166, 37.

Perrotta J., Kibby C., Mitchell B.R. and Tucci E.R. (1978). J. Catal., 55(2) 240.

Petushkov A., Freeman J. and Larsen S.C., (2010). Langmuir, 26(9), 6695.

Poinsot V., Gavard P., Feurer B. and Couderc F., (2010). Electrophoresis, 31, 105.

Polikarpov M., Snigireva I. and Snigirev A., (2014). J. Synchrotron Radiat., 21(3), 484.

Price G.D., Pluth J.J., Smith J.V., Bennett J.M. and Patton, R.L., (1982). J. Am. Chem. Soc., 104(22), 5971.

Primo A. and Garcia H., (2014). Chem. Soc. Rev., 43(22), 7548.

Rabo J.A. and Schoonover M.W., (2001). Appl. Catal. A-Gen., 222, 261.

Rabo J.A and Gajda G.J., (1990), In: D. Barthomeuf, E.G. Derouane, W. Hoelderich (Eds.), Guidelines for mastering the properties of molecular sieves, Plenum, New York, Ser. B, vol. 221.

Ravel B. and Newville M., (2005). J. Synchrotron Radiat., 12, 537.

Reck G., Marlow F., Kornatowski J., Hill W. and Caro J., (1996). J. Phys. Chem., 100, 1698.

Remler D. and Madden P., (1990). Mol. Phys., 70, 921.

Rietveld H.M.J., (1969). Applied Crystallography, 2, 69.

Rinaldi R., Pluth J.J. and Smith J.V., (1975). Acta Crystallogr. B, 31(6), 1603.

Rodante F. and Marrosu G., (1990). Thermochim. Acta, 171, 15.

Rodeghero E., Chenet T., Martucci A., Ardit M., Sarti E. and Pasti L., (2019). Catal. Today, https://doi.org/10.1016/j.cattod.2019.09.015.

Rodeghero E., Pasti L., Sarti E., Cruciani G., Bagatin R. and Martucci A., (2017a). Minerals, 7(3), 34.

Rodeghero E., Martucci A. Cruciani G., Sarti E., Cavazzini A., Costa V., Bagatin R. and Pasti L., (2017b). J. Phys. Chem. C, 121(33), 17958.

Rodeghero E., Martucci A., Cruciani G., Bagatin R., Sarti E., Bosi V. and Pasti L., (2016). Catal. Today, 277, 118.

Rostamizadeh M. and Taeb A., (2015). J. Ind. Eng. Chem., 27, 297.

Roth W.J., Nachtigall P., Morris R.E. and Cejka J., (2014). Chem. Rev., 114(9), 4807.

Saadi R., Saadi Z., Fazaeli R. and Fard N.E., (2015). Korean J. Chem. Eng., 32(5), 787.

Saikia M.D., (2008). Colloid Surface A, 329, 177.

Sani A. and Cruciani G., (2002). Phys. Chem. Miner., 29(5), 351.

Sani A., Vezzalini G., Ciambelli P. and Rapacciuolo M.T., (1999). Micropor. Mesopor. Mat., 31(3), 263.

Sarti E., Chenet T., Pasti L., Cavazzini A., Rodeghero E. and Martucci A., (2017). Minerals, 7(2), 22.

Sastre G., Lewis D.W. and Corma A., (2000). Phys. Chem. Chem. Phys., 2(1), 177.

Sauer J., Ugliengo P., Garrone E. and Saunders V.R., (1994). Chem. Rev., 94, 2095.

Sauer J., (1989). Chem. Rev., 89(1), 199.

Sears V.F., (1992). Neutron news, 3(3), 26.

Sen S., Wusirika R.R. and Youngman R.E., (2006). Micropor. Mesopor. Mat., 87(3), 217.

Senchenya I.N., Kazanskii V.B. and Beran S., (1986). J. Phys. Chem., 90(20), 4857.

Shamzhy M., Opanasenko M., Concepción P. and Martínez A., (2019). Chem. Soc. Rev., 48, 1095.

Shannon R.D., (1976). Acta Crystallogr., A32, 751.

Simoncic P., Armbruster T. and Pattison P., (2004). J. Phys. Chem. B, 108, 17352.

Simonin J.P., (2016). Chem. Eng. J., 300, 254.

Solinas V., Monaci R., Marongiu B. and Forni L., (1983). Appl. Catal., 5, 171.

Stuckenschmidt E., Joswig W. and Baur W.H., (1996). Eur. J. Mineral., 8, 85.

Sugi Y. and Ajayan V., (2015). Catal. Surv. Asia, 19, 188.

Szostak R., (1992). Handbook of Molecular Sieves, New York: Van Nostrand Reihold.

Szostak R., (1989). Molecular sieves. New York: Van Nostrand Reihold.

Tabacchi G. (2018). ChemPhysChem, 19(11), 1249.

Tabacchi G., Calzaferri G. and Fois E., (2016). Chem. Comm., 52(75), 11195-11198.

Tabacchi G., Fois E. and Calzaferri G., (2015). Angew. Chem. Int. Edit., 54(38), 11112.

Terrab I., Boukoussa B., Hamacha R., Bouchida N., Roy R., Bengueddach A. and Azzouz A., (2016). Thermochim. Acta, 624, 95.

Titus E., Kalkar A.K. and Gaikar V.G., (2003). Colloid Surface A, 223(1-3), 55.

Toby B.H., (2001). J. Appl. Crystallogr., 34(2), 210.

Trudu F., Tabacchi G. and Fois E., (2019). Am. Mineral., 104(11), 1546.

Tsitsishvili G.V., Andronikashvili T.G., Kirov G.N., Filizova L.D., (1992). Natural Zeolites Ellis Horwood, Chichester.

Uguina M.a., Sotelo J.L. and Serrano D.P., (1991), Appl. Catal., 76(2), 183.

Uslamin E.A., Luna-Murillo B., Kosinov N., Bruijnincx P.C., Pidko E.A., Weckhuysen B.M. and Hensen E.J.M., (2019). Chem. Eng. Sci., 198, 305.

Van Koningsveld H., (1998). J. Mol. Catal. A-Chem., 134(1-3), 89.

Van Koningsveld H. and Jansen J.C., (1996). Micropor. Mesopor. Mat., 6, 159.

Van Koningsveld H., Jansen J. C. and van Bekkum H., (1990). Zeolites, 10(4), 235.

Van Koningsveld H., Tuinstra F., van Bekkum H. and Jansen J.C., (1989a). Acta Crystallogr., 45(4), 423.

Van Koningsveld H. and Tuinstra F., (1989b). Zeolites, 9, 253.

Van Koningsveld H., van Bekkum H. and Jansen J.C., (1987). Acta Crystallogr. B, 43(2), 127.

Van Santen R.A. and Kramer G.J., (1995). Chem. Rev., 95(3), 637.

Van Speybroeck V., Hemelsoet K., Joos L., Waroquier M., Bell R.G. and Catlow C.R.A., (2015). Chem. Soc. Rev., 44(20), 7044.

Vaughan P.A., (1966). Acta Crystallogr., 21(6), 983.

Vener M.V., Rozanska X. and Sauer J., (2009). Phys. Chem. Chem. Phys, 11(11), 1702.

Vezzalini G., Quartieri S., Galli E., Alberti A., Cruciani G. and Kvik Å., (1997). Zeolites, 19, 323.

Wakabayashi F., Kondo J.N., Domen K. and Hirose C., (1996). J. Phys. Chem., 100(5), 1442.

Wang A., Austin D., Karmakar A., Bernard G.M., Michaelis V.K., Yung M.M., Zeng H. and Song H., (2017). ACS Catal., 7(5), 3681.

Wang X., Hanson J.C., Szanyi J. and Rodriguez J.A., (2004). J. Phys. Chem. B, 108, 16613.

Wijntje R., Bosch H., de Haan A.B. and Bussmann P.J.T., (2007). J. Chromatogr. A, 1142, 39.

Woodtli P., Giger S., Müller P., Sägesser L., Zucchetto N., Reber M.J., Ecker A. and Brühwiler D., (2018). Dye. Pigment. 149, 456.

Wragg D.S., Morris R.E. and Burton A.W., (2008). Chem. Mater., 20, 1561.

Wright J.P., Vaughan G.B. and Fitch A.N., (2003). Commission on Crystallographic Computing, 92.

Wu R. and McMahon T.B., 2008. Chem. Phys. Chem., 9(18), 2826.

www.cpmd.org

Xinzhe J. (2013). In: J. Xinzhe (Ed.), Novinka. Neutron diffraction principles, instrumentation and applications, chapter 1, 1.

Xu W.Q., Yiu Y.G., Suib S.C., Edwards J.C. and O'Young C.L., (1995). J. Phys. Chem., 99, 9443.

Yamazaki T., Nishimura H. and Ozawa S., (2000). Micropor. Mesopor. Mat., 38, 187.

Yao D., Wang S., Li P. and Li H., (2019). J. Lumin., 215.

Yogo K., Tanaka S., Ihara M., Hishiki T. and Kikuchi E., (1992). Chem. Lett., 21(6) 1025.

Yokomori Y. and Idaka S., (1999). Micropor. Mesopor. Mat., 28(3), 405.

You Y., Chen S., Li J., Zeng J., Chang H., Ma L. and Li J., (2020). J. Hazard. Mater., 383, 121117.

Young R.A., (1995). The Rietveld method, Oxford University Press, New York.

Yu X., Liu B. and Zhang Y., (2019). Heliyon, 5(5), e01640.

Zaarour M., El Siblani H., Arnault N., Boullay P. and Mintova S., (2019). Materials (Basel), 12(17), 2830.

Zhang J., Zhang H., Yang X., Huang Z. and Cao W., (2011). J. Nat. Gas Chem., 20, 266.

Zheng Z.X., Lin J.M. and Qu F., (2003). J. Chromatogr. A, 1007, 189.

Zhou X., Wesolowski T.A., Tabacchi G., Fois E., Calzaferri G. and Devaux A., (2013). Phys. Chem. Chem. Phys. 15(1), 159.

Appendix 1

Framework atomic coordinates, fraction and Atomic Displacement Parameters at room temperature of 423_AS-ZSM-5, 425_AS-ZSM-5, 422_AS-ZSM-5 and 424_AS-ZSM-5 are reported in Table A, B, C and D, respectively.

Room temperature atomic coordinates, fraction and Atomic Displacement Parameters of extraframework TPA^+ template are reported in Table E.

Framework atomic coordinates, fraction and Atomic Displacement Parameters of 423_AS-ZSM-5 at 200, 400, 600 and 800 °C are reported in Table F, G, H and I, respectively. For 425_AS-ZSM-5 are reported in Table J, K, L and M, respectively. For 422_AS-ZSM-5 are reported in Table N, O, P and Q, respectively. For 424_AS-ZSM-5 are reported in Table R, S, T and U, respectively.

T-O bond distances and T-O-T angles of 423_AS-ZSM-5, 425_AS-ZSM-5, 422_AS-ZSM-5 and 424_AS-ZSM-5 at room temperature, 200, 400, 600 and 800 °C are reported in Table V, W, X and Y, respectively.

T-O-T angles of the 423_AS-ZSM-5, 425_AS-ZSM-5, 422_AS-ZSM-5 and 424_AS-ZSM-5 at room temperature are reported in Figure A.

The evolution of the C.F.A values at high temperature for samples 423, 425, 422 and 424_AS-ZSM-5 is reported in Figure B1, B2, B3 and B4, respectively.

Table A

423_AS-ZSM-5, room temperature

Site	x/a	y/b	z/c	Fraction	Ui/Ue*100
T1	0.4228(10)	0.0565(11)	-0.3371(21)	1.0	0.2(1)
T2	0.3108(14)	0.0302(10)	-0.1877(24)	1.0	0.2(1)
T3	0.2823(10)	0.0597(13)	0.0333(21)	1.0	0.2(1)
T4	0.1243(10)	0.0660(12)	0.0279(21)	1.0	0.2(1)
T5	0.0722(12)	0.0286(12)	-0.1846(22)	1.0	0.2(1)
T6	-0.1846(22)	0.0620(15)	-0.3202(24)	1.0	0.2(1)
T7	0.4229(12)	-0.1724(7)	-0.3231(21)	1.0	0.2(1)
T8	0.3069(15)	-0.1285(11)	-0.1863(26)	1.0	0.2(1)
T9	0.2718(12)	-0.1726(9)	0.0318(23)	1.0	0.2(1)
T10	0.1147(12)	-0.1752(9)	0.0271(27)	1.0	0.2(1)
T11	0.0693(15)	-0.1287(12)	-0.1868(29)	1.0	0.2(1)
T12	0.1851(14)	-0.1729(8)	-0.3210(28)	1.0	0.2(1)
O1	0.3716(17)	0.0627(16)	-0.2470(33)	1.0	0.5(1)
O2	0.3161(13)	0.0503(28)	-0.0732(25)	1.0	0.5(1)
O3	0.2034(8)	0.0620(17)	0.0204(28)	1.0	0.5(1)
O4	0.0932(15)	0.0621(27)	-0.0814(23)	1.0	0.5(1)
O5	0.1158(14)	0.0590(22)	-0.2727(27)	1.0	0.5(1)
O6	0.2426(16)	0.0571(30)	-0.2334(31)	1.0	0.5(1)
O7	0.3701(24)	-0.1640(18)	-0.2351(38)	1.0	0.5(1)
O8	0.3026(24)	-0.1473(23)	-0.0711(23)	1.0	0.5(1)

O9	0.1930(10)	-0.1624(36)	0.0304(42)	1.0	0.5(1)
O10	0.0881(21)	-0.1639(19)	-0.0838(23)	1.0	0.5(1)
O11	0.1132(18)	-0.1602(26)	-0.2738(27)	1.0	0.5(1)
O12	0.2410(23)	-0.1529(30)	-0.2420(43)	1.0	0.5(1)
O13	0.3139(31)	-0.0493(9)	-0.1980(46)	1.0	0.5(1)
O14	0.0836(18)	-0.0504(11)	-0.1790(55)	1.0	0.5(1)
O15	0.4221(18)	0.1243(10)	-0.3998(22)	1.0	0.5(1)
O16	0.4021(15)	-0.0046(13)	-0.4071(35)	1.0	0.5(1)
O17	0.3967(19)	-0.1346(13)	-0.4203(26)	1.0	0.5(1)
O18	0.1971(23)	0.1309(14)	-0.3785(23)	1.0	0.5(1)
O19	0.1979(21)	0.0011(15)	-0.3957(35)	1.0	0.5(1)
O20	0.1930(22)	-0.1284(14)	-0.4188(26)	1.0	0.5(1)
O21	-0.0044(11)	0.0436(20)	-0.2061(17)	1.0	0.5(1)
O22	-0.0077(15)	-0.1408(18)	-0.2104(27)	1.0	0.5(1)
O23	0.4325(24)	-1/2	-0.3471(33)	1.0	0.5(1)
O24	0.1927(33)	-1/2	-0.3494(54)	1.0	0.5(1)
O25	0.2885(36)	-1/2	0.0463(51)	1.0	0.5(1)
O26	0.0991(37)	-1/2	0.0611(40)	1.0	0.5(1)

Table B

425_AS-ZSM-5, room temperature

Site	x/a	y/b	z/c	Fraction	Ui/Ue*100
T1	0.4228(10)	0.0567(14)	-0.3394(33)	1.0	0.2(1)
T2	0.3105(17)	0.0302(11)	-0.1891(39)	1.0	0.2(1)
T3	0.2823(10)	0.0605(21)	0.0315 (35)	1.0	0.2(1)
T4	0.1240(11)	0.0658(15)	0.0256(30)	1.0	0.2(1)
T5	0.0717(13)	0.0281(24)	-0.1859(32)	1.0	0.2(1)
T6	0.1878(19)	0.0611(15)	-0.3222(40)	1.0	0.2(1)
T7	0.4224(14)	-0.1725(7)	-0.3244(27)	1.0	0.2(1)
T8	0.3067(19)	-0.1287(13)	-0.1860(43)	1.0	0.2(1)
T9	0.2707(13)	-0.1719(8)	0.0315(34)	1.0	0.2(1)
T10	0.1146(15)	-0.1745(10)	0.0256(37)	1.0	0.2(1)
T11	0.0685(22)	-0.1291(13)	-0.1875(42)	1.0	0.2(1)
T12	0.1848(18)	-0.1726(9)	-0.3200(47)	1.0	0.2(1)
O1	0.3701(22)	0.0627(21)	-0.2511(54)	1.0	0.6(1)
O2	0.3160(18)	0.0526(50)	-0.0755(45)	1.0	0.6(1)
O3	0.2033(9)	0.0619(17)	0.0189(36)	1.0	0.6(1)
O4	0.0934(19)	0.0629(41)	-0.0840(36)	1.0	0.6(1)
O5	0.1147(19)	0.0579(31)	-0.2755(42)	1.0	0.6(1)
O6	0.2413(20)	0.0548(50)	-0.2348(47)	1.0	0.6(1)
O7	0.3686(37)	-0.1650(18)	-0.2377(59)	1.0	0.6(1)

O8	0.3037(35)	-0.1487(41)	-0.0710(35)	1.0	0.6(1)
O9	0.1924(10)	-0.1581(41)	0.0278(68)	1.0	0.6(1)
O10	0.0870(33)	-0.1651(25)	-0.0850(28)	1.0	0.6(1)
O11	0.1122(24)	-0.1603(38)	-0.2751(34)	1.0	0.6(1)
O12	0.2395(35)	-0.1514(44)	-0.2398(68)	1.0	0.6(1)
O13	0.3150(39)	-0.0495(11)	-0.1960(87)	1.0	0.6(1)
O14	0.0832(23)	-0.0508(10)	-0.1786(86)	1.0	0.6(1)
O15	0.4239(21)	0.1249(15)	-0.4013(28)	1.0	0.6(1)
O16	0.4028(20)	-0.0038(16)	-0.4109(57)	1.0	0.6(1)
O17	0.3971(27)	-0.1342(15)	-0.4217(37)	1.0	0.6(1)
O18	0.1973(34)	0.1308(20)	-0.3785(32)	1.0	0.6(1)
O19	0.1972(28)	0.0011(19)	-0.3993(61)	1.0	0.6(1)
O20	0.1937(28)	-0.1288(21)	-0.4184(39)	1.0	0.6(1)
O21	-0.0052(12)	0.0429(25)	-0.2065(18)	1.0	0.6(1)
O22	-0.0086(22)	-0.1407(20)	-0.2111(42)	1.0	0.6(1)
O23	0.4328(26)	-1/2	-0.3493(38)	1.0	0.6(1)
O24	0.1935(49)	-1/2	-0.3467(90)	1.0	0.6(1)
O25	0.2836(46)	-1/2	0.0477(81)	1.0	0.6(1)
O26	0.1028(47)	-1/2	0.0605(10)	1.0	0.6(1)

Table C

422_AS-ZSM-5, room temperature

Site	x/a	y/b	z/c	Fraction	Ui/Ue*100
T1	0.4228(9)	0.0567(9)	-0.3389(14)	1.0	0.9(1)
T2	0.3094(11)	0.0305(9)	-0.1886(15)	1.0	0.9(1)
T3	0.2815(9)	0.0601(10)	0.0311(14)	1.0	0.9(1)
T4	0.1236(9)	0.0653(10)	0.0251(15)	1.0	0.9(1)
T5	0.0713(10)	0.0279(10)	-0.1852(15)	1.0	0.9(1)
T6	0.1868(10)	0.0609(11)	-0.3235(15)	1.0	0.9(1)
T7	0.4227(10)	-0.1721(7)	-0.3235(15)	1.0	0.9(1)
T8	0.3077(11)	-0.1293(10)	-0.1835(16)	1.0	0.9(1)
T9	0.2721(11)	-0.1718(7)	0.0350(15)	1.0	0.9(1)
T10	0.1168(11)	-0.1743(7)	0.0298(17)	1.0	0.9(1)
T11	0.0704(11)	-0.1298(10)	-0.1847(18)	1.0	0.9(1)
T12	0.1866(11)	-0.1729(7)	-0.3197(16)	1.0	0.9(1)
O1	0.3699(12)	0.0605(14)	-0.2508(19)	1.0	1.5(2)
O2	0.3148(12)	0.0549(18)	-0.0763(16)	1.0	1.5(2)
O3	0.2026(7)	0.0610(14)	0.0189(22)	1.0	1.5(2)
O4	0.0933(13)	0.0641(15)	-0.0846(15)	1.0	1.5(2)
O5	0.1143(10)	0.0554(15)	-0.2759(17)	1.0	1.5(2)
O6	0.2410(12)	0.0550(21)	-0.2368(24)	1.0	1.5(2)
O7	0.3719(15)	-0.1619(16)	-0.2335(22)	1.0	1.5(2)

O8	0.3038(15)	-0.1500(17)	-0.0692(14)	1.0	1.5(2)
O9	0.1941(9)	-0.1566(19)	0.0341(26)	1.0	1.5(2)
O10	0.0904(16)	-0.1647(13)	-0.0817(16)	1.0	1.5(2)
O11	0.1151(12)	-0.1593(19)	-0.2721(19)	1.0	1.5(2)
O12	0.2428(15)	-0.1544(20)	-0.2404(24)	1.0	1.5(2)
O13	0.3125(23)	-0.0495(8)	-0.1921(29)	1.0	1.5(2)
O14	0.0822(15)	-0.0510(8)	-0.1754(31)	1.0	1.5(2)
O15	0.4236(12)	0.1260(9)	-0.3976(18)	1.0	1.5(2)
O16	0.4036(13)	-0.0025(11)	-0.4134(21)	1.0	1.5(2)
O17	0.3972(14)	-0.1328(11)	-0.4197(18)	1.0	1.5(2)
O18	0.1936(15)	0.1316(10)	-0.3769(13)	1.0	1.5(2)
O19	0.1971(17)	0.0023(11)	-0.4023(24)	1.0	1.5(2)
O20	0.1951(15)	-0.1278(10)	-0.4166(17)	1.0	1.5(2)
O21	-0.0054(8)	0.0427(14)	-0.2068(15)	1.0	1.5(2)
O22	-0.0060(10)	-0.1441(17)	-0.2083(20)	1.0	1.5(2)
O23	0.4283(23)	-1/2	-0.3487(26)	1.0	1.5(2)
O24	0.1929(22)	-1/2	-0.3492(33)	1.0	1.5(2)
O25	0.2838(23)	-1/2	0.0513(32)	1.0	1.5(2)
O26	0.1056(24)	-1/2	0.0634(26)	1.0	1.5(2)

Table D

424_AS-ZSM-5, room temperature

Site	x/a	y/b	z/c	Fraction	Ui/Ue*100
T1	0.4229(9)	0.0562(10)	-0.3393(16)	1.0	0.3(3)
T2	0.3092(12)	0.0302(10)	-0.1885(18)	1.0	0.3(3)
T3	0.2813(9)	0.0598(10)	0.0309(16)	1.0	0.3(3)
T4	0.1234(9)	0.0658(10)	0.0246(16)	1.0	0.3(3)
T5	0.0713(10)	0.0275(10)	-0.1845(17)	1.0	0.3(3)
T6	0.1871(11)	0.0611(12)	-0.3224(19)	1.0	0.3(3)
T7	0.4230(11)	-0.1721(7)	-0.3230(16)	1.0	0.3(3)
T8	0.3077(12)	-0.1294(10)	-0.1837(19)	1.0	0.3(3)
T9	0.2718(11)	-0.1717(7)	0.0350(17)	1.0	0.3(3)
T10	0.1165(12)	-0.1745(7)	0.0309(20)	1.0	0.3(3)
T11	0.0710(12)	-0.1297(11)	-0.1831(21)	1.0	0.3(3)
T12	0.1866(11)	-0.1730(7)	-0.3203(19)	1.0	0.3(3)
O1	0.3697(13)	0.0602(16)	-0.2514(22)	1.0	0.7(2)
O2	0.3158(12)	0.0536(21)	-0.0756(19)	1.0	0.7(2)
O3	0.2025(7)	0.0613(14)	0.0167(22)	1.0	0.7(2)
O4	0.0922(13)	0.0655(17)	-0.0847(17)	1.0	0.7(2)
O5	0.1143(11)	0.0546(17)	-0.2757(20)	1.0	0.7(2)
O6	0.2409(13)	0.0562(24)	-0.2351(26)	1.0	0.7(2)
O7	0.3728(17)	-0.1616(19)	-0.2322(24)	1.0	0.7(2)

O8	0.3031(17)	-0.1493(19)	-0.0691(17)	1.0	0.7(2)
O9	0.1938(10)	-0.1561(22)	0.0355(30)	1.0	0.7(2)
O10	0.0905(18)	-0.1659(13)	-0.0810(18)	1.0	0.7(2)
O11	0.1156(14)	-0.1586(21)	-0.2713(22)	1.0	0.7(2)
O12	0.2436(18)	-0.1561(22)	-0.2415(30)	1.0	0.7(2)
O13	0.3114(26)	-0.0497(8)	-0.1936(35)	1.0	0.7(2)
O14	0.0832(16)	-0.0510(9)	-0.1722(37)	1.0	0.7(2)
O15	0.4244(12)	0.1257(10)	-0.3976(20)	1.0	0.7(2)
O16	0.4034(14)	-0.0027(12)	-0.4143(24)	1.0	0.7(2)
O17	0.3966(15)	-0.1332(12)	-0.4191(19)	1.0	0.7(2)
O18	0.1933(18)	0.1319(11)	-0.3765(18)	1.0	0.7(2)
O19	0.1987(18)	0.0026(12)	-0.4012(27)	1.0	0.7(2)
O20	0.1953(17)	-0.1275(11)	-0.4169(20)	1.0	0.7(2)
O21	-0.0055(9)	-0.1434(19)	-0.2074(22)	1.0	0.7(2)
O22	-0.0056(12)	-0.1441(17)	-0.2083(20)	1.0	0.7(2)
O23	0.4289(24)	-1/2	-0.3476(29)	1.0	0.7(2)
O24	0.1914(25)	-1/2	-0.3511(38)	1.0	0.7(2)
O25	0.2834(26)	-1/2	0.0505(38)	1.0	0.7(2)
O26	0.1059(27)	-1/2	0.0659(29)	1.0	0.7(2)

Table E

Site	x/a	y/b	z/c	Fraction	Ui/Ue*100
N	0.474(1)	1/2	-0.104(1)	1.00(1)	3.9(7)
C1	0.472(1)	0.224(1)	-0.207(1)	0.50(1)	3.9(7)
C24	0.543(1)	1/2	-0.212(1)	1.00(1)	3.9(7)
C4	0.342(1)	1/2	-0.123(1)	1.00(1)	3.9(7)
C6	0.278(1)	0.225(1)	-0.147(1)	0.50(1)	3.9(7)
C21	0.408(1)	0.225(1)	-0.138(1)	0.50(1)	3.9(7)
C7	0.520(1)	0.306(1)	-0.079(1)	0.50(1)	3.9(7)
C11	0.506(1)	0.134(1)	-0.024(1)	0.50(1)	3.9(7)
C27	0.469(1)	0.304(1)	-0.030(1)	0.50(1)	3.9(7)
C25	0.602(1)	0.224(1)	-0.199(1)	0.25(1)	3.9(7)
C3	0.552(1)	0.421(1)	-0.000(1)	0.25(1)	3.9(7)
C5	0.502(1)	0.420(1)	0.049(1)	0.25(1)	3.9(7)

Table F

423_AS-ZSM-5, 200 °C

Site	x/a	y/b	z/c	Fraction	Ui/Ue*100
T1	0.4227(10)	0.0566(11)	-0.3367(20)	1.0	0.3(1)
T2	0.3111(14)	0.0300(10)	-0.1865(23)	1.0	0.3(1)
T3	0.2818(10)	0.0600(14)	0.0337(21)	1.0	0.3(1)
T4	0.1241(10)	0.0660(12)	0.0281(21)	1.0	0.3(1)
T5	0.0719(11)	0.0291(12)	-0.1842(22)	1.0	0.3(1)
T6	0.1888(12)	0.0614(16)	-0.3194(24)	1.0	0.3(1)
T7	0.4229(12)	-0.1724(7)	-0.3225(20)	1.0	0.3(1)
T8	0.3075(14)	-0.1287(11)	-0.1847(26)	1.0	0.3(1)
T9	0.2718(11)	-0.1728(9)	0.0329(23)	1.0	0.3(1)
T10	0.1147(12)	-0.1753(9)	0.0270(27)	1.0	0.3(1)
T11	0.0692(15)	-0.1283(12)	-0.1868(29)	1.0	0.3(1)
T12	0.1857(13)	-0.1726(8)	-0.3197(27)	1.0	0.3(1)
O1	0.3715(17)	0.0625(16)	-0.2467(32)	1.0	0.6(4)
O2	0.3164(13)	0.0509(29)	-0.0723(25)	1.0	0.6(4)
O3	0.2031(8)	0.0613(16)	0.0199(28)	1.0	0.6(4)
O4	0.0925(15)	0.0627(26)	-0.0809(23)	1.0	0.6(4)
O5	0.1161(13)	0.0591(22)	-0.2720(27)	1.0	0.6(4)
O6	0.2426(16)	0.0560(31)	-0.2323(31)	1.0	0.6(4)
O7	0.3704(23)	-0.1643(17)	-0.2341(37)	1.0	0.6(4)
O8	0.3034(23)	-0.1480(24)	-0.0697(22)	1.0	0.6(4)
O9	0.1930(9)	-0.1630(35)	0.0300(41)	1.0	0.6(4)
O10	0.0880(21)	-0.1637(20)	-0.0838(22)	1.0	0.6(4)
O11	0.1137(17)	-0.1591(26)	-0.2737(27)	1.0	0.6(4)
O12	0.2414(23)	-0.1525(30)	-0.2403(41)	1.0	0.6(4)
O13	0.3148(30)	-0.0495(9)	-0.1956(48)	1.0	0.6(4)
O14	0.0828(18)	-0.0499(10)	-0.1782(55)	1.0	0.6(4)
O15	0.4217(18)	0.1243(10)	-0.3996(22)	1.0	0.6(4)
O16	0.4026(15)	-0.0046(13)	-0.4069(34)	1.0	0.6(4)
O17	0.3962(18)	-0.1346(12)	-0.4194(26)	1.0	0.6(4)
O18	0.1980(23)	0.1304(15)	-0.3774(22)	1.0	0.6(4)
O19	0.1979(21)	0.0005(15)	-0.3950(35)	1.0	0.6(4)
O20	0.1945(21)	-0.1289(15)	-0.4181(25)	1.0	0.6(4)
O21	-0.0045(10)	0.0444(21)	-0.2067(17)	1.0	0.6(4)
O22	-0.0076(15)	-0.1409(17)	-0.2106(27)	1.0	0.6(4)
O23	0.4325(24)	-1/4	-0.3470(32)	1.0	0.6(4)
O24	0.1929(33)	-1/4	-0.3468(55)	1.0	0.6(4)
O25	0.2889(35)	-1/4	0.0489(52)	1.0	0.6(4)

O26	0.0987(36)	-1/4	0.0608(41)	1.0	0.6(4)

Table G

423_AS-ZSM-5, 400 °C

Site	x/a	y/b	z/c	Fraction	Ui/Ue*100
T1	0.4229(3)	0.0568(4)	-0.3350(7)	1.0	0.5(3)
T2	0.3107(5)	0.0309(3)	-0.1861(8)	1.0	0.5(3)
T3	0.2813(3)	0.0579(4)	0.0351(7)	1.0	0.5(3)
T4	0.1238(3)	0.0652(4)	0.0287(7)	1.0	0.5(3)
T5	0.0719(4)	0.0281(4)	-0.1834(7)	1.0	0.5(3)
T6	0.1892(4)	0.0639(4)	-0.3177(7)	1.0	0.5(3)
T7	0.4229(4)	-0.1719(2)	-0.3217(7)	1.0	0.5(3)
T8	0.3073(4)	-0.1275(3)	-0.1851(8)	1.0	0.5(3)
T9	0.2720(4)	-0.1716(2)	0.0320(7)	1.0	0.5(3)
T10	0.1158(4)	-0.1745(3)	0.0294(9)	1.0	0.5(3)
T11	0.0702(5)	-0.1294(4)	-0.1848(9)	1.0	0.5(3)
T12	0.1862(4)	-0.1733(2)	-0.3200(9)	1.0	0.5(3)
O1	0.3721(6)	0.0630(5)	-0.2444(11)	1.0	1.3(5)
O2	0.3167(4)	0.0482(8)	-0.0705(8)	1.0	1.3(5)
O3	0.2028(2)	0.0611(5)	0.0189(9)	1.0	1.3(5)
O4	0.0912(4)	0.0619(8)	-0.0796(8)	1.0	1.3(5)
O5	0.1166(4)	0.0586(6)	-0.2704(9)	1.0	1.3(5)
O6	0.2431(5)	0.0607(9)	-0.2304(10)	1.0	1.3(5)
O7	0.3718(7)	-0.1619(7)	-0.2319(12)	1.0	1.3(5)
O8	0.3034(8)	-0.1440(7)	-0.0691(7)	1.0	1.3(5)
O9	0.1936(3)	-0.1589(11)	0.0320(14)	1.0	1.3(5)
O10	0.0885(6)	-0.1644(6)	-0.0814(8)	1.0	1.3(5)
O11	0.1147(6)	-0.1609(8)	-0.2713(9)	1.0	1.3(5)
O12	0.2425(8)	-0.1555(9)	-0.2402(14)	1.0	1.3(5)
O13	0.3115(10)	-0.0483(3)	-0.2006(13)	1.0	1.3(5)
O14	0.0838(6)	-0.0508(3)	-0.1771(17)	1.0	1.3(5)
O15	0.4226(5)	0.1249(4)	-0.3972(8)	1.0	1.3(5)
O16	0.4016(5)	-0.0037(4)	-0.4057(12)	1.0	1.3(5)
O17	0.3963(6)	-0.1339(4)	-0.4183(9)	1.0	1.3(5)
O18	0.1955(7)	0.1334(4)	-0.3755(7)	1.0	1.3(5)
O19	0.2007(6)	0.0033(4)	-0.3934(11)	1.0	1.3(5)
O20	0.1941(7)	-0.1264(4)	-0.4155(8)	1.0	1.3(5)
O21	-0.0042(3)	0.0430(6)	-0.2076(6)	1.0	1.3(5)
O22	-0.0064(5)	-0.1418(6)	-0.2094(9)	1.0	1.3(5)
O23	0.4305(8)	-1/4	-0.3453(13)	1.0	1.3(5)
O24	0.1928(10)	-1/4	-0.3521(16)	1.0	1.3(5)

O25	0.2865(11)	-1/4	0.0412(16)	1.0	1.3(5)
O26	0.1032(12)	-1/4	0.0637(13)	1.0	1.3(5)

Table H

423_AS-ZSM-5, 600 °C

Site	x/a	y/b	z/c	Fraction	Ui/Ue*100
T1	0.4229(3)	0.0566(3)	-0.3348(7)	1.0	1.0(3)
T2	0.3115(4)	0.0307(3)	-0.1846(7)	1.0	1.0(3)
T3	0.2815(3)	0.0579(4)	0.0356(7)	1.0	1.0(3)
T4	0.1241(3)	0.0656(4)	0.0286(7)	1.0	1.0(3)
T5	0.0719(3)	0.0281(3)	-0.1831(7)	1.0	1.0(3)
T6	0.1901(4)	0.0635(4)	-0.3158(7)	1.0	1.0(3)
T7	0.4225(4)	-0.1721(2)	-0.3213(7)	1.0	1.0(3)
T8	0.3072(4)	-0.1277(3)	-0.1839(8)	1.0	1.0(3)
T9	0.2711(3)	-0.1715(2)	0.0328(7)	1.0	1.0(3)
T10	0.1145(4)	-0.1747(3)	0.0286(9)	1.0	1.0(3)
T11	0.0693(4)	-0.1292(4)	-0.1852(9)	1.0	1.0(3)
T12	0.1859(4)	-0.1730(2)	-0.3187(9)	1.0	1.0(3)
O1	0.3720(5)	0.0639(5)	-0.2442(11)	1.0	2.1(5)
O2	0.3185(4)	0.0476(8)	-0.0688(8)	1.0	2.1(5)
O3	0.2030(2)	0.0611(5)	0.0168(9)	1.0	2.1(5)
O4	0.0902(4)	0.0622(8)	-0.0790(8)	1.0	2.1(5)
O5	0.1169(4)	0.0589(6)	-0.2698(9)	1.0	2.1(5)
O6	0.2431(5)	0.0597(9)	-0.2271(9)	1.0	2.1(5)
O7	0.3707(7)	-0.1638(6)	-0.2317(12)	1.0	2.1(5)
O8	0.3037(7)	-0.1440(7)	-0.0676(7)	1.0	2.1(5)
O9	0.1924(3)	-0.1592(11)	0.0303(13)	1.0	2.1(5)
O10	0.0867(6)	-0.1652(5)	-0.0821(7)	1.0	2.1(5)
O11	0.1137(5)	-0.1609(8)	-0.2720(9)	1.0	2.1(5)
O12	0.2413(7)	-0.1542(9)	-0.2378(13)	1.0	2.1(5)
O13	0.3133(10)	-0.0486(3)	-0.1998(13)	1.0	2.1(5)
O14	0.0843(6)	-0.0508(3)	-0.1763(17)	1.0	2.1(5)
O15	0.4235(5)	0.1244(3)	-0.3981(8)	1.0	2.1(5)
O16	0.4009(5)	-0.0041(4)	-0.4049(11)	1.0	2.1(5)
O17	0.3951(6)	-0.1344(4)	-0.4180(8)	1.0	2.1(5)
O18	0.1978(6)	0.1329(4)	-0.3738(7)	1.0	2.1(5)
O19	0.2016(6)	0.0028(4)	-0.3914(10)	1.0	2.1(5)
O20	0.1946(7)	-0.1268(4)	-0.4150(8)	1.0	2.1(5)
O21	-0.0044(3)	0.0422(6)	-0.2083(6)	1.0	2.1(5)
O22	-0.0076(4)	-0.1402(6)	-0.2106(9)	1.0	2.1(5)
O23	0.4321(7)	-1/4	-0.3454(12)	1.0	2.1(5)

O24	0.1935(10)	-1/4	-0.3496(16)	1.0	2.1(5)
O25	0.2857(11)	-1/4	0.0429(16)	1.0	2.1(5)
O26	0.1017(11)	-1/4	0.0643(13)	1.0	2.1(5)

Table I

423_AS-ZSM-5, 800 °C

Site	x/a	y/b	z/c	Fraction	Ui/Ue*100
T1	0.4227(3)	0.0560(4)	-0.3365(7)	1.0	2.0(4)
T2	0.3104(5)	0.0308(3)	-0.1862(8)	1.0	2.0(4)
T3	0.2819(3)	0.0573(4)	0.0343(7)	1.0	2.0(4)
T4	0.1243(3)	0.0660(4)	0.0269(8)	1.0	2.0(4)
T5	0.0720(4)	0.0276(3)	-0.1837(8)	1.0	2.0(4)
T6	0.1895(4)	0.0641(5)	-0.3168(8)	1.0	2.0(4)
T7	0.4221(4)	-0.1718(2)	-0.3220(7)	1.0	2.0(4)
T8	0.3061(5)	-0.1275(4)	-0.1853(9)	1.0	2.0(4)
T9	0.2709(4)	-0.1712(2)	0.0319(8)	1.0	2.0(4)
T10	0.1145(4)	-0.1745(3)	0.0289(10)	1.0	2.0(4)
T11	0.0696(5)	-0.1293(4)	-0.1848(10)	1.0	2.0(4)
T12	0.1851(4)	-0.1732(2)	-0.3204(9)	1.0	2.0(4)
O1	0.3710(6)	0.0634(6)	-0.2467(12)	1.0	3.7(6)
O2	0.3188(4)	0.0469(9)	-0.0702(8)	1.0	3.7(6)
O3	0.2034(2)	0.0615(5)	0.0149(9)	1.0	3.7(6)
O4	0.0905(4)	0.0631(9)	-0.0808(8)	1.0	3.7(6)
O5	0.1159(5)	0.0582(7)	-0.2718(10)	1.0	3.7(6)
O6	0.2420(5)	0.0611(10)	-0.2273(9)	1.0	3.7(6)
O7	0.3705(8)	-0.1628(7)	-0.2324(13)	1.0	3.7(6)
O8	0.3027(9)	-0.1430(7)	-0.0688(8)	1.0	3.7(6)
O9	0.1923(3)	-0.1578(12)	0.0316(15)	1.0	3.7(6)
O10	0.0874(7)	-0.1660(6)	-0.0824(8)	1.0	3.7(6)
O11	0.1129(6)	-0.1612(9)	-0.2727(10)	1.0	3.7(6)
O12	0.2408(8)	-0.1557(10)	-0.2392(15)	1.0	3.7(6)
O13	0.3108(11)	-0.0484(3)	-0.2025(14)	1.0	3.7(6)
O14	0.0855(6)	-0.0511(3)	-0.1755(19)	1.0	3.7(6)
O15	0.4246(5)	0.1242(4)	-0.3990(8)	1.0	3.7(6)
O16	0.4006(5)	-0.0042(5)	-0.4074(13)	1.0	3.7(6)
O17	0.3946(6)	-0.1347(5)	-0.4191(9)	1.0	3.7(6)
O18	0.1965(7)	0.1338(4)	-0.3746(8)	1.0	3.7(6)
O19	0.2024(6)	0.0038(4)	-0.3928(11)	1.0	3.7(6)
O20	0.1937(7)	-0.1258(4)	-0.4155(9)	1.0	3.7(6)
O21	-0.0050(3)	0.0404(6)	-0.2078(6)	1.0	3.7(6)
O22	-0.0078(5)	-0.1396(6)	-0.2088(10)	1.0	3.7(6)

O23	0.4317(8)	-1/4	-0.3449(14)	1.0	3.7(6)
O24	0.1921(11)	-1/4	-0.3531(18)	1.0	3.7(6)
O25	0.2846(12)	-1/4	0.0398(17)	1.0	3.7(6)
O26	0.1027(13)	-1/4	0.0650(14)	1.0	3.7(6)

Table J

425_AS-ZSM-5, 200 °C

Site	x/a	y/b	z/c	Fraction	Ui/Ue*100
T1	0.4229(10)	0.0566(14)	-0.3381(33)	1.0	0.4(4)
T2	0.3113(17)	0.0300(11)	-0.1871(39)	1.0	0.4(4)
T3	0.2820(10)	0.0606(22)	0.0329(36)	1.0	0.4(4)
T4	0.1240(11)	0.0659(15)	0.0268(31)	1.0	0.4(4)
T5	0.0718(13)	0.0284(12)	-0.1849(34)	1.0	0.4(4)
T6	0.1886(19)	0.0609(25)	-0.3203(39)	1.0	0.4(4)
T7	0.4226(14)	-0.1726(7)	-0.3233(27)	1.0	0.4(4)
T8	0.3074(19)	-0.1288(13)	-0.1843(44)	1.0	0.4(4)
T9	0.2706(13)	-0.1721(9)	0.0327(35)	1.0	0.4(4)
T10	0.1144(14)	-0.1747(10)	0.0261(39)	1.0	0.4(4)
T11	0.0684(22)	-0.1289(13)	-0.1868(43)	1.0	0.4(4)
T12	0.1854(18)	-0.1725(9)	-0.3183(48)	1.0	0.4(4)
O1	0.3708(23)	0.0628(20)	-0.2489(55)	1.0	0.7(2)
O2	0.3166(18)	0.0525(52)	-0.0734(45)	1.0	0.7(2)
O3	0.2031(9)	0.0618(17)	0.0191(37)	1.0	0.7(2)
O4	0.0927(19)	0.0629(42)	-0.0823(38)	1.0	0.7(2)
O5	0.1156(19)	0.0582(32)	-0.2735(44)	1.0	0.7(2)
O6	0.2421(21)	0.0544(51)	-0.2328(46)	1.0	0.7(2)
O7	0.3690(38)	-0.1653(17)	-0.2362(60)	1.0	0.7(2)
O8	0.3043(35)	-0.1490(42)	-0.0694(35)	1.0	0.7(2)
O9	0.1923(10)	-0.1591(43)	0.0275(69)	1.0	0.7(2)
O10	0.0863(32)	-0.1650(27)	-0.0842(29)	1.0	0.7(2)
O11	0.1128(24)	-0.1599(38)	-0.2739(36)	1.0	0.7(2)
O12	0.2400(35)	-0.1510(45)	-0.2382(69)	1.0	0.7(2)
O13	0.3161(39)	-0.0496(11)	-0.1940(90)	1.0	0.7(2)
O14	0.0831(23)	-0.0506(11)	-0.1776(89)	1.0	0.7(2)
O15	0.4233(22)	0.1246(14)	-0.4004(28)	1.0	0.7(2)
O16	0.4026(21)	-0.0042(16)	-0.4090(58)	1.0	0.7(2)
O17	0.3967(27)	-0.1344(15)	-0.4204(38)	1.0	0.7(2)
O18	0.1985(34)	0.1304(21)	-0.3770(31)	1.0	0.7(2)
O19	0.1977(28)	0.0006(20)	-0.3971(60)	1.0	0.7(2)
O20	0.1945(29)	-0.1292(22)	-0.4172(39)	1.0	0.7(2)
O21	-0.0048(13)	0.0433(27)	-0.2067(18)	1.0	0.7(2)

O22	-0.0085(22)	-0.1404(20)	-0.2116(42)	1.0	0.7(2)
O23	0.4333(25)	-1/4	-0.3482(37)	1.0	0.7(2)
O24	0.1941(50)	-1/4	-0.3442(93)	1.0	0.7(2)
O25	0.2842(48)	-1/4	0.0498(83)	1.0	0.7(2)
O26	0.1019(47)	-1/4	0.0612(58)	1.0	0.7(2)

Table K

425_AS-ZSM-5, 400 °C

Site	x/a	y/b	z/c	Fraction	Ui/Ue*100
T1	0.4227(2)	0.0571(3)	-0.3372(8)	1.0	1.2(5)
T2	0.3110(3)	0.0305(2)	-0.1868(9)	1.0	1.2(5)
T3	0.2820(2)	0.0595(4)	0.0338(8)	1.0	1.2(5)
T4	0.1240(2)	0.0653(3)	0.0268(7)	1.0	1.2(5)
T5	0.0717(3)	0.0280(2)	-0.1859(8)	1.0	1.2(5)
T6	0.1890(4)	0.0625(4)	-0.3190(8)	1.0	1.2(5)
T7	0.4221(3)	-0.1724(1)	-0.3237(6)	1.0	1.2(5)
T8	0.3064(4)	-0.1282(2)	-0.1853(9)	1.0	1.2(5)
T9	0.2700(2)	-0.1714(1)	0.0311(8)	1.0	1.2(5)
T10	0.1143(3)	-0.1741(2)	0.0253(9)	1.0	1.2(5)
T11	0.0677(4)	-0.1293(2)	-0.1882(10)	1.0	1.2(5)
T12	0.1848(3)	-0.1728(1)	-0.3186(11)	1.0	1.2(5)
O1	0.3707(5)	0.0639(4)	-0.2479(13)	1.0	1.9(6)
O2	0.3172(3)	0.0504(10)	-0.0720(10)	1.0	1.9(6)
O3	0.2032(1)	0.06201(3)	0.0185(8)	1.0	1.9(6)
O4	0.0924(4)	0.0613(9)	-0.0822(9)	1.0	1.9(6)
O5	0.1156(4)	0.0592(6)	-0.2736(10)	1.0	1.9(6)
O6	0.2419(5)	0.0569(10)	-0.2305(9)	1.0	1.9(6)
O7	0.3677(8)	-0.1652(3)	-0.2375(14)	1.0	1.9(6)
O8	0.3046(8)	-0.1468(8)	-0.0697(8)	1.0	1.9(6)
O9	0.1919(2)	-0.1569(9)	0.0255(16)	1.0	1.9(6)
O10	0.0852(6)	-0.1646(6)	-0.0846(6)	1.0	1.9(6)
O11	0.1117(5)	-0.1620(8)	-0.2746(8)	1.0	1.9(6)
O12	0.2386(7)	-0.1515(9)	-0.2371(16)	1.0	1.9(6)
O13	0.3147(8)	-0.0490(2)	-0.1978(18)	1.0	1.9(6)
O14	0.0833(5)	-0.0510(2)	-0.1809(21)	1.0	1.9(6)
O15	0.4237(5)	0.1250(3)	-0.3999(6)	1.0	1.9(6)
O16	0.4017(4)	-0.0037(3)	-0.4078(14)	1.0	1.9(6)
O17	0.3971(6)	-0.1341(3)	-0.4213(9)	1.0	1.9(6)
O18	0.1989(7)	0.1319(3)	-0.3764(7)	1.0	1.9(6)
O19	0.1993(5)	0.0019(3)	-0.3952(13)	1.0	1.9(6)
O20	0.1937(6)	-0.1279(4)	-0.4162(9)	1.0	1.9(6)

O21	-0.0049(3)	0.0430(6)	-0.2076(4)	1.0	1.9(6)
O22	-0.0092(4)	-0.1402(4)	-0.2128(9)	1.0	1.9(6)
O23	0.4331(5)	-1/4	-0.3485(9)	1.0	1.9(6)
O24	0.1948(10)	-1/4	-0.3467(20)	1.0	1.9(6)
O25	0.2821(11)	-1/4	0.0449(17)	1.0	1.9(6)
O26	0.1037(11)	-1/4	0.0600(14)	1.0	1.9(6)

Table L

425_AS-ZSM-5, 600 °C

Site	x/	y/b	z/c	Fraction	Ui/Ue*100
T1	0.4227(24)	0.0565(3)	-0.3363(7)	1.0	1.7(4)
T2	0.3117(3)	0.0303(2)	-0.1843(8)	1.0	1.7(4)
T3	0.2816(2)	0.0586(3)	0.0346(7)	1.0	1.7(4)
T4	0.1242(2)	0.0657(3)	0.0270(7)	1.0	1.7(4)
T5	0.0715(3)	0.0276(2)	-0.1836(8)	1.0	1.7(4)
T6	0.1899(3)	0.0626(4)	-0.3158(7)	1.0	1.7(4)
T7	0.4222(3)	-0.1723(1)	-0.3216(6)	1.0	1.7(4)
T8	0.3075(4)	-0.1285(3)	-0.1823(9)	1.0	1.7(4)
T9	0.2699(2)	-0.1711(1)	0.0344(7)	1.0	1.7(4)
T10	0.1141(3)	-0.1743(2)	0.0285(9)	1.0	1.7(4)
T11	0.0687(4)	-0.1293(2)	-0.1849(10)	1.0	1.7(4)
T12	0.1859(3)	-0.1728(2)	-0.3172(9)	1.0	1.7(4)
O1	0.3708(5)	0.0638(4)	-0.2467(12)	1.0	2.1(5)
O2	0.3196(3)	0.0493(9)	-0.0692(8)	1.0	2.1(5)
O3	0.2032(2)	0.0612(3)	0.0144(7)	1.0	2.1(5)
O4	0.0900(3)	0.0634(8)	-0.0806(8)	1.0	2.1(5)
O5	0.1161(4)	0.0578(6)	-0.2715(9)	1.0	2.1(5)
O6	0.2421(4)	0.0573(9)	-0.2260(8)	1.0	2.1(5)
O7	0.3699(7)	-0.1653(4)	-0.2322(12)	1.0	2.1(5)
O8	0.3046(7)	-0.1458(7)	-0.0661(7)	1.0	2.1(5)
O9	0.1916(2)	-0.1562(9)	0.0291(14)	1.0	2.1(5)
O10	0.0855(6)	-0.1663(5)	-0.0822(7)	1.0	2.1(5)
O11	0.1131(5)	-0.1607(8)	-0.2721(8)	1.0	2.1(5)
O12	0.2405(7)	-0.1533(8)	-0.2354(14)	1.0	2.1(5)
O13	0.3148(8)	-0.0493(2)	-0.1966(16)	1.0	2.1(5)
O14	0.0844(5)	-0.0511(2)	-0.1746(19)	1.0	2.1(5)
O15	0.4250(4)	0.1248(3)	-0.3984(6)	1.0	2.1(5)
O16	0.4008(4)	-0.0035(4)	-0.4078(12)	1.0	2.1(5)
O17	0.3946(5)	-0.1342(3)	-0.4180(8)	1.0	2.1(5)
O18	0.1989(6)	0.1326(3)	-0.3721(7)	1.0	2.1(5)
O19	0.2017(5)	0.0026(3)	-0.3929(11)	1.0	2.1(5)

O20	0.1953(6)	-0.1272(4)	-0.4141(8)	1.0	2.1(5)
O21	-0.0051(3)	0.0409(5)	-0.2086(4)	1.0	2.1(5)
O22	-0.0083(4)	-0.1397(4)	-0.2110(9)	1.0	2.1(5)
O23	0.4329(5)	-1/4	-0.3469(9)	1.0	2.1(5)
O24	0.1941(10)	-1/4	-0.3468(17)	1.0	2.1(5)
O25	0.2817(10)	-1/4	0.0467(16)	1.0	2.1(5)
O26	0.1041(10)	-1/4	0.0650(13)	1.0	2.1(5)

Table M

425_AS-ZSM-5, 800 °C

Site	x/a	y/b	z/c	Fraction	Ui/Ue*100
T1	0.4227(24)	0.0563(3)	-0.3363(7)	1.0	1.9(4)
T2	0.3114(3)	0.0303(2)	-0.1847(8)	1.0	1.9(4)
T3	0.2817(2)	0.0581(3)	0.0347(7)	1.0	1.9(4)
T4	0.1242(2)	0.0658(3)	0.0269(7)	1.0	1.9(4)
T5	0.0716(3)	0.0276(2)	-0.1840(8)	1.0	1.9(4)
T6	0.1900(3)	0.0632(4)	-0.3156(7)	1.0	1.9(4)
T7	0.4221(3)	-0.1723(1)	-0.3218(6)	1.0	1.9(4)
T8	0.3068(4)	-0.1282(3)	-0.1834(8)	1.0	1.9(4)
T9	0.2698(2)	-0.1711(1)	0.0335(7)	1.0	1.9(4)
T10	0.1137(3)	-0.1743(2)	0.0282(9)	1.0	1.9(4)
T11	0.0685(4)	-0.1292(2)	-0.1855(10)	1.0	1.9(4)
T12	0.1853(3)	-0.1729(2)	-0.3181(9)	1.0	1.9(4)
O1	0.3707(5)	0.0640(4)	-0.2466(12)	1.0	3.4(5)
O2	0.3197(3)	0.0480(9)	-0.0690(8)	1.0	3.4(5)
O3	0.2033(1)	0.0615(3)	0.0142(8)	1.0	3.4(5)
O4	0.0900(3)	0.0631(8)	-0.0808(8)	1.0	3.4(5)
O5	0.1160(4)	0.0583(6)	-0.2719(9)	1.0	3.4(5)
O6	0.2420(4)	0.0585(9)	-0.2254(8)	1.0	3.4(5)
O7	0.3694(7)	-0.1651(4)	-0.2329(12)	1.0	3.4(5)
O8	0.3041(7)	-0.1448(7)	-0.0668(7)	1.0	3.4(5)
O9	0.1914(2)	-0.1567(9)	0.0290(14)	1.0	3.4(5)
O10	0.0852(6)	-0.1662(5)	-0.0826(7)	1.0	3.4(5)
O11	0.1125(5)	-0.1612(7)	-0.2728(8)	1.0	3.4(5)
O12	0.2399(7)	-0.1538(8)	-0.2360(14)	1.0	3.4(5)
O13	0.3137(8)	-0.0491(2)	-0.1990(15)	1.0	3.4(5)
O14	0.0848(5)	-0.0511(2)	-0.1757(19)	1.0	3.4(5)
O15	0.4251(4)	0.1245(3)	-0.3987(6)	1.0	3.4(5)
O16	0.4006(4)	-0.0039(4)	-0.4074(12)	1.0	3.4(5)
O17	0.3947(5)	-0.1346(3)	-0.4188(8)	1.0	3.4(5)
O18	0.1989(6)	0.1331(3)	-0.3725(7)	1.0	3.4(5)

O19	0.2024(5)	0.0030(3)	-0.3922(11)	1.0	3.4(5)
O20	0.1946(6)	-0.1267(3)	-0.4146(8)	1.0	3.4(5)
O21	-0.0052(3)	0.0406(5)	-0.2088(4)	1.0	3.4(5)
O22	-0.0087(4)	-0.1391(4)	-0.2111(9)	1.0	3.4(5)
O23	0.4332(55)	-1/4	-0.3464(10)	1.0	3.4(5)
O24	0.1936(10)	-1/4	-0.3487(17)	1.0	3.4(5)
O25	0.2821(10)	-1/4	0.0443(15)	1.0	3.4(5)
O26	0.1033(11)	-1/4	0.0646(13)	1.0	3.4(5)

Table N

422_AS-ZSM-5, 200 °C

Site	x/a	y/b	z/c	Fraction	Ui/Ue*100
T1	0.4228(9)	0.0564(9)	-0.3378(13)	1.0	1.0(5)
T2	0.3105(11)	0.0302(9)	-0.1859(15)	1.0	1.0(5)
T3	0.2811(9)	0.0608(10)	0.0325(14)	1.0	1.0(5)
T4	0.1235(9)	0.0658(10)	0.0262(14)	1.0	1.0(5)
T5	0.0712(10)	0.0288(10)	-0.1836(15)	1.0	1.0(5)
T6	0.1876(9)	0.0599(11)	-0.3210(16)	1.0	1.0(5)
T7	0.4231(10)	-0.1722(7)	-0.3218(14)	1.0	1.0(5)
T8	0.3093(11)	-0.1294(9)	-0.1806(16)	1.0	1.0(5)
T9	0.2723(10)	-0.1720(7)	0.0371(15)	1.0	1.0(5)
T10	0.1167(10)	-0.1743(7)	0.0302(17)	1.0	1.0(5)
T11	0.0703(10)	-0.1289(10)	-0.1837(18)	1.0	1.0(5)
T12	0.1878(11)	-0.1725(7)	-0.3167(16)	1.0	1.0(5)
O1	0.3706(12)	0.0603(14)	-0.2489(18)	1.0	1.7(7)
O2	0.3155(12)	0.0559(18)	-0.0741(16)	1.0	1.7(7)
O3	0.2024(7)	0.0608(13)	0.0188(21)	1.0	1.7(7)
O4	0.0923(12)	0.0653(15)	-0.0828(14)	1.0	1.7(7)
O5	0.1152(10)	0.0556(15)	-0.2735(17)	1.0	1.7(7)
O6	0.2419(12)	0.0533(20)	-0.2347(23)	1.0	1.7(7)
O7	0.3729(14)	-0.1625(15)	-0.2312(21)	1.0	1.7(7)
O8	0.3052(14)	-0.1511(17)	-0.0666(13)	1.0	1.7(7)
O9	0.1941(8)	-0.1576(19)	0.0333(26)	1.0	1.7(7)
O10	0.0896(16)	-0.1644(13)	-0.0808(15)	1.0	1.7(7)
O11	0.1162(12)	-0.1575(19)	-0.2703(19)	1.0	1.7(7)
O12	0.2439(15)	-0.1533(20)	-0.2377(23)	1.0	1.7(7)
O13	0.3149(21)	-0.0497(7)	-0.1875(29)	1.0	1.7(7)
O14	0.0818(15)	-0.0501(8)	-0.1726(30)	1.0	1.7(7)
O15	0.4226(12)	0.1256(9)	-0.3968(18)	1.0	1.7(7)
O16	0.4037(13)	-0.0032(11)	-0.4117(20)	1.0	1.7(7)
O17	0.3964(14)	-0.1334(10)	-0.4177(17)	1.0	1.7(7)

O18	0.1954(15)	0.1305(10)	-0.3748(15)	1.0	1.7(7)
O19	0.1972(17)	0.0011(11)	-0.4001(23)	1.0	1.7(7)
O20	0.1971(15)	-0.1290(11)	-0.4151(16)	1.0	1.7(7)
O21	-0.0050(8)	0.0435(14)	-0.2070(15)	1.0	1.7(7)
O22	-0.0057(10)	-0.1434(16)	-0.2089(19)	1.0	1.7(7)
O23	0.4295(21)	-1/4	-0.3469(25)	1.0	1.7(7)
O24	0.1935(23)	-1/4	-0.3437(33)	1.0	1.7(7)
O25	0.2844(23)	-1/4	0.0557(32)	1.0	1.7(7)
O26	0.1050(23)	-1/4	0.0640(25)	1.0	1.7(7)

Table O

422_AS-ZSM-5, 400 °C

Site	x/a	y/b	z/c	Fraction	Ui/Ue*100
T1	0.4232(3)	0.0569(3)	-0.3358(5)	1.0	1.2(1)
T2	0.3112(4)	0.0307(3)	-0.1851(5)	1.0	1.2(1)
T3	0.2810(3)	0.0584(3)	0.0346(5)	1.0	1.2(1)
T4	0.1234(3)	0.0650(3)	0.0283(5)	1.0	1.2(1)
T5	0.0717(3)	0.0277(3)	-0.1823(6)	1.0	1.2(1)
T6	0.1890(3)	0.0625(3)	-0.3181(5)	1.0	1.2(1)
T7	0.4230(3)	-0.1721(2)	-0.3217(6)	1.0	1.2(1)
T8	0.3085(4)	-0.1283(3)	-0.1821(6)	1.0	1.2(1)
T9	0.2717(3)	-0.1710(2)	0.0345(6)	1.0	1.2(1)
T10	0.1164(3)	-0.1739(2)	0.0300(6)	1.0	1.2(1)
T11	0.0704(3)	-0.1294(3)	-0.1833(6)	1.0	1.2(1)
T12	0.1873(4)	-0.1727(2)	-0.3179(6)	1.0	1.2(1)
O1	0.3719(4)	0.0628(5)	-0.2455(7)	1.0	2.4(2)
O2	0.3170(3)	0.0509(5)	-0.0708(5)	1.0	2.4(2)
O3	0.2024(2)	0.0601(5)	0.0181(7)	1.0	2.4(2)
O4	0.0905(4)	0.0634(5)	-0.0799(5)	1.0	2.4(2)
O5	0.1165(3)	0.0569(5)	-0.2703(7)	1.0	2.4(2)
O6	0.2431(4)	0.0579(6)	-0.2308(8)	1.0	2.4(2)
O7	0.3724(5)	-0.1631(5)	-0.2308(8)	1.0	2.4(2)
O8	0.3050(5)	-0.1460(5)	-0.0667(5)	1.0	2.4(2)
O9	0.1936(3)	-0.1553(6)	0.0320(9)	1.0	2.4(2)
O10	0.0884(5)	-0.1655(4)	-0.0807(6)	1.0	2.4(2)
O11	0.1155(4)	-0.1594(7)	-0.2705(7)	1.0	2.4(2)
O12	0.2431(5)	-0.1546(6)	-0.2375(8)	1.0	2.4(2)
O13	0.3139(7)	-0.0489(2)	-0.1959(9)	1.0	2.4(2)
O14	0.0835(5)	-0.0509(3)	-0.1730(11)	1.0	2.4(2)
O15	0.4238(4)	0.1257(3)	-0.3966(7)	1.0	2.4(2)
O16	0.4024(4)	-0.0029(4)	-0.4078(8)	1.0	2.4(2)

O17	0.3957(5)	-0.1333(0)	-0.4171(7)	1.0	2.4(2)
O18	0.1954(5)	0.1330(3)	-0.3733(5)	1.0	2.4(2)
O19	0.1999(5)	0.0030(4)	-0.3954(8)	1.0	2.4(2)
O20	0.1961(5)	-0.1270(3)	-0.4143(6)	1.0	2.4(2)
O21	-0.0044(3)	0.0422(5)	-0.2081(6)	1.0	2.4(2)
O22	-0.0061(3)	-0.1420(5)	-0.2093(7)	1.0	2.4(2)
O23	0.4306(7)	-1/4	-0.3469(10)	1.0	2.4(2)
O24	0.1936(8)	-1/4	-0.3481(11)	1.0	2.4(2)
O25	0.2828(8)	-1/4	0.0462(12)	1.0	2.4(2)
O26	0.1069(8)	-1/4	0.0651(9)	1.0	2.4(2)

Table P

422_AS-ZSM-5, 600 °C

Site	x/a	y/b	z/c	Fraction	Ui/Ue*100
T1	0.4228(2)	0.0562(3)	-0.3371(5)	1.0	1.5(1)
T2	0.3112(3)	0.0303(3)	-0.1842(5)	1.0	1.5(1)
T3	0.2810(2)	0.0581(3)	0.0350(5)	1.0	1.5(1)
T4	0.1238(2)	0.0658(3)	0.0273(5)	1.0	1.5(1)
T5	0.0713(3)	0.0273(3)	-0.1818(5)	1.0	1.5(1)
T6	0.1893(3)	0.0626(3)	-0.3164(5)	1.0	1.5(1)
T7	0.4227(3)	-0.1721(2)	-0.3213(5)	1.0	1.5(1)
T8	0.3085(3)	-0.1285(3)	-0.1807(5)	1.0	1.5(1)
T9	0.2712(3)	-0.1708(2)	0.0356(5)	1.0	1.5(1)
T10	0.1164(3)	-0.174(2)	0.0303(6)	1.0	1.5(1)
T11	0.0699(3)	-0.1291(3)	-0.1818(6)	1.0	1.5(1)
T12	0.1872(3)	-0.1726(2)	-0.3159(5)	1.0	1.5(1)
O1	0.3708(4)	0.0625(4)	-0.2472(6)	1.0	3.4(2)
O2	0.3187(3)	0.0504(6)	-0.0696(5)	1.0	3.4(2)
O3	0.2027(2)	0.0603(4)	0.0146(6)	1.0	3.4(2)
O4	0.0896(3)	0.0651(5)	-0.0803(5)	1.0	3.4(2)
O5	0.1161(3)	0.0558(4)	-0.2708(6)	1.0	3.4(2)
O6	0.2422(3)	0.0576(6)	-0.2274(7)	1.0	3.4(2)
O7	0.3721(4)	-0.1637(5)	-0.2301(7)	1.0	3.4(2)
O8	0.3060(4)	-0.1457(5)	-0.0647(5)	1.0	3.4(2)
O9	0.1933(2)	-0.1540(6)	0.0311(9)	1.0	3.4(2)
O10	0.0876(5)	-0.1673(4)	-0.0805(5)	1.0	3.4(2)
O11	0.1149(4)	-0.1586(6)	-0.2698(6)	1.0	3.4(2)
O12	0.2425(5)	-0.1551(6)	-0.2343(8)	1.0	3.4(2)
O13	0.3139(7)	-0.0492(2)	-0.1955(9)	1.0	3.4(2)
O14	0.0842(4)	-0.0510(2)	-0.1692(10)	1.0	3.4(2)
O15	0.4243(3)	0.1252(3)	-0.3975(6)	1.0	3.4(2)

O16	0.4015(4)	-0.0033(3)	-0.4093(7)	1.0	3.4(2)
O17	0.3941(4)	-0.1340(3)	-0.4167(6)	1.0	3.4(2)
O18	0.1964(4)	0.1334(3)	-0.3709(5)	1.0	3.4(2)
O19	0.2018(5)	0.0037(3)	-0.3946(7)	1.0	3.4(2)
O20	0.1970(5)	-0.1265(3)	-0.4122(6)	1.0	3.4(2)
O21	-0.0051(2)	0.0404(4)	-0.2076(5)	1.0	3.4(2)
O22	-0.0068(3)	-0.1404(5)	-0.2082(7)	1.0	3.4(2)
O23	0.4317(6)	-1/4	-0.3460(9)	1.0	3.4(2)
O24	0.1931(7)	-1/4	-0.3461(11)	1.0	3.4(2)
O25	0.2812(7)	-1/4	0.0464(11)	1.0	3.4(2)
O26	0.1083(7)	-1/4	0.0671(8)	1.0	3.4(2)

Table Q

422_AS-ZSM-5, 800 °C

Site	x/a	y/b	z/c	Fraction	Ui/Ue*100
T1	0.4230(2)	0.0565(2)	-0.3357(4)	1.0	1.7(1)
T2	0.3118(3)	0.0302(2)	-0.1834(5)	1.0	1.7(1)
T3	0.2807(2)	0.0585(2)	0.0353(4)	1.0	1.7(1)
T4	0.1235(2)	0.0654(3)	0.0284(5)	1.0	1.7(1)
T5	0.0715(3)	0.0274(3)	-0.1811(5)	1.0	1.7(1)
T6	0.1895(2)	0.0621(3)	-0.3164(5)	1.0	1.7(1)
T7	0.4230(3)	-0.1722(2)	-0.3207(5)	1.0	1.7(1)
T8	0.3095(3)	-0.1287(3)	-0.1796(5)	1.0	1.7(1)
T9	0.2717(3)	-0.1712(2)	0.0366(5)	1.0	1.7(1)
T10	0.1165(3)	-0.1743(2)	0.0311(5)	1.0	1.7(1)
T11	0.0706(3)	-0.1293(3)	-0.1815(6)	1.0	1.7(1)
T12	0.1881(3)	-0.1727(2)	-0.3157(5)	1.0	1.7(1)
O1	0.3717(3)	0.0627(4)	-0.2454(6)	1.0	3.9(2)
O2	0.3183(3)	0.0512(5)	-0.0692(4)	1.0	3.9(2)
O3	0.2024(2)	0.0600(4)	0.0158(6)	1.0	3.9(2)
O4	0.0894(3)	0.0647(4)	-0.0792(5)	1.0	3.9(2)
O5	0.1167(3)	0.0558(4)	-0.2695(6)	1.0	3.9(2)
O6	0.2430(3)	0.0568(5)	-0.2283(6)	1.0	3.9(2)
O7	0.3732(4)	-0.1638(4)	-0.2286(7)	1.0	3.9(2)
O8	0.3061(4)	-0.1465(4)	-0.0641(4)	1.0	3.9(2)
O9	0.1936(2)	-0.1554(5)	0.0324(8)	1.0	3.9(2)
O10	0.0881(4)	-0.1670(3)	-0.0797(5)	1.0	3.9(2)
O11	0.1161(3)	-0.1586(5)	-0.2689(6)	1.0	3.9(2)
O12	0.2438(4)	-0.1548(5)	-0.2348(7)	1.0	3.9(2)
O13	0.3151(6)	-0.0493(2)	-0.1934(8)	1.0	3.9(2)
O14	0.0839(4)	-0.0510(5)	-0.1691(9)	1.0	3.9(2)

O15	0.4239(3)	0.12540(8)	-0.3964(5)	1.0	3.9(2)
O16	0.4017(4)	-0.0030(3)	-0.4079(7)	1.0	3.9(2)
O17	0.3944(4)	-0.1335(3)	-0.4155(6)	1.0	3.9(2)
O18	0.1962(4)	0.1329(3)	-0.3706(5)	1.0	3.9(2)
O19	0.2011(4)	0.0032(3)	-0.3946(6)	1.0	3.9(2)
O20	0.1975(4)	-0.1271(2)	-0.4124(5)	1.0	3.9(2)
O21	-0.0046(2)	0.0411(4)	-0.2082(5)	1.0	3.9(2)
O22	-0.0059(3)	-0.1415(4)	-0.2086(6)	1.0	3.9(2)
O23	0.4311(6)	-1/4	-0.3464(8)	1.0	3.9(2)
O24	0.1939(7)	-1/4	-0.3455(10)	1.0	3.9(2)
O25	0.2829(7)	-1/4	0.0490(10)	1.0	3.9(2)
O26	0.1072(7)	-1/4	0.0679(8)	1.0	3.9(2)

Table R

424_AS-ZSM-5, 200 °C

Site	x/a	y/b	z/c	Fraction	Ui/Ue*100
T1	0.4228(9)	0.0561(10)	-0.3376(16)	1.0	0.4(7)
T2	0.3104(12)	0.0302(10)	-0.1854(19)	1.0	0.4(7)
T3	0.2809(9)	0.0596(11)	0.0332(17)	1.0	0.4(7)
T4	0.1235(9)	0.0659(11)	0.0262(17)	1.0	0.4(7)
T5	0.0713(10)	0.0278(10)	-0.1826(18)	1.0	0.4(7)
T6	0.1884(11)	0.0612(13)	-0.3188(19)	1.0	0.4(7)
T7	0.4230(11)	-0.1721(7)	-0.3214(16)	1.0	0.4(7)
T8	0.3086(12)	-0.1292(10)	-0.1813(20)	1.0	0.4(7)
T9	0.2717(11)	-0.1716(7)	0.0366(18)	1.0	0.4(7)
T10	0.1164(12)	-0.1745(8)	0.0314(21)	1.0	0.4(7)
T11	0.0708(12)	-0.1293(11)	-0.1820(23)	1.0	0.4(7)
T12	0.1874(12)	-0.1729(8)	-0.3175(20)	1.0	0.4(7)
O1	0.3706(14)	0.0606(16)	-0.2484(24)	1.0	0.8(1)
O2	0.3172(11)	0.0528(22)	-0.0720(20)	1.0	0.8(1)
O3	0.2024(7)	0.0610(14)	0.0159(21)	1.0	0.8(1)
O4	0.0909(12)	0.0657(18)	-0.0821(18)	1.0	0.8(1)
O5	0.1156(11)	0.0550(18)	-0.2725(21)	1.0	0.8(1)
O6	0.2419(13)	0.0564(25)	-0.2311(25)	1.0	0.8(1)
O7	0.3733(18)	-0.1621(18)	-0.2299(25)	1.0	0.8(1)
O8	0.3044(17)	-0.1488(20)	-0.0663(17)	1.0	0.8(1)
O9	0.1937(9)	-0.1563(23)	0.0345(32)	1.0	0.8(1)
O10	0.0894(18)	-0.1662(14)	-0.0799(19)	1.0	0.8(1)
O11	0.1162(15)	-0.1580(22)	-0.2695(23)	1.0	0.8(1)
O12	0.2440(18)	-0.1558(23)	-0.2382(31)	1.0	0.8(1)
O13	0.3127(27)	-0.0497(8)	-0.1917(37)	1.0	0.8(1)

O14	0.0833(16)	-0.0508(9)	-0.1700(40)	1.0	0.8(1)
O15	0.4238(12)	0.1255(10)	-0.3966(21)	1.0	0.8(1)
O16	0.4027(14)	-0.0030(12)	-0.4116(26)	1.0	0.8(1)
O17	0.3955(15)	-0.1335(12)	-0.4170(20)	1.0	0.8(1)
O18	0.1950(19)	0.1318(12)	-0.3735(18)	1.0	0.8(1)
O19	0.2002(18)	0.0024(13)	-0.3972(27)	1.0	0.8(1)
O20	0.1967(17)	-0.1277(12)	-0.4144(20)	1.0	0.8(1)
O21	-0.0052(9)	0.0413(15)	-0.2073(16)	1.0	0.8(1)
O22	-0.0056(12)	-0.1426(18)	-0.2078(22)	1.0	0.8(1)
O23	0.4296(24)	-1/4	-0.3460(29)	1.0	0.8(1)
O24	0.1922(26)	-1/4	-0.3476(40)	1.0	0.8(1)
O25	0.2833(27)	-1/4	0.0520(40)	1.0	0.8(1)
O26	0.1060(28)	-1/4	0.0670(30)	1.0	0.8(1)

Table S

424_AS-ZSM-5, 400 °C

Site	x/a	y/b	z/c	Fraction	Ui/Ue*100
T1	0.4231(2)	0.0568(3)	-0.3359(5)	1.0	0.6(2)
T2	0.3114(3)	0.0308(2)	-0.1855(6)	1.0	0.6(2)
T3	0.2813(2)	0.0584(3)	0.0341(5)	1.0	0.6(2)
T4	0.1239(2)	0.0653(3)	0.0275(5)	1.0	0.6(2)
T5	0.0715(3)	0.0276(3)	-0.1826(6)	1.0	0.6(2)
T6	0.1892(3)	0.0627(4)	-0.3172(6)	1.0	0.6(2)
T7	0.4230(3)	-0.1721(2)	-0.3208(5)	1.0	0.6(2)
T8	0.3084(3)	-0.1281(3)	-0.1825(6)	1.0	0.6(2)
T9	0.2709(3)	-0.1711(2)	0.0351(6)	1.0	0.6(2)
T10	0.1156(3)	-0.1743(2)	0.0311(7)	1.0	0.6(2)
T11	0.0705(3)	-0.1295(3)	-0.1829(7)	1.0	0.6(2)
T12	0.1870(3)	-0.1729(2)	-0.3186(7)	1.0	0.6(2)
O1	0.3714(4)	0.0636(4)	-0.2463(8)	1.0	1.0(3)
O2	0.3184(3)	0.0500(6)	-0.0705(6)	1.0	1.0(3)
O3	0.2029(2)	0.06091(4)	0.0154(7)	1.0	1.0(3)
O4	0.0899(3)	0.0641(6)	-0.0802(6)	1.0	1.0(3)
O5	0.1162(3)	0.0567(5)	-0.2709(7)	1.0	1.0(3)
O6	0.2426(4)	0.0583(7)	-0.2291(7)	1.0	1.0(3)
O7	0.3728(5)	-0.1632(5)	-0.2293(9)	1.0	1.0(3)
O8	0.3036(5)	-0.1455(6)	-0.0666(6)	1.0	1.0(3)
O9	0.1928(2)	-0.1554(7)	0.0339(10)	1.0	1.0(3)
O10	0.0883(5)	-0.1665(4)	-0.0804(6)	1.0	1.0(3)
O11	0.1155(4)	-0.1596(7)	-0.2703(7)	1.0	1.0(3)
O12	0.2434(6)	-0.1549(7)	-0.2389(10)	1.0	1.0(3)

O13	0.3139(8)	-0.0488(2)	-0.1970(11)	1.0	1.0(3)
O14	0.0843(4)	-0.0511(2)	-0.1720(13)	1.0	1.0(3)
O15	0.4251(3)	0.1256(3)	-0.3968(6)	1.0	1.0(3)
O16	0.4011(4)	-0.0026(3)	-0.4085(9)	1.0	1.0(3)
O17	0.39501(4)	-0.1333(3)	-0.4162(7)	1.0	1.0(3)
O18	0.1957(5)	0.1332(3)	-0.3727(6)	1.0	1.0(3)
O19	0.2011(5)	0.0032(3)	-0.3947(8)	1.0	1.0(3)
O20	0.1954(5)	-0.1269(3)	-0.4150(7)	1.0	1.0(3)
O21	-0.0048(2)	0.0408(4)	-0.2084(5)	1.0	1.0(3)
O22	-0.0061(3)	-0.1415(5)	-0.2090(7)	1.0	1.0(3)
O23	0.43096(7)	-1/4	-0.3462(9)	1.0	1.0(3)
O24	0.1932(8)	-1/4	-0.3495(13)	1.0	1.0(3)
O25	0.2824(8)	-1/4	0.0461(13)	1.0	1.0(3)
O26	0.1060(8)	-1/4	0.0672(10)	1.0	1.0(3)

Table T

424_AS-ZSM-5, 600 °C

Site	x/a	y/b	z/c	Fraction	Ui/Ue*100
T1	0.4230(2)	0.0563(3)	-0.3362(5)	1.0	0.8(2)
T2	0.3112(3)	0.0303(3)	-0.1842(6)	1.0	0.8(2)
T3	0.2808(2)	0.0580(3)	0.0346(5)	1.0	0.8(2)
T4	0.1237(2)	0.0657(3)	0.0271(5)	1.0	0.8(2)
T5	0.0713(3)	0.0272(3)	-0.1816(6)	1.0	0.8(2)
T6	0.1894(3)	0.0627(3)	-0.3159(6)	1.0	0.8(2)
T7	0.4231(3)	-0.1720(2)	-0.3203(5)	1.0	0.8(2)
T8	0.3089(4)	-0.1285(3)	-0.1807(6)	1.0	0.8(2)
T9	0.2710(3)	-0.1710(2)	0.0368(6)	1.0	0.8(2)
T10	0.1159(3)	-0.1744(2)	0.0325(7)	1.0	0.8(2)
T11	0.0708(3)	-0.1294(34)	-0.1809(7)	1.0	0.8(2)
T12	0.1876(3)	-0.1730(2)	-0.3171(6)	1.0	0.8(2)
O1	0.3710(4)	0.0625(4)	-0.2466(8)	1.0	1.8(2)
O2	0.3192(3)	0.0498(6)	-0.0693(6)	1.0	1.8(2)
O3	0.2026(2)	0.06068(4)	0.0134(7)	1.0	1.8(2)
O4	0.0890(3)	0.0655(5)	-0.0803(6)	1.0	1.8(2)
O5	0.1162(3)	0.0554(5)	-0.2706(7)	1.0	1.8(2)
O6	0.2423(4)	0.0583(7)	-0.2268(7)	1.0	1.8(2)
O7	0.3737(5)	-0.1630(5)	-0.2276(8)	1.0	1.8(2)
O8	0.3044(5)	-0.1456(5)	-0.0646(5)	1.0	1.8(2)
O9	0.1930(2)	-0.1547(7)	0.0350(10)	1.0	1.8(2)
O10	0.0884(5)	-0.16747(4)	-0.0791(6)	1.0	1.8(2)
O11	0.1161(4)	-0.1589(6)	-0.2687(7)	1.0	1.8(2)

O12	0.2442(5)	-0.1564(9)	-0.2368(9)	1.0	1.8(2)
O13	0.3132(8)	-0.0493(2)	-0.1957(10)	1.0	1.8(2)
O14	0.0847(4)	-0.0511(2)	-0.1684(12)	1.0	1.8(2)
O15	0.4253(3)	0.1255(3)	-0.3960(6)	1.0	1.8(2)
O16	0.4012(4)	-0.0027(3)	-0.4096(8)	1.0	1.8(2)
O17	0.3940(4)	-0.1335(3)	-0.4154(6)	1.0	1.8(2)
O18	0.1956(5)	0.1336(3)	-0.3704(6)	1.0	1.8(2)
O19	0.2026(5)	0.0039(3)	-0.3942(8)	1.0	1.8(2)
O20	0.1967(5)	-0.1263(3)	-0.4130(6)	1.0	1.8(2)
O21	-0.0051(2)	0.0396(4)	-0.2085(5)	1.0	1.8(2)
O22	-0.0057(3)	-0.1412(5)	-0.2077(7)	1.0	1.8(2)
O23	0.4309(7)	-1/4	-0.3454(9)	1.0	1.8(2)
O24	0.1926(8)	-1/4	-0.3490(12)	1.0	1.8(2)
O25	0.2818(8)	-1/4	0.0476(12)	1.0	1.8(2)
O26	0.1070(8)	-1/4	0.0695(9)	1.0	1.8(2)

Table U

424_AS-ZSM-5, 800 °C

Site	x/a	y/b	z/c	Fraction	Ui/Ue*100
T1	0.4229(5)	0.0564(2)	-0.3353(5)	1.0	1.3(2)
T2	0.3118(5)	0.0303(2)	-0.1828(5)	1.0	1.3(2)
T3	0.2808(5)	0.0582(3)	0.0355(5)	1.0	1.3(2)
T4	0.1240(4)	0.0656(2)	0.0278(5)	1.0	1.3(2)
T5	0.0714(8)	0.0272(2)	-0.1811(5)	1.0	1.3(2)
T6	0.1900(3)	0.0625(3)	-0.3146(5)	1.0	1.3(2)
T7	0.4228(3)	-0.1720(1)	-0.3199(5)	1.0	1.3(2)
T8	0.3090(3)	-0.1285(2)	-0.1798(6)	1.0	1.3(2)
T9	0.2708(3)	-0.1711(1)	0.0373(5)	1.0	1.3(2)
T10	0.1157(3)	-0.1744(2)	0.0323(6)	1.0	1.3(2)
T11	0.0706(3)	-0.1295(3)	-0.1810(7)	1.0	1.3(2)
T12	0.1878(3)	-0.1729(2)	-0.3160(6)	1.0	1.3(2)
O1	0.3714(4)	0.0629(4)	-0.2451(7)	1.0	3.7(3)
O2	0.3198(2)	0.0498(6)	-0.0678(6)	1.0	3.7(3)
O3	0.2027(1)	0.0606(3)	0.0133(6)	1.0	3.7(3)
O4	0.0887(3)	0.0650(5)	-0.0792(5)	1.0	3.7(3)
O5	0.1167(3)	0.0556(5)	-0.2695(6)	1.0	3.7(3)
O6	0.2428(3)	0.0581(6)	-0.2254(6)	1.0	3.7(3)
O7	0.3734(5)	-0.1633(5)	-0.2272(8)	1.0	3.7(3)
O8	0.3049(5)	-0.1458(5)	-0.0636(5)	1.0	3.7(3)
O9	0.1928(2)	-0.1549(6)	0.0341(10)	1.0	3.7(3)
O10	0.0878(5)	-0.1675(3)	-0.0790(5)	1.0	3.7(3)

O11	0.1160(4)	-0.1590(6)	-0.2685(7)	1.0	3.7(3)
O12	0.2439(5)	-0.1556(6)	-0.2354(9)	1.0	3.7(3)
O13	0.3140(7)	-0.0492(2)	-0.1944(10)	1.0	3.7(3)
O14	0.0844(4)	-0.0512(2)	-0.1685(12)	1.0	3.7(3)
O15	0.4250(3)	0.1254(2)	-0.3958(6)	1.0	3.7(3)
O16	0.4007(3)	-0.0028(3)	-0.4082(8)	1.0	3.7(3)
O17	0.3937(4)	-0.1335(3)	-0.4149(6)	1.0	3.7(3)
O18	0.1966(5)	0.1333(3)	-0.3695(5)	1.0	3.7(3)
O19	0.2029(4)	0.0034(3)	-0.3927(7)	1.0	3.7(3)
O20	0.1971(4)	-0.1267(3)	-0.4123(6)	1.0	3.7(3)
O21	-0.0049(2)	0.0399(4)	-0.2085(4)	1.0	3.7(3)
O22	-0.0060(3)	-0.1413(4)	-0.2082(7)	1.0	3.7(3)
O23	0.4307(6)	-1/4	-0.3453(8)	1.0	3.7(3)
O24	0.1934(7)	-1/4	-0.3472(12)	1.0	3.7(3)
O25	0.2817(7)	-1/4	0.0488(12)	1.0	3.7(3)
O26	0.1068(8)	-1/4	0.0696(9)	1.0	3.7(3)

Table V

423_AS-ZSM-5

Bond distances (Å)	**25 °C**	**200 °C**	**400 °C**	**600 °C**	**800 °C**
T1-O1	1.591(1)	1.591(1)	1.591(4)	1.591(4)	1.592(4)
T1-O15	1.593(1)	1.593(1)	1.593(4)	1.593(4)	1.594(4)
T1-O16	1.594(1)	1.594(1)	1.592(4)	1.593(4)	1.592(4)
T1-O21	1.591(1)	1.591(1)	1.591(4)	1.591(4)	1.593(4)
T2-O1	1.592(1)	1.593(1)	1.593(4)	1.593(4)	1.595(4)
T2-O2	1.591(1)	1.591(1)	1.592(4)	1.592(4)	1.593(4)
T2-O6	1.593(1)	1.593(1)	1.593(4)	1.593(4)	1.593(4)
T2-O13	1.594(1)	1.594(1)	1.592(4)	1.593(4)	1.593(4)
T3-O2	1.592(1)	1.592(1)	1.593(4)	1.594(4)	1.594(4)
T3-O3	1.591(1)	1.591(1)	1.592(4)	1.592(4)	1.592(4)
T3-O19	1.593(1)	1.593(1)	1.593(4)	1.592(4)	1.592(4)
T3-O20	1.593(1)	1.594(1)	1.594(4)	1.594(4)	1.595(4)
T4-O3	1.590(1)	1.591(1)	1.592(4)	1.592(4)	1.591(4)
T4-O4	1.595(1)	1.595(1)	1.593(4)	1.593(4)	1.593(4)
T4-O16	1.595(1)	1.596(1)	1.593(4)	1.593(4)	1.593(4)
T4-O17	1.593(1)	1.593(1)	1.592(4)	1.593(4)	1.593(4)
T5-O4	1.595(1)	1.595(1)	1.593(4)	1.592(4)	1.592(4)
T5-O5	1.591(1)	1.591(1)	1.591(4)	1.591(4)	1.592(4)
T5-O14	1.594(1)	1.594(1)	1.593(4)	1.594(4)	1.594(4)
T5-O21	1.592(1)	1.592(1)	1.591(4)	1.592(4)	1.594(4)
T6-O5	1.591(1)	1.592(1)	1.592(4)	1.593(4)	1.594(4)
T6-O6	1.595(1)	1.595(1)	1.595(4)	1.594(4)	1.593(4)

T6-O18	1.592(1)	1.592(1)	1.592(4)	1.593(4)	1.594(4)
T6-O19	1.593(1)	1.593(1)	1.594(4)	1.592(4)	1.594(4)
T7-O7	1.594(1)	1.593(1)	1.594(4)	1.593(4)	1.593(4)
T7-O17	1.595(1)	1.595(1)	1.592(4)	1.592(4)	1.593(4)
T7-O22	1.594(1)	1.594(1)	1.592(4)	1.594(4)	1.594(4)
T7-O23	1.594(1)	1.594(1)	1.594(4)	1.596(4)	1.596(4)
T8-O7	1.593(1)	1.592(1)	1.593(4)	1.594(4)	1.594(4)
T8-O8	1.592(1)	1.592(1)	1.590(4)	1.591(4)	1.591(4)
T8-O12	1.594(1)	1.595(1)	1.596(4)	1.595(4)	1.594(4)
T8-O13	1.595(1)	1.594(1)	1.592(4)	1.593(4)	1.593(4)
T9-O8	1.595(1)	1.594(1)	1.592(4)	1.592(4)	1.592(4)
T9-O9	1.593(1)	1.593(1)	1.592(4)	1.594(4)	1.593(4)
T9-O18	1.592(1)	1.592(1)	1.593(4)	1.593(4)	1.594(4)
T9-O25	1.592(1)	1.592(1)	1.593(4)	1.594(4)	1.595(4)
T10-O9	1.590(1)	1.590(1)	1.590(4)	1.591(4)	1.595(4)
T10-O10	1.597(1)	1.597(1)	1.595(4)	1.594(4)	1.594(4)
T10-O15	1.595(1)	1.594(1)	1.595(4)	1.595(4)	1.596(4)
T10-O26	1.591(1)	1.591(1)	1.592(4)	1.593(4)	1.594(4)
T11-O10	1.596(1)	1.597(1)	1.594(4)	1.594(4)	1.593(4)
T11-O11	1.592(1)	1.592(1)	1.593(4)	1.593(4)	1.593(4)
T11-O14	1.593(1)	1.593(1)	1.593(4)	1.593(4)	1.593(4)
T11-O22	1.593(1)	1.592(1)	1.592(4)	1.593(4)	1.594(4)
T12-O11	1.594(1)	1.594(1)	1.594(4)	1.594(4)	1.595(4)
T12-O12	1.593(1)	1.594(1)	1.595(4)	1.594(4)	1.593(4)
T12-O20	1.592(1)	1.592(1)	1.593(4)	1.592(4)	1.593(4)
T12-O24	1.593(1)	1.593(1)	1.593(4)	1.594(4)	1.595(4)
<T-O>	1.593	1.593	1.592	1.593	1.593
			T-O-T angles (°C)		
T1_O1_T2	147.4(2)	147.9(2)	147.0(8)	146.0(8)	147.0(8)
T2_O2_T3	150.2(2)	149.4(2)	148.8(7)	147.2(7)	146.3(7)
T3_O3_T4	170.1(2)	169.2(2)	167.4(7)	165.2(7)	164.8(7)
T4_O4_T5	157.0(2)	156.5(3)	155.9(1)	155.0(1)	153.8(1)
T5_O5_T6	144.6(1)	144.7(1)	146.3(7)	145.6(6)	144.8(7)
T2_O6_T6	152.4(2)	152.8(2)	149.8(9)	149.0(8)	147.1(8)
T7_O7_T8	151.5(2)	151.4(2)	150.9(9)	150.0(8)	150.4(9)
T8_O8_T9	159.4(3)	158.9(3)	157.2(1)	156.3(1)	156.1(1)
T9_O9_T10	163.0(1)	164.0(2)	159.6(1)	160.3(1)	158.3(5)
T10_O10_T11	161.5(2)	161.6(2)	160.6(8)	159.2(8)	158.2(8)
T11_O11_T12	148.6(2)	149.0(2)	149.6(9)	148.6(9)	147.8(9)
T8_O12_T12	166.2(3)	166.0(3)	164.6(9)	164.2(9)	163.2(9)
T2_O13_T8	167.2(2)	167.6(2)	165.0(8)	164.0(8)	163.4(9)

T5_O14_T11	160.3(2)	160.8(2)	160.3(7)	158.8(7)	157.1(7)
T1_O15_T10	150.5(2)	151.0(2)	148.5(9)	148.8(9)	147.0(1)
T1_O16_T4	175.2(2)	174.7(2)	176.0(8)	177.2(8)	176.5(9)
T4_O17_T7	148.3(2)	148.5(2)	148.8(8)	148.5(7)	148.2(8)
T6_O18_T9	150.0(3)	151.0(4)	145.8(8)	147.2(8)	145.3(8)
SI3_O19_SI6	172.2(2)	171.6(2)	175.0(9)	175.9(8)	177.4(9)
T3_O20_T12	147.5(2)	147.4(2)	150.1(7)	149.7(7)	151.0(7)
T1_O21_T5	148.2(1)	147.6(1)	147.3(6)	146.4(6)	146.3(6)
T7_O22_T11	148.3(2)	148.4(2)	149.6(8)	148.0(8)	148.4(8)
T7_O23_T7	152.8(2)	152.3(2)	154.7(1)	152.7(9)	153.8(1)
T12_O24_T12	150.2(3)	151.5(3)	147.1(1)	148.0(1)	146.5(1)
T9_O25_T9	152.0(3)	151.0(3)	157.2(1)	156.3(1)	158.8(1)
T10_O26_T10	139.3(3)	139.1(3)	141.4(1)	140.1(1)	140.6(1)
<T-O-T>	155.1	155.1	154.7	154.1	153.7

Table W

425_AS-ZSM-5

Bond distances (Å)	**25 °C**	**200 °C**	**400 °C**	**600 °C**	**800 °C**
T1-O1	1.593(1)	1.592(1)	1.592(2)	1.592(2)	1.592(2)
T1-O15	1.593(1)	1.593(1)	1.593(2)	1.592(2)	1.592(2)
T1-O16	1.593(1)	1.593(1)	1.592(2)	1.592(2)	1.592(2)
T1-O21	1.593(1)	1.593(1)	1.593(2)	1.592(2)	1.593(2)
T2-O1	1.593(1)	1.593(1)	1.593(2)	1.593(2)	1.593(2)
T2-O2	1.593(1)	1.593(1)	1.592(2)	1.592(2)	1.592(2)
T2-O6	1.593(1)	1.593(1)	1.593(2)	1.593(2)	1.593(2)
T2-O13	1.594(1)	1.593(1)	1.593(2)	1.593(2)	1.593(2)
T3-O2	1.593(1)	1.593(1)	1.593(2)	1.592(2)	1.593(2)
T3-O3	1.593(1)	1.593(1)	1.593(2)	1.593(2)	1.593(2)
T3-O19	1.593(1)	1.593(1)	1.593(2)	1.592(2)	1.592(2)
T3-O20	1.593(1)	1.593(1)	1.593(2)	1.593(2)	1.594(2)
T4-O3	1.593(1)	1.593(1)	1.593(2)	1.592(2)	1.593(2)
T4-O4	1.594(1)	1.594(1)	1.593(2)	1.592(2)	1.593(2)
T4-O16	1.593(1)	1.594(1)	1.593(2)	1.592(2)	1.592(2)
T4-O17	1.593(1)	1.593(1)	1.593(2)	1.593(2)	1.593(2)
T5-O4	1.593(1)	1.593(1)	1.593(2)	1.592(2)	1.592(2)
T5-O5	1.593(1)	1.593(1)	1.593(2)	1.592(2)	1.593(2)
T5-O14	1.593(1)	1.593(1)	1.593(2)	1.592(2)	1.592(2)
T5-O21	1.594(1)	1.593(1)	1.593(2)	1.593(2)	1.593(2)
T6-O5	1.593(1)	1.593(1)	1.593(2)	1.593(2)	1.593(2)
T6-O6	1.594(1)	1.594(1)	1.594(2)	1.594(2)	1.594(2)
T6-O18	1.593(1)	1.593(1)	1.593(2)	1.593(2)	1.593(2)
T6-O19	1.594(1)	1.594(1)	1.593(2)	1.593(2)	1.593(2)

T7-O7	1.594(1)	1.594(1)	1.594(2)	1.593(2)	1.594(2)
T7-O17	1.594(1)	1.594(1)	1.594(2)	1.593(2)	1.593(2)
T7-O22	1.595(1)	1.595(1)	1.594(2)	1.594(2)	1.594(2)
T7-O23	1.594(1)	1.594(1)	1.594(2)	1.594(2)	1.594(2)
T8-O7	1.594(1)	1.594(1)	1.594(2)	1.594(2)	1.594(2)
T8-O8	1.593(1)	1.594(1)	1.593(2)	1.592(2)	1.592(2)
T8-O12	1.594(1)	1.594(1)	1.594(2)	1.594(2)	1.594(2)
T8-O13	1.594(1)	1.594(1)	1.593(2)	1.593(2)	1.593(2)
T9-O8	1.594(1)	1.595(1)	1.593(2)	1.593(2)	1.593(2)
T9-O9	1.594(1)	1.594(1)	1.594(2)	1.594(2)	1.594(2)
T9-O18	1.593(1)	1.593(1)	1.593(2)	1.593(2)	1.593(2)
T9-O25	1.594(1)	1.594(1)	1.593(2)	1.594(2)	1.594(2)
T10-O9	1.593(1)	1.593(1)	1.593(2)	1.592(2)	1.593(2)
T10-O10	1.595(1)	1.595(1)	1.594(2)	1.593(2)	1.594(2)
T10-O15	1.593(1)	1.593(1)	1.593(2)	1.593(2)	1.593(2)
T10-O26	1.593(1)	1.593(1)	1.593(2)	1.593(2)	1.594(2)
T11-O10	1.594(1)	1.594(1)	1.593(2)	1.593(2)	1.593(2)
T11-O11	1.593(1)	1.594(1)	1.593(2)	1.593(2)	1.593(2)
T11-O14	1.593(1)	1.593(1)	1.593(2)	1.592(2)	1.592(2)
T11-O22	1.594(1)	1.593(1)	1.593(2)	1.594(2)	1.594(2)
T12-O11	1.594(1)	1.594(1)	1.593(2)	1.593(2)	1.594(2)
T12-O12	1.593(1)	1.593(1)	1.593(2)	1.593(2)	1.593(2)
T12-O20	1.593(1)	1.593(1)	1.593(2)	1.592(2)	1.593(2)
T12-O24	1.593(1)	1.593(1)	1.593(2)	1.593(2)	1.594(2)
<T-O>	1.593	1.593	1.593	1.592	1.593
			T-O-T angles (°)		
T1_O1_T2	148.8(3)	148.3(3)	147.2(7)	147.2(7)	146.7(7)
T2_O2_T3	149.3(2)	148.8(2)	148.4(5)	145.3(5)	145.2(5)
T3_O3_T4	170.5(3)	169.4(3)	168.6(7)	164.2(6)	164.0(6)
T4_O4_T5	156.0(6)	156.0(6)	157.4(1)	153.2(1)	153.6(1)
T5_O5_T6	144.0(2)	144.4(2)	143.8(5)	144.6(5)	144.2(5)
T2_O6_T6	153.0(3)	153.0(2)	151.0(7)	149.2(6)	147.9(6)
T7_O7_T8	153.0(2)	152.0(2)	152.4(8)	150.3(7)	150.3(7)
T8_O8_T9	157.0(5)	157.0(5)	154.7(1)	154.9(1)	154.7(1)
T9_O9_T10	158.0(5)	159.0(6)	157.0(1)	156.2(1)	156.8(1)
T10_O10_T11	159.4(3)	159.3(3)	159.5(7)	157.1(7)	157.3(7)
T11_O11_T12	147.0(4)	148.0(2)	146.4(8)	147.7(8)	147.2(8)
T8_O12_T12	164.0(5)	164.0(5)	162.3(1)	163.1(9)	162.6(9)
T2_O13_T8	167.7(2)	167.4(2)	165.8(7)	165.1(7)	164.1(7)
T5_O14_T11	159.5(3)	159.5(3)	159.4(6)	157.3(6)	156.9(6)
T1_O15_T10	147.6(3)	149.0(3)	147.8(8)	146.4(8)	146.6(8)

T1_O16_T4	174.0(4)	174.0(3)	175.7(8)	176.0(8)	176.5(8)
T4_O17_T7	149.1(2)	148.9(2)	148.5(6)	149.5(6)	148.8(6)
T6_O18_T9	149.0(3)	150.0(4)	148.3(7)	146.6(7)	146.4(7)
SI3_O19_SI6	171.0(1)	171.0(4)	173.4(8)	175.8(8)	176.9(7)
T3_O20_T12	148.5(2)	148.1(2)	149.1(5)	150.5(5)	150.6(5)
T1_O21_T5	147.3(2)	147.2(2)	147.5(5)	145.7(5)	145.7(5)
T7_O22_T11	147.0(3)	146.7(3)	145.7(6)	146.7(7)	146.3(6)
T7_O23_T7	151.4(2)	151.2(2)	151.0(5)	150.9(6)	151.2(6)
T12_O24_T12	151.0(2)	152.0(4)	149.0(8)	148.8(9)	147.9(8)
T9_O25_T9	155.0(2)	154.0(2)	157.8(9)	159.1(1)	159.3(1)
T10_O26_T10	142.0(2)	141.0(3)	142.6(9)	141.4(9)	141.2(9)
<T-O-T>	154.6	154.5	154.2	153.5	153.4

Table X

422_AS-ZSM-5,

Bond distances (Å)	**25 °C**	**200 °C**	**400 °C**	**600 °C**	**800 °C**
T1-O1	1.590(1)	1.590(1)	1.591(5)	1.594(4)	1.591(4)
T1-O15	1.591(1)	1.591(1)	1.593(5)	1.592(4)	1.592(4)
T1-O16	1.594(1)	1.594(1)	1.588(5)	1.587(4)	1.588(4)
T1-O21	1.590(1)	1.590(1)	1.590(5)	1.593(4)	1.592(4)
T2-O1	1.592(1)	1.591(1)	1.594(5)	1.595(4)	1.594(4)
T2-O2	1.587(1)	1.587(1)	1.585(5)	1.591(4)	1.588(4)
T2-O6	1.593(1)	1.594(1)	1.592(5)	1.593(4)	1.592(4)
T2-O13	1.598(1)	1.597(1)	1.594(5)	1.592(4)	1.592(4)
T3-O2	1.592(1)	1.591(1)	1.591(5)	1.596(4)	1.593(4)
T3-O3	1.591(1)	1.592(1)	1.591(5)	1.593(4)	1.591(4)
T3-O19	1.592(1)	1.592(1)	1.589(5)	1.588(4)	1.587(4)
T3-O20	1.592(1)	1.592(1)	1.594(5)	1.594(4)	1.593(4)
T4-O3	1.589(1)	1.590(1)	1.592(5)	1.592(4)	1.592(4)
T4-O4	1.593(1)	1.591(1)	1.591(5)	1.594(4)	1.592(4)
T4-O16	1.596(1)	1.598(1)	1.590(5)	1.589(4)	1.589(4)
T4-O17	1.592(1)	1.593(1)	1.591(5)	1.590(4)	1.590(4)
T5-O4	1.593(1)	1.593(1)	1.590(5)	1.593(4)	1.592(4)
T5-O5	1.589(1)	1.588(1)	1.591(5)	1.593(4)	1.592(4)
T5-O14	1.595(1)	1.595(1)	1.589(5)	1.589(4)	1.589(4)
T5-O21	1.592(1)	1.591(1)	1.592(5)	1.593(4)	1.592(4)
T6-O5	1.591(1)	1.590(1)	1.592(5)	1.594(4)	1.593(4)
T6-O6	1.595(1)	1.596(1)	1.595(5)	1.596(4)	1.596(4)
T6-O18	1.589(1)	1.589(1)	1.591(5)	1.592(4)	1.590(4)
T6-O19	1.591(1)	1.593(1)	1.586(5)	1.590(4)	1.587(4)
T7-O7	1.592(1)	1.592(1)	1.593(5)	1.594(4)	1.594(4)
T7-O17	1.594(1)	1.595(1)	1.589(5)	1.590(4)	1.590(4)

T7-O22	1.594(1)	1.594(1)	1.595(5)	1.596(4)	1.596(4)
T7-O23	1.593(1)	1.592(1)	1.593(5)	1.593(4)	1.593(4)
T8-O7	1.591(1)	1.590(1)	1.595(5)	1.597(4)	1.596(4)
T8-O8	1.590(1)	1.591(1)	1.586(5)	1.588(4)	1.586(4)
T8-O12	1.591(1)	1.593(1)	1.594(5)	1.594(4)	1.595(4)
T8-O13	1.598(1)	1.596(1)	1.596(5)	1.593(4)	1.594(4)
T9-O8	1.595(1)	1.596(1)	1.589(5)	1.591(4)	1.589(4)
T9-O9	1.595(1)	1.597(1)	1.597(5)	1.597(4)	1.597(4)
T9-O18	1.585(1)	1.583(1)	1.589(5)	1.591(4)	1.591(4)
T9-O25	1.592(1)	1.593(1)	1.595(5)	1.595(4)	1.592(4)
T10-O9	1.592(1)	1.592(1)	1.592(5)	1.592(4)	1.591(4)
T10-O10	1.598(1)	1.598(1)	1.592(5)	1.594(4)	1.593(4)
T10-O15	1.591(1)	1.589(1)	1.592(5)	1.595(4)	1.595(4)
T10-O26	1.591(1)	1.592(1)	1.597(5)	1.596(4)	1.594(4)
T11-O10	1.597(1)	1.599(1)	1.592(5)	1.593(4)	1.592(4)
T11-O11	1.589(1)	1.589(1)	1.592(5)	1.594(4)	1.593(4)
T11-O14	1.595(1)	1.594(1)	1.590(5)	1.590(4)	1.590(4)
T11-O22	1.591(1)	1.590(1)	1.594(5)	1.594(4)	1.595(4)
T12-O11	1.594(1)	1.595(1)	1.596(5)	1.597(4)	1.596(4)
T12-O12	1.593(1)	1.593(1)	1.594(5)	1.593(4)	1.594(4)
T12-O20	1.589(1)	1.590(1)	1.588(5)	1.593(4)	1.590(4)
T12-O24	1.593(1)	1.591(1)	1.594(5)	1.595(4)	1.593(4)
<T-O>	1.592	1.592	1.591	1.592	1.592
			T-O-T angles (°)		
T1_O1_T2	151.8(1)	151.7(3)	148.1(7)	148.7(6)	148.2(6)
T2_O2_T3	148.2(1)	147.2(6)	147.7(6)	145.3(5)	145.9(5)
T3_O3_T4	170.8(3)	169.1(2)	167.0(7)	163.9(6)	164.3(5)
T4_O4_T5	153.6(3)	152.6(5)	153.0(8)	150.6(7)	150.9(6)
T5_O5_T6	145.7(1)	146.2(1)	147.0(6)	146.5(5)	147.3(5)
T2_O6_T6	154.8(2)	155.9(2)	152.1(8)	150.1(6)	151.7(6)
T7_O7_T8	152.8(1)	152.4(2)	150.6(7)	150.4(6)	149.8(6)
T8_O8_T9	159.4(2)	158.5(2)	156.6(8)	154.6(6)	155.7(6)
T9_O9_T10	156.2(2)	157.4(5)	155.4(1)	153.4(8)	155.0(8)
T10_O10_T11	160.9(1)	160.3(1)	158.4(6)	155.6(5)	156.3(5)
T11_O11_T12	150.1(1)	151.1(1)	150.1(7)	149.4(6)	150.4(5)
T8_O12_T12	166.5(2)	167.0(1)	164.9(7)	163.1(6)	164.5(6)
T2_O13_T8	171.9(2)	171.7(2)	166.8(7)	166.1(6)	166.9(6)
T5_O14_T11	161.1(1)	160.7(2)	159.6(7)	156.8(6)	157.9(5)
T1_O15_T10	145.6(1)	146.9(3)	146.1(7)	145.3(6)	146.1(5)
T1_O16_T4	171.2(1)	171.5(1)	174.4(7)	174.4(6)	174.6(6)
T4_O17_T7	151.2(1)	151.1(2)	150.3(7)	149.9(6)	150.5(6)

T6_O18_T9	145.5(1)	147.4(1)	144.5(7)	143.9(6)	144.5(5)
SI3_O19_SI6	169.7(2)	169.2(1)	172.9(8)	174.6(7)	173.5(6)
T3_O20_T12	150.6(1)	149.8(1)	150.5(7)	152.0(6)	151.4(5)
T1_O21_T5	146.9(1)	146.3 (7)	145.7(6)	145.3(5)	145.2(3)
T7_O22_T11	151.0(1)	150.5(6)	149.3(7)	148.7(6)	149.2(6)
T7_O23_T7	154.2(2)	153.8(5)	153.0(9)	152.7(7)	152.4(7)
T12_O24_T12	149.8(2)	152.4(6)	149.2(9)	149.4(8)	149.8(8)
T9_O25_T9	156.7(2)	154.7(5)	160.1(1)	162.3(8)	159.9(8)
T10_O26_T10	143.1(2)	142.5(7)	143.1(8)	142.1(7)	141.4(7)
<T-O-T>	155.3	155.3	154.4	153.6	153.9

Table Y

424_AS-ZSM-5

Bond distances (Å)	**25 °C**	**200 °C**	**400 °C**	**600 °C**	**800 °C**
T1-O1	1.590(1)	1.591(1)	1.589(5)	1.591(4)	1.590(3)
T1-O15	1.592(1)	1.591(1)	1.591(3)	1.591(4)	1.592(3)
T1-O16	1.594(1)	1.593(1)	1.592(3)	1.591(4)	1.591(3)
T1-O21	1.592(1)	1.592(1)	1.591(3)	1.591(4)	1.592(3)
T2-O1	1.593(1)	1.593(1)	1.591(3)	1.594(4)	1.593(3)
T2-O2	1.589(1)	1.590(2)	1.590(3)	1.592(4)	1.591(3)
T2-O6	1.593(1)	1.593(1)	1.592(3)	1.593(4)	1.593(3)
T2-O13	1.595(1)	1.594(1)	1.592(3)	1.591(4)	1.591(3)
T3-O2	1.592(1)	1.593(1)	1.592(3)	1.594(4)	1.593(3)
T3-O3	1.592(1)	1.592(1)	1.592(3)	1.592(4)	1.592(3)
T3-O19	1.592(1)	1.592(1)	1.591(3)	1.591(4)	1.591(3)
T3-O20	1.592(1)	1.592(1)	1.591(3)	1.592(4)	1.592(3)
T4-O3	1.592(1)	1.592(2)	1.592(3)	1.592(4)	1.592(3)
T4-O4	1.593(1)	1.593(1)	1.593(3)	1.594(4)	1.593(3)
T4-O16	1.594(1)	1.594(1)	1.592(3)	1.592(4)	1.592(3)
T4-O17	1.592(1)	1.592(1)	1.593(3)	1.592(4)	1.592(3)
T5-O4	1.593(1)	1.593(1)	1.593(3)	1.594(4)	1.593(3)
T5-O5	1.591(1)	1.591(2)	1.590(3)	1.592(4)	1.592(3)
T5-O14	1.593(1)	1.592(2)	1.592(3)	1.591(4)	1.591(3)
T5-O21	1.593(1)	1.593(2)	1.591(3)	1.591(4)	1.592(3)
T6-O5	1.592(1)	1.592(2)	1.593(5)	1.593(4)	1.593(3)
T6-O6	1.594(1)	1.595(2)	1.597(3)	1.595(4)	1.595(3)
T6-O18	1.590(1)	1.591(2)	1.591(3)	1.591(4)	1.591(3)
T6-O19	1.591(1)	1.592(2)	1.591(5)	1.591(4)	1.591(3)
T7-O7	1.593(2)	1.593(2)	1.594(3)	1.594(4)	1.593(3)
T7-O17	1.593(2)	1.594(2)	1.593(3)	1.593(4)	1.592(3)
T7-O22	1.595(1)	1.596(2)	1.593(3)	1.594(4)	1.594(3)
T7-O23	1.593(1)	1.593(2)	1.593(3)	1.593(4)	1.594(3)

T8-O7	1.592(1)	1.593(1)	1.595(3)	1.596(4)	1.595(3)
T8-O8	1.591(1)	1.592(1)	1.590(3)	1.591(4)	1.590(3)
T8-O12	1.593(1)	1.593(1)	1.596(3)	1.596(4)	1.595(3)
T8-O13	1.595(1)	1.593(1)	1.591(3)	1.591(4)	1.591(3)
T9-O8	1.594(2)	1.594(1)	1.593(3)	1.593(4)	1.592(3)
T9-O9	1.594(2)	1.595(2)	1.595(3)	1.596(4)	1.594(3)
T9-O18	1.589(1)	1.590(2)	1.591(5)	1.592(4)	1.593(3)
T9-O25	1.592(2)	1.592(2)	1.591(3)	1.591(4)	1.591(3)
T10-O9	1.593(1)	1.592(2)	1.591(5)	1.591(4)	1.591(3)
T10-O10	1.597(1)	1.596(1)	1.595(3)	1.596(4)	1.594(3)
T10-O15	1.592(1)	1.593(1)	1.593(3)	1.594(4)	1.594(3)
T10-O26	1.591(2)	1.592(1)	1.592(5)	1.592(4)	1.592(3)
T11-O10	1.596(1)	1.597(1)	1.594(3)	1.595(4)	1.594(3)
T11-O11	1.591(1)	1.591(1)	1.592(3)	1.594(4)	1.593(3)
T11-O14	1.594(1)	1.592(1)	1.591(3)	1.590(4)	1.590(3)
T11-O22	1.592(1)	1.594(1)	1.592(3)	1.593(4)	1.594(3)
T12-O11	1.594(1)	1.595(1)	1.593(3)	1.595(4)	1.594(3)
T12-O12	1.593(1)	1.592(1)	1.595(3)	1.594(4)	1.593(3)
T12-O20	1.590(1)	1.591(1)	1.590(3)	1.592(4)	1.591(3)
T12-O24	1.592(1)	1.592(1)	1.592(3)	1.592(4)	1.592(3)
<T-O>	1.592	1.592	1.592	1.592	1.592
			T-O-T angles (°)		
T1_O1_T2	152.0(2)	151.1(2)	147.5(6)	148.6(7)	148.0(6)
T2_O2_T3	147.2(1)	146.1(1)	146.5(5)	144.7(5)	144.3(1)
T3_O3_T4	169.1(1)	166.4(1)	165.1(6)	163.1(6)	162.2(5)
T4_O4_T5	151.4(2)	150.9(2)	152.0(8)	149.6(7)	150.0(7)
T5_O5_T6	145.8(1)	146.5(1)	146.4(5)	146.6(5)	146.8(5)
T2_O6_T6	152.8(2)	152.1(2)	150.5(7)	149.4(6)	149.3(6)
T7_O7_T8	151.9(2)	151.2(2)	149.3(6)	149.0(6)	149.1(6)
T8_O8_T9	159.9(2)	158.4(2)	157.7(8)	157.0(8)	156.3(7)
T9_O9_T10	155.4(2)	155.8(3)	155.0(9)	154.0(9)	154.3(9)
T10_O10_T11	159.0(1)	158.0(1)	157.5(6)	156.1(6)	155.9(5)
T11_O11_T12	150.9(1)	151.2(2)	150.2(7)	150.8(7)	150.5(6)
T8_O12_T12	166.5(2)	166.0(2)	165.7(7)	164.6(6)	164.6(6)
T2_O13_T8	171.7(2)	170.7(2)	166.2(6)	166.5(7)	166.3(6)
T5_O14_T11	159.2(1)	158.6(2)	158.1(6)	156.7(6)	157.0(5)
T1_O15_T10	144.8(1)	145.8(2)	144.9(6)	144.4(6)	145.0(6)
T1_O16_T4	170.9(1)	172.3(2)	174.8(7)	173.9(7)	174.7(6)
T4_O17_T7	151.3(1)	151.1(1)	150.8(6)	150.9(6)	150.8(6)
T6_O18_T9	144.9(1)	145.6(2)	144.4(6)	143.4(6)	144.2(6)
SI3_O19_SI6	171.5(2)	173.0(2)	174.7(7)	175.2(7)	175.8(6)

T3_O20_T12	150.9(1)	151.0(1)	150.4(6)	152.0(6)	151.7(5)
T1_O21_T5	146.1(1)	145.8(1)	145.6(5)	144.7(5)	145.0(3)
T7_O22_T11	151.0(1)	150.6(2)	149.3(6)	149.7(7)	149.6(6)
T7_O23_T7	154.5(2)	154.2(2)	152.8(7)	153.1(8)	152.8(7)
T12_O24_T12	149.1(2)	149.8(2)	148.6(9)	148.0(9)	148.6(8)
T9_O25_T9	157.4(2)	157.5(3)	160.2(9)	161.1(9)	160.7(8)
T10_O26_T10	142.2(2)	141.8(2)	141.9(7)	141.4(7)	141.2(7)
<T-O-T>	154.9	154.6	154.0	153.6	153.6

Figure A

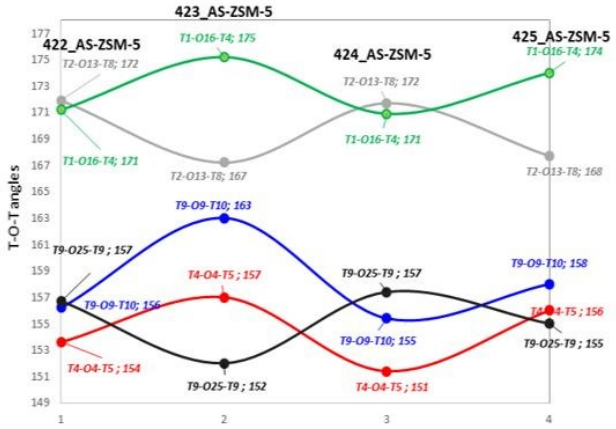

Figure B1, B2, B3 and B4

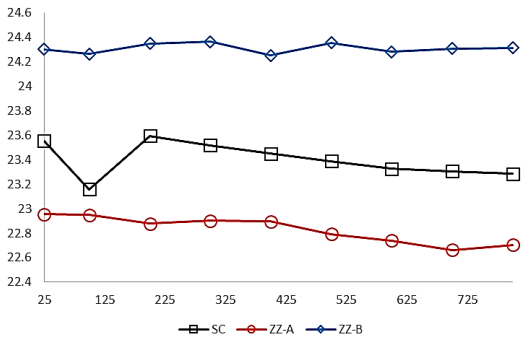

B1) 423_AS-ZSM-5

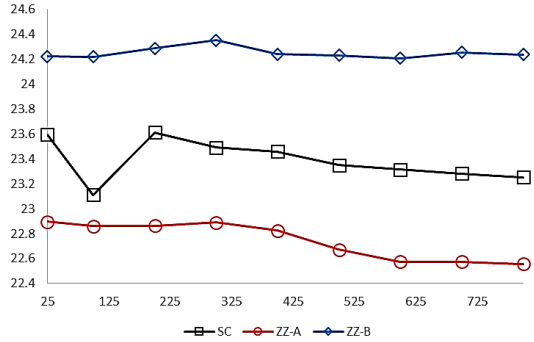

B2) 425_AS-ZSM-5

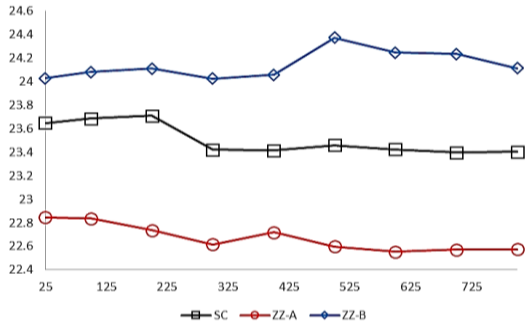

B3) 422_AS-ZSM-5

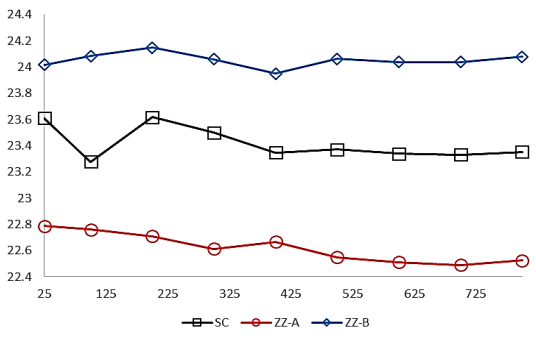

B4) 424_AS-ZSM-5

Appendix 2

Framework atomic coordinates, fraction and Atomic Displacement Parameters of H^+-ZSM-5_15, H^+-ZSM-5_20, H^+-ZSM-5_37 and H^+-ZSM-5_69 are reported in Table A, B, C and D, respectively.

Framework atomic coordinates, fraction and Atomic Displacement Parameters at selected temperature of 200, 400, 600 and 800 °C for H^+-ZSM-5_15 are reported in Appendix 2, Table E, F, G and H, respectively; for H^+-ZSM-5_20 in Table I, J, K and L, respectively; for H^+-ZSM-5_37 in Table M, N, O and P, respectively; for H^+-ZSM-5_69 in Table Q, R, S and T, respectively.

T-O bond distance and T-O-T angles at room temperature of H^+-ZSM-5_15 are reported in Table U.

T-O bond distances and T-O-T angles at room temperature of H^+-ZSM-5_20, H^+-ZSM-5_37 and H^+-ZSM-5_69 are reported in Table V.

T-O bond distances and T-O-T angles at 200, 400, 600 and 800 °C of H^+-ZSM-5_15, H^+-ZSM-5_20, H^+-ZSM-5_37 and H^+-ZSM-5_69 are reported in Table W, X, Y and Z, respectively.

Table A

H^+-ZSM-5_15, room temperature

Site	x/a	y/b	z/c	Fraction	Ui/Ue*100
T1	0.4240(1)	0.05658(8)	-0.3330(4)	1.0	0.40(2)
T2	0.3128(1)	0.02987(8)	-0.1804(4)	1.0	0.40(2)
T3	0.2815(1)	0.05902(8)	0.0377(4)	1.0	0.40(2)
T4	0.1244(1)	0.06556(8)	0.0309(4)	1.0	0.40(2)
T5	0.0722(1)	0.02759(8)	-0.1781(4)	1.0	0.40(2)
T6	0.1904(1)	0.06149(8)	-0.3132(4)	1.0	0.40(2)
T7	0.4242(1)	-0.17245(8)	-0.3172(4)	1.0	0.40(2)
T8	0.3107(1)	-0.12937(8)	-0.1761(4)	1.0	0.40(2)
T9	0.2719(1)	-0.17118(8)	0.0406(4)	1.0	0.40(2)
T10	0.11692(1)	-0.17428(8)	0.0346(4)	1.0	0.40(2)
T11	0.07135(1)	-0.12930(8)	-0.1780(4)	1.0	0.40(2)
T12	0.1890(1)	-0.17267(8)	-0.3123(4)	1.0	0.40(2)
O1	0.3749(3)	0.0591(3)	-0.2395(6)	1.0	0.81(5)
O2	0.3169(3)	0.0536(4)	-0.0673(5)	1.0	0.81(5)
O3	0.2028(1)	0.0607(4)	0.0218(6)	1.0	0.81(5)
O4	0.0911(3)	0.0639(3)	-0.0762(5)	1.0	0.81(5)
O5	0.1188(2)	0.0555(3)	-0.2648(6)	1.0	0.81(5)
O6	0.2462(3)	0.0567(4)	-0.2303(6)	1.0	0.81(5)
O7	0.3764(3)	-0.1604(4)	-0.2239(6)	1.0	0.81(5)
O8	0.3055(3)	-0.1506(4)	-0.0622(4)	1.0	0.81(5)
O9	0.1943(1)	-0.1569(5)	0.0362(7)	1.0	0.81(5)
O10	0.0883(4)	-0.1647(3)	-0.0745(5)	1.0	0.81(5)
O11	0.1192(3)	-0.1583(4)	-0.2622(7)	1.0	0.81(5)
O12	0.2474(3)	-0.1559(4)	-0.2359(6)	1.0	0.81(5)

O13	0.3140(5)	-0.0497(1)	-0.1843(8)	1.0	0.81(5)
O14	0.0819(4)	-0.0508(1)	-0.1679(8)	1.0	0.81(5)
O15	0.4209(3)	0.1263(2)	-0.3896(6)	1.0	0.81(5)
O16	0.4017(4)	-0.0024(3)	-0.4056(6)	1.0	0.81(5)
O17	0.3957(4)	-0.1323(2)	-0.4114(6)	1.0	0.81(5)
O18	0.1955(3)	0.1315(2)	-0.3701(5)	1.0	0.81(5)
O19	0.1996(4)	0.0025(2)	-0.3930(6)	1.0	0.81(5)
O20	0.1965(4)	-0.1274(2)	-0.4095(5)	1.0	0.81(5)
O21	0.0027(2)	0.0438(3)	-0.2064(4)	1.0	0.81(5)
O22	0.0035(2)	-0.1448(4)	-0.2083(5)	1.0	0.81(5)
O23	0.4276(6)	-1/4	-0.3421(8)	1.0	0.81(5)
O24	0.1932(5)	-1/4	-0.3437(7)	1.0	0.81(5)
O25	0.2834(6)	-1/4	0.0580(9)	1.0	0.81(5)
O26	0.1070(6)	-1/4	0.0697(7)	1.0	0.81(5)

Table B

H^+-ZSM-5_20, room temperature

Site	x/a	y/b	z/c	Fraction	Ui/Ue*100
T1	0.0565(3)	0.4223(3)	-0.3308(7)	1.0	0.42(3)
T2	0.0334(4)	0.3148(4)	-0.1755(7)	1.0	0.42(3)
T3	0.0616(4)	0.2787(3)	0.0405(8)	1.0	0.42(3)
T4	0.0633(3)	0.1226(3)	0.0311(6)	1.0	0.42(3)
T5	0.0283(3)	0.0727(4)	-0.1776(7)	1.0	0.42(3)
T6	0.0602(4)	0.1924(4)	-0.3140(8)	1.0	0.42(3)
T7	-0.1725(2)	0.4259(3)	-0.3193(7)	1.0	0.42(3)
T8	-0.1261(4)	0.3114(3)	-0.1798(7)	1.0	0.42(3)
T9	-0.1725(3)	0.2718(3)	0.0358(7)	1.0	0.42(3)
T10	-0.1752(3)	0.1175(4)	0.0371(9)	1.0	0.42(3)
T11	-0.1291(3)	0.0708(4)	-0.1739(8)	1.0	0.42(3)
T12	-0.1682(5)	0.1881(3)	-0.3154(7)	1.0	0.42(3)
T13	0.4436(3)	0.4250(4)	-0.3326(7)	1.0	0.42(3)
T14	0.4728(3)	0.3098(4)	-0.1852(7)	1.0	0.42(3)
T15	0.4404(3)	0.2803(3)	0.0353(8)	1.0	0.42(3)
T16	0.4337(3)	0.1234(3)	0.0327(6)	1.0	0.42(3)
T17	0.4735(3)	0.0721(4)	-0.1793(7)	1.0	0.42(3)
T18	0.4394(4)	0.1881(4)	-0.3187(9)	1.0	0.42(3)
T19	0.6709(3)	0.4233(3)	-0.3163(6)	1.0	0.42(3)
T20	0.6318(3)	0.3108(4)	-0.1737(7)	1.0	0.42(3)
T21	0.6713(3)	0.2731(4)	0.0425(7)	1.0	0.42(3)
T22	0.6733(3)	0.1189(4)	0.0346(8)	1.0	0.42(3)
T23	0.6319(3)	0.0735(5)	-0.1808(8)	1.0	0.42(3)
T24	0.6778(5)	0.1931(4)	-0.3095(7)	1.0	0.42(3)

O1	0.0627(6)	0.3760(5)	-0.2352(11)	1.0	0.82(4)
O2	0.0609(9)	0.3160(6)	-0.0640(7)	1.0	0.82(4)
O3	0.0542(6)	0.2009(3)	0.0223(15)	1.0	0.82(4)
O4	0.0675(5)	0.0912(8)	-0.0776(9)	1.0	0.82(4)
O5	0.0507(8)	0.1211(4)	-0.2652(11)	1.0	0.82(4)
O6	0.0565(8)	0.2474(5)	-0.2288(9)	1.0	0.82(4)
O7	-0.1569(8)	0.3765(6)	-0.2294(11)	1.0	0.82(4)
O8	-0.1546(8)	0.3029(6)	-0.0700(9)	1.0	0.82(4)
O9	-0.1563(7)	0.1943(3)	0.0350(14)	1.0	0.82(4)
O10	-0.1660(4)	0.0867(8)	-0.0715(8)	1.0	0.82(4)
O11	-0.1558(7)	0.1199(6)	-0.2582(11)	1.0	0.82(4)
O12	-0.1462(10)	0.2483(7)	-0.2453(14)	1.0	0.82(4)
O13	-0.0464(3)	0.3178(8)	-0.1750(16)	1.0	0.82(4)
O14	-0.0503(2)	0.0802(6)	-0.1599(14)	1.0	0.82(4)
O15	0.1246(2)	0.4199(4)	-0.3920(8)	1.0	0.82(4)
O16	-0.0035(4)	0.3972(8)	-0.3999(12)	1.0	0.82(4)
O17	-0.1334(4)	0.4022(7)	-0.4163(10)	1.0	0.82(4)
O18	0.1326(3)	0.1956(8)	-0.3652(7)	1.0	0.82(4)
O19	0.0039(4)	0.2050(7)	-0.3956(12)	1.0	0.82(4)
O20	-0.1250(5)	0.1891(8)	-0.4148(7)	1.0	0.82(4)
O21	0.0450(5)	0.0016(4)	-0.2085(6)	1.0	0.82(4)
O22	-0.1444(7)	0.0036(4)	-0.2063(9)	1.0	0.82(4)
O23	-0.2511(2)	0.4262(8)	-0.3418(9)	1.0	0.82(4)
O24	-0.2456(4)	0.1946(7)	-0.3434(11)	1.0	0.82(4)
O25	-0.2500(2)	0.2829(7)	0.0581(10)	1.0	0.82(4)
O26	-0.2511(2)	0.1093(7)	0.0712(9)	1.0	0.82(4)
O27	0.4464(9)	0.3741(4)	-0.2422(10)	1.0	0.82(4)
O28	0.4506(7)	0.3130(6)	-0.0716(8)	1.0	0.82(4)
O29	0.4312(7)	0.2021(2)	0.0229(14)	1.0	0.82(4)
O30	0.4407(8)	0.0913(8)	-0.0752(9)	1.0	0.82(4)
O31	0.4431(7)	0.1176(3)	-0.2652(12)	1.0	0.82(4)
O32	0.4423(7)	0.2452(4)	-0.2367(11)	1.0	0.82(4)
O33	0.6600(8)	0.3778(6)	-0.2207(9)	1.0	0.82(4)
O34	0.6482(6)	0.3091(6)	-0.0576(7)	1.0	0.82(4)
O35	0.6548(6)	0.1958(7)	0.0351(14)	1.0	0.82(4)
O36	0.6652(6)	0.0904(7)	-0.0756(7)	1.0	0.82(4)
O37	0.6608(7)	0.1222(6)	-0.2636(9)	1.0	0.82(4)
O38	0.6660(18)	0.2488(6)	-0.2271(11)	1.0	0.82(4)
O39	0.5527(3)	0.3074(11)	-0.1906(12)	1.0	0.82(4)
O40	0.5526(3)	0.0822(6)	-0.1735(16)	1.0	0.82(4)
O41	0.3723(3)	0.4244(5)	-0.3862(9)	1.0	0.82(4)

O42	0.5010(4)	0.4078(9)	-0.4109(11)	1.0	0.82(4)
O43	0.6306(4)	0.3932(5)	-0.4087(8)	1.0	0.82(4)
O44	0.3709(5)	0.1930(7)	-0.3796(12)	1.0	0.82(4)
O45	0.5009(5)	0.1957(8)	-0.3930(10)	1.0	0.82(4)
O46	0.6307(5)	0.2067(7)	-0.4033(8)	1.0	0.82(4)
O47	0.4577(5)	-0.0035(3)	-0.2041(7)	1.0	0.82(4)
O48	0.6487(7)	-0.0011(5)	-0.2103(9)	1.0	0.82(4)

Table C

H^+-ZSM-5_37, room temperature

Site	x/a	y/b	z/c	Fraction	Ui/Ue*100
T1	0.0556(2)	0.4224(2)	-0.3298(4)	1.0	0.27(3)
T2	0.0349(2)	0.3160(3)	-0.1725(5)	1.0	0.27(3)
T3	0.0627(3)	0.2786(2)	0.0428(5)	1.0	0.27(3)
T4	0.0637(2)	0.1230(2)	0.0319(4)	1.0	0.27(3)
T5	0.0281(2)	0.0735(2)	-0.1758(5)	1.0	0.27(3)
T6	0.0614(2)	0.1940(2)	-0.3114(5)	1.0	0.27(3)
T7	-0.1727(1)	0.4268(2)	-0.3201(5)	1.0	0.27(3)
T8	-0.1241(2)	0.3115(2)	-0.1809(5)	1.0	0.27(3)
T9	-0.1726(2)	0.2708(2)	0.0334(5)	1.0	0.27(3)
T10	-0.1758(2)	0.1164(2)	0.0378(6)	1.0	0.27(3)
T11	-0.1289(2)	0.0700(3)	-0.1717(6)	1.0	0.27(3)
T12	-0.1657(3)	0.1875(2)	-0.3156(5)	1.0	0.27(3)
T13	0.4444(2)	0.4255(2)	-0.3322(5)	1.0	0.27(3)
T14	0.4745(2)	0.3094(3)	-0.1859(5)	1.0	0.27(3)
T15	0.4412(2)	0.2805(2)	0.0358(5)	1.0	0.27(3)
T16	0.4330(2)	0.1241(2)	0.0336(5)	1.0	0.27(3)
T17	0.4746(2)	0.0732(3)	-0.1793(6)	1.0	0.27(3)
T18	0.4394(2)	0.1881(2)	-0.3187(6)	1.0	0.27(3)
T19	0.6709(2)	0.4229(2)	-0.3147(4)	1.0	0.27(3)
T20	0.6329(2)	0.3103(2)	-0.1725(5)	1.0	0.27(3)
T21	0.6709(2)	0.2728(2)	0.0442(5)	1.0	0.27(3)
T22	0.6728(2)	0.1186(2)	0.0357(6)	1.0	0.27(3)
T23	0.6328(2)	0.0746(3)	-0.1816(6)	1.0	0.27(3)
T24	0.680(3)	0.1942(3)	-0.3076(5)	1.0	0.27(3)
O1	0.0641(3)	0.3779(4)	-0.2322(7)	1.0	0.49(4)
O2	0.0631(6)	0.3174(4)	-0.0609(5)	1.0	0.49(4)
O3	0.0531(4)	0.2013(2)	0.0223(9)	1.0	0.49(4)
O4	0.0691(3)	0.0912(5)	-0.0767(6)	1.0	0.49(4)
O5	0.0492(6)	0.1227(3)	-0.2632(7)	1.0	0.49(4)
O6	0.0577(5)	0.2491(3)	-0.2261(7)	1.0	0.49(4)
O7	-0.1559(5)	0.3763(5)	-0.2316(9)	1.0	0.49(4)

O8	-0.1555(5)	0.3018(4)	-0.0728(6)	1.0	0.49(4)
O9	-0.1568(5)	0.1932(2)	0.0325(11	1.0	0.49(4)
O10	-0.1673(2)	0.0838(5)	-0.0698(6)	1.0	0.49(4)
O11	-0.1555(4)	0.1200(4)	-0.2553(8)	1.0	0.49(4)
O12	-0.1415(7)	0.2484(5)	-0.2483(10)	1.0	0.49(4)
O13	-0.0449(2)	0.3197(5)	-0.1713(12)	1.0	0.49(4)
O14	-0.0502(1)	0.0806(4)	-0.1553(10)	1.0	0.49(4)
O15	0.1234(2)	0.4207(3)	-0.3923(5)	1.0	0.49(4)
O16	-0.0042(3)	0.3943(5)	-0.3965(8)	1.0	0.49(4)
O17	-0.1341(2)	0.4040(4)	-0.4185(7)	1.0	0.49(4)
O18	0.1336(2)	0.1960(5)	-0.3619(5)	1.0	0.49(4)
O19	0.0051(2)	0.2082(4)	-0.3940(8)	1.0	0.49(4)
O20	-0.12274(3)	0.1852(5)	-0.4153(5)	1.0	0.49(4)
O21	0.0445(4)	-0.0003(2)	-0.2083(4)	1.0	0.49(4)
O22	-0.1424(4)	-0.0048(6)	-0.2068(6)	1.0	0.49(4)
O23	-0.2511(1)	0.42739(4)	-0.3407(7)	1.0	0.49(4)
O24	-0.2432(2)	0.1962(5)	-0.3435(8)	1.0	0.49(4)
O25	-0.2500(1)	0.2824(5)	0.0572(7)	1.0	0.49(4)
O26	-0.2516(1)	0.1088(5)	0.0731(7)	1.0	0.49(4)
O27	0.4484(6)	0.3746(3)	-0.2413(8)	1.0	0.49(4)
O28	0.4542(4)	0.3123(4)	-0.0712(6)	1.0	0.49(4)
O29	0.4277(4)	0.2028(1)	0.0236(9)	1.0	0.49(4)
O30	0.443(5)	0.0924(5)	-0.0741(6)	1.0	0.49(4)
O31	0.4412(4)	0.1176(2)	-0.2646(8)	1.0	0.49(4)
O32	0.4417(4)	0.2456(3)	-0.2369(8)	1.0	0.49(4)
O33	0.6612(6)	0.3777(4)	-0.2183(6)	1.0	0.49(4)
O34	0.6462(4)	0.3092(3)	-0.0551(5)	1.0	0.49(4)
O35	0.6542(4)	0.1955(2)	0.0368(10)	1.0	0.49(4)
O36	0.6653(4)	0.0906(5)	-0.0752(5)	1.0	0.49(4)
O37	0.6641(4)	0.1226(4)	-0.2635(6)	1.0	0.49(4)
O38	0.6699(6)	0.2489(5)	-0.2230(7)	1.0	0.49(4)
O39	0.5543(2)	0.3053(7)	-0.1943(7)	1.0	0.49(4)
O40	0.5536(2)	0.0859(4)	-0.1768(11)	1.0	0.49(4)
O41	0.3726(2)	0.4201(3)	-0.3846(6)	1.0	0.49(4)
O42	0.5013(2)	0.4084(6)	-0.4111(8)	1.0	0.49(4)
O43	0.6309(2)	0.3914(3)	-0.4067(5)	1.0	0.49(4)
O44	0.3720(3)	0.1940(5)	-0.3828(9)	1.0	0.49(4)
O45	0.5025(3)	0.1948(5)	-0.3904(7)	1.0	0.49(4)
O46	0.6321(3)	0.2093(4)	-0.3999(5)	1.0	0.49(4)
O47	0.4603(3)	-0.0039(2)	-0.2022(5)	1.0	0.49(4)
O48	0.6479(4)	-0.00054(3)	-0.2107(6)	1.0	0.49(4)

Table D

H^+-ZSM-5_69, room temperature

Site	x/a	y/b	z/c	Fraction	Ui/Ue*100
T1	0.0555(2)	0.4220(2)	-0.3298(4)	1.0	0.19(6)
T2	0.0332(2)	0.3153(2)	-0.1714(4)	1.0	0.19(6)
T3	0.0626(2)	0.2790(2)	0.0431(5)	1.0	0.19(6)
T4	0.0636(2)	0.1233(2)	0.0313(4)	1.0	0.19(6)
T5	0.0281(2)	0.0735(2)	-0.1761(4)	1.0	0.19(6)
T6	0.0595(2)	0.1937(2)	-0.3117(4)	1.0	0.19(6)
T7	-0.1721(2)	0.4261(2)	-0.3201(4)	1.0	0.19(6)
T8	-0.1259(2)	0.3118(2)	-0.1781(4)	1.0	0.19(6)
T9	-0.1732(2)	0.2704(2)	0.0352(5)	1.0	0.19(6)
T10	-0.1758(2)	0.1165(2)	0.0360(5)	1.0	0.19(6)
T11	-0.1286(2)	0.0697(2)	-0.1728(5)	1.0	0.19(6)
T12	-0.1663(6)	0.1881(2)	-0.3137(4)	1.0	0.19(6)
T13	0.4439(2)	0.4255(2)	-0.3341(4)	1.0	0.19(6)
T14	0.4735(2)	0.3103(2)	-0.1855(4)	1.0	0.19(6)
T15	0.4403(2)	0.2800(2)	0.0345(5)	1.0	0.19(6)
T16	0.4330(2)	0.1236(2)	0.0323(4)	1.0	0.19(6)
T17	0.4737(2)	0.0722(2)	-0.1799(5)	1.0	0.19(6)
T18	0.4394(2)	0.188(2)	-0.3184(5)	1.0	0.19(6)
T19	0.6707(2)	0.4228(2)	-0.3149(4)	1.0	0.19(6)
T20	0.6324(2)	0.3110(2)	-0.1704(4)	1.0	0.19(6)
T21	0.6703(2)	0.2722(2)	0.0452(4)	1.0	0.19(6)
T22	0.6723(2)	0.1184(2)	0.0352(5)	1.0	0.19(6)
T23	0.6317(2)	0.0734(2)	-0.1812(5)	1.0	0.19(6)
T24	0.6791(2)	0.1939(2)	-0.3055(4)	1.0	0.19(6)
O1	0.0626(3)	0.3761(3)	-0.2334(6)	1.0	0.65(4)
O2	0.0636(4)	0.3171(3)	-0.0612(4)	1.0	0.65(4)
O3	0.0528(3)	0.2015(1)	0.0230(9)	1.0	0.65(4)
O4	0.0695(3)	0.0924(5)	-0.0778(5)	1.0	0.65(4)
O5	0.0486(4)	0.1217(2)	-0.2651(6)	1.0	0.65(4)
O6	0.0535(5)	0.2477(3)	-0.2253(6)	1.0	0.65(4)
O7	-0.1570(4)	0.3755(4)	-0.2314(7)	1.0	0.65(4)
O8	-0.1578(4)	0.3032(3)	-0.0704(5)	1.0	0.65(4)
O9	-0.1560(4)	0.1932(2)	0.0315(9)	1.0	0.65(4)
O10	-0.1680(2)	0.0843(4)	-0.0720(5)	1.0	0.65(4)
O11	-0.1544(4)	0.1192(3)	-0.2577(6)	1.0	0.65(4)
O12	-0.1416(6)	0.2475(4)	-0.2439(7)	1.0	0.65(4)
O13	-0.046(2)	0.3208(4)	-0.1671(9)	1.0	0.65(4)
O14	-0.0507(1)	0.0806(4)	-0.1549(8)	1.0	0.65(4)

O15	0.1231(2)	0.4204(3)	-0.3910(5)	1.0	0.65(4)
O16	-0.0045(2)	0.3957(4)	-0.3984(7)	1.0	0.65(4)
O17	-0.1345(2)	0.4025(4)	-0.4182(6)	1.0	0.65(4)
O18	0.1322(2)	0.1979(4)	-0.3606(4)	1.0	0.65(4)
O19	0.0039(2)	0.2071(4)	-0.3955(7)	1.0	0.65(4)
O20	-0.1247(3)	0.1887(4)	-0.4149(5)	1.0	0.65(4)
O21	0.0445(3)	0.0010(2)	-0.2072(4)	1.0	0.65(4)
O22	-0.1420(4)	0.0048(2)	-0.2072(6)	1.0	0.65(4)
O23	-0.2514(1)	0.4280(4)	-0.3414(5)	1.0	0.65(4)
O24	-0.2441(2)	0.1967(4)	-0.3390(7)	1.0	0.65(4)
O25	-0.2506(8)	0.2805(4)	0.0607(6)	1.0	0.65(4)
O26	-0.2517(7)	0.1097(4)	0.0717(6)	1.0	0.65(4)
O27	0.4472(4)	0.3743(2)	-0.2436(6)	1.0	0.65(4)
O28	0.4511(4)	0.3138(3)	-0.0717(4)	1.0	0.65(4)
O29	0.4296(4)	0.2021(1)	0.0203(8)	1.0	0.65(4)
O30	0.4416(4)	0.0902(5)	-0.0748(5)	1.0	0.65(4)
O31	0.4408(4)	0.1172(2)	-0.2648(7)	1.0	0.65(4)
O32	0.4431(4)	0.2452(2)	-0.2364(6)	1.0	0.65(4)
O33	0.6618(4)	0.377(7)	-0.2186(5)	1.0	0.65(4)
O34	0.6472(4)	0.3105(3)	-0.0534(4)	1.0	0.65(4)
O35	0.6528(4)	0.1952(2)	0.0344(9)	1.0	0.65(4)
O36	0.6644(4)	0.0891(5)	-0.0747(4)	1.0	0.65(4)
O37	0.6628(4)	0.1219(3)	-0.2627(6)	1.0	0.65(4)
O38	0.6670(5)	0.2480(4)	-0.2206(6)	1.0	0.65(4)
O39	0.5535(1)	0.3078(5)	-0.1902(7)	1.0	0.65(4)
O40	0.5526(2)	0.0847(3)	-0.1758(9)	1.0	0.65(4)
O41	0.3722(3)	0.4209(3)	-0.3871(6)	1.0	0.65(4)
O42	0.5011(2)	0.4085(5)	-0.4128(6)	1.0	0.65(4)
O43	0.6307()	0.3912(3)	-0.4068(5)	1.0	0.65(4)
O44	0.3715(3)	0.1947(4)	-0.3810(7)	1.0	0.65(4)
O45	0.5019(3)	0.1941(4)	-0.3913(6)	1.0	0.65(4)
O46	0.6316(2)	0.2090(4)	-0.3989(5)	1.0	0.65(4)
O47	0.4596(3)	-0.0038(2)	-0.2048(5)	1.0	0.65(4)
O48	0.6470(4)	-0.0016(2)	-0.2108(6)	1.0	0.65(4)

Table E

H^+-ZSM-5_15, 200 °C

Site	x/a	y/b	z/c	Fraction	Ui/Ue*100
T1	0.42322(9)	0.05659(6)	-0.3372(1)	1.0	1.6(1)
T2	0.31197(9)	0.02987(6)	-0.1846(1)	1.0	1.6(1)
T3	0.28075(9)	0.05903(6)	0.0334(1)	1.0	1.6(1)
T4	0.12365(9)	0.06557(6)	0.0266(1)	1.0	1.6(1)
T5	0.07138(9)	0.02760(6)	-0.1823(1)	1.0	1.6(1)
T6	0.18962(9)	0.06149(6)	-0.3174(1)	1.0	1.6(1)
T7	0.42337(9)	-0.17244(6)	-0.3214(1)	1.0	1.6(1)
T8	0.30987(9)	-0.12936(6)	-0.1803(1)	1.0	1.6(1)
T9	0.27108(9)	-0.17117(6)	0.0364(1)	1.0	1.6(1)
T10	0.11608(9)	-0.17428(6)	0.0304(1)	1.0	1.6(1)
T11	0.07051(9)	-0.12930(6)	-0.1822(1)	1.0	1.6(1)
T12	0.18817(9)	-0.17267(6)	-0.3165(1)	1.0	1.6(1)
O1	0.3720(2)	0.0608(2)	-0.2465(4)	1.0	3.1(2)
O2	0.3168(2)	0.0531(2)	-0.0714(2)	1.0	3.1(2)
O3	0.2023(1)	0.0609(2)	0.0178(4)	1.0	3.1(2)
O4	0.0911(2)	0.0645(2)	-0.0811(2)	1.0	3.1(2)
O5	0.1168(1)	0.0554(2)	-0.2709(4)	1.0	3.1(2)
O6	0.2435(2)	0.0553(3)	-0.2317(4)	1.0	3.1(2)
O7	0.3737(2)	-0.1628(2)	-0.2298(4)	1.0	3.1(2)
O8	0.3051(2)	-0.1496(3)	-0.0658(2)	1.0	3.1(2)
O9	0.1934(1)	-0.1566(4)	0.0324(5)	1.0	3.1(2)
O10	0.0884(2)	-0.1657(2)	-0.0799(2)	1.0	3.1(2)
O11	0.1169(1)	-0.1581(3)	-0.2688(4)	1.0	3.1(2)
O12	0.2447(2)	-0.1544(3)	-0.2378(4)	1.0	3.1(2)
O13	0.3150(3)	-0.0498(1)	-0.1900(5)	1.0	3.1(2)
O14	0.0820(2)	-0.0508(1)	-0.1716(5)	1.0	3.1(2)
O15	0.4230(2)	0.1258(1)	-0.3959(4)	1.0	3.1(2)
O16	0.4027(2)	-0.0029(2)	-0.4098(4)	1.0	3.1(2)
O17	0.3962(2)	-0.1328(1)	-0.4162(3)	1.0	3.1(2)
O18	0.1962(2)	0.1315(1)	-0.3732(3)	1.0	3.1(2)
O19	0.1997(3)	0.0023(2)	-0.3967(4)	1.0	3.1(2)
O20	0.19692(2)	-0.1277(1)	-0.4140(3)	1.0	3.1(2)
O21	-0.0044(1)	0.0429(2)	-0.2073(3)	1.0	3.1(2)
O22	-0.0053(1)	-0.1436(2)	-0.2092(3)	1.0	3.1(2)
O23	0.4297(4)	-1/4	-0.3472(5)	1.0	3.1(2)
O24	0.1933(4)	-1/4	-0.3459(5)	1.0	3.1(2)
O25	0.2827(4)	-1/4	0.0525(6)	1.0	3.1(2)
O26	0.1061(4)	-1/4	0.0657(4)	1.0	3.1(2)

Table F

H^+-ZSM-5_15, 400 °C

Site	x/a	y/b	z/c	Fraction	Ui/Ue*100
T1	0.42313(9)	0.05656(6)	-0.3368(2)	1.0	2.3(1)
T2	0.31189(9)	0.02984(6)	-0.1843(2)	1.0	2.3(1)
T3	0.28067(9)	0.05900(6)	0.0337(2)	1.0	2.3(1)
T4	0.12357(9)	0.06554(6)	0.0269(2)	1.0	2.3(1)
T5	0.07130(9)	0.02757(6)	-0.1819(2)	1.0	2.3(1)
T6	0.18954(9)	0.06146(6)	-0.3170(2)	1.0	2.3(1)
T7	0.42329(9)	-0.17247(6)	-0.3210(2)	1.0	2.3(1)
T8	0.30979(9)	-0.12939(6)	-0.1800(2)	1.0	2.3(1)
T9	0.27099(9)	-0.17120(6)	0.0367(2)	1.0	2.3(1)
T10	0.11600(9)	-0.17431(6)	0.0307(2)	1.0	2.3(1)
T11	0.07043(9)	-0.12933(6)	-0.1818(2)	1.0	2.3(1)
T12	0.18809(9)	-0.17270(6)	-0.3161(2)	1.0	2.3(1)
O1	0.3716(2)	0.0612(2)	-0.2466(4)	1.0	4.3(2)
O2	0.3174(2)	0.0523(2)	-0.0707(2)	1.0	4.3(2)
O3	0.2023(1)	0.0606(3)	0.0169(4)	1.0	4.3(2)
O4	0.0904(2)	0.0646(2)	-0.0806(3)	1.0	4.3(2)
O5	0.1167(1)	0.0555(2)	-0.2704(4)	1.0	4.3(2)
O6	0.2431(2)	0.0555(3)	-0.2303(4)	1.0	4.3(2)
O7	0.37354(2)	-0.1631(2)	-0.2294(4)	1.0	4.3(2)
O8	0.3052(2)	-0.1487(3)	-0.0652(2)	1.0	4.3(2)
O9	0.1932(1)	-0.1562(4)	0.0324(5)	1.0	4.3(2)
O10	0.0881(3)	-0.1662(2)	-0.0798(3)	1.0	4.3(2)
O11	0.1167(2)	-0.1583(3)	-0.2686(4)	1.0	4.3(2)
O12	0.2445(2)	-0.1548(3)	-0.2369(4)	1.0	4.3(2)
O13	0.3150(4)	-0.0498(1)	-0.1912(5)	1.0	4.3(2)
O14	0.0826(2)	-0.0509(1)	-0.1707(5)	1.0	4.3(2)
O15	0.4235(2)	0.1256(1)	-0.3962(4)	1.0	4.3(2)
O16	0.4025(2)	-0.0029(2)	-0.4095(4)	1.0	4.3(2)
O17	0.3957(2)	-0.1329(2)	-0.4159(4)	1.0	4.3(2)
O18	0.1965(2)	0.1317(1)	-0.3724(3)	1.0	4.3(2)
O19	0.2002(3)	0.0023(2)	-0.3959(4)	1.0	4.3(2)
O20	0.1971(2)	-0.1275(1)	-0.4134(3)	1.0	4.3(2)
O21	-0.0046(1)	0.0422(2)	-0.2076(3)	1.0	4.3(2)
O22	-0.0055(1)	-0.1429(3)	-0.2090(4)	1.0	4.3(2)
O23	0.4302(4)	-1/4	-0.3470(5)	1.0	4.3(2)
O24	0.1933(4)	-1/4	-0.3458(5)	1.0	4.3(2)
O25	0.2823(5)	-1/4	0.0516(6)	1.0	4.3(2)
O26	0.1062(5)	-1/4	0.0664(5)	1.0	4.3(2)

Table G

H^+-ZSM-5_15, 600 °C

Site	x/a	y/b	z/c	Fraction	Ui/Ue*100
T1	0.42304(9)	0.05658(6)	-0.3368(2)	1.0	2.7(1)
T2	0.31180(9)	0.02986(6)	-0.1842(2)	1.0	2.7(1)
T3	0.28057(9)	0.05901(6)	0.0338(2)	1.0	2.7(1)
T4	0.12347(9)	0.06556(6)	0.0270(2)	1.0	2.7(1)
T5	0.07121(9)	0.02758(6)	-0.1819(2)	1.0	2.7(1)
T6	0.18944(9)	0.06148(6)	-0.3170(2)	1.0	2.7(1)
T7	0.42319(9)	-0.17245(6)	-0.3210(2)	1.0	2.7(1)
T8	0.30970(9)	-0.12937(6)	-0.1799(2)	1.0	2.7(1)
T9	0.27090(9)	-0.17119(6)	0.0367(2)	1.0	2.7(1)
T10	0.11590(9)	-0.17429(6)	0.0307(2)	1.0	2.7(1)
T11	0.07033(9)	-0.12931(6)	-0.1818(2)	1.0	2.7(1)
T12	0.18799(9)	-0.17268(6)	-0.3161(2)	1.0	2.7(1)
O1	0.3712(2)	0.0616(2)	-0.2471(4)	1.0	5.0(2)
O2	0.3178(2)	0.0519(2)	-0.0705(2)	1.0	5.0(2)
O3	0.2022(1)	0.0605(3)	0.0158(4)	1.0	5.0(2)
O4	0.0899(2)	0.0648(2)	-0.0805(3)	1.0	5.0(2)
O5	0.1165(1)	0.0554(2)	-0.2705(4)	1.0	5.0(2)
O6	0.2428(2)	0.0556(3)	-0.2294(3)	1.0	5.0(2)
O7	0.3732(2)	-0.1636(2)	-0.2293(4)	1.0	5.0(2)
O8	0.3053(2)	-0.1482(3)	-0.0649(2)	1.0	5.0(2)
O9	0.1930(1)	-0.1554(3)	0.0323(4)	1.0	5.0(2)
O10	0.0880(3)	-0.1666(2)	-0.0799(3)	1.0	5.0(2)
O11	0.1164(2)	-0.1582(3)	-0.2688(4)	1.0	5.0(2)
O12	0.2441(2)	-0.15480(3)	-0.2362(4)	1.0	5.0(2)
O13	0.3151(3)	-0.0498(1)	-0.1919(5)	1.0	5.0(2)
O14	0.0829(2)	-0.0509(1)	-0.1700(5)	1.0	5.0(2)
O15	0.4241(2)	0.1255(1)	-0.3965(4)	1.0	5.0(2)
O16	0.4022(2)	-0.0028(2)	-0.4097(4)	1.0	5.0(2)
O17	0.3953(2)	-0.1330(2)	-0.4157(3)	1.0	5.0(2)
O18	0.1967(2)	0.1319(1)	-0.3719(3)	1.0	5.0(2)
O19	0.2007(3)	0.0025(2)	-0.3956(4)	1.0	5.0(2)
O20	0.1974(2)	-0.1275(1)	-0.4132(3)	1.0	5.0(2)
O21	-0.0048(1)	0.0416(2)	-0.2078(3)	1.0	5.0(2)
O22	-0.0058(1)	-0.1424(2)	-0.2089(3)	1.0	5.0(2)
O23	0.4306(4)	-1/4	-0.3471(5)	1.0	5.0(2)
O24	0.1933(4)	-1/4	-0.3455(5)	1.0	5.0(2)
O25	0.2815(4)	-1/4	0.0510(6)	1.0	5.0(2)
O26	0.1067(4)	-1/4	0.0666(4)	1.0	5.0(2)

Table H

H^+-ZSM-5_15, 800 °C

Site	x/a	y/b	z/c	Fraction	Ui/Ue*100
T1	0.4229(1)	0.05661(6)	-0.3369(2)	1.0	2.9(1)
T2	0.3117(1)	0.02990(6)	-0.1844(2)	1.0	2.9(1)
T3	0.2805(1)	0.05905(6)	0.0336(2)	1.0	2.9(1)
T4	0.1234(1)	0.06559(6)	0.0268(2)	1.0	2.9(1)
T5	0.0711(1)	0.02762(6)	-0.1821(2)	1.0	2.9(1)
T6	0.1893(1)	0.06152(6)	-0.3172(2)	1.0	2.9(1)
T7	0.4231(1)	-0.17242(6)	-0.3212(2)	1.0	2.9(1)
T8	0.3096(1)	-0.12934(6)	-0.1801(2)	1.0	2.9(1)
T9	0.2708(1)	-0.17115(6)	0.0366(2)	1.0	2.9(1)
T10	0.1158(1)	-0.17426(6)	0.0306(2)	1.0	2.9(1)
T11	0.0702(1)	-0.12927(6)	-0.1820(2)	1.0	2.9(1)
T12	0.1879(1)	-0.17264(6)	-0.3162(2)	1.0	2.9(1)
O1	0.3709(2)	0.0618(2)	-0.2475(4)	1.0	5.9(3)
O2	0.3179(2)	0.0520(3)	-0.0706(3)	1.0	5.9(3)
O3	0.2022(1)	0.0604(3)	0.0152(4)	1.0	5.9(3)
O4	0.0898(2)	0.0649(2)	-0.0807(3)	1.0	5.9(3)
O5	0.1163(1)	0.0554(2)	-0.2708(4)	1.0	5.9(3)
O6	0.2425(2)	0.0555(3)	-0.2293(4)	1.0	5.9(3)
O7	0.3731(2)	-0.1636(2)	-0.2295(4)	1.0	5.9(3)
O8	0.3052(2)	-0.1481(3)	-0.0650(2)	1.0	5.9(3)
O9	0.1930(1)	-0.1554(3)	0.0323(5)	1.0	5.9(3)
O10	0.0881(3)	-0.1666(2)	-0.0803(3)	1.0	5.9(3)
O11	0.1162(2)	-0.1580(3)	-0.2693(4)	1.0	5.9(3)
O12	0.2439(2)	-0.1546(3)	-0.2362(4)	1.0	5.9(3)
O13	0.3151(3)	-0.0498(1)	-0.1920(5)	1.0	5.9(3)
O14	0.0829(3)	-0.0508(1)	-0.1700(5)	1.0	5.9(3)
O15	0.4243(2)	0.1255(1)	-0.3969(4)	1.0	5.9(3)
O16	0.4023(3)	-0.0028(2)	-0.4099(4)	1.0	5.9(3)
O17	0.3951(3)	-0.1330(2)	-0.4158(3)	1.0	5.9(3)
O18	0.1967(2)	0.1319(1)	-0.3720(3)	1.0	5.9(3)
O19	0.2008(3)	0.0025(2)	-0.3958(4)	1.0	5.9(3)
O20	0.1976(3)	-0.1275(1)	-0.4134(3)	1.0	5.9(3)
O21	-0.0050(1)	0.0416(2)	-0.2081(3)	1.0	5.9(3)
O22	-0.0059(1)	-0.1424(3)	-0.2088(3)	1.0	5.9(3)
O23	0.4306(4)	-1/4	-0.3472(5)	1.0	5.9(3)
O24	0.1932(4)	-1/4	-0.3455(5)	1.0	5.9(3)
O25	0.2815(4)	-1/4	0.0510(6)	1.0	5.9(3)
O26	0.1066(4)	-1/4	0.0666(4)	1.0	5.9(3)

Table I

H^+-ZSM-5_20, 200 °C

Site	x/a	y/b	z/c	Fraction	Ui/Ue*100
T1	0.42323(8)	0.05658(5)	-0.3368(1)	1.0	0.9(6)
T2	0.31199(8)	0.02987(5)	-0.1843(1)	1.0	0.9(6)
T3	0.28076(8)	0.05902(5)	0.0337(1)	1.0	0.9(6)
T4	0.12366(8)	0.06556(5)	0.0270(1)	1.0	0.9(6)
T5	0.07140(8)	0.02759(5)	-0.1819(1)	1.0	0.9(6)
T6	0.18963(8)	0.06149(5)	-0.3170(1)	1.0	0.9(6)
T7	0.42338(8)	-0.17245(5)	-0.3210(1)	1.0	0.9(6)
T8	0.30989(8)	-0.12937(5)	-0.1800(1)	1.0	0.9(6)
T9	0.27109(8)	-0.17118(5)	0.0367(1)	1.0	0.9(6)
T10	0.11609(8)	-0.17428(5)	0.0307(1)	1.0	0.9(6)
T11	0.07052(8)	-0.12930(5)	-0.1818(1)	1.0	0.9(6)
T12	0.18818(8)	-0.17267(5)	-0.3161(1)	1.0	0.9(6)
O1	0.3719(2)	0.0608(2)	-0.2463(3)	1.0	1.9(1)
O2	0.3171(1)	0.0531(2)	-0.0710(2)	1.0	1.9(1)
O3	0.2023(1)	0.0606(2)	0.0176(3)	1.0	1.9(1)
O4	0.0909(2)	0.0648(2)	-0.0808(2)	1.0	1.9(1)
O5	0.1168(1)	0.0553(2)	-0.2705(3)	1.0	1.9(1)
O6	0.2435(1)	0.0555(2)	-0.2311(3)	1.0	1.9(1)
O7	0.3737(2)	-0.1629(2)	-0.2293(3)	1.0	1.9(1)
O8	0.3052(2)	-0.1494(2)	-0.0653(2)	1.0	1.9(1)
O9	0.1934(1)	-0.1559(3)	0.0326(4)	1.0	1.9(1)
O10	0.0883(2)	-0.1659(2)	-0.0796(2)	1.0	1.9(1)
O11	0.1170(1)	-0.1580(3)	-0.2683(3)	1.0	1.9(1)
O12	0.2447(2)	-0.1548(2)	-0.2372(3)	1.0	1.9(1)
O13	0.3149(3)	-0.0498(1)	-0.1900(4)	1.0	1.9(1)
O14	0.0823(2)	-0.0508(1)	-0.1704(4)	1.0	1.9(1)
O15	0.4232(1)	0.1258(1)	-0.3956(3)	1.0	1.9(1)
O16	0.4027(2)	-0.0027(1)	-0.4099(3)	1.0	1.9(1)
O17	0.3960(2)	-0.1328(1)	-0.4157(3)	1.0	1.9(1)
O18	0.1962(2)	0.1317(1)	-0.3726(2)	1.0	1.9(1)
O19	0.1999(2)	0.0025(1)	-0.3966(3)	1.0	1.9(1)
O20	0.1970(2)	-0.1275(1)	-0.4134(2)	1.0	1.9(1)
O21	-0.0044(1)	0.0426(2)	-0.2074(2)	1.0	1.9(1)
O22	-0.0053(1)	-0.1434(2)	-0.2091(3)	1.0	1.9(1)
O23	0.4299(3)	-1/4	-0.3471(4)	1.0	1.9(1)
O24	0.1932(3)	-1/4	-0.3457(4)	1.0	1.9(1)
O25	0.2821(3)	-1/4	0.0528(5)	1.0	1.9(1)
O26	0.1066(3)	-1/4	0.0665(3)	1.0	1.9(1)

Table J

H^+-ZSM-5_20, 400 °C

Site	x/a	y/b	z/c	Fraction	Ui/Ue*100
T1	0.42320(8)	0.05658(5)	-0.3364(1)	1.0	1.4(1)
T2	0.31196(8)	0.02986(5)	-0.1838(1)	1.0	1.4(1)
T3	0.28073(8)	0.05901(5)	0.0342(1)	1.0	1.4(1)
T4	0.12363(8)	0.06556(5)	0.0274(1)	1.0	1.4(1)
T5	0.07137(8)	0.02758(5)	-0.1815(1)	1.0	1.4(1)
T6	0.18960(8)	0.06148(5)	-0.3166(1)	1.0	1.4(1)
T7	0.42335(8)	-0.17245(5)	-0.3206(1)	1.0	1.4(1)
T8	0.30986(8)	-0.12937(5)	-0.1795(1)	1.0	1.4(1)
T9	0.27106(8)	-0.17119(5)	0.0371(1)	1.0	1.4(1)
T10	0.11607(8)	-0.17429(5)	0.0311(1)	1.0	1.4(1)
T11	0.07050(8)	-0.12931(5)	-0.1814(1)	1.0	1.4(1)
T12	0.18815(8)	-0.17268(5)	-0.3157(1)	1.0	1.4(1)
O1	0.3717(2)	0.0614(2)	-0.2462(3)	1.0	2.9(1)
O2	0.3176(1)	0.0522(2)	-0.0702(2)	1.0	2.9(1)
O3	0.2023(1)	0.0604(2)	0.0167(3)	1.0	2.9(1)
O4	0.0901(2)	0.0649(2)	-0.0800(2)	1.0	2.9(1)
O5	0.1168(1)	0.0553(2)	-0.2698(3)	1.0	2.9(1)
O6	0.2433(1)	0.0555(2)	-0.2298(3)	1.0	2.9(1)
O7	0.3736(2)	-0.1636(2)	-0.2287(3)	1.0	2.9(1)
O8	0.3055(2)	-0.1484(2)	-0.0645(2)	1.0	2.9(1)
O9	0.1932(1)	-0.1552(3)	0.0322(4)	1.0	2.9(1)
O10	0.0878(2)	-0.1665(2)	-0.0793(2)	1.0	2.9(1)
O11	0.1168(1)	-0.1581(3)	-0.2679(3)	1.0	2.9(1)
O12	0.24451(2)	-0.1548(3)	-0.2360(3)	1.0	2.9(1)
O13	0.3152(3)	-0.0499(1)	-0.1912(4)	1.0	2.9(1)
O14	0.0829(2)	-0.0509(1)	-0.1693(4)	1.0	2.9(1)
O15	0.4237(2)	0.1257(1)	-0.3958(3)	1.0	2.9(1)
O16	0.4023(2)	-0.0027(1)	-0.4094(3)	1.0	2.9(1)
O17	0.3953(2)	-0.1329(1)	-0.4151(3)	1.0	2.9(1)
O18	0.1966(2)	0.1320(1)	-0.3715(3)	1.0	2.9(1)
O19	0.2005(2)	0.0027(1)	-0.3957(3)	1.0	2.9(1)
O20	0.1973(2)	-0.1274(1)	-0.4127(3)	1.0	2.9(1)
O21	-0.0045(1)	0.0418(2)	-0.2076(2)	1.0	2.9(1)
O22	-0.0056(1)	-0.1425(2)	-0.2090(3)	1.0	2.9(1)
O23	0.4307(3)	-1/4	-0.3468(4)	1.0	2.9(1)
O24	0.1934(3)	-1/4	-0.3449(4)	1.0	2.9(1)
O25	0.2815(4)	-1/4	0.0516(5)	1.0	2.9(1)
O26	0.1072(4)	-1/4	0.0670(4)	1.0	2.9(1)

Table K

H^+-ZSM-5_20, 600 °C

Site	x/a	y/b	z/c	Fraction	Ui/Ue*100
T1	0.42318(8)	0.05660(5)	-0.3362(1)	1.0	1.6(1)
T2	0.31194(8)	0.02988(5)	-0.1837(1)	1.0	1.6(1)
T3	0.28071(8)	0.05903(5)	0.0343(1)	1.0	1.6(1)
T4	0.12361(8)	0.06558(5)	0.02760(1)	1.0	1.6(1)
T5	0.07135(8)	0.02760(5)	-0.1813(1)	1.0	1.6(1)
T6	0.18959(8)	0.06150(5)	-0.3164(1)	1.0	1.6(1)
T7	0.42333(8)	-0.17243(5)	-0.3204(1)	1.0	1.6(1)
T8	0.30984(8)	-0.12935(5)	-0.1794(1)	1.0	1.6(1)
T9	0.27104(8)	-0.17117(5)	0.0373(1)	1.0	1.6(1)
T10	0.11604(8)	-0.17427(5)	0.03135(1)	1.0	1.6(1)
T11	0.07047(8)	-0.12929(5)	-0.1812(1)	1.0	1.6(1)
T12	0.18813(8)	-0.17266(5)	-0.3155(1)	1.0	1.6(1)
O1	0.3715(2)	0.0618(2)	-0.2462(3)	1.0	3.6(2)
O2	0.3182(1)	0.0521(2)	-0.06993(2)	1.0	3.6(2)
O3	0.2023(1)	0.0603(2)	0.0158(3)	1.0	3.6(2)
O4	0.0897(2)	0.0651(2)	-0.0799(2)	1.0	3.6(2)
O5	0.1166(1)	0.0554(2)	-0.2699(3)	1.0	3.6(2)
O6	0.2430(1)	0.0556(2)	-0.2289(3)	1.0	3.6(2)
O7	0.3735(2)	-0.1638(2)	-0.2284(3)	1.0	3.6(2)
O8	0.3056(2)	-0.1481(2)	-0.0641(2)	1.0	3.6(2)
O9	0.1931(1)	-0.15519(3)	0.0326(4)	1.0	3.6(2)
O10	0.0878(2)	-0.1667(2)	-0.0793(2)	1.0	3.6(2)
O11	0.1165(1)	-0.1581(3)	-0.2682(3)	1.0	3.6(2)
O12	0.2443(2)	-0.1548(3)	-0.2356(3)	1.0	3.6(2)
O13	0.3154(3)	-0.0498(1)	-0.1913(4)	1.0	3.6(2)
O14	0.0832(2)	-0.0509(1)	-0.1690(4)	1.0	3.6(2)
O15	0.4241(1)	0.1257(1)	-0.3958(3)	1.0	3.6(2)
O16	0.4021(2)	-0.0027(1)	-0.4092(3)	1.0	3.6(2)
O17	0.3949(2)	-0.1331(1)	-0.4150(3)	1.0	3.6(2)
O18	0.1966(2)	0.1321(1)	-0.3710(3)	1.0	3.6(2)
O19	0.2007(2)	0.0026(1)	-0.3953(3)	1.0	3.6(2)
O20	0.1974(2)	-0.1274(1)	-0.4127(3)	1.0	3.6(2)
O21	-0.0042(1)	0.0414(2)	-0.2081(2)	1.0	3.6(2)
O22	-0.0057(1)	-0.1421(2)	-0.2090(3)	1.0	3.6(2)
O23	0.4309(3)	-1/4	-0.3467(4)	1.0	3.6(2)
O24	0.1934(3)	-1/4	-0.3451(4)	1.0	3.6(2)
O25	0.2816(4)	-1/4	0.0517(5)	1.0	3.6(2)
O26	0.1070(4)	-1/4	0.0676(4)	1.0	3.6(2)

Table L

H^+-ZSM-5_20, 800 °C

Site	x/a	y/b	z/c	Fraction	Ui/Ue*100
T1	0.42317(9)	0.05661(6)	-0.3363(1)	1.0	2.6(1)
T2	0.31192(9)	0.02990(6)	-0.1838(1)	1.0	2.6(1)
T3	0.28070(9)	0.05905(6)	0.0342(1)	1.0	2.6(1)
T4	0.12360(9)	0.06560(6)	0.0275(1)	1.0	2.6(1)
T5	0.07133(9)	0.02762(6)	-0.1814(1)	1.0	2.6(1)
T6	0.18957(9)	0.06152(6)	-0.3165(1)	1.0	2.6(1)
T7	0.42332(9)	-0.17241(6)	-0.3205(1)	1.0	2.6(1)
T8	0.30982(9)	-0.12934(6)	-0.1795(1)	1.0	2.6(1)
T9	0.27103(9)	-0.17115(6)	0.0372(1)	1.0	2.6(1)
T10	0.11603(9)	-0.17425(6)	0.0312(1)	1.0	2.6(1)
T11	0.07046(9)	-0.12927(6)	-0.1813(1)	1.0	2.6(1)
T12	0.18812(9)	-0.17264(6)	-0.3156(1)	1.0	2.6(1)
O1	0.3713(2)	0.0622(2)	-0.2465(3)	1.0	5.5(2)
O2	0.3183(2)	0.0518(2)	-0.0699(2)	1.0	5.5(2)
O3	0.2024(1)	0.0603(2)	0.0154(4)	1.0	5.5(2)
O4	0.0895(2)	0.0652(2)	-0.0799(2)	1.0	5.5(2)
O5	0.1165(1)	0.05540(2)	-0.2701(3)	1.0	5.5(2)
O6	0.2428(2)	0.0556(3)	-0.2286(3)	1.0	5.5(2)
O7	0.3734(2)	-0.1642(2)	-0.2285(3)	1.0	5.5(2)
O8	0.3056(2)	-0.1475(3)	-0.0640(5)	1.0	5.5(2)
O9	0.1931(1)	-0.1548(3)	0.0325(4)	1.0	5.5(2)
O10	0.0878(2)	-0.1670(2)	-0.0796(2)	1.0	5.5(2)
O11	0.1164(1)	-0.1581(3)	-0.2685(3)	1.0	5.5(2)
O12	0.2441(2)	-0.1547(3)	-0.2353(3)	1.0	5.5(2)
O13	0.3156(3)	-0.0498(1)	-0.1923(4)	1.0	5.5(2)
O14	0.0835(2)	-0.0509(1)	-0.1687(5)	1.0	5.5(2)
O15	0.4244(2)	0.1256(1)	-0.3962(3)	1.0	5.5(2)
O16	0.4019(2)	-0.0027(2)	-0.4092(4)	1.0	5.5(2)
O17	0.3947(2)	-0.1331(1)	-0.4150(3)	1.0	5.5(2)
O18	0.1967(2)	0.1323(1)	-0.3707(3)	1.0	5.5(2)
O19	0.2009(3)	0.0027(2)	-0.3953(4)	1.0	5.5(2)
O20	0.1975(2)	-0.1274(1)	-0.4127(3)	1.0	5.5(2)
O21	-0.0048(1)	0.0410(2)	-0.2082(3)	1.0	5.5(2)
O22	-0.0058(1)	-0.1417(2)	-0.2090(3)	1.0	5.5(2)
O23	0.4314(3)	-1/4	-0.3468(5)	1.0	5.5(2)
O24	0.1936(4)	-1/4	-0.3449(5)	1.0	5.5(2)
O25	0.2814(4)	-1/4	0.0508(5)	1.0	5.5(2)
O26	0.1073(4)	-1/4	0.0676(4)	1.0	5.5(2)

Table M

H^+-ZSM-5_37, 200 °C

Site	x/a	y/b	z/c	Fraction	Ui/Ue*100
T1	0.42312(5)	0.0565(3)	-0.3365(1)	1.0	0.89(8)
T2	0.31188(5)	0.0298(3)	-0.1839(1)	1.0	0.89(8)
T3	0.28066(5)	0.0589(3)	0.0341(1)	1.0	0.89(8)
T4	0.12356(5)	0.0655(3)	0.0273(1)	1.0	0.89(8)
T5	0.07129(5)	0.0275(3)	-0.1816(1)	1.0	0.89(8)
T6	0.18953(5)	0.0614(3)	-0.3167(1)	1.0	0.89(8)
T7	0.42328(5)	-0.1724(30)	-0.3207(1)	1.0	0.89(8)
T8	0.30978(5)	-0.1294(3)	-0.1796(1)	1.0	0.89(8)
T9	0.27099(5)	-0.1712(3)	0.0370(1)	1.0	0.89(8)
T10	0.11599(5)	-0.1743(3)	0.0310(1)	1.0	0.89(8)
T11	0.07042(5)	-0.1293(3)	-0.1815(1)	1.0	0.89(8)
T12	0.18808(5)	-0.1727(3)	-0.3158(1)	1.0	0.89(8)
O1	0.3717(1)	0.0609(1)	-0.2463(2)	1.0	2.0(1)
O2	0.3174(1)	0.0526(1)	-0.0704(1)	1.0	2.0(1)
O3	0.2022(6)	0.0605(1)	0.0168(2)	1.0	2.0(1)
O4	0.0904(1)	0.0649(1)	-0.0804(1)	1.0	2.0(1)
O5	0.1168(9)	0.0551(1)	-0.2700(2)	1.0	2.0(1)
O6	0.2432(1)	0.0556(1)	-0.2300(2)	1.0	2.0(1)
O7	0.3736(1)	-0.1631(1)	-0.2290(2)	1.0	2.0(1)
O8	0.3052(1)	-0.1491(1)	-0.0649(5)	1.0	2.0(1)
O9	0.1932(6)	-0.1554(1)	0.0323(2)	1.0	2.0(1)
O10	0.0879(1)	-0.1664(1)	-0.0793(1)	1.0	2.0(1)
O11	0.1169(1)	-0.1579(1)	-0.2680(2)	1.0	2.0(1)
O12	0.2446(1)	-0.1550(1)	-0.2366(2)	1.0	2.0(1)
O13	0.3146(1)	-0.04994(6)	-0.1903(2)	1.0	2.0(1)
O14	0.0825(1)	-0.05094(6)	-0.1694(2)	1.0	2.0(1)
O15	0.4234(1)	0.12576(9)	-0.3956(2)	1.0	2.0(1)
O16	0.4025(1)	-0.0026(1)	-0.4099(2)	1.0	2.0(1)
O17	0.3955(1)	-0.1329(1)	-0.4154(1)	1.0	2.0(1)
O18	0.1966(1)	0.13178(9)	-0.3719(1)	1.0	2.0(1)
O19	0.2004(1)	0.0025(1)	-0.3958(2)	1.0	2.0(1)
O20	0.1973(1)	-0.12751(9)	-0.4129(1)	1.0	2.0(1)
O21	-0.00457(7)	0.0421(1)	-0.2073(1)	1.0	2.0(1)
O22	-0.00550(8)	-0.1431(1)	-0.2088(1)	1.0	2.0(1)
O23	0.4300(2)	-1/4	-0.3468(2)	1.0	2.0(1)
O24	0.1930(2)	-1/4	-0.3453(2)	1.0	2.0(1)
O25	0.2814(2)	-1/4	0.0528(3)	1.0	2.0(1)
O26	0.1070(2)	-1/4	0.0670(2)	1.0	2.0(1)

Table N

H^+-ZSM-5_37, 400 °C

Site	x/a	y/b	z/c	Fraction	Ui/Ue*100
T1	0.42314(5)	0.0565(3)	-0.3362(1)	1.0	1.44(8)
T2	0.31190(5)	0.02985(3)	-0.1836(1)	1.0	1.44(8)
T3	0.28068(5)	0.05900(3)	0.0344(1)	1.0	1.44(8)
T4	0.12358(5)	0.06555(3)	0.0276(1)	1.0	1.44(8)
T5	0.07131(5)	0.02757(3)	-0.1813(1)	1.0	1.44(8)
T6	0.18955(5)	0.06147(3)	-0.3164(1)	1.0	1.44(8)
T7	0.42330(5)	-0.17241(3)	-0.3204(1)	1.0	1.44(8)
T8	0.30980(5)	-0.12938(3)	-0.1793(1)	1.0	1.44(8)
T9	0.27101(5)	-0.17119(3)	0.0373(1)	1.0	1.44(8)
T10	0.11601(5)	-0.17430(3)	0.0313(1)	1.0	1.44(8)
T11	0.07044(5)	-0.12931(3)	-0.1812(1)	1.0	1.44(8)
T12	0.18810(5)	-0.17268(3)	-0.3155(1)	1.0	1.44(8)
O1	0.3716(1)	0.0613(1)	-0.2461(2)	1.0	3.5(1)
O2	0.3178(1)	0.0523(1)	-0.0700(1)	1.0	3.5(1)
O3	0.20234(6)	0.0605(1)	0.0162(2)	1.0	3.5(1)
O4	0.0900(1)	0.0651(1)	-0.0800(1)	1.0	3.5(1)
O5	0.11685(9)	0.0552(1)	-0.2697(2)	1.0	3.5(1)
O6	0.2432(1)	0.0556(1)	-0.2293(2)	1.0	3.5(1)
O7	0.3736(1)	-0.1634(1)	-0.2285(2)	1.0	3.5(1)
O8	0.3053(1)	-0.1487(1)	-0.0644(1)	1.0	3.5(1)
O9	0.19318(6)	-0.1552(1)	0.0325(2)	1.0	3.5(1)
O10	0.0878(1)	-0.1666(1)	-0.0792(1)	1.0	3.5(1)
O11	0.1168(1)	-0.1579(1)	-0.2678(2)	1.0	3.5(1)
O12	0.2445(1)	-0.1550(1)	-0.2360(2)	1.0	3.5(1)
O13	0.3149(1)	-0.04991(6)	-0.1905(2)	1.0	3.5(1)
O14	0.0828(1)	-0.05094(6)	-0.1688(2)	1.0	3.5(1)
O15	0.4237(1)	0.12573(9)	-0.3956(2)	1.0	3.5(1)
O16	0.4022(1)	-0.0026(1)	-0.4095(2)	1.0	3.5(1)
O17	0.3951(1)	-0.1330(1)	-0.4150(1)	1.0	3.5(1)
O18	0.1967(1)	0.13194(9)	-0.3713(1)	1.0	3.5(1)
O19	0.2007(1)	0.0025(1)	-0.3953(2)	1.0	3.5(1)
O20	0.1975(1)	-0.12749(9)	-0.4126(1)	1.0	3.5(1)
O21	-0.00463(7)	0.0418(1)	-0.2075(1)	1.0	3.5(1)
O22	-0.00559(8)	-0.1426(1)	-0.2088(1)	1.0	3.5(1)
O23	0.4304(2)	-1/4	-0.3465(2)	1.0	3.5(1)
O24	0.1931(2)	-1/4	-0.3449(2)	1.0	3.5(1)
O25	0.28132(2)	-1/4	0.0526(3)	1.0	3.5(1)
O26	0.1071(2)	-1/4	0.0675(2)	1.0	3.5(1)

Table O

H^+-ZSM-5_37, 600 °C

Site	x/a	y/b	z/c	Fraction	Ui/Ue*100
T1	0.42308(5)	0.05656(2)	-0.3362(1)	1.0	2.3(1)
T2	0.31183(5)	0.02985(2)	-0.1837(1)	1.0	2.3(1)
T3	0.28061(5)	0.0590(2)	0.0343(1)	1.0	2.3(1)
T4	0.12351(5)	0.06554(2)	0.0275(1)	1.0	2.3(1)
T5	0.07124(5)	0.02757(2)	-0.1819(1)	1.0	2.3(1)
T6	0.18948(5)	0.06147(2)	-0.3164(1)	1.0	2.3(1)
T7	0.42323(5)	-0.17246(2)	-0.3204(1)	1.0	2.3(1)
T8	0.30973(5)	-0.12938(2)	-0.1794(1)	1.0	2.3(1)
T9	0.27094(5)	-0.17119(2)	0.0373(1)	1.0	2.3(1)
T10	0.11594(5)	-0.17430(2)	0.0313(1)	1.0	2.3(1)
T11	0.07037(5)	-0.12932(2)	-0.1812(1)	1.0	2.3(1)
T12	0.18803(5)	-0.17269(2)	-0.3158(1)	1.0	2.3(1)
O1	0.3713(1)	0.0616(12)	-0.2465(2)	1.0	5.4(1)
O2	0.3181(1)	0.0520(1)	-0.0699(1)	1.0	5.4(1)
O3	0.20232(6)	0.0604(1)	0.0155(2)	1.0	5.4(1)
O4	0.0897(1)	0.0652(1)	-0.0800(1)	1.0	5.4(1)
O5	0.11669(9)	0.0552(1)	-0.2699(2)	1.0	5.4(1)
O6	0.2429(1)	0.0556(1)	-0.2287(1)	1.0	5.4(1)
O7	0.3734(1)	-0.1638(1)	-0.2286(2)	1.0	5.4(1)
O8	0.3054(1)	-0.1484(1)	-0.0642(1)	1.0	5.4(1)
O9	0.19306(6)	-0.1548(1)	0.0323(2)	1.0	5.4(1)
O10	0.0876(1)	-0.1669(1)	-0.0794(1)	1.0	5.4(1)
O11	0.1165(1)	-0.1580(1)	-0.2681(2)	1.0	5.4(1)
O12	0.2443(1)	-0.1549(1)	-0.2356(2)	1.0	5.4(1)
O13	0.3151(1)	-0.04993(5)	-0.1911(2)	1.0	5.4(1)
O14	0.0830(1)	-0.05096(5)	-0.1685(2)	1.0	5.4(1)
O15	0.4241(1)	0.1256(8)	-0.3960(2)	1.0	5.4(1)
O16	0.4021(1)	-0.0027(1)	-0.4096(2)	1.0	5.4(1)
O17	0.3948(1)	-0.1331(9)	-0.4150(1)	1.0	5.4(1)
O18	0.1969(1)	0.1320(8)	-0.3710(1)	1.0	5.4(1)
O19	0.2010(1)	0.00264(1)	-0.3952(2)	1.0	5.4(1)
O20	0.1976(1)	-0.12744(9)	-0.4126(1)	1.0	5.4(1)
O21	-0.0048(7)	0.0413(1)	-0.2078(1)	1.0	5.4(1)
O22	-0.0058(7)	-0.1422(1)	-0.2088(1)	1.0	5.4(1)
O23	0.4308(1)	-1/4	-0.3467(2)	1.0	5.4(1)
O24	0.1932(2)	-1/4	-0.3449(2)	1.0	5.4(1)
O25	0.2809(2)	-1/4	0.0521(2)	1.0	5.4(1)
O26	0.10745(2)	-1/4	0.0676(2)	1.0	5.4(1)

Table P

H^+-ZSM-5_37, 800 °C

Site	x/a	y/b	z/c	Fraction	Ui/Ue*100
T1	0.42308(5)	0.05658(2)	-0.3363(1)	1.0	2.8(1)
T2	0.31183(5)	0.02987(2)	-0.1838(1)	1.0	2.8(1)
T3	0.28061(5)	0.05902(2)	0.0342(1)	1.0	2.8(1)
T4	0.12351(5)	0.06557(2)	0.0275(1)	1.0	2.8(1)
T5	0.07124(5)	0.02759(2)	-0.1814(1)	1.0	2.8(1)
T6	0.18948(5)	0.06149(2)	-0.3165(1)	1.0	2.8(1)
T7	0.42323(5)	-0.17240(2)	-0.3205(1)	1.0	2.8(1)
T8	0.30973(5)	-0.12936(2)	-0.1795(1)	1.0	2.8(1)
T9	0.27094(5)	-0.17117(2)	0.0372(1)	1.0	2.8(1)
T10	0.11594(5)	-0.17427(2)	0.0312(1)	1.0	2.8(1)
T11	0.07037(5)	-0.12929(2)	-0.1813(1)	1.0	2.8(1)
T12	0.18803(5)	-0.17266(2)	-0.3156(1)	1.0	2.8(1)
O1	0.3712(1)	0.0619(1)	-0.2467(2)	1.0	5.2(2)
O2	0.3183(1)	0.0520(1)	-0.0699(1)	1.0	5.2(2)
O3	0.2023(6)	0.0604(1)	0.0150(2)	1.0	5.2(2)
O4	0.0896(1)	0.0654(1)	-0.0801(1)	1.0	5.2(2)
O5	0.1165(9)	0.0552(1)	-0.2701(2)	1.0	5.2(2)
O6	0.2427(1)	0.0556(1)	-0.2285(2)	1.0	5.2(2)
O7	0.3733(1)	-0.1640(1)	-0.2286(2)	1.0	5.2(2)
O8	0.3054(1)	-0.1482(1)	-0.0642(1)	1.0	5.2(2)
O9	0.1930(6)	-0.1548(1)	0.0324(2)	1.0	5.2(2)
O10	0.0877(1)	-0.1671(1)	-0.0796(1)	1.0	5.2(2)
O11	0.1164(1)	-0.1579(1)	-0.2685(2)	1.0	5.2(2)
O12	0.2442(1)	-0.1549(1)	-0.2356(2)	1.0	5.2(2)
O13	0.3153(1)	-0.04989(5)	-0.1914(2)	1.0	5.2(2)
O14	0.0832(1)	-0.05095(6)	-0.1684(2)	1.0	5.2(2)
O15	0.4243(1)	0.12566(8)	-0.3962(2)	1.0	5.2(2)
O16	0.4020(1)	-0.0027(1)	-0.4097(2)	1.0	5.2(2)
O17	0.3947(1)	-0.1331(1)	-0.4151(1)	1.0	5.2(2)
O18	0.1968(1)	0.1321(9)	-0.3709(1)	1.0	5.2(2)
O19	0.2011(1)	0.0026(1)	-0.3953(2)	1.0	5.2(2)
O20	0.1976(1)	-0.1278(9)	-0.4128(1)	1.0	5.2(2)
O21	0.0048(7)	0.0412(1)	-0.2079(1)	1.0	5.2(2)
O22	0.0058(8)	-0.1420(1)	-0.2088(1)	1.0	5.2(2)
O23	0.4310(1)	-1/z	-0.3469(2)	1.0	5.2(2)
O24	0.1932(2)	-1/4	-0.3450(2)	1.0	5.2(2)
O25	0.2809(2)	-1/4	0.0519(3)	1.0	5.2(2)
O26	0.1073(2)	-1/4	0.0678(2)	1.0	5.2(2)

Table Q

H^+-ZSM-5_69, 200 °C

Site	x/a	y/b	z/c	Fraction	Ui/Ue*100
T1	0.42307(6)	0.05661(4)	-0.3376(1)	1.0	0.90(7)
T2	0.31183(6)	0.02990(4)	-0.1850(1)	1.0	0.90(7)
T3	0.28060(6)	0.05905(4)	0.0330(1)	1.0	0.90(7)
T4	0.12350(6)	0.06559(4)	0.0262(1)	1.0	0.90(7)
T5	0.07124(6)	0.02762(4)	-0.1827(1)	1.0	0.90(7)
T6	0.18947(6)	0.06151(4)	-0.3178(1)	1.0	0.90(7)
T7	0.42322(6)	-0.17242(4)	-0.3218(1)	1.0	0.90(7)
T8	0.30972(6)	-0.12934(4)	-0.1807(1)	1.0	0.90(7)
T9	0.27093(6)	-0.17115(4)	0.0359(1)	1.0	0.90(7)
T10	0.11593(6)	-0.17426(4)	0.0299(1)	1.0	0.90(7)
T11	0.07036(6)	-0.12928(4)	-0.1826(1)	1.0	0.90(7)
T12	0.18802(6)	-0.17265(4)	-0.3169(1)	1.0	0.90(7)
O1	0.3713(1)	0.0610(1)	-0.2479(2)	1.0	1.8(1)
O2	0.3170(1)	0.0532(1)	-0.0719(1)	1.0	1.8(1)
O3	0.2022(7)	0.0605(2)	0.0168(2)	1.0	1.8(1)
O4	0.0911(1)	0.0651(1)	-0.0819(2)	1.0	1.8(1)
O5	0.1165(1)	0.0550(1)	-0.2717(2)	1.0	1.8(1)
O6	0.2430(1)	0.0552(2)	-0.2315(2)	1.0	1.8(1)
O7	0.3732(1)	-0.1632(1)	-0.2304(2)	1.0	1.8(1)
O8	0.3051(1)	-0.1494(2)	-0.0660(1)	1.0	1.8(1)
O9	0.19325(8)	-0.1551(2)	0.0318(3)	1.0	1.8(1)
O10	0.0884(1)	-0.1663(1)	-0.0806(2)	1.0	1.8(1)
O11	0.1166(1)	-0.1578(2)	-0.2695(2)	1.0	1.8(1)
O12	0.2442(1)	-0.1545(2)	-0.2374(2)	1.0	1.8(1)
O13	0.3148(2)	-0.04988(7)	-0.1907(3)	1.0	1.8(1)
O14	0.0824(1)	-0.05087(7)	-0.1705(3)	1.0	1.8(1)
O15	0.4236(1)	0.1258(1)	-0.3967(2)	1.0	1.8(1)
O16	0.4030(1)	-0.0026(1)	-0.4112(2)	1.0	1.8(1)
O17	0.3959(1)	-0.1329(1)	-0.4166(2)	1.0	1.8(1)
O18	0.1963(1)	0.1318(1)	-0.3731(2)	1.0	1.8(1)
O19	0.1999(2)	0.0026(1)	-0.3976(2)	1.0	1.8(1)
O20	0.1973(1)	-0.1276(1)	-0.4141(2)	1.0	1.8(1)
O21	-0.00476(9)	0.0423(1)	-0.2073(2)	1.0	1.8(1)
O22	-0.0056(1)	-0.1430(2)	-0.2089(2)	1.0	1.8(1)
O23	0.4302(2)	-1/4	-0.3478(3)	1.0	1.8(1)
O24	0.1930(2)	-1/4	-0.3458(3)	1.0	1.8(1)
O25	0.2810(3)	-1/4	0.0520(3)	1.0	1.8(1)
O26	0.10743(3)	-1/4	0.0659(3)	1.0	1.8(1)

Table R

H^+-ZSM-5_69, 400 °C

Site	x/a	y/b	z/c	Fraction	Ui/Ue*100
T1	0.42322(6)	0.05658(4)	-0.3362(1)	1.0	1.83(8)
T2	0.31198(6)	0.02987(4)	-0.1836(1)	1.0	1.83(8)
T3	0.28075(6)	0.05902(4)	0.0344(1)	1.0	1.83(8)
T4	0.12365(6)	0.06556(4)	0.0276(1)	1.0	1.83(8)
T5	0.07139(6)	0.02759(4)	-0.1813(1)	1.0	1.83(8)
T6	0.18962(6)	0.06149(4)	-0.3164(1)	1.0	1.83(8)
T7	0.42337(6)	-0.17245(4)	-0.3204(1)	1.0	1.83(8)
T8	0.30988(6)	-0.12937(4)	-0.1793(1)	1.0	1.83(8)
T9	0.27108(6)	-0.17118(4)	0.03739(1)	1.0	1.83(8)
T10	0.11608(6)	-0.17429(4)	0.0314(1)	1.0	1.83(8)
T11	0.07051(6)	-0.12931(4)	-0.1812(1)	1.0	1.83(8)
T12	0.18817(6)	-0.17267(4)	-0.3155(1)	1.0	1.83(8)
O1	0.3717(1)	0.0614(1)	-0.2461(2)	1.0	3.9(1)
O2	0.3178(1)	0.0523(1)	-0.0700(1)	1.0	3.9(1)
O3	0.20238(7)	0.0605(1)	0.0164(2)	1.0	3.9(1)
O4	0.0901(1)	0.0651(1)	-0.0800(2)	1.0	3.9(1)
O5	0.1168(1)	0.0552(1)	-0.2698(2)	1.0	3.9(1)
O6	0.2432(1)	0.0556(2)	-0.2293(2)	1.0	3.9(1)
O7	0.3737(1)	-0.1635(1)	-0.2284(2)	1.0	3.9(1)
O8	0.3054(1)	-0.1485(2)	-0.0643(1)	1.0	3.9(1)
O9	0.19327(8)	-0.1553(2)	0.0326(3)	1.0	3.9(1)
O10	0.0879(1)	-0.1667(1)	-0.0792(2)	1.0	3.9(1)
O11	0.1168(1)	-0.1579(2)	-0.2679(2)	1.0	3.9(1)
O12	0.2445(1)	-0.1548(2)	-0.2359(2)	1.0	3.9(1)
O13	0.3152(2)	-0.0498(7)	-0.1907(3)	1.0	3.9(1)
O14	0.0830(1)	-0.0509(7)	-0.1687(3)	1.0	3.9(1)
O15	0.4237(1)	0.1256(1)	-0.3957(2)	1.0	3.9(1)
O16	0.4022(1)	-0.0027(1)	-0.4094(2)	1.0	3.9(1)
O17	0.3950(1)	-0.1331(1)	-0.4150(2)	1.0	3.9(1)
O18	0.1966(1)	0.1320(1)	-0.3712(2)	1.0	3.9(1)
O19	0.2006(2)	0.0026(1)	-0.3955(2)	1.0	3.9(1)
O20	0.1974(1)	-0.1275(1)	-0.4126(2)	1.0	3.9(1)
O21	-0.00457(9)	0.0416(1)	-0.2076(2)	1.0	3.9(1)
O22	-0.00556(9)	-0.1424(1)	-0.2087(2)	1.0	3.9(1)
O23	0.4306(2)	-1/4	-0.3465(3)	1.0	3.9(1)
O24	0.1933(2)	-1/4	-0.3448(3)	1.0	3.9(1)
O25	0.2816(2)	-1/4	0.0523(3)	1.0	3.9(1)
O26	0.1071(2)	-1/4	0.0677(2)	1.0	3.9(1)

Table S

H^+-ZSM-5_69, 600 °C

Site	x/a	y/b	z/c	Fraction	Ui/Ue*100
T1	0.42325(6)	0.05660(4)	-0.3361(1)	1.0	1.99(8)
T2	0.31201(6)	0.02988(4)	-0.1835(1)	1.0	1.99(8)
T3	0.28078(6)	0.05903(4)	0.0345(1)	1.0	1.99(8)
T4	0.12368(6)	0.06558(4)	0.0277(1)	1.0	1.99(8)
T5	0.07142(6)	0.02760(4)	-0.1812(1)	1.0	1.99(8)
T6	0.18965(6)	0.06150(4)	-0.3163(1)	1.0	1.99(8)
T7	0.42340(6)	-0.17243(4)	-0.3203(1)	1.0	1.99(8)
T8	0.30991(6)	-0.12935(4)	-0.1792(1)	1.0	1.99(8)
T9	0.27111(6)	-0.17117(4)	0.0374(1)	1.0	1.99(8)
T10	0.11611(6)	-0.17427(4)	0.0314(1)	1.0	1.99(8)
T11	0.07054(6)	-0.12929(4)	-0.1811(1)	1.0	1.99(8)
T12	0.18820(6)	-0.17266(4)	-0.3154(1)	1.0	1.99(8)
O1	0.3716(1)	0.0618(1)	-0.2461(2)	1.0	4.3(1)
O2	0.3181(1)	0.0522(1)	-0.0698(1)	1.0	4.3(1)
O3	0.2024(7)	0.0605(1)	0.0160(2)	1.0	4.3(1)
O4	0.0899(1)	0.0652(1)	-0.0798(2)	1.0	4.3(1)
O5	0.1168(1)	0.0553(1)	-0.2698(2)	1.0	4.3(1)
O6	0.2431(1)	0.0555(2)	-0.2289(2)	1.0	4.3(1)
O7	0.3736(1)	-0.1639(1)	-0.2283(2)	1.0	4.3(1)
O8	0.3056(1)	-0.1483(2)	-0.0640(1)	1.0	4.3(1)
O9	0.1932(8)	-0.1550(2)	0.0325(3)	1.0	4.3(1)
O10	0.0878(1)	-0.1669(1)	-0.0792(2)	1.0	4.3(1)
O11	0.1167(1)	-0.1581(2)	-0.2680(2)	1.0	4.3(1)
O12	0.2444(1)	-0.1547(2)	-0.2356(2)	1.0	4.3(1)
O13	0.3155(2)	-0.04986(7)	-0.1909(3)	1.0	4.3(1)
O14	0.0834(1)	-0.05093(7)	-0.1685(3)	1.0	4.3(1)
O15	0.4240(1)	0.1256(1)	-0.3958(2)	1.0	4.3(1)
O16	0.4020(1)	-0.0027(1)	-0.4092(2)	1.0	4.3(1)
O17	0.3949(1)	-0.1331(1)	-0.4149(2)	1.0	4.3(1)
O18	0.1967(1)	0.1322(1)	-0.3708(2)	1.0	4.3(1)
O19	0.2008(2)	0.0027(1)	-0.3954(2)	1.0	4.3(1)
O20	0.1974(1)	-0.1274(1)	-0.4125(2)	1.0	4.3(1)
O21	-0.00463(9)	0.0413(1)	-0.2078(2)	1.0	4.3(1)
O22	-0.0056(1)	-0.1420(1)	-0.2088(2)	1.0	4.3(1)
O23	0.4310(2)	-1/4	-0.3466(3)	1.0	4.3(1)
O24	0.1936(2)	-1/4	-0.3448(3)	1.0	4.3(1)
O25	0.2814(3)	-1/4	0.0520(3)	1.0	4.3(1)
O26	0.1074(3)	-1/4	0.0679(2)	1.0	4.3(1)

Table T

H^+-ZSM-5_69, 800 °C

Site	x/a	y/b	z/c	Fraction	Ui/Ue*100
T1	0.42324(6)	0.05660(4)	-0.3358(1)	1.0	2.72(8)
T2	0.31200(6)	0.02988(4)	-0.1833(1)	1.0	2.72(8)
T3	0.28077(6)	0.05904(4)	0.0347(1)	1.0	2.72(8)
T4	0.12367(6)	0.06558(4)	0.0280(1)	1.0	2.72(8)
T5	0.07141(6)	0.02761(4)	-0.1809(1)	1.0	2.72(8)
T6	0.18965(6)	0.06151(4)	-0.3160(1)	1.0	2.72(8)
T7	0.42339(6)	-0.17243(4)	-0.3200(1)	1.0	2.72(8)
T8	0.30990(6)	-0.12935(4)	-0.1790(1)	1.0	2.72(8)
T9	0.27110(6)	-0.17116(4)	0.0377(1)	1.0	2.72(8)
T10	0.11610(6)	-0.17427(4)	0.0317(1)	1.0	2.72(8)
T11	0.07053(6)	-0.12929(4)	-0.1808(1)	1.0	2.72(8)
T12	0.18819(6)	-0.17266(4)	-0.3151(1)	1.0	2.72(8)
O1	0.3715(1)	0.0620(1)	-0.2460(2)	1.0	6.2(1)
O2	0.3185(1)	0.0519(1)	-0.0694(1)	1.0	6.2(1)
O3	0.20244(7)	0.0604(1)	0.0153(2)	1.0	6.2(1)
O4	0.0895(1)	0.0654(1)	-0.0794(2)	1.0	6.2(1)
O5	0.1168(1)	0.0551(1)	-0.2695(2)	1.0	6.2(1)
O6	0.2430(1)	0.0556(1)	-0.2282(2)	1.0	6.2(1)
O7	0.3736(1)	-0.1641(1)	-0.2278(2)	1.0	6.2(1)
O8	0.30573(1)	-0.1479(2)	-0.0636(1)	1.0	6.2(1)
O9	0.19319(8)	-0.1548(2)	0.0327(3)	1.0	6.2(1)
O10	0.0878(1)	-0.1672(1)	-0.0791(1)	1.0	6.2(1)
O11	0.1166(1)	-0.1579(2)	-0.2679(2)	1.0	6.2(1)
O12	0.2443(1)	-0.1547(2)	-0.2350(2)	1.0	6.2(1)
O13	0.3157(2)	-0.04985(7)	-0.1912(3)	1.0	6.2(1)
O14	0.0835(1)	-0.05095(7)	-0.1677(3)	1.0	6.2(1)
O15	0.4242(1)	0.1256(1)	-0.3959(2)	1.0	6.2(1)
O16	0.4018(1)	-0.0027(1)	-0.4090(2)	1.0	6.2(1)
O17	0.3944(1)	-0.1332(1)	-0.4145(2)	1.0	6.2(1)
O18	0.1968(1)	0.13229(1)	-0.3702(2)	1.0	6.2(1)
O19	0.2011(1)	0.0027(1)	-0.3949(2)	1.0	6.2(1)
O20	0.1977(1)	-0.1274(1)	-0.4123(2)	1.0	6.2(1)
O21	-0.00470(8)	0.0409(1)	-0.2078(1)	1.0	6.2(1)
O22	-0.00572(9)	-0.1417(1)	-0.2086(2)	1.0	6.2(1)
O23	0.4312(2)	-1/4	-0.3464(3)	1.0	6.2(1)
O24	0.1936(2)	-1/4	-0.3442(3)	1.0	6.2(1)
O25	0.2812(2)	-1/4	0.0518(3)	1.0	6.2(1)
O26	0.1076(2)	-1/4	0.0684(2)	1.0	6.2(1)

Table U

H^+-ZSM-5_15, room temperature

Bond distances (Å)	H*-ZSM-5_15
T1-O1	1.600(3)
T1-O15	1.588(3)
T1-O16	1.593(3)
T1-O21	1.586(3)
T2-O1	1.592(3)
T2-O2	1.593(3)
T2-O6	1.593(3)
T2-O13	1.590(2)
T3-O2	1.583(3)
T3-O3	1.601(3)
T3-O19	1.587(3)
T3-O20	1.600(3)
T4-O3	1.587(3)
T4-O4	1.587(3)
T4-O16	1.611(3)
T4-O17	1.595(3)
T5-O4	1.595(3)
T5-O5	1.596(3)
T5-O14	1.583(3)
T5-O21	1.591(3)
T6-O5	1.587(3)
T6-O6	1.584(4)
T6-O18	1.596(3)
T6-O19	1.602(3)
T7-O7	1.598(3)
T7-O17	1.602(3)
T7-O22	1.593(3)
T7-O23	1.585(2)
T8-O7	1.597(3)
T8-O8	1.591(3)
T8-O12	1.597(3)
T8-O13	1.593(2)
T9-O8	1.592(3)
T9-O9	1.590(4)
T9-O18	1.580(3)
T9-O25	1.607(2)
T10-O9	1.598(4)

T10-O10	1.586(3)
T10-O15	1.591(3)
T10-O26	1.595(2)
T11-O10	1.596(3)
T11-O11	1.595(3)
T11-O14	1.586(3)
T11-O22	1.594(3)
T12-O11	1.585(3)
T12-O12	1.596(3)
T12-O20	1.594(3)
T12-O24	1.602(2)
<T-O >	1.592
T-O-T angles (°)	
T1_O1_T2	149.9(5)
T2_O2_T3	147.7(4)
T3_O3_T4	167.7(6)
T4_O4_T5	152.5(5)
T5_O5_T6	149.3(5)
T2_O6_T6	155.9(6)
T7_O7_T8	150.8(5)
T8_O8_T9	158.5(5)
T9_O9_T10	157.1(8)
T10_O10_T11	159.3(5)
T11_O11_T12	154.6(5)
T8_O12_T12	168.8(6)
T2_O13_T8	173.3(7)
T5_O14_T11	162.2(5)
T1_O15_T10	148.5(5)
T1_O16_T4	174.1(6)
T4_O17_T7	153.2(5)
T6_O18_T9	146.0(4)
T3_O19_T6	171.2(7)
T3_O20_T12	150.7(5)
T1_O21_T5	146.7(4)
T7_O22_T11	151.4(5)
T7_O23_T7	155.1(7)
T12_O24_T12	148.9(7)
T9_O25_T9	156.3(8)
T10_O26_T10	142.6(6)
<T-O-T>	155.8

Table V

H^+-ZSM-5_20, H^+-ZSM-5_37 and H^+-ZSM-5_69, room temperature

Bond distances (Å)	H^+-ZSM-5_20	H^+-ZSM-5_37	H^+-ZSM-5_69
T1-O1	1.591(2)	1.592(2)	1.592(3)
T1-O15	1.594(2)	1.594(2)	1.594(4)
T1-O16	1.592(2)	1.592(2)	1.591(3)
T1-O47	1.592(2)	1.592(2)	1.591(3)
T2-O1	1.593(3)	1.593(2)	1.594(3)
T2-O2	1.591(2)	1.592(2)	1.595(4)
T2-O6	1.593(2)	1.593(2)	1.595(3)
T2-O13	1.594(2)	1.593(2)	1.596(4)
T3-O2	1.592(2)	1.593(2)	1.593(3)
T3-O3	1.593(2)	1.593(2)	1.593(3)
T3-O45	1.593(2)	1.594(2)	1.594(3)
T3-O46	1.593(2)	1.592(2)	1.591(4)
T4-O3	1.593(2)	1.593(2)	1.593(3)
T4-O4	1.592(2)	1.593(2)	1.593(4)
T4-O42	1.594(2)	1.594(2)	1.594(3)
T4-O43	1.594(2)	1.593(2)	1.592(4)
T5-O4	1.592(2)	1.593(2)	1.593(4)
T5-O5	1.592(2)	1.593(2)	1.593(3)
T5-O14	1.594(2)	1.593(2)	1.594(4)
T5-O21	1.592(2)	1.593(2)	1.598(3)
T6-O5	1.593(3)	1.593(2)	1.591(3)
T6-O6	1.594(2)	1.594(2)	1.597(3)
T6-O18	1.594(2)	1.594(2)	1.594(4)
T6-O19	1.592(2)	1.592(2)	1.592(4)
T7-O7	1.593(2)	1.593(2)	1.593(3)
T7-O17	1.594(2)	1.594(2)	1.594(4)
T7-O23	1.594(2)	1.593(2)	1.593(4)
T7-O48	1.594(2)	1.594(2)	1.594(3)
T8-O7	1.592(2)	1.593(2)	1.593(3)
T8-O8	1.594(2)	1.592(2)	1.592(4)
T8-O12	1.594(2)	1.594(2)	1.594(3)
T8-O13	1.594(2)	1.594(2)	1.595(4)
T9-O8	1.594(2)	1.593(2)	1.595(3)
T9-O9	1.594(2)	1.593(2)	1.593(3)
T9-O25	1.593(2)	1.593(2)	1.594(4)
T9-O44	1.591(2)	1.591(2)	1.589(3)
T10-O9	1.593(2)	1.593(2)	1.593(3)
T10-O10	1.594(2)	1.594(2)	1.594(4)

T10-O26	1.593(2)	1.594(2)	1.596(4)
T10-O41	1.592(2)	1.592(2)	1.591(3)
T11-O10	1.595(2)	1.594(2)	1.594(4)
T11-O11	1.592(2)	1.593(2)	1.594(3)
T11-O14	1.593(2)	1.593(2)	1.594(4)
T11-O22	1.592(2)	1.593(2)	1.592(3)
T12-O11	1.593(2)	1.593(2)	1.593(3)
T12-O12	1.593(2)	1.593(2)	1.593(3)
T12-O20	1.593(2)	1.593(2)	1.593(4)
T12-O24	1.594(2)	1.593(2)	1.593(4)
T13-O21	1.592(2)	1.593(2)	1.593(3)
T13-O27	1.591(2)	1.592(2)	1.592(3)
T13-O41	1.592(2)	1.592(2)	1.591(4)
T13-O42	1.594(2)	1.594(2)	1.593(4)
T14-O27	1.591(2)	1.592(2)	1.591(3)
T14-O28	1.593(2)	1.593(2)	1.593(4)
T14-O32	1.593(2)	1.593(2)	1.592(3)
T14-O39	1.594(2)	1.594(2)	1.594(4)
T15-O19	1.592(2)	1.592(2)	1.590(4)
T15-O20	1.594(2)	1.594(2)	1.595(3)
T15-O28	1.593(2)	1.593(2)	1.593(3)
T15-O29	1.593(2)	1.593(2)	1.593(3)
T16-O16	1.593(2)	1.593(2)	1.593(4)
T16-O17	1.594(2)	1.594(2)	1.594(3)
T16O29	1.593(2)	1.593(2)	1.593(3)
T16-O30	1.593(2)	1.593(2)	1.593(3)
T17-O30	1.593(2)	1.593(2)	1.592(4)
T17-O31	1.590(2)	1.592(2)	1.591(3)
T17-O40	1.593(2)	1.593(2)	1.593(4)
T17-O47	1.592(2)	1.592(2)	1.591(3)
T18-O31	1.592(2)	1.593(2)	1.592(3)
T18-O32	1.593(2)	1.593(2)	1.594(3)
T18-O44	1.591(2)	1.591(2)	1.590(4)
T18-O45	1.593(2)	1.593(2)	1.593(4)
T19-O22	1.593(3)	1.593(2)	1.593(3)
T19-O23	1.595(2)	1.594(2)	1.595(4)
T19-O33	1.593(2)	1.593(2)	1.593(3)
T19-O43	1.593(2)	1.593(2)	1.596(3)
T20-O33	1.593(2)	1.593(2)	1.597(3)
T20-O34	1.591(2)	1.592(2)	1.592(1)
T20-O38	1.595(3)	1.593(2)	1.594(3)

T20-O39	1.594(2)	1.593(2)	1.593(4)
T21-O18	1.593(2)	1.594(2)	1.595(3)
T21-O25	1.593(2)	1.593(2)	1.593(4)
T21-O34	1.592(2)	1.593(2)	1.593(3)
T21-O35	1.594(2)	1.594(2)	1.595(3)
T22-O15	1.593(2)	1.594(2)	1.593(3)
T22-O26	1.593(2)	1.593(2)	1.593(4)
T22-O35	1.593(2)	1.593(2)	1.594(3)
T22-O36	1.593(2)	1.593(2)	1.593(4)
T23-O36	1.593(2)	1.593(2)	1.593(4)
T23-O37	1.593(2)	1.593(2)	1.593(3)
T23-O40	1.593(2)	1.593(2)	1.592(4)
T23-O48	1.592(2)	1.593(2)	1.592(3)
T24-O24	1.595(2)	1.594(2)	1.595(4)
T24-O37	1.593(2)	1.593(2)	1.593(3)
T24-O38	1.594(2)	1.594(2)	1.594(3)
T24-O46	1.591(2)	1.592(2)	1.590(4)
<T-O>	1.592	1.593	1.593
	T-O-T angles (°)		
T1_O1_T2	147.4(8)	145.1(6)	146.7(1)
T2_O2_T3	144.8(7)	143.1(5)	142.7(1)
T3_O3_T4	162.5(7)	159.1(3)	159.9(1)
T4_O4_T5	149.0(7)	145.3(5)	143.9(1)
T5_O5_T6	151.0(6)	153.9(5)	152.0(1)
T2_O6_T6	157.5(7)	157.7(6)	158.8(1)
T7_O7_T8	157.0(8)	158.0(7)	157.0(1)
T8_O8_T9	158.5(9)	160.0(7)	158.6(1)
T9_O9_T10	155.5(7)	155.3(6)	152.9(1)
T10_O10_T11	156.9(6)	154.2(3)	153.6(1)
T11_O11_T12	154.9(8)	158.1(7)	157.7(1)
T8_O12_T12	171.1(1)	172.6(8)	172.6(1)
T2_O13_T8	169.4(8)	168.9(7)	167.0(1)
T5_O14_T11	160.5(6)	158.3(5)	156.9(1)
T1_O15_T22	150.1(6)	149.5(5)	148.6(1)
T1_O16_T16	178.6(7)	173.5(5)	174.4(1)
T7_O17_T16	148.0(7)	146.2(6)	148.2(1)
T6_O18_T21	145.0(7)	141.4(5)	141.5(1)
T6_O19_T15	172.9(6)	172.4(5)	171.0(1)
T12_O20_T15	143.5(7)	139.8(6)	142.6(1)
T5_O21_T13	145.4(4)	144.4(3)	144.3(1)
T11_O22_T19	149.2(6)	149.6(5)	150.1(1)

T7_O23_T19	154.4(5)	156.7(5)	156.2(1)
T12_O24_T24	150.8(6)	148.4(3)	150.1(1)
T9_O25_T21	155.2(7)	155.9(6)	156.0(1)
T10_O26_T22	143.3(5)	142.2(2)	142.8(1)
T13_O27_T14	152.1(8)	152.8(7)	155.3(1)
T14_O28_T15	152.6(8)	154.5(6)	151.0(1)
T15_O29_T16	168.1(9)	163.7(6)	163.7(1)
T16_O30_T17	161.0(9)	163.5(7)	159.7(1)
T17_O31_T18	146.6(6)	145.6(5)	147.0(1)
T14_O32_T18	155.6(7)	153.3(5)	154.7(1)
T19_O33_T20	149.6(6)	147.7(2)	148.6(1)
T20_O34_T21	151.3(6)	150.8(5)	150.1(1)
T21_O35_T22	155.2(7)	154.8(6)	152.7(1)
T22_O36_T23	160.6(7)	160.4(5)	159.8(1)
T23_O37_T24	151.2(7)	151.3(6)	152.2(1)
T20_O38_T24	159.0(7)	154.9(5)	155.8(1)
T14_O39_T20	168.8(8)	164.3(6)	167.1(1)
T17_O40_T23	163.6(5)	162.0(1)	162.7(1)
T10_O41_T13	149.4(6)	149.8(5)	148.0(1)
T4_O42_T13	168.3(9)	166.2(8)	163.(1)
T4_O43_T19	152.1(5)	151.8(3)	152.5(1)
T9_O44_T18	152.0(8)	152.6(7)	151.3(1)
T3_O45_T18	166.0(8)	165.3(7)	164.3(1)
T3_O46_T24	154.7(5)	156.8(3)	156.6(1)
T1_O47_T17	150.4(6)	153.4(4)	150.9(1)
T7_O48_T23	148.6(6)	149.4(5)	149.6(1)
<T-O-T>	155.6	154.88	154.6

Table W

H^+-ZSM-5_15

Bond distances (Å)	**200 °C**	**400 °C**	**600 °C**	**800 °C**
T1-O1	1.595(2)	1.594(2)	1.5926(8)	1.5921(9)
T1-O15	1.589(2)	1.590(2)	1.5914(9)	1.5916(11)
T1-O16	1.589(2)	1.590(2)	1.5906(7)	1.5908(9)
T1-O21	1.596(2)	1.594(2)	1.5936(9)	1.5941(11)
T2-O1	1.590(2)	1.591(2)	1.5918(7)	1.5918(9)
T2-O2	1.591(2)	1.590(2)	1.5915(1)	1.5919(12)
T2-O6	1.597(2)	1.596(2)	1.5959(8)	1.5964(10)
T2-O13	1.592(2)	1.593(2)	1.5933(1)	1.5927(13)
T3-O2	1.587(2)	1.589(2)	1.5913(8)	1.5929(10)
T3-O3	1.591(2)	1.590(2)	1.5901(1)	1.5896(13)

T3-O19	1.589(2)	1.591(2)	1.5927(7)	1.5931(9)
T3-O20	1.605(2)	1.602(2)	1.5999(8)	1.5992(10)
T4-O3	1.590(2)	1.590(2)	1.5921(1)	1.5926(13)
T4-O4	1.586(2)	1.588(2)	1.5904(9)	1.5916(11)
T4-O16	1.603(2)	1.598(2)	1.5959(7)	1.5959(9)
T4-O17	1.596(2)	1.595(2)	1.5935(8)	1.5924(10)
T5-O4	1.594(2)	1.594(2)	1.5937(8)	1.5933(10)
T5-O5	1.598(2)	1.596(2)	1.5952(7)	1.5953(8)
T5-O14	1.586(2)	1.588(2)	1.5904(1)	1.5903(13)
T5-O21	1.591(2)	1.590(2)	1.5916(1)	1.5919(12)
T6-O5	1.596(2)	1.595(2)	1.5945(9)	1.5953(12)
T6-O6	1.585(2)	1.589(2)	1.5930(8)	1.5933(9)
T6-O18	1.590(2)	1.591(2)	1.5917(9)	1.5905(11)
T6-O19	1.602(2)	1.597(2)	1.5946(7)	1.5952(9)
T7-O7	1.595(2)	1.594(2)	1.5944(8)	1.5948(9)
T7-O17	1.593(2)	1.593(2)	1.5935(7)	1.5932(9)
T7-O22	1.597(2)	1.597(2)	1.5963(9)	1.5953(11)
T7-O23	1.590(1)	1.590(1)	1.5917(1)	1.5922(13)
T8-O7	1.591(2)	1.591(2)	1.5915(8)	1.5907(9)
T8-O8	1.590(2)	1.588(2)	1.5894(1)	1.5898(12)
T8-O12	1.600(2)	1.599(2)	1.5987(8)	1.5988(10)
T8-O13	1.595(2)	1.596(2)	1.5968(1)	1.5969(13)
T9-O8	1.592(2)	1.594(2)	1.5945(8)	1.5936(10)
T9-O9	1.589(2)	1.591(2)	1.5940(1)	1.5934(13)
T9-O18	1.588(2)	1.589(2)	1.5906(7)	1.5913(9)
T9-O25	1.604(1)	1.599(1)	1.5968(1)	1.5975(13)
T10-O9	1.596(2)	1.594(2)	1.5943(1)	1.5936(13)
T10-O10	1.590(2)	1.592(2)	1.5936(9)	1.5938(11)
T10-O15	1.590(2)	1.591(2)	1.5920(6)	1.5920(8)
T10-O26	1.595(1)	1.595(3)	1.5943(1)	1.5953(12)
T11-O10	1.593(2)	1.593(2)	1.5933(8)	1.5937(10)
T11-O11	1.597(2)	1.596(2)	1.5960(7)	1.5969(8)
T11-O14	1.588(2)	1.589(2)	1.5904(1)	1.5906(13)
T11-O22	1.594(2)	1.593(2)	1.5930(1)	1.5922(12)
T12-O11	1.595(2)	1.595(2)	1.5956(9)	1.5959(11)
T12-O12	1.593(2)	1.594(2)	1.5946(7)	1.5940(9)
T12-O20	1.595(2)	1.594(2)	1.5938(8)	1.5938(10)
T12-O24	1.595(1)	1.594(1)	1.594(10)	1.5941(13)
<T-O>	1.593	1.592	1.593	1.593
T-O-T angles (°)				
T1_O1_T2	150.1(3)	149.8(3)	149.64(2)	149.61(2)

T2_O2_T3	146.9(2)	146.6(2)	146.06(3)	145.80(4)
T3_O3_T4	168.0(2)	166.8(3)	165.62(1)	165.23(2)
T4_O4_T5	152.2(3)	151.6(3)	151.20(2)	151.05(4)
T5_O5_T6	147.2(3)	147.2(3)	147.17(1)	147.00(1)
T2_O6_T6	154.2(2)	153.2(3)	152.39(1)	152.17(1)
T7_O7_T8	151.2(3)	150.9(3)	150.61(1)	150.55(1)
T8_O8_T9	157.8(3)	157.4(3)	157.0(2)	157.03(2)
T9_O9_T10	156.6(5)	156.0(5)	154.96(2)	154.97(4)
T10_O10_T11	158.3(3)	157.5(3)	156.96(2)	156.89(2)
T11_O11_T12	151.8(3)	151.6(3)	151.30(2)	151.02(4)
T8_O12_T12	167.1(2)	166.3(4)	165.69(2)	165.53(1)
T2_O13_T8	170.6(3)	169.4(2)	168.62(1)	168.60(1)
T5_O14_T11	160.7(3)	159.7(2)	158.87(2)	158.75(2)
T1_O15_T10	146.8(3)	146.4(3)	145.84(2)	145.58(2)
T1_O16_T4	173.5(3)	173.7(3)	173.68(3)	173.60(3)
T4_O17_T7	152.3(3)	152.1(2)	151.90(3)	151.80(5)
T6_O18_T9	146.2(3)	146.0(3)	145.76(1)	145.73(1)
T3_O19_T6	171.7(5)	172.6(5)	173.17(3)	173.24(5)
T3_O20_T12	150.4(3)	150.9(3)	151.26(4)	151.23(1)
T1_O21_T5	145.8(2)	145.5(4)	145.30(3)	145.06(7)
T7_O22_T11	149.8(3)	149.6(3)	149.39(2)	149.47(2)
T7_O23_T7	153.2(2)	152.7(5)	152.33(2)	152.33(2)
T12_O24_T12	150.4(5)	150.2(5)	150.37(4)	150.46(3)
T9_O25_T9	157.1(5)	158.2(6)	159.29(2)	159.19(2)
T10_O26_T10	142.4(3)	142.2(3)	142.32(3)	142.21(2)
<T-O-T>	155.0	154.7	154.4	154.3

Table X

H^+-ZSM-5_20

Bond distances (Å)	**200 °C**	**400 °C**	**600 °C**	**800 °C**
T1-O1	1.593(1)	1.592(2)	1.592(1)	1.591(2)
T1-O15	1.589(1)	1.590(2)	1.590(2)	1.590(2)
T1-O16	1.590(1)	1.590(2)	1.590(2)	1.590(2)
T1-O21	1.595(1)	1.593(2)	1.592(2)	1.591(2)
T2-O1	1.590(1)	1.592(2)	1.592(2)	1.593(2)
T2-O2	1.589(1)	1.590(2)	1.591(2)	1.589(2)
T2-O6	1.596(1)	1.594(2)	1.593(2)	1.593(2)
T2-O13	1.592(1)	1.593(1)	1.592(1)	1.592(2)
T3-O2	1.588(1)	1.589(1)	1.591(1)	1.592(2)
T3-O3	1.591(1)	1.591(2)	1.590(1)	1.589(2)
T3-O19	1.589(1)	1.591(2)	1.591(1)	1.592(2)

T3-O20	1.602(1)	1.598(2)	1.596(2)	1.594(3)
T4-O3	1.590(1)	1.59(2)	1.591(1)	1.591(2)
T4-O4	1.587(2)	1.589(2)	1.591(1)	1.591(2)
T4-O16	1.601(2)	1.597(2)	1.595(2)	1.594(2)
T4-O17	1.594(2)	1.594(2)	1.592(2)	1.592(2)
T5-O4	1.594(2)	1.594(2)	1.593(2)	1.593(2)
T5-O5	1.596(2)	1.594(2)	1.593(2)	1.592(2)
T5-O14	1.586(2)	1.589(2)	1.590(2)	1.591(2)
T5-O21	1.591(2)	1.590(2)	1.591(2)	1.591(2)
T6-O5	1.595(2)	1.593(2)	1.593(2)	1.593(2)
T6-O6	1.585(2)	1.590(2)	1.592(2)	1.593(2)
T6-O18	1.591(2)	1.592(2)	1.591(2)	1.591(2)
T6-O19	1.600(1)	1.595(1)	1.593(2)	1.591(2)
T7-O7	1.594(1)	1.594(2)	1.594(2)	1.594(2)
T7-O17	1.593(2)	1.593(2)	1.593(2)	1.592(2)
T7-O22	1.597(2)	1.596(2)	1.595(2)	1.595(2)
T7-O23	1.590(1)	1.591(1)	1.591(1)	1.592(1)
T8-O7	1.592(1)	1.593(2)	1.593(2)	1.593(2)
T8-O8	1.590(1)	1.589(2)	1.589(3)	1.588(2)
T8-O12	1.599(1)	1.597(1)	1.597(2)	1.596(2)
T8-O13	1.593(1)	1.595(1)	1.595(1)	1.596(1)
T9-O8	1.591(1)	1.594(2)	1.597(3)	1.593(2)
T9-O9	1.591(2)	1.595(2)	1.595(2)	1.596(2)
T9-O18	1.589(2)	1.588(2)	1.589(2)	1.590(2)
T9-O25	1.601(1)	1.596(1)	1.595(1)	1.593(1)
T10-O9	1.597(2)	1.596(2)	1.593(3)	1.593(2)
T10-O10	1.589(3)	1.593(2)	1.593(3)	1.594(2)
T10-O15	1.590(2)	1.591(2)	1.592(2)	1.592(2)
T10-O26	1.594(1)	1.593(1)	1.594(1)	1.594(1)
T11-O10	1.594(2)	1.593(2)	1.593(2)	1.593(2)
T11-O11	1.593(2)	1.593(2)	1.594(2)	1.593(2)
T11-O14	1.589(1)	1.590(2)	1.590(2)	1.591(2)
T11-O22	1.593(1)	1.594(1)	1.593(2)	1.593(2)
T12-O11	1.594(1)	1.595(2)	1.594(2)	1.595(2)
T12-O12	1.593(1)	1.595(2)	1.594(2)	1.594(2)
T12-O20	1.593(2)	1.592(2)	1.592(2)	1.592(2)
T12-O24	1.594(1)	1.593(1)	1.599(1)	1.592(1)
<T-O>	1.592	1.592	1.592	1.592
	T-O-T angles (°)			
T1-O1-T2	150.2(3)	149.7(3)	149.2(3)	148.9(3)
T2-O2-T3	146.7(2)	146.3(2)	145.7(2)	145.6(2)

T3-O3-T4	167.4(2)	166.1(3)	165.1(3)	164.7(2)
T4-O4-T5	151.6(2)	151.1(3)	150.7(3)	150.5(3)
T5-O5-T6	147.4(2)	147.5(2)	147.1(2)	147.1(3)
T2-O6-T6	154.0(3)	153.2(2)	152.5(3)	152.2(3)
T7-O7-T8	151.0(3)	150.4(3)	150.0(3)	149.7(3)
T8-O8-T9	157.5(3)	156.9(3)	156.7(3)	156.4(3)
T9-O9-T10	155.8(2)	154.7(5)	154.6(3)	154.1(5)
T10-O10-T11	157.9(3)	156.9(3)	156.6(3)	156.2(3)
T11-O11-T12	152.0(3)	151.8(3)	151.2(3)	151.0(3)
T8-O12-T12	166.8(2)	165.9(2)	165.7(2)	165.3(3)
T2-O13-T8	170.5(2)	168.9(2)	168.5(2)	167.6(2)
T5-O14-T11	160.0(3)	158.9(3)	158.4(3)	157.8(3)
T1-O15-T10	146.5(2)	146.2(2)	145.6(2)	145.4(3)
T1-O16-T4	173.0(2)	173.5(3)	173.6(2)	173.9(2)
T4-O17-T7	152.3(3)	152.0(3)	151.8(3)	151.6(3)
T6-O18-T9	145.8(2)	145.6(2)	145.3(2)	145.0(3)
T3-O19-T6	171.7(2)	172.5(2)	172.9(2)	173.2(5)
T3-O20-T12	150.8(3)	151.3(3)	151.2(3)	151.3(3)
T1-O21-T5	145.7(2)	145.5(2)	145.0(2)	144.9(2)
T7-O22-T11	149.8(3)	149.3(3)	149.1(3)	148.9(3)
T7-O23-T7	152.9(3)	152.3(2)	152.1(2)	151.8(4)
T12-O24-T12	150.3(3)	150.5(1)	150.2(3)	150.4(5)
T9-O25-T9	157.6(5)	159.4(5)	159.3(5)	160.1(5)
T10-O26-T10	142.3(3)	142.5(1)	142.1(3)	142.2(4)
<T-O-T>	154.9	154.5	154.2	154.0

Table Y

H^+-ZSM-5_37

Bond distances (Å)	**200 °C**	**400 °C**	**600 °C**	**800 °C**
T1-O1	1.592(1)	1.592(1)	1.591(1)	1.591(1)
T1-O15	1.591(1)	1.591(1)	1.592(1)	1.592(1)
T1-O16	1.591(1)	1.592(1)	1.592(1)	1.592(1)
T1-O21	1.594(1)	1.592(1)	1.592(1)	1.592(1)
T2-O1	1.591(1)	1.591(1)	1.592(1)	1.592(1)
T2-O2	1.591(1)	1.592(1)	1.592(1)	1.592(1)
T2-O6	1.596(1)	1.594(1)	1.594(1)	1.593(1)
T2-O13	1.593(1)	1.593(1)	1.593(1)	1.593(1)
T3-O2	1.589(1)	1.590(1)	1.592(1)	1.592(1)
T3-O3	1.593(1)	1.593(1)	1.592(1)	1.591(1)
T3-O19	1.590(1)	1.590(1)	1.591(1)	1.590(1)
T3-O20	1.601(1)	1.599(1)	1.597(1)	1.596(1)

T4-O3	1.592(1)	1.592(1)	1.593(1)	1.593(1)
T4-O4	1.589(1)	1.591(1)	1.592(1)	1.593(1)
T4-O16	1.597(1)	1.595(1)	1.593(1)	1.592(1)
T4-O17	1.594(2)	1.593(1)	1.593(1)	1.592(1)
T5-O4	1.595(1)	1.595(1)	1.594(1)	1.594(1)
T5-O5	1.596(1)	1.595(1)	1.594(1)	1.593(1)
T5-O14	1.589(1)	1.590(1)	1.591(1)	1.592(1)
T5-O21	1.591(1)	1.591(1)	1.591(1)	1.591(1)
T6-O5	1.594(1)	1.593(1)	1.593(1)	1.593(1)
T6-O6	1.591(1)	1.593(1)	1.594(1)	1.595(1)
T6-O18	1.592(1)	1.591(1)	1.591(1)	1.591(1)
T6-O19	1.597(1)	1.595(1)	1.593(1)	1.593(1)
T7-O7	1.594(1)	1.594(1)	1.594(1)	1.594(1)
T7-O17	1.594(1)	1.594(1)	1.594(1)	1.593(1)
T7-O22	1.597(1)	1.596(1)	1.596(1)	1.595(1)
T7-O23	1.590(8)	1.590(8)	1.591(8)	1.591(8)
T8-O7	1.593(1)	1.593(1)	1.593(1)	1.593(1)
T8-O8	1.590(1)	1.590(1)	1.590(1)	1.590(1)
T8-O12	1.600(1)	1.598(1)	1.597(1)	1.597(1)
T8-O13	1.593(1)	1.594(1)	1.594(1)	1.594(1)
T9-O8	1.592(1)	1.592(1)	1.592(1)	1.591(1)
T9-O9	1.596(1)	1.596(1)	1.598(1)	1.598(1)
T9-O18	1.589(1)	1.589(1)	1.590(1)	1.591(1)
T9-O25	1.598(8)	1.597(8)	1.594(8)	1.594(8)
T10-O9	1.598(1)	1.596(1)	1.595(1)	1.594(1)
T10-O10	1.591(1)	1.593(1)	1.594(1)	1.594(1)
T10-O15	1.590(1)	1.590(1)	1.591(1)	1.591(1)
T10-O26	1.593(1)	1.594(1)	1.593(1)	1.594(1)
T11-O10	1.595(1)	1.594(1)	1.595(1)	1.595(1)
T11-O11	1.595(1)	1.590(1)	1.594(1)	1.594(1)
T11-O14	1.589(1)	1.593(1)	1.590(1)	1.590(1)
T11-O22	1.594(1)	1.593(1)	1.593(1)	1.593(1)
T12-O11	1.595(1)	1.594(1)	1.595(1)	1.595(1)
T12-O12	1.595(1)	1.595(1)	1.595(1)	1.594(1)
T12-O20	1.593(1)	1.593(1)	1.592(1)	1.592(1)
T12-O24	1.593(9)	1.593(9)	1.592(9)	1.592(9)
<T-O>	1.593	1.593	1.593	1.592
	T-O-T angles (°)			
T1-O1-T2	150.2(1)	149.9(1)	149.6(1)	149.4(1)
T2-O2-T3	146.4(4)	146.0(1)	145.6(1)	145.4(1)
T3-O3-T4	166.3(2)	165.5(2)	164.8(2)	164.4(1)

T4-O4-T5	151.2(1)	150.9(1)	150.5(1)	150.3(1)
T5-O5-T6	147.6(1)	147.5(1)	147.4(1)	147.2(1)
T2-O6-T6	153.2(2)	152.8(1)	152.3(1)	152.0(1)
T7-O7-T8	150.9(1)	150.5(1)	150.2(1)	150.0(1)
T8-O8-T9	157.4(1)	157.1(1)	156.8(1)	156.7(1)
T9-O9-T10	155.0(2)	154.7(2)	154.1(2)	154.1(2)
T10-O10-T11	157.2(1)	156.8(1)	156.3(1)	156.1(1)
T11-O11-T12	152.1(1)	151.9(1)	151.5(1)	151.3(1)
T8-O12-T12	166.3(3)	166.0(2)	165.6(2)	165.5(2)
T2-O13-T8	170.1(2)	169.4(2)	168.8(2)	168.5(2)
T5-O14-T11	159.3(1)	158.8(1)	158.2(1)	157.9(1)
T1-O15-T10	146.4(1)	146.1(1)	145.7(1)	145.5(1)
T1-O16-T4	173.0(2)	173.2(2)	173.3(2)	173.4(2)
T4-O17-T7	152.1(1)	151.9(1)	151.7(1)	151.6(1)
T6-O18-T9	145.9(1)	145.7(1)	145.5(1)	145.3(1)
T3-O19-T6	172.5(2)	172.9(2)	173.2(2)	173.4(2)
T3-O20-T12	151.2(1)	151.2(1)	151.4(1)	151.3(1)
T1-O21-T5	145.8(1)	145.6(1)	145.3(1)	145.2(1)
T7-O22-T11	149.8(1)	149.6(1)	149.3(1)	149.2(1)
T7-O23-T7	152.7(2)	152.4(2)	152.0(2)	151.9(2)
T12-O24-T12	150.3(2)	150.4(2)	150.4(2)	150.4(2)
T9-O25-T9	158.5(2)	159.0(2)	159.6(2)	159.6(2)
T10-O26-T10	142.3(2)	142.2(2)	142.2(2)	142.0(2)
<T-O-T>	154.7	154.5	154.2	154.1

Table Z

H^+-ZSM-5_69

Bond distances (Å)	**200 °C**	**400 °C**	**600 °C**	**800 °C**
T1-O1	1.591(1)	1.591(1)	1.591(1)	1.591(1)
T1-O15	1.591(1)	1.590(1)	1.590(1)	1.591(1)
T1-O16	1.591(1)	1.592(1)	1.592(1)	1.593(1)
T1-O21	1.596(1)	1.592(1)	1.591(1)	1.589(1)
T2-O1	1.589(1)	1.592(1)	1.592(1)	1.593(1)
T2-O2	1.588(1)	1.590(1)	1.590(1)	1.591(1)
T2-O6	1.598(1)	1.594(1)	1.593(1)	1.592(1)
T2-O13	1.592(1)	1.592(1)	1.592(1)	1.592(1)
T3-O2	1.589(1)	1.590(1)	1.590(1)	1.592(1)
T3-O3	1.591(1)	1.592(1)	1.591(1)	1.592(1)
T3-O19	1.590(1)	1.590(1)	1.590(1)	1.590(1)
T3-O20	1.601(1)	1.598(1)	1.596(1)	1.594(1)
T4-O3	1.591(1)	1.591(1)	1.591(1)	1.592(1)

T4-O4	1.588(1)	1.590(1)	1.591(1)	1.599(1)
T4-O16	1.599(1)	1.595(1)	1.594(1)	1.520(1)
T4-O17	1.593(1)	1.594(1)	1.593(1)	1.592(1)
T5-O4	1.594(1)	1.594(1)	1.593(1)	1.594(1)
T5-O5	1.597(1)	1.594(1)	1.593(1)	1.591(1)
T5-O14	1.588(1)	1.590(1)	1.591(1)	1.592(1)
T5-O21	1.590(1)	1.590(1)	1.590(1)	1.590(1)
T6-O5	1.597(1)	1.593(1)	1.593(1)	1.593(1)
T6-O6	1.585(1)	1.591(1)	1.591(1)	1.594(1)
T6-O18	1.591(1)	1.591(1)	1.591(1)	1.591(1)
T6-O19	1.600(1)	1.595(1)	1.593(1)	1.591(1)
T7-O7	1.594(1)	1.594(1)	1.594(1)	1.594(1)
T7-O17	1.591(1)	1.594(1)	1.593(1)	1.594(1)
T7-O22	1.599(1)	1.596(1)	1.595(1)	1.594(1)
T7-O23	1.591(1)	1.590(1)	1.591(1)	1.591(1)
T8-O7	1.590(1)	1.593(1)	1.593(1)	1.594(1)
T8-O8	1.591(1)	1.589(1)	1.589(1)	1.589(1)
T8-O12	1.600(1)	1.597(1)	1.596(1)	1.595(1)
T8-O13	1.592(1)	1.594(1)	1.594(1)	1.595(1)
T9-O8	1.590(1)	1.591(1)	1.591(1)	1.591(1)
T9-O9	1.595(1)	1.595(1)	1.596(1)	1.597(1)
T9-O18	1.590(1)	1.589(1)	1.588(1)	1.589(1)
T9-O25	1.599(1)	1.596(1)	1.595(1)	1.593(1)
T10-O9	1.601(1)	1.595(1)	1.594(1)	1.594(1)
T10-O10	1.589(1)	1.592(1)	1.593(1)	1.594(1)
T10-O15	1.589(1)	1.590(1)	1.591(1)	1.590(1)
T10-O26	1.593(1)	1.594(1)	1.594(1)	1.594(1)
T11-O10	1.595(1)	1.594(1)	1.594(1)	1.594(1)
T11-O11	1.595(1)	1.594(1)	1.594(1)	1.593(1)
T11-O14	1.589(1)	1.590(1)	1.590(1)	1.591(1)
T11-O22	1.593(1)	1.593(1)	1.593(1)	1.593(1)
T12-O11	1.594(1)	1.594(1)	1.594(1)	1.594(1)
T12-O12	1.594(1)	1.594(1)	1.594(1)	1.594(1)
T12-O20	1.592(1)	1.592(1)	1.591(1)	1.591(1)
T12-O24	1.592(1)	1.592(1)	1.592(1)	1.591(1)
<T-O>	1.592	1.592	1.592	1.591
		T-O-T angles (°)		
T1-O1-T2	150.5(2)	149.7(2)	149.3(2)	149.1(2)
T2-O2-T3	146.6(1)	146.1(1)	145.8(1)	145.4(1)
T3-O3-T4	167.3(2)	165.6(2)	165.1(2)	164.2(2)
T4-O4-T5	151.4(2)	150.8(2)	150.6(2)	150.1(2)

T5-O5-T6	147.1(3)	147.4(2)	147.3(2)	147.4(2)
T2-O6-T6	153.7(2)	152.9(2)	152.6(2)	152.3(2)
T7-O7-T8	151.1(2)	150.3(2)	150.0(2)	149.7(2)
T8-O8-T9	157.4(2)	157.1(2)	156.7(2)	156.5(2)
T9-O9-T10	154.6(3)	154.8(3)	154.3(3)	154.0(3)
T10-O10-T11	157.4(2)	156.7(2)	156.3(2)	155.8(2)
T11-O11-T12	151.6(2)	151.7(2)	151.4(2)	151.3(2)
T8-O12-T12	166.1(2)	166.0(2)	165.8(2)	165.5(2)
T2-O13-T8	170.4(4)	169.1(2)	168.6(2)	168.0(2)
T5-O14-T11	159.2(2)	158.5(2)	158.1(2)	157.6(2)
T1-O15-T10	146.0(2)	146.1(2)	145.8(1)	145.9(3)
T1-O16-T4	172.4(2)	173.4(2)	173.6(2)	173.8(2)
T4-O17-T7	152.1(2)	151.8(2)	151.7(2)	151.5(2)
T6-O18-T9	145.6(3)	145.5(3)	145.2(2)	145.1(3)
T3-O19-T6	171.6(3)	172.7(3)	172.8(3)	173.3(3)
T3-O20-T12	151.0(2)	151.2(2)	151.2(2)	151.3(2)
T1-O21-T5	145.9(1)	145.6(1)	145.3(1)	145.2(1)
T7-O22-T11	149.8(2)	149.6(2)	149.2(2)	149.2(2)
T7-O23-T7	152.6(3)	152.3(2)	152.0(3)	151.8(2)
T12-O24-T12	150.8(3)	150.4(3)	150.3(3)	150.6(3)
T9-O25-T9	158.6(2)	159.0(1)	159.5(2)	160.0(2)
T10-O26-T10	142.6(2)	142.1(2)	142.1(2)	142.0(2)
<T-O-T>	154.7	154.4	154.2	154.1

Appendix 3

Atomic coordinates, fraction and Atomic Displacement Parameters of framework atoms of ZSM-$5_{(37)}$ and ZSM-$5_{(15)}$ are reported in Table A and B, respectively.

Extraframework atomic coordinates, fraction and Atomic Displacement Parameters of L-lysine and water molecules are reported in Table C.

T-O bond distances and T-O-T angles of ZSM-$5_{(37)}$ and ZSM-$5_{(15)}$ are reported in Table D.

Table A

ZSM-$5_{(37)}$

Site	x/a	y/b	z/c	Fraction	Ui/Ue*100
T1	0.0555(6)	0.4231(5)	-0.3303(11)	1.0	0.4(8)
T2	0.0353(5)	0.3167(7)	-0.1726(13)	1.0	0.4(8)
T3	0.0635(8)	0.2795(5)	0.0427(12)	1.0	0.4(8)
T4	0.0640(5)	0.1239(5)	0.0331(11)	1.0	0.4(8)
T5	0.0287(4)	0.0732(5)	-0.1755(12)	1.0	0.4(8)
T6	0.0617(6)	0.1942(6)	-0.3104(13)	1.0	0.4(8)
T7	-0.1719(4)	0.4267(6)	-0.3228(13)	1.0	0.4(8)
T8	-0.1237(5)	0.3108(6)	-0.1829(11)	1.0	0.4(8)
T9	-0.1732(5)	0.2705(5)	0.0301(12)	1.0	0.4(8)
T10	-0.1764(5)	0.1154(5)	0.0342(18)	1.0	0.4(8)
T11	-0.1285(4)	0.0682(8)	-0.1741(16)	1.0	0.4(8)
T12	-0.1650(8)	0.1864(5)	-0.3159(13)	1.0	0.4(8)
T13	0.4439(6)	0.4248(6)	-0.3316(12)	1.0	0.4(8)
T14	0.4747(5)	0.3097(8)	-0.1859(14)	1.0	0.4(8)
T15	0.4412(5)	0.2806(4)	0.0369(13)	1.0	0.4(8)
T16	0.4330(6)	0.1240(4)	0.0331(11)	1.0	0.4(8)
T17	0.4742(5)	0.0743(7)	-0.1818(14)	1.0	0.4(8)
T18	0.4395(6)	0.1887(7)	-0.3199(17)	1.0	0.4(8)
T19	0.6717(5)	0.4221(6)	-0.3148(10)	1.0	0.4(8)
T20	0.6330(5)	0.3095(6)	-0.1733(12)	1.0	0.4(8)
T21	0.6708(4)	0.2726(6)	0.0433(12)	1.0	0.4(8)
T22	0.6723(5)	0.1177(6)	0.0333(14)	1.0	0.4(8)
T23	0.6321(5)	0.0740(9)	-0.1847(13)	1.0	0.4(8)
T24	0.6811(7)	0.1932(8)	-0.3077(12)	1.0	0.4(8)
O1	0.0645(8)	0.3783(10)	-0.2330(18)	1.0	0.6(1)

O2	0.0635(14)	0.3184(8)	-0.0609(13)	1.0	0.6(1)
O3	0.0537(8)	0.2021(4)	0.0221(19)	1.0	0.6(1)
O4	0.0680(10)	0.0911(11)	-0.0749(15)	1.0	0.6(1)
O5	0.0510(14)	0.1228(8)	-0.2619(19)	1.0	0.6(1)
O6	0.0579(12)	0.2494(9)	-0.2253(15)	1.0	0.6(1)
O7	-0.1555(12)	0.3739(13)	-0.2374(23)	1.0	0.6(1)
O8	-0.1561(14)	0.3027(12)	-0.0753(16)	1.0	0.6(1)
O9	-0.1594(12)	0.1925(4)	0.0261(30)	1.0	0.6(1)
O10	-0.1668(7)	0.0812(12)	-0.0721(15)	1.0	0.6(1)
O11	-0.1559(11)	0.1179(11)	-0.2575(19)	1.0	0.6(1)
O12	-0.1386(15)	0.2459(13)	-0.2476(27)	1.0	0.6(1)
O13	-0.0446(4)	0.3207(10)	-0.1715(29)	1.0	0.6(1)
O14	-0.0500(3)	0.0799(10)	-0.1579(28)	1.0	0.6(1)
O15	0.1226(5)	0.4208(7)	-0.3942(11)	1.0	0.6(1)
O16	-0.0056(6)	0.3956(12)	-0.3957(19)	1.0	0.6(1)
O17	-0.1348(5)	0.4056(9)	-0.4230(18)	1.0	0.6(1)
O18	0.1334(4)	0.1972(14)	-0.3623(11)	1.0	0.6(1)
O19	0.0045(6)	0.2076(10)	-0.3919(19)	1.0	0.6(1)
O20	-0.1230(7)	0.1842(12)	-0.4166(13)	1.0	0.6(1)
O21	0.0460(10)	-0.0011(6)	-0.2074(8)	1.0	0.6(1)
O22	-0.1413(8)	-0.0064(9)	-0.2093(15)	1.0	0.6(1)
O23	-0.2509(3)	0.4293(10)	-0.3422(15)	1.0	0.6(1)
O24	-0.2425(6)	0.1974(12)	-0.3418(21)	1.0	0.6(1)
O25	-0.2502(3)	0.2834(13)	0.0554(15)	1.0	0.6(1)
O26	-0.2521(3)	0.1064(11)	0.0695(21)	1.0	0.6(1)
O27	0.4465(14)	0.3749(8)	-0.2393(20)	1.0	0.6(1)
O28	0.4556(9)	0.3110(11)	-0.0707(15)	1.0	0.6(1)
O29	0.4273(10)	0.2029(4)	0.0267(21)	1.0	0.6(1)
O30	0.4451(12)	0.0946(13)	-0.0756(16)	1.0	0.6(1)
O31	0.4389(11)	0.1180(7)	-0.2665(20)	1.0	0.6(1)
O32	0.4425(9)	0.2457(8)	-0.2374(20)	1.0	0.6(1)
O33	0.6642(12)	0.3754(13)	-0.2195(16)	1.0	0.6(1)
O34	0.6450(7)	0.3089(9)	-0.0555(11)	1.0	0.6(1)
O35	0.6553(10)	0.1951(5)	0.0354(24)	1.0	0.6(1)

O36	0.6633(11)	0.0903(14)	-0.0776(11)	1.0	0.6(1)
O37	0.6658(9)	0.1205(11)	-0.2665(15)	1.0	0.6(1)
O38	0.6681(17)	0.2462(14)	-0.2217(18)	1.0	0.6(1)
O39	0.5543(4)	0.3072(17)	-0.1966(16)	1.0	0.6(1)
O40	0.5531(4)	0.0871(9)	-0.1832(28)	1.0	0.6(1)
O41	0.3729(4)	0.4186(10)	-0.3866(14)	1.0	0.6(1)
O42	0.5022(5)	0.4069(13)	-0.4078(21)	1.0	0.6(1)
O43	0.6319(5)	0.3904(7)	-0.4069(13)	1.0	0.6(1)
O44	0.3729(8)	0.1968(14)	-0.3855(22)	1.0	0.6(1)
O45	0.5035(8)	0.1941(12)	-0.3900(17)	1.0	0.6(1)
O46	0.6331(7)	0.2086(10)	-0.4006(13)	1.0	0.6(1)
O47	0.4595(8)	-0.0023(6)	-0.2022(12)	1.0	0.6(1)
O48	0.6460(9)	-0.0019(9)	-0.2115(14)	1.0	0.6(1)

Table B

ZSM-5$_{(15)}$

Site	x/a	y/b	z/c	Fraction	Ui/Ue*100
T1	0.0564(2)	0.4237(2)	-0.3337(5)	1.0	0.1(2)
T2	0.0333(2)	0.3147(3)	-0.1796(6)	1.0	0.1(2)
T3	0.0632(4)	0.2807(1)	0.0381(6)	1.0	0.1(2)
T4	0.0640(2)	0.1239(1)	0.0321(5)	1.0	0.1(2)
T5	0.0292(1)	0.0723(2)	-0.1793(6)	1.0	0.1(2)
T6	0.0613(3)	0.1916(3)	-0.3158(6)	1.0	0.1(2)
T7	-0.1720(1)	0.4254(2)	-0.3255(5)	1.0	0.1(2)
T8	-0.1254(2)	0.3095(2)	-0.1853(6)	1.0	0.1(2)
T9	-0.17316(2)	0.2706(2)	0.0282(5)	1.0	0.1(2)
T10	-0.1758(2)	0.1153(2)	0.0285(8)	1.0	0.1(2)
T11	-0.1285(2)	0.0670(4)	-0.1808(8)	1.0	0.1(2)
T12	-0.1676(4)	0.1855(4)	-0.3170(7)	1.0	0.1(2)
T13	0.4424(2)	0.4236(2)	-0.3335(5)	1.0	0.1(2)
T14	0.4728(2)	0.3101(3)	-0.1875(6)	1.0	0.1(2)
T15	0.4400(3)	0.2810(2)	0.0357(6)	1.0	0.1(2)
T16	0.4339(2)	0.1235(2)	0.0309(5)	1.0	0.1(2)
T17	0.4726(2)	0.0742(3)	-0.1850(6)	1.0	0.1(2)
T18	0.4396(3)	0.1885(3)	-0.3231(8)	1.0	0.1(2)

T19	0.6724(2)	0.4219(2)	-0.3186(5)	1.0	0.1(2)
T20	0.6314(2)	0.3082(2)	-0.1782(6)	1.0	0.1(2)
T21	0.6714(2)	0.2721(2)	0.0381(6)	1.0	0.1(2)
T22	0.6725(2)	0.1170(2)	0.0284(6)	1.0	0.1(2)
T23	0.6304(2)	0.0717(4)	-0.1878(5)	1.0	0.1(2)
T24	0.6779(4)	0.1895(3)	-0.3123(7)	1.0	0.6(4)
O1	0.0635(4)	0.3761(5)	-0.2396(8)	1.0	0.6(4)
O2	0.0608(8)	0.3161(4)	-0.0680(7)	1.0	0.6(4)
O3	0.0567(4)	0.2025(1)	0.0239(9)	1.0	0.6(4)
O4	0.0642(6)	0.0925(6)	-0.0768(7)	1.0	0.6(4)
O5	0.0547(6)	0.1202(4)	-0.2657(9)	1.0	0.6(4)
O6	0.0556(7)	0.2473(4)	-0.2320(7)	1.0	0.6(4)
O7	-0.1586(6)	0.3709(6)	-0.2417(10)	1.0	0.6(4)
O8	-0.1552(8)	0.3045(6)	-0.0756(7)	1.0	0.6(4)
O9	-0.1601(6)	0.1927(1)	0.0212(13)	1.0	0.6(4)
O10	-0.1648(4)	0.0816(5)	-0.0775(7)	1.0	0.6(4)
O11	-0.1578(5)	0.1154(4)	-0.2642(9)	1.0	0.6(4)
O12	-0.1417(8)	0.2429(5)	-0.2447(13)	1.0	0.6(4)
O13	-0.0463(2)	0.3196(5)	-0.1792(15)	1.0	0.6(4)
O14	-0.0500(1)	0.0791(5)	-0.1688(14)	1.0	0.6(4)
O15	0.1235(2)	0.4209(3)	-0.3975(5)	1.0	0.6(4)
O16	-0.0051(2)	0.4003(6)	-0.4008(9)	1.0	0.6(4)
O17	-0.1345(2)	0.4045(5)	-0.4253(8)	1.0	0.6(4)
O18	0.1321(3)	0.1974(6)	-0.3696(6)	1.0	0.6(4)
O19	0.0028(3)	0.2014(6)	-0.3956(9)	1.0	0.6(4)
O20	-0.1259(4)	0.1871(7)	-0.4179(6)	1.0	0.6(4)
O21	0.0480(5)	-0.0023(2)	-0.2060(4)	1.0	0.6(4)
O22	-0.1418(3)	-0.0080(3)	-0.2127(7)	1.0	0.6(4)
O23	-0.2504(1)	0.4309(4)	-0.3465(6)	1.0	0.6(4)
O24	-0.2450(3)	0.1967(6)	-0.3413(13)	1.0	0.6(4)
O25	-0.2500(1)	0.2837(6)	0.0530(9)	1.0	0.6(4)
O26	-0.2517(1)	0.1050(5)	0.0620(9)	1.0	0.6(4)
O27	0.4423(5)	0.3739(4)	-0.2413(9)	1.0	0.6(4)
O28	0.4515(7)	0.3103(5)	-0.0732(7)	1.0	0.6(4)

O29	0.4315(5)	0.2025(2)	0.0293(10)	1.0	0.6(4)
O30	0.4439(6)	0.0965(6)	-0.0796(7)	1.0	0.6(4)
O31	0.4387(5)	0.1175(3)	-0.2707(9)	1.0	0.6(4)
O32	0.4450(6)	0.2448(4)	-0.2402(10)	1.0	0.6(4)
O33	0.6660(4)	0.3714(6)	-0.2280(9)	1.0	0.6(4)
O34	0.6474(5)	0.3076(5)	-0.0619(6)	1.0	0.6(4)
O35	0.6566(5)	0.1945(2)	0.0310(12)	1.0	0.6(4)
O36	0.6617(5)	0.0898(7)	-0.0819(4)	1.0	0.6(4)
O37	0.6644(5)	0.1165(4)	-0.2714(5)	1.0	0.6(4)
O38	0.6600(9)	0.2423(6)	-0.2281(9)	1.0	0.6(4)
O39	0.5524(2)	0.3118(8)	-0.1952(11)	1.0	0.6(4)
O40	0.5517(2)	0.0849(5)	-0.1866(13)	1.0	0.6(4)
O41	0.3730(2)	0.4180(5)	-0.3919(6)	1.0	0.6(4)
O42	0.5025(2)	0.4052(5)	-0.4064(9)	1.0	0.6(4)
O43	0.6324(2)	0.3938(4)	-0.4124(7)	1.0	0.6(4)
O44	0.3726(4)	0.1985(6)	-0.3861(9)	1.0	0.6(4)
O45	0.5027(4)	0.1931(6)	-0.3954(9)	1.0	0.6(4)
O46	0.6325(4)	0.2026(5)	-0.4081(6)	1.0	0.6(4)
O47	0.4560(5)	-0.0021(3)	-0.2032(6)	1.0	0.6(4)
O48	0.6442(4)	-0.0046(4)	-0.2115(7)	1.0	0.6(4)

Table C

Site	**x/a**	**y/b**	**z/c**	**Fraction** *ZSM-5(37)*	**Ui/Ue*100** *ZSM-5(37)*	**Fraction** *ZSM-5(15)*	**Ui/Ue*100** *ZSM-5(15)*
C7a	0.871(1)	0.480(1)	0.048(1)	0.23(3)	1.4(1)	0.41(1)	9.7(5)
C4a	0.806(1)	0.477(1)	0.046(1)	0.23(3)	1.4(1)	0.41(1)	9.7(5)
C3a	0.763(1)	0.527(1)	0.048(1)	0.23(3)	1.4(1)	0.41(1)	9.7(5)
C1a	0.696(1)	0.525(1)	0.046(1)	0.23(3)	1.4(1)	0.41(1)	9.7(5)
C14b	0.237(1)	0.004(1)	0.771(1)	0.24(3)	1.2(1)	0.28(1)	8.8(6)
C8b	0.237(1)	0.180(1)	0.816(1)	0.24(3)	1.2(1)	0.28(1)	8.8(6)
C9b	0.237(1)	0.120(1)	0.771(1)	0.24(3)	1.2(1)	0.28(1)	8.8(6)
C13b	0.237(1)	0.060(1)	0.816(1)	0.24(3)	1.2(1)	0.28(1)	8.8(6)
C98a	0.652(1)	0.573(1)	0.048(1)	0.23(3)	1.4(1)	0.41(1)	9.7(5)
C99a	0.912(1)	0.433(1)	0.046(1)	0.23(3)	1.4(1)	0.41(1)	9.7(5)

Nb1	0.237(1)	-0.058(1)	0.816(1)	0.24(3)	1.2(1)	0.28(1)	8.8(6)
C101b	0.237(1)	0.236(1)	0.771(1)	0.24(3)	1.2(1)	0.28(1)	8.8(6)
Na1	0.980(1)	0.432(1)	0.048(1)	0.23(3)	1.4(1)	0.41(1)	9.7(5)
Oa1	0.587(1)	0.575(1)	0.047(1)	0.23(3)	1.4(1)	0.41(1)	9.7(5)
Oa2	0.676(1)	0.632(1)	0.050(1)	0.23(3)	1.4(1)	0.41(1)	9.7(5)
Na2	0.672(1)	0.467(1)	0.045(1)	0.23(3)	1.4(1)	0.41(1)	9.7(5)
C100b	0.237(1)	0.302(1)	0.813(1)	0.24(3)	1.2(1)	0.28(1)	8.8(6)
Ob1	0.237(1)	0.362(1)	0.768(1)	0.24(3)	1.2(1)	0.28(1)	8.8(6)
Ob2	0.238(1)	0.308(1)	0.911(1)	0.24(3)	1.2(1)	0.28(1)	8.8(6)
Nb2	0.237(1)	0.234(1)	0.667(1)	0.24(3)	1.2(1)	0.28(1)	8.8(6)
W1	1/2	1/2	0.0	0.34(1)	9.94(1)	0.14(1)	6.3(1)

Table D

Bond distances (Å)	**ZSM-5$_{(37)}$**	**ZSM-5$_{(15)}$**
T1-O1	1.594(4)	1.593(1)
T1-O15	1.594(4)	1.593(1)
T1-O16	1.593(4)	1.593(1)
T1-O47	1.593(4)	1.593(1)
T2-O1	1.594(4)	1.593(1)
T2-O2	1.593(4)	1.593(1)
T2-O6	1.594(4)	1.593(1)
T2-O13	1.593(4)	1.593(1)
T3-O2	1.594(4)	1.593(1)
T3-O3	1.593(4)	1.593(1)
T3-O45	1.594(4)	1.593(1)
T3-O46	1.593(4)	1.593(1)
T4-O3	1.594(4)	1.593(1)
T4-O4	1.594(4)	1.593(1)
T4-O42	1.594(4)	1.593(1)
T4-O43	1.593(4)	1.593(1)
T5-O4	1.594(4)	1.593(1)
T5-O5	1.594(4)	1.593(1)
T5-O14	1.594(4)	1.593(1)
T5-O21	1.594(4)	1.593(1)
T6-O5	1.594(4)	1.593(1)
T6-O6	1.594(4)	1.593(1)
T6-O18	1.594(4)	1.593(1)

T6-O19	1.594(4)	1.593(1)
T7-O7	1.594(4)	1.593(1)
T7-O17	1.594(4)	1.593(1)
T7-O23	1.593(4)	1.593(1)
T7-O48	1.594(4)	1.593(1)
T8-O7	1.594(4)	1.593(1)
T8-O8	1.594(4)	1.593(1)
T8-O12	1.594(4)	1.594(1)
T8-O13	1.594(4)	1.593(1)
T9-O8	1.593(4)	1.593(1)
T9-O9	1.593(4)	1.594(1)
T9-O25	1.594(4)	1.594(1)
T9-O44	1.593(4)	1.593(1)
T10-O9	1.594(4)	1.593(1)
T10-O10	1.594(4)	1.593(1)
T10-O26	1.594(4)	1.593(1)
T10-O41	1.593(4)	1.593(1)
T11-O10	1.594(4)	1.593(1)
T11-O11	1.594(4)	1.593(1)
T11-O14	1.593(4)	1.593(1)
T11-O22	1.594(4)	1.593(1)
T12-O11	1.594(4)	1.593(1)
T12-O12	1.594(4)	1.593(1)
T12-O20	1.594(4)	1.593(1)
T12-O24	1.593(4)	1.593(1)
T13-O21	1.594(4)	1.593(1)
T13-O27	1.594(4)	1.593(1)
T13-O41	1.593(4)	1.593(1)
T13-O42	1.594(4)	1.593(1)
T14-O27	1.594(4)	1.593(1)
T14-O28	1.594(4)	1.593(1)
T14-O32	1.594(4)	1.593(1)
T14-O39	1.594(4)	1.593(1)
T15-O19	1.593(4)	1.593(1)
T15-O20	1.594(4)	1.593(1)
T15-O28	1.594(4)	1.593(1)
T15-O29	1.594(4)	1.593(1)
T16-O16	1.593(4)	1.593(1)

T16-O17	1.594(4)	1.593(1)
T16O29	1.594(4)	1.593(1)
T16-O30	1.593(4)	1.593(1)
T17-O30	1.593(4)	1.593(1)
T17-O31	1.593(4)	1.593(1)
T17-O40	1.593(4)	1.593(1)
T17-O47	1.593(4)	1.593(1)
T18-O31	1.593(4)	1.593(1)
T18-O32	1.593(4)	1.593(1)
T18-O44	1.593(4)	1.593(1)
T18-O45	1.594(4)	1.593(1)
T19-O22	1.594(4)	1.593(1)
T19-O23	1.594(4)	1.593(1)
T19-O33	1.594(4)	1.593(1)
T19-O43	1.593(4)	1.593(1)
T20-O33	1.594(4)	1.593(1)
T20-O34	1.593(4)	1.593(1)
T20-O38	1.594(4)	1.594(1)
T20-O39	1.594(4)	1.593(1)
T21-O18	1.594(4)	1.593(1)
T21-O25	1.594(4)	1.593(1)
T21-O34	1.594(4)	1.593(1)
T21-O35	1.594(4)	1.593(1)
T22-O15	1.594(4)	1.593(1)
T22-O26	1.594(4)	1.593(1)
T22-O35	1.594(4)	1.593(1)
T22-O36	1.594(4)	1.593(1)
T23-O36	1.593(4)	1.593(1)
T23-O37	1.594(4)	1.594(1)
T23-O40	1.594(4)	1.593(1)
T23-O48	1.594(4)	1.593(1)
T24-O24	1.594(4)	1.593(1)
T24-O37	1.594(4)	1.593(1)
T24-O38	1.594(4)	1.593(1)
T24-O46	1.593(4)	1.593(1)
<T-O>	1.593	1.593
T-O-T angles (°)		
T1_O1_T2	144.7(3)	146.8(7)

T2_O2_T3	143.5(1)	147.4(5)
T3_O3_T4	159.1(1)	165.3(6)
T4_O4_T5	146.5(5)	153.0(8)
T5_O5_T6	154.2(2)	151.7(6)
T2_O6_T6	157.5(3)	158.8(7)
T7_O7_T8	159.8(8)	159.9(9)
T8_O8_T9	159.2(2)	157.1(1)
T9_O9_T10	157.0(4)	158.0(7)
T10_O10_T11	154.0(9)	157.1(5)
T11_O11_T12	157.5(7)	154.2(7)
T8_O12_T12	170.7(2)	168.6(1)
T2_O13_T8	168.2(7)	168.7(7)
T5_O14_T11	158.9(2)	162.6(6)
T1_O15_T22	150.3(1)	150.7(5)
T1_O16_T16	173.7(1)	179.2(5)
T7_O17_T16	144.1(3)	144.1(6)
T6_O18_T21	141.9(2)	145.3(6)
T6_O19_T15	173.3(3)	171.6(7)
T12_O20_T15	138.3(4)	140.9(6)
T5_O21_T13	144.9(7)	146.8(3)
T11_O22_T19	148.2(1)	146.3(5)
T7_O23_T19	156.2(1)	154.0(4)
T12_O24_T24	148.6(9)	150.7(5)
T9_O25_T21	154.9(4)	153.5(6)
T10_O26_T22	141.9(1)	143.1(5)
T13_O27_T14	151.2(6)	149.1(6)
T14_O28_T15	156.3(5)	157.4(7)
T15_O29_T16	163.9(3)	171.3(8)
T16_O30_T17	166.1(6)	165.9(8)
T17_O31_T18	143.8(1)	143.5(4)
T14_O32_T18	153.5(2)	157.1(7)
T19_O33_T20	147.4(1)	150.1(6)
T20_O34_T21	150.5(2)	152.7(6)
T21_O35_T22	156.4(4)	157.6(7)
T22_O36_T23	161.9(3)	163.7(6)
T23_O37_T24	149.3(5)	147.1(6)
T20_O38_T24	154.7(1)	159.3(5)
T14_O39_T20	163.2(2)	167.4(6)

T17_O40_T23	161.3(7)	162.6(3)
T10_O41_T13	151.7(2)	152.8(6)
T4_O42_T13	167.3(8)	170.4(8)
T4_O43_T19	151.2(8)	151.1(4)
T9_O44_T18	155.0(7)	155.6(8)
T3_O45_T18	164.4(5)	164.0(8)
T3_O46_T24	156.3(8)	153.0(4)
T1_O47_T17	154.3(1)	152.9(5)
T7_O48_T23	148.9(2)	148.3(5)
<T-O-T>	154.9	156.0

Appendix 4

Atomic coordinates, fraction and Atomic Displacement Parameters of framework and extraframework atoms of L-LTL, ND_4-LTL and D-LTL are reported in table A, B and C, respectively.
Framework and extraframework bond distances of L-LTL, ND_4-LTL and D-LTL are reported in table D.
Calculated fraction crystallographic coordinates (*x*, *y*, *z*) of D-LTL are reported in Table E.

Table A

L-LTL

Site	x/a	y/b	z/c	Fraction	Ui/Ue*100
KB	2/3	1/3	1/2	1.0(1)	1.72(2)
KC	1/2	0.0	1/2	1.0(1)	3.32(2)
KD	0.2993(1)	0.0	0.0	0.85(1)	8.17(3)
Al1	0.0933(6)	0.3570(10)	1/2	0.30(1)	1.12(3)
Si1	0.0933(6)	0.3570(10)	1/2	0.70(1)	1.12(3)
Si2	0.1657(6)	0.4983(2)	0.2102(13)	0.78(1)	1.12(3)
Al2	0.1657(6)	0.4983(2)	0.2102(13)	0.22(1)	1.12(3)
O1	0.0	0.2709(13)	1/2	1.0	1.18(3)
O2	0.1639(13)	0.3278(26)	1/2	1.0	1.18(3)
O3	0.2642(8)	0.5285(17)	0.2530(35)	1.0	1.18(3)
O4	0.1007(10)	0.4122(8)	0.3255(19)	1.0	1.18(3)
O5	0.4247(2)	0.8493(4)	0.2730(25)	1.0	1.18(3)
O6	0.1443(18)	0.4760(18)	0.0	1.0	1.18(3)
W1	0.0657(11)	0.0	0.0	0.22(4)	12.67(3)
W2	0.1258(10)	0.2517(13)	0.0	0.95(3)	12.67(3)
W3	0.1295(13)	0.0	0.2486(9)	0.58(3)	12.67(3)
W4	0.1189(10)	0.0	1/2	0.64(2)	12.67(3)
W5	0.0	0.0	1/2	0.09(4)	12.67(3)

Table B

ND_4-LTL

Site	x/a	y/b	z/c	Fraction	Ui/Ue*100
KB	2/3	1/3	1/2	1.0(1)	4.20(1)
Si1	0.0957(6)	0.3635(8)	1/2	0.70(1)	1.74(1)
Al1	0.0957(6)	0.3635(8)	1/2	0.30(1)	1.74(1)
Si2	0.1646(5)	0.5005(6)	0.2076(10)	0.78(1)	1.74(1)
Al2	0.1646(5)	0.5005(6)	0.2076(10)	0.22(1)	1.74(1)

O1	0.0	0.2900(13)	1/2	1.0	1.62(2)
O2	0.1747(4)	0.3493(8)	1/2	1.0	1.62(2)
O3	0.2625(7)	0.5251(13)	0.2292(20)	1.0	1.62(2)
O4	0.1095(9)	0.4204(7)	0.3286(8)	1.0	1.62(2)
O5	0.4359(4)	0.8718(7)	0.2630(4)	1.0	1.62(2)
O6	0.1412(5)	0.4780(4)	0.0	1.0	1.62(2)
N1	1/2	0.0	1/2	0.98(1)	1.25(2)
N2	0. 294(2)	0.0	0.0	0.48(1)	1.00(2)
N3	0.125(4)	0.250(7)	0.0	0.17(1)	1.00(2)
N4	0.137(1)	0.068(3)	0.318(2)	0.16(1)	1.00(2)

Table C

D-LTL

Site	x/a	y/b	z/c	Fraction	Ui/Ue*100
KB	2/3	1/3	1/2	1.0(1)	7.67(2)
Si1	0.09394(3)	0.3575(7)	1/2	0.70(1)	1.34(2)
Al1	0.09394(3)	0.3575(7)	1/2	0.30(1)	1.34(2)
Si2	0.1654(4)	0.4964(7)	0.2084(8)	0.78(1)	1.34(2)
Al2	0.1654(4)	0.4964(7)	0.2084(8)	0.22(1)	1.34(2)
O1	0.0	0.2774(8)	1/2	1.0	1.62(4)
O2	0.1654(5)	0.3307(10)	1/2	1.0	1.62(4)
O3	0.2633(7)	0.5266(15)	0.2371(43)	1.0	1.62(4)
O4	0.1070(7)	0.4124(8)	0.3228(12)	1.0	1.62(4)
O5	0.4359(6)	0.8718(6)	0.2630(8)	1.0	1.62(4)
O6	0.1411(18)	0.4780(13)	0.0	1.0	1.62(4)
D1	0.0600(6)	0.5300(7)	0.2527(5)	0.58(1)	1.87(1)
D2	0.0	0.2124(11)	1/2	0.14(1)	2.50(1)
W1	1/2	0.0	1/2	0.52(1)	3.51(2)
W2	0.2930(3)	0.0	0.0	0.40(1)	2.00(1)

Table D

Bond distances (Å)	L-LTL	ND_4-L	D-LTL
T1-O1	1.662(9)	1.670(8)	1.615(10)
T1-O2	1.641(9)	1.670(8)	1.616(10)
T1-O4 [x2]	1.629(9)	1.681(7)	1.616(12)
<T1-O>	1.640	1.674	1.616

T2-O3	1.647(9)	1.710(7)	1.610(9)
T2-O4	1.680(8)	1.670(6)	1.618(9)
T2-O5	1.651(9)	1.740(7)	1.743(10)
T2-O6	1.637(13)	1.700(9)	1.620(12)
<T2-O>	1.654	1.705	1.648
	T-O-T angles (°)		
T1-O1-T1	128.0(1)	145.6(9)	135.6(9)
T1-O2-T1	146.9(1)	163.7(1)	149.3(9)
T2-O3-T2	138.6(1)	149.9(1)	141.7(1)
T1-O4-T2	143.92(9)	152.5(7)	148.7(1)
T2-O5-T2	142.3(2)	129.2(7)	131.1(1)
T2-O6-T2	151.3(2)	148.8(2)	151.2(1)
<T-O-T>	141.8	148.2	149.9

KB-O3 [x6]	2.89(1)	3.18(1)		2.98(1)	
KC-O4 [x8]	3.29(1)	**N1-O5 [x4]**	2.84(1)	**D2-O1**	1.19(6)
KC-O5 [x4]	2.95(1)	**N2-O6 [x2]**	3.20(1)	**D1-O5**	1.09(3)
KD-O4 [x4]	3.15(1)	**N2-N3 [x2]**	2.90(1)	**D1-W1[x4]**	2.09(1)
KD-O6 [x2]	3.01(1)	**N3-N4 [x2]**	3.00(1)	**W1-O5[x4]**	2.71(1)
KD-W2 [x2]	2.86(1)	**N4-N4**	2.74(1)	**W2-O6[x2]**	3.07(1)
W1-W2 [x2]	3.03(1)			**W2-O4[x4]**	3.20(1)
W1-W3 [x2]	2.21(1)				
W1-W3 [x4]	2.79(1)				
W2-W3 [x4]	2.96(1)				
W5-W3 [x12]	3.05(1)				
W5-W4 [x6]	2.19(1)				
W3-O1	3.22(1)				
W4-O1	2.80(1)				

Table E

Sites	x/a (calc)	y/b (calc)	z/c (calc)
T1	0.0992	0.3620	0.5000
T11	0.9008	0.6380	0.5000
T12	0.3620	0.0992	0.5000
T13	0.6380	0.9008	0.5000
T14	0.6380	0.7372	0.5000
T15	0.2628	0.9008	0.5000
T16	0.0992	0.7372	0.5000
T17	0.2628	0.3620	0.5000
T18	0.9008	0.2628	0.5000
T19	0.7372	0.6380	0.5000

T110	0.7372	0.0992	0.5000
T111	0.3620	0.2628	0.5000
T2	0.1629	0.4969	0.2107
T21	0.8371	0.5031	0.2107
T22	0.4969	0.1629	0.7893
T23	0.5031	0.8371	0.7893
T24	0.5031	0.6660	0.2107
T25	0.3340	0.8371	0.2107
T26	0.1629	0.6660	0.7893
T27	0.3340	0.4969	0.7893
T28	0.8371	0.3340	0.7893
T29	0.6660	0.5031	0.7893
T210	0.6660	0.1629	0.2107
T211	0.4969	0.3340	0.2107
T212	0.8371	0.5031	0.7893
T213	0.1629	0.4969	0.7893
T214	0.5031	0.8371	0.2107
T215	0.4969	0.1629	0.2107
T216	0.4969	0.3340	0.7893
T217	0.6660	0.1629	0.7893
T218	0.8371	0.3340	0.2107
T219	0.6660	0.5031	0.2107
T220	0.1629	0.6660	0.2107
T221	0.3340	0.4969	0.2107
T222	0.3340	0.8371	0.7893
T223	0.5031	0.6660	0.7893
O1	0.0050	0.2710	0.5000
H2	0.0042	0.2261	0.5000
O11	-0.0050	0.2660	0.5000
H21	-0.0042	0.2219	0.5000
O12	1.0050	0.2710	0.5000
H22	1.0042	0.2261	0.5000
O13	0.9950	0.2660	0.5000
H23	0.9958	0.2219	0.5000
O14	-0.0050	0.7290	0.5000
H24	-0.0042	0.7739	0.5000
O15	0.0050	0.7340	0.5000
H25	0.0042	0.7781	0.5000
O16	0.9950	0.7290	0.5000
H26	0.9958	0.7739	0.5000
O17	1.0050	0.7340	0.5000
H27	1.0042	0.7781	0.5000
O18	0.2710	0.0050	0.5000
H28	0.2261	0.0042	0.5000
O19	0.2660	-0.0050	0.5000
H29	0.2219	-0.0042	0.5000
O110	0.2710	1.0050	0.5000
H210	0.2261	1.0042	0.5000
O111	0.2660	0.9950	0.5000

H211	0.2219	0.9958	0.5000
O112	0.7290	-0.0050	0.5000
H212	0.7739	-0.0042	0.5000
O113	0.7340	0.0050	0.5000
H213	0.7781	0.0042	0.5000
O114	0.7290	0.9950	0.5000
H214	0.7739	0.9958	0.5000
O115	0.7340	1.0050	0.5000
H215	0.7781	1.0042	0.5000
O116	0.7290	0.7340	0.5000
H216	0.7739	0.7781	0.5000
O117	0.7340	0.7290	0.5000
H217	0.7781	0.7739	0.5000
O118	0.2660	0.2710	0.5000
H218	0.2219	0.2261	0.5000
O119	0.2710	0.2660	0.5000
H219	0.2261	0.2219	0.5000
O2	0.1597	0.3194	0.5000
O21	0.8403	0.6806	0.5000
O22	0.3194	0.1597	0.5000
O23	0.6806	0.8403	0.5000
O24	0.1597	0.8403	0.5000
O25	0.8403	0.1597	0.5000
O4	0.1008	0.4093	0.3207
O41	0.8992	0.5907	0.3207
O42	0.4093	0.1008	0.6793
O43	0.5907	0.8992	0.6793
O44	0.5907	0.6915	0.3207
O45	0.3085	0.8992	0.3207
O46	0.1008	0.6915	0.6793
O47	0.3085	0.4093	0.6793
O48	0.8992	0.3085	0.6793
O49	0.6915	0.5907	0.6793
O410	0.6915	0.1008	0.3207
O411	0.4093	0.3085	0.3207
O412	0.8992	0.5907	0.6793
O413	0.1008	0.4093	0.6793
O414	0.5907	0.8992	0.3207
O415	0.4093	0.1008	0.3207
O416	0.4093	0.3085	0.6793
O417	0.6915	0.1008	0.6793
O418	0.8992	0.3085	0.3207
O419	0.6915	0.5907	0.3207
O420	0.1008	0.6915	0.3207
O421	0.3085	0.4093	0.3207
O422	0.3085	0.8992	0.6793
O423	0.5907	0.6915	0.6793
O5	0.4252	0.8504	0.2829
H11	0.4239	0.8877	0.4244

H12	0.4249	0.9037	0.3750
H111	0.4638	0.8877	0.4244
H121	0.4788	0.9037	0.3750
K1	0.3333	0.6667	0.5000
O3	0.2619	0.5238	0.2568
O51	0.1496	0.5748	0.7171
H112	0.1123	0.5761	0.5756
H122	0.0963	0.5751	0.6250
H113	0.1123	0.5362	0.5756
H123	0.0963	0.5212	0.6250
O31	0.4762	0.7381	0.7432
O52	0.1496	0.5748	0.2829
H114	0.1123	0.5362	0.4244
H124	0.0963	0.5212	0.3750
H115	0.1123	0.5761	0.4244
H125	0.0963	0.5751	0.3750
O32	0.4762	0.7381	0.2568
O53	0.4252	0.5748	0.2829
H116	0.4638	0.5761	0.4244
H126	0.4788	0.5751	0.3750
H117	0.4239	0.5362	0.4244
H127	0.4249	0.5212	0.3750
O33	0.2619	0.7381	0.2568
O54	0.4252	0.5748	0.7171
H118	0.4239	0.5362	0.5756
H128	0.4249	0.5212	0.6250
H119	0.4638	0.5761	0.5756
H129	0.4788	0.5751	0.6250
O34	0.2619	0.7381	0.7432
O55	0.4252	0.8504	0.7171
H1110	0.4638	0.8877	0.5756
H1210	0.4788	0.9037	0.6250
H1111	0.4239	0.8877	0.5756
H1211	0.4249	0.9037	0.6250
O35	0.2619	0.5238	0.7432
O56	0.5748	0.1496	0.2829
H1112	0.5761	0.1123	0.4244
H1212	0.5751	0.0963	0.3750
H1113	0.5362	0.1123	0.4244
H1213	0.5212	0.0963	0.3750
K11	0.6667	0.3333	0.5000
O36	0.7381	0.4762	0.2568
O57	0.8504	0.4252	0.7171
H1114	0.8877	0.4239	0.5756
H1214	0.9037	0.4249	0.6250
H1115	0.8877	0.4638	0.5756
H1215	0.9037	0.4788	0.6250
O37	0.5238	0.2619	0.7432
O58	0.8504	0.4252	0.2829

H1116	0.8877	0.4638	0.4244
H1216	0.9037	0.4788	0.3750
H1117	0.8877	0.4239	0.4244
H1217	0.9037	0.4249	0.3750
O38	0.5238	0.2619	0.2568
O59	0.5748	0.4252	0.2829
H1118	0.5362	0.4239	0.4244
H1218	0.5212	0.4249	0.3750
H1119	0.5761	0.4638	0.4244
H1219	0.5751	0.4788	0.3750
O39	0.7381	0.2619	0.2568
O510	0.5748	0.4252	0.7171
H1120	0.5761	0.4638	0.5756
H1220	0.5751	0.4788	0.6250
H1121	0.5362	0.4239	0.5756
H1221	0.5212	0.4249	0.6250
O310	0.7381	0.2619	0.7432
O511	0.5748	0.1496	0.7171
H1122	0.5362	0.1123	0.5756
H1222	0.5212	0.0963	0.6250
H1123	0.5761	0.1123	0.5756
H1223	0.5751	0.0963	0.6250
O311	0.7381	0.4762	0.7432
O6	0.1413	0.4781	0.0001
O61	0.1413	0.4781	1.0001
O62	0.8587	0.5219	0.0001
O63	0.8587	0.5219	1.0001
O64	0.4781	0.1413	-0.0001
O65	0.4781	0.1413	0.9999
O66	0.5219	0.8587	-0.0001
O67	0.5219	0.8587	0.9999
O68	0.5219	0.6632	0.0001
O69	0.5219	0.6632	1.0001
O610	0.3368	0.8587	0.0001
O611	0.3368	0.8587	1.0001
O612	0.1413	0.6632	-0.0001
O613	0.1413	0.6632	0.9999
O614	0.3368	0.4781	-0.0001
O615	0.3368	0.4781	0.9999
O616	0.8587	0.3368	-0.0001
O617	0.8587	0.3368	0.9999
O618	0.6632	0.5219	-0.0001
O619	0.6632	0.5219	0.9999
O620	0.6632	0.1413	0.0001
O621	0.6632	0.1413	1.0001
O622	0.4781	0.3368	0.0001
O623	0.4781	0.3368	1.0001

Appendix 5

Atomic coordinates, fraction and Atomic Displacement Parameters of framework and extraframework atoms at selected temperature of 30, 190, 550 and 810 °C of H-LTL are reported in Table A, B, C and D, respectively. T-O bond distances and T-OT angles are reported in Table E for 30 and 190 °C and in Table F for 550 and 810 °C.

Table A

30 °C

Site	x/a	y/b	z/c	Fraction	Ui/Ue*100
Al1	0.0927(3)	0.3623(3)	1/2	0.30	1.8(1)
Si1	0.0927(3)	0.3623(3)	1/2	0.70	1.8(1)
Si2	0.1652(2)	0.5020(2)	0.2090(5)	0.78	1.8(1)
Al2	0.1652(2)	0.5020(2)	0.2090(5)	0.22	1.8(1)
O1	0	0.2783(9)	1/2	1.0	2.9(1)
O2	0.1757(5)	0.3515(9)	1/2	1.0	2.9(1)
O3	0.2630(3)	0.5260(6)	0.2406(3)	1.0	2.9(1)
O4	0.1017(4)	0.4170(4)	0.3233(9)	1.0	2.9(1)
O5	0.4359(3)	0.8718(5)	0.2630(4)	1.0	2.9(1)
O6	0.1411(6)	0.4780(7)	0	1.0	2.9(1)
W1	0	0.1052(4)	1/2	0.46(1)	8.4(1)
W2	0	0.1014(8)	0.1666(6)	0.54(1)	8.4(1)
W3	0.1349(3)	0.2697(7)	0	0.39(1)	8.4(1)
W4	0	0.2828(6)	0	0.60(1)	8.4(1)
KB	1/3	2/3	1/2	1.00(1)	6.76(3)

Table B

190 °C

Site	x/a	y/b	z/c	Fraction	Ui/Ue*100
Al1	0.1000(3)	0.3669(3)	1/2	0.30	2.9(1)
Si1	0.1000(3)	0.3669(3)	1/2	0.70	2.9(1)
Si2	0.1562(2)	0.4979(2)	0.1990(5)	0.78	2.9(1)
Al2	0.1562(2)	0.4979(2)	0.1990(5)	0.22	2.9(1)
O1	0.0	0.2911(9)	1/2	1.0	6.0(1)
O2	0.1677(6)	0.335(11)	1/2	1.0	6.0(1)
O3	0.2605(3)	0.5211(7)	0.2312(14)	1.0	6.0(1)
O4	0.0988(5)	0.4180(5)	0.3186(9)	1.0	6.0(1)
O5	0.4356(3)	0.8713(6)	0.2733(15)	1.0	6.0(1)
O6	0.1297(6)	0.4757(8)	0.0	1.0	6.0(1)
W1	0.0	0.079(16)	1/2	0.030(9)	9.0(1)
W2	0.0	0.056(22)	0.15(4)	0.015(6)	9.0(1)
W4	0.0	0.323(7)	0.0	0.139(13)	9.0(1)
KB	1/3	2/3	1/2	1.00(1)	10.95(2)

Table C

550 °C

Site	x/a	y/b	z/c	Fraction	Ui/Ue*100
Al1	0.1007(4)	0.3753(4)	1/2	0.30	6.8(1)
Si1	0.1007(4)	0.3753(4)	1/2	0.70	6.8(1)
Si2	0.1587(2)	0.5062(3)	0.1991(6)	0.78	6.8(1)
Al2	0.1587(2)	0.5062(3)	0.1991(6)	0.22	6.8(1)
O1	0.0	0.2892(11)	1/2	1.0	12.0(1)
O2	0.1697(6)	0.3393(12)	1/2	1.0	12.0(1)
O3	0.2564(4)	0.5129(9)	0.2348(16)	1.0	12.0(1)
O4	0.0955(5)	0.4107(6)	0.2960(10)	1.0	12.0(1)
O5	0.4513(31)	0.9027(6)	0.2997(14)	1.0	12.0(1)
O6	0.1211(7)	0.4707(9)	0.0	1.0	12.0(1)
KB	1/3	2/3	1/2	1.00(1)	10.94(1)

Table D

810 °C

Site	x/a	y/b	z/c	Fraction	Ui/Ue*100
Al1	0.1009(5)	0.3799(4)	1/2	0.30	7.7(1)
Si1	0.1009(5)	0.3799(4)	1/2	0.70	7.7(1)
Si2	0.1570(3)	0.5091(3)	0.2026(7)	0.78	7.7(1)
Al2	0.1570(3)	0.5091(3)	0.2026(7)	0.22	7.7(1)
O1	0.0	0.2899(13)	1/2	1.0	15.1(1)
O2	0.1718(7)	0.3434(14)	1/2	1.0	15.1(1)
O3	0.2561(6)	0.5122(11)	0.2386(20)	1.0	15.1(1)
O4	0.0973(7)	0.4076(7)	0.2859(11)	1.0	15.1(1)
O5	0.4632(4)	0.9263(7)	0.3127(14)	1.0	15.1(1)
O6	0.1179(9)	0.4698(11)	0.0	1.0	15.1(1)
KB	1/3	2/3	1/2	1.00(1)	10.98(1)

Table E

T-O bond distances (Å)	30 °C	190 °C
T1-O1	1.621(7)	1.652(6)
T1-O2	1.624(6)	1.605(7)
T1-O4 [x2]	1.628(5)	1.665(6)
<T-O>	1.625	1.647
T2-O3	1.631(5)	1.698(5)
T2-O4	1.644(6)	1.586(7)
T2-O5	1.635(5)	1.639(6)
T2-O6	1.641(4)	1.586(4)
<T2-O>	1.638	1.627
	T-O-T angles (°)	
T1-O1-T1	129.8(1)	146.8(2)
T1-O2-T1	167.8(1)	143.6(4)
T2-O3-T2	148.1(7)	151.0(9)
T1-O4-T2	144.9(6)	142.8(6)
T2-O5-T2	128.2(8)	128.8(8)
T2-O6-T2	148.9(8)	146.4(9)
<T-O-T>	144.6	143.1

Table F

T-O bond distances (Å)	550 °C	810 °C
T1-O1	1.727(8)	1.751(5)
T1-O2	1.691(8)	1.725(9)
T1-O4 [x2]	1.690(6)	1.698(7)
<T1-O>	1.700	1.718
T2-O3	1.751(5)	1.800(5)
T2-O4	1.703(8)	1.730(4)
T2-O5	1.818(8)	2.005(10)
T2-O6	1.641(6)	1.684(7)
<T2-O>	1.728	1.805
	T-O-T angles (°)	
T1-O1-T1	135.8(4)	131.2(7)
T1-O2-T1	140.5(4)	140.9(7)
T2-O3-T2	160.8(4)	162.4(5)
T1-O4-T2	130.2(7)	124.3(8)
T2-O6-T2	132.5(1)	129.7(9)

Appendix 6

Atomic coordinates, fraction and Atomic Displacement Parameters of framework atoms obtained through synchrotron and neutron refinements are reported in Table A and B, respectively.

Atomic coordinates, fraction and Atomic Displacement Parameters of extraframework molecules are reported in Table C.

T-O bond distances and T-O-T angles obtained from synchrotron and neutron refinements are reported in Table D.

Atomic coordinates of the extraframework molecule in the triclinic *P*1 symmetry are reported in Table E.

Table A

Synchrotron refinement

Site	x/a	y/b	z/c	Fraction	Ui/Ue*100
KB	2/3	1/3	1/2	1.0(1)	1.72(2)
KC	1/2	0.0	1/2	1.0(1)	3.32(2)
KD	0.2917(17)	0.0	0.0	0.85(1)	8.17(3)
Al1	0.0938(3)	0.3576(3)	1/2	0.30	0.56(2)
Si1	0.0938(3)	0.3576(3)	1/2	0.70	0.56(2)
Si2	0.1656(2)	0.4994(2)	0.2089(2)	0.78	0.56(2)
Al2	0.1656(2)	0.4994(2)	0.2089(2)	0.22	0.56(2)
O1	0.0	0.2735(5)	1/2	1.0	1.16(3)
O2	0.1630(3)	0.3260(5)	1/2	1.0	1.16(3)
O3	0.2648(2)	0.5295(4)	0.2518(9)	1.0	1.16(3)
O4	0.1026(3)	0.4128(2)	0.3212(5)	1.0	1.16(3)
O5	0.4400(2)	0.8800(3)	0.2475(8)	1.0	1.16(3)
O6	0.1419(4)	0.4711(4)	0.0	1.0	1.16(3)

Table B

Neutron refinement

Site	x/a	y/b	z/c	Fraction	Ui/Ue*100
KB	2/3	1/3	1/2	1.0(1)	1.26(3)
KC	1/2	0.0	1/2	1.0(1)	1.37(1)
KD	0.2915(35)	0.0	0.0	0.85(1)	1.68(3)
Al1	0.0941(7)	0.3588(8)	1/2	0.30	0.44(2)
Si1	0.0941(7)	0.3588(8)	1/2	0.70	0.44(2)
Si2	0.1664(8)	0.5012(8)	0.2089(13)	0.78	0.44(2)
Al2	0.1664(8)	0.5012(8)	0.2089(13)	0.22	0.44(2)

O1	0.0	0.2806(9)	1/2	1.0	1.04(3)
O2	0.1664(6)	0.3328(13)	1/2	1.0	1.04(3)
O3	0.2654(5)	0.5308(9)	0.2550(23)	1.0	1.04(3)
O4	0.1077(7)	0.4157(6)	0.3241(8)	1.0	1.04(3)
O5	0.4377(2)	0.8755(5)	0.2546(20)	1.0	1.04(3)
O6	0.1505(11)	0.4784(8)	0.0	1.0	1.04(3)

Table C

Site	x/a	y/b	z/c	Fraction	Ui/Ue*100
C3	0.1915(30)	0.1226(35)	0.168(9)	0.14(1)	5.8(7)
C4	0.1950(40)	0.2544(33)	0.2001(10)	0.14(1)	5.8(7)
C1	0.1337(12)	0.0	0.2300(27)	0.07(1)	5.8(7)
C2	0.0659(3)	0.0	0.198(19)	0.07(1)	5.8(7)
W1	0.0	0.1540(2)	0.0	0.50(1)	13.30(4)
W2	0.0723(7)	0.1446(14)	1/2	0.89(1)	15.25(2)

Table D

Bond distances (Å)	Synchrotron refinement	Neutron refinement
T1_O1	1.644(5)	1.606(1)
T1_O2	1.643(2)	1.625(1)
T1_O4 [x2]	1.644(3)	1.626(7)
<T1-O>	1.643	1.620
T2_O3	1.653(4)	1.656(1)
T2_O4	1.658(4)	1.641(1)
T2_O5	1.723(3)	1.686(3)
T2_O6	1.644(3)	1.614(1)
<T2-O>	1.669	1.649
T-O-T angles (°)		
T1-O1-T1	130.7(6)	137.7(3)
T1-O2-T1	144.4(7)	150.4(5)
T2-O3-T2	139.0(4)	138.2(3)
T1-O4-T2	144.7(4)	149.4(8)
T2-O5-T2	126.0(4)	126.3(9)
T2-O6-T2	145.8(4)	153.7(1)
<T-O-T>	138.4	142.6

Table E

Site	x/a	y/b	z/c
C1	-0.132973	-0.196778	-0.209990
C2	-0.196792	-0.133004	-0.209989
H1	-0.251331	-0.187795	-0.210946
H2	-0.197069	-0.078963	-0.227612
C3	-0.063760	-0.196739	-0.209956
H3	-0.063499	-0.251223	-0.202588
O1	-0.204867	-0.267262	-0.213198
H4	-0.244656	-0.259887	-0.281952
C4	-0.132102	-0.132119	-0.187979
O2	-0.067479	-0.067462	-0.197981
H5	-0.013335	-0.067596	-0.206423
C5	-0.067514	-0.000037	-0.198055
H6	-0.121840	-0.000035	-0.197994
H7	-0.022209	0.134527	-0.057935
H8	-0.043613	0.129723	-0.285200
C6	-0.000001	0.067472	-0.198002
C7	0.063778	0.196777	-0.209925
H9	0.119068	0.202020	-0.175629
H10	0.062588	0.246364	-0.262989
C8	-0.000034	0.132097	-0.188068
H11	0.054237	0.067590	-0.206353
C9	-0.063778	-0.196777	0.209925
H12	-0.119068	-0.202020	0.175629
H13	-0.062588	-0.246364	0.262989
H14	-0.054237	-0.067590	0.206353
C10	0.000034	-0.132097	0.188068
H15	0.022209	-0.134527	0.057935
H16	0.043613	-0.129723	0.285200
C11	0.000001	-0.067472	0.198002
C12	0.132973	0.196778	0.209990
N13	0.196792	0.133004	0.209989
H17	0.251331	0.187795	0.210946
H18	0.197069	0.078963	0.227612
C14	0.063760	0.196739	0.209956
H19	0.063499	0.251223	0.202588
O3	0.204867	0.267262	0.213198
H20	0.244656	0.259887	0.281952
C15	0.132102	0.132119	0.187979
O4	0.067479	0.067462	0.197981

H21	0.013335	0.067596	0.206423
C16	0.067514	0.000037	0.198055
H22	0.121840	0.000035	0.197994
H1	-0.054281	-0.067634	-0.206396
N1	-0.063721	-0.196746	-0.210009
H2	-0.115452	-0.209360	-0.140410
H3	-0.066150	-0.238978	-0.298330
N2	0.000017	-0.067512	-0.197942
N3	0.000004	-0.132125	-0.188042
H4	0.053149	-0.132217	-0.161247
N4	0.204880	0.267286	-0.213252
H5	0.262286	0.266716	-0.236292
H6	0.206807	0.326133	-0.192799
N5	0.132983	0.196723	-0.210064
N6	0.063740	0.196759	-0.209943
H7	0.010050	0.148260	-0.278975
H8	0.058558	0.245233	-0.140998
N7	0.132160	0.132127	-0.187972
N8	0.196760	0.132134	-0.187969
H9	0.197084	0.077860	-0.199567
H10	0.251378	0.186422	-0.176367
N9	0.067534	0.067527	-0.197940
H11	0.013398	0.067660	-0.206383
N10	0.067511	-0.000024	-0.197951
H12	0.121854	0.000006	-0.198030
N11	-0.204880	-0.267286	0.213252
H13	-0.262286	-0.266716	0.236292
H14	-0.206807	-0.326133	0.192799
N12	-0.132983	-0.196723	0.210064
N13	-0.063740	-0.196759	0.209943
H15	-0.010050	-0.148260	0.278975
H16	-0.058558	-0.245233	0.140998
N14	-0.132160	-0.132127	0.187972
N15	-0.196760	-0.132134	0.187969
H17	-0.197084	-0.077860	0.199567
H18	-0.251378	-0.186422	0.176367
N16	-0.067534	-0.067527	0.197940
H19	-0.013398	-0.067660	0.206383
N17	-0.067511	0.000024	0.197951
H20	-0.121854	-0.000006	0.198030
H21	-0.053149	0.132217	0.161247

N18	-0.000017	0.067512	0.197942
H22	0.054281	0.067634	0.206396
N19	-0.000004	0.132125	0.188042
N20	0.063721	0.196746	0.210009
H23	0.115452	0.209360	0.140410
H24	0.066150	0.238978	0.298330
N1a	-0.132973	-0.196778	-0.209990
N2a	-0.196792	-0.133004	-0.209989
H1a	-0.251331	-0.187795	-0.210946
H2a	-0.197069	-0.078963	-0.227612
N3a	-0.063760	-0.196739	-0.209956
H3a	-0.063499	-0.251223	-0.202588
O1a	-0.204867	-0.267262	-0.213198
H4a	-0.244656	-0.259887	-0.281952
N4a	-0.132102	-0.132119	-0.187979
O2a	-0.067479	-0.067462	-0.197981
H5a	-0.013335	-0.067596	-0.206423
N5a	-0.067514	-0.000037	-0.198055
H6a	-0.121840	-0.000035	-0.197994
H7a	-0.022209	0.134527	-0.057935
H8a	-0.043613	0.129723	-0.285200
N6a	-0.000001	0.067472	-0.198002
N7a	0.063778	0.196777	-0.209925
H9a	0.119068	0.202020	-0.175629
H10a	0.062588	0.246364	-0.262989
N8a	-0.000034	0.132097	-0.188068
H11a	0.054237	0.067590	-0.206353
N9a	-0.063778	-0.196777	0.209925
H12a	-0.119068	-0.202020	0.175629
H13a	-0.062588	-0.246364	0.262989
H14a	-0.054237	-0.067590	0.206353
N10a	0.000034	-0.132097	0.188068
H15a	0.022209	-0.134527	0.057935
H16a	0.043613	-0.129723	0.285200
N11a	0.000001	-0.067472	0.198002
N12a	0.132973	0.196778	0.209990
N13a	0.196792	0.133004	0.209989
H17a	0.251331	0.187795	0.210946
H18a	0.197069	0.078963	0.227612
N14a	0.063760	0.196739	0.209956
H19a	0.063499	0.251223	0.202588

O3a	0.204867	0.267262	0.213198
H20a	0.244656	0.259887	0.281952
N15a	0.132102	0.132119	0.187979
O4a	0.067479	0.067462	0.197981
H21a	0.013335	0.067596	0.206423
N16a	0.067514	0.000037	0.198055
H22a	0.121840	0.000035	0.197994

Appendix 7

Atomic coordinates, fraction and Atomic Displacement Parameters of the NH_4-omega framework and extraframework atoms at selected temperature of 30, 250, 430, 600 and 770 °C are reported in Table A, B, C, D and E, respectively.

T-O bond distances and T-O-T angles of the NH_4-omega at selected temperature of 30, 250, 430, 600 and 770 °C are reported in Table F.

Atomic coordinates, fraction and Atomic Displacement Parameters of D-omega are reported in table G.

T-O bond distances and T-O-T angles of D-omega are reported in Table H.

Table A

30 °C

Site	x/a	y/b	z/c	Fraction	Ui/Ue*100
T1	0.1598(2)	0.4904(4)	1/4	1.0	0.47(1)
T2	0.3548(6)	0.0947(3)	0.0474(7)	1.0	0.47(1)
O1	0.2587(3)	0.5177(6)	1/4	1.0	0.93(1)
O2	0.4229(2)	0.8460(9)	1/4	1.0	0.93(1)
O3	0.3872(4)	0.0983(6)	1/4	1.0	0.93(1)
O4	0.4383(6)	0.1129(2)	-0.0729(5)	1.0	0.93(1)
O5	0.1618(3)	0.3233(8)	-0.0097(9)	1.0	0.93(1)
O6	0.2774(6)	0.0	0.0	1.0	0.93(1)
NaI	1/2	0.0	0.0	0.413(8)	7.91(1)
W5	0.0	0.1185(1)	0.0	0.582(4)	15.30(1)
NH4-1	0.0841(1)	0.1681(2)	1/4	0.995(1)	7.01(1)
N	1/3	2/3	-1/4	0.5740(4)	8.10(1)
C2	1/3	2/3	-0.019(3)	0.353(7)	8.10(1)
W1	0.5230(1)	0.0460(14)	1/4	0.674(1)	4.12(1)
C1	0.3015(6)	0.6035(8)	-0.1478(13)	0.630(8)	8.10(1)

Table B

250 °C

Site	x/a	y/b	z/c	Fraction	Ui/Ue*100
T1	0.1587(8)	0.4903(5)	1/4	1.0	1.70(1)
T2	0.3552(2)	0.0936(5)	0.0447(5)	1.0	1.70(1)
O1	0.2594(2)	0.5187(11)	1/4	1.0	3.54(1)
O2	0.4243(6)	0.8487(8)	1/4	1.0	3.54(1)
O3	0.3814(2)	0.0961(6)	1/4	1.0	3.54(1)
O4	0.4375(6)	0.1127(11)	-0.0736(8)	1.0	3.54(1)

O5	0.1624(4)	0.3248(7)	-0.0122(25)	1.0	3.54(1)
O6	0.2752(3)	0.0	0.0	1.0	3.54(1)
NaI	1/2	0.0	0.0	0.375(1)	8.74(1)
NH4-1	0.0873(7)	0.1744(14)	1/4	0.738(1)	8.72(1)
N	1/3	2/3	-1/4	0.344(1)	8.14(1)
W1	0.5244(12)	0.0488(24)	1/4	0.359(1)	12.61(1)
C1	0.3053(4)	0.6110(14)	-0.113(11)	0.727(1)	8.14(1)

Table C

430 °C

Site	x/a	y/b	z/c	Fraction	Ui/Ue*100
T1	0.1592(4)	0.4909(9)	1/4	1.0	2.22(1)
T2	0.3557(3)	0.0939(3)	0.0470(6)	1.0	2.22(1)
O1	0.2600(6)	0.5201(10)	1/4	1.0	5.07(1)
O2	0.4238(3)	0.8477(5)	1/4	1.0	5.07(1)
O3	0.3858(2)	0.0983(5)	1/4	1.0	5.07(1)
O4	0.4376(7)	0.1140(3)	-0.0727(4)	1.0	5.07(1)
O5	0.1623(2)	0.3246(1)	-0.0098(9)	1.0	5.07(1)
O6	0.2774(7)	0.0	0.0	1.0	5.07(1)
NaI	1/2	0.0	0.0	0.171(2)	13.18(1)
NH4-1	0.0946(12)	0.1891(14)	1/4	0.314(1)	12.70(1)
N	1/3	2/3	0.6062(3)	0.307(6)	8.42(1)
W1	0.5229(15)	0.0458(31)	1/4	0.198(2)	14.94(1)
C1	0.2895(1)	0.5789(1)	0.6508(17)	0.171(2)	8.42(1)

Table D

600 °C

Site	x/a	y/b	z/c	Fraction	Ui/Ue*100
T1	0.1587(3)	0.4909(3)	1/4	1.0	2.56(1)
T2	0.3552(2)	0.0939(2)	0.0487(5)	1.0	2.56(1)
O1	0.2613(4)	0.5226(9)	1/4	1.0	5.97(1)
O2	0.4221(3)	0.8442(6)	1/4	1.0	5.97(1)
O3	0.3856(6)	0.0966(7)	1/4	1.0	5.97(1)
O4	0.4387(3)	0.1150(4)	-0.0694(7)	1.0	5.97(1)
O5	0.1646(2)	0.3291(4)	-0.0043 (12)	1.0	5.97(1)
O6	0.2792(5)	0.0	0.0	1.0	5.97(1)

NaI	1/2	0.0	0.0	0.376(8)	13.18(1)
W1	0.5398(45)	0.0796(90)	1/4	0.138(1)	15.20(1)

Table E

770 °C

Site	x/a	y/b	z/c	Fraction	Ui/Ue*100
T1	0.1620(11)	0.4920(12)	1/4	1.0	3.31(1)
T2	0.3632(6)	0.0982(6)	0.0613(19)	1.0	3.31(1)
O1	0.2668(14)	0.5335(29)	1/4	1.0	6.44(1)
O2	0.4138(11)	0.8276(22)	1/4	1.0	6.44(1)
O3	0.4062(47)	0.1207(61)	1/4	1.0	6.44(1)
O4	0.4454(10)	0.1098(10)	-0.0735(20)	1.0	6.44(1)
O5	0.1633(6)	0.3265(11)	0.0056(33)	1.0	6.44(1)
O6	0.2912(15)	0.0	0.0	1.0	6.44(1)
NaI	1/2	0.0	0.0	0.39(5)	14.71(1)

Table F

T-O bond distances (Å)	30 °C	250 °C	430 °C	600 °C	770 °C
T1-O1	1.620(6)	1.637(4)	1.638(5)	1.657(5)	1.643(30)
T1-O2	1.614(6)	1.625(6)	1.621(5)	1.612(5)	1.610(30)
T1-O4 (x2)	1.657(5)	1.625(28)	1.631(6)	1.633(6)	1.601(6)
<T1-O>	1.637	1.625	1.630	1.633	1.613
T2-O3	1.621(6)	1.639(3)	1.634(7)	1.622(6)	1.682(7)
T2-O4	1.606(5)	1.641(4)	1.629(4)	1.634(6)	1.718(3)
T2-O5	1.642(6)	1.620(5)	1.631(4)	1.614(5)	1.679(3)
T2-O6	1.607(6)	1.625(4)	1.629(5)	1.616(6)	1.648(4)
<T2-O>	1.619	1.631	1.630	1.621	1.681
			T-O-T angles (°)		
T1-O1-T1	154.3(2)	150.0(4)	147.2(7)	144.8(5)	133.4(2)
T1-O2-T1	171.6(1)	174.4(8)	172.3(8)	176.8(5)	168.9(8)
T2-O3-T2	152.0(7)	146.1(8)	143.1(8)	141.8(6)	115.4(5)
T1-O4-T1	145.4(6)	143.7(3)	145.8(7)	145.3(6)	136.5(4)
T2-O5-T2	139.4(6)	141.2(9)	139.1(2)	141.5(6)	126.4(4)
T2-O6-T2	139.9(7)	138.4(8)	138.8(6)	141.7(5)	151.3(4)
<T-O-T>	150.4	148.9	147.7	148.6	138.6

Table G

D-omega

Site	x/a	y/b	z/c	Fraction	Ui/Ue*100
T1	0.1554(3)	0.4872(4)	1/4	1.0	3.0(1)
T2	0.3561(3)	0.0958(3)	0.0465(3)	1.0	3.0(1)
O1	0.2634(5)	0.5268(3)	1/4	1.0	5.3(1)
O2	0.4269(5)	0.8538(7)	1/4	1.0	5.3(1)
O3	0.3849(6)	0.0979(6)	1/4	1.0	5.3(1)
O4	0.4333(2)	0.1168(6)	-0.0798(3)	1.0	5.3(1)
O5	0.1586(2)	0.3174(8)	-0.0281(3)	1.0	5.3(1)
O6	0.2771(2)	0.0	0.0	1.0	5.3(1)
NaI	1/2	0.0	0.0	0.41(1)	6.3(1)
N	1/3	2/3	0.6042(4)	0.15(1)	3.2(1)
C1	0.2902(2)	0.5803(6)	0.5514(3)	0.15(1)	3.2(1)
D2	0.3879(6)	0.7757(3)	1/4	0.28(1)	10.2(1)
D1	0.1241(6)	-0.1241(5)	0.0130(3)	0.19(1)	9.7(1)
W4	0.5610(5)	0.4390(2)	1/4	1.00(1)	10.2(1)
W5	0.0	0.1050(2)	0.0	0.50(1)	9.6(1)
W6	0.0770(2)	0.1540(3)	1/4	1.00(1)	15.4(1)

Table H

T-O distances (Å)	
T1-O1	1.724(1)
T1-O2	1.655(1)
T1-O4 [x2]	1.562(1)
<T1-O>	1.625
T2-O3	1.627(1)
T2-O4	1.584(1)
T2-O5	1.625(1)
T2-O6	1.653(1)
<T2-O>	1.622
T-O-T angles (°)	
T1-O1-T1	137.47(1)
T1-O2-T1	169.94(1)
T2-O3-T2	143.63(6)
T1-O4-T1	153.16(1)
T2-O5-T2	134.59(1)
T2-O6-T2	139.88(1)
<T-O-T>	145.9

D-O distances (Å)	
D1-O5	1.12(1)
D2-O2	1.23(1)
Trimethylamine molecule distances (Å)	
N-C [x3]	1.420(2)
C-C [x3]	2.361(4)
Trimethylamine molecule angles (°)	
C-N-C [x3]	112.36(4)

Appendix 8

Atomic coordinates, fraction and Atomic Displacement Parameters of Ga-L, Ga-MOR and Ga-FER framework and extraframework atoms are reported in Table A, B and C, respectively.

T-O bond distances and T-O-T angles of Ga-L, Ga-MOR and Ga-FER are reported in Table D, E and F, respectively.

Table A

Ga-L

Site	x/a	y/b	z/c	Fraction	Ui/Ue*100
KB	2/3	1/3	1/2	1.0	8.89(2)
Ga1	0.3824(24)	0.0	0.0	0.15(1)	8.96(2)
Ga2	0.1418(25)	0.0	0.0	0.28(1)	13.3(1)
T1	0.0879(5)	0.3516(5)	1/2	1.0	0.82(32)
T2	0.1635(4)	0.4961(4)	0.2079(4)	1.0	0.82(32)
O1	0.0	0.2569(5)	1/2	1.0	1.67(6)
O2	0.1610(2)	0.3219(4)	1/2	1.0	1.67(6)
O3	0.2608(3)	0.5216(6)	0.2594(14)	1.0	1.67(6)
O4	0.0907(2)	0.4028(3)	0.3208(5)	1.0	1.67(6)
O5	0.4454(1)	0.8907(1)	0.2728(1)	1.0	1.67(6)
O6	0.1390(4)	0.4684(5)	0.0	1.0	1.67(6)
W1	0.0	0.0	0.090(20)	0.55(1)	3.33(8)
W2	0.1286(17)	0.2572(34)	0.0	0.93(1)	13.0(4)
W3	0.1093(26)	0.0546(13)	0.2851(6)	0.60(1)	13.36(4)

Table B

Ga-MOR

Site	x/a	y/b	z/c	Fraction	Ui/Ue*100
Na2	0.0	0.4283(34)	3/4	0.49(2)	19.20(5)
Ga1	0.0	0.0349(2)	3/4	0.296(7)	12.1(2)
T1	0.1947(2)	0.4248(2)	0.5406(2)	1.0	1.88(11)
T2	0.1944(1)	0.1876(1)	0.5395(1)	1.0	1.88(11)
T3	0.0890(2)	0.3859(2)	1/4	1.0	1.88(11)
T4	0.0826(1)	0.2240(1)	1/4	1.0	1.88(11)
O1	0.1146(5)	0.3991(8)	0.4595(7)	1.0	2.12(27)
O2	0.1240(7)	0.1778(4)	0.4020(17)	1.0	2.12(27)
O3	0.2714(5)	0.3876(3)	0.4748(22)	1.0	2.12(27)
O4	0.0791(12)	0.3052(2)	1/4	1.0	2.12 (27)
O5	0.1728(12)	0.2047(11)	3/4	1.0	2.12(27)

O6	0.1654(8)	0.4155(12)	3/4	1.0	2.12(27)
O7	0.2269(9)	1/2	1/2	1.0	2.12(27)
O8	1/4	1/4	1/2	1.0	2.12(27)
O9	0.0	0.4058(10)	1/4	1.0	2.12(27)
O10	0.0	0.1889(4)	1/4	1.0	2.12(27)
W1	0.0	0.1381(3)	3/4	1.0	11.45(23)
W2	0.0917(14)	-0.0278(15)	3/4	0.68(2)	8.89(29)
W3	1/2	1/2	0.0	0.98(5)	16.27(32)

Table C

Ga-FER

Site	x/a	y/b	z/c	Fraction	Ui/Ue*100
Ga1	1/2	0.0	0.0	0.447(9)	10.30(10)
Ga2	0.556(2)	0.0	1/2	0.123(6)	16.05(30)
T1	0.1528(4)	0.0	0.0	1.0	1.78(11)
T2	0.0855(3)	0.2041(3)	0.0	1.0	1.78(11)
T3	0.2735(2)	0.0	0.2908(2)	1.0	1.78(11)
T4	0.3258(1)	0.2015(1)	0.2086(1)	1.0	1.78(11)
O1	0.0	0.2316(14)	0.0	1.0	2.02(20)
O2	0.2437(4)	0.0	0.5	1.0	2.02(20)
O3	0.0943(4)	0.0875(3)	0.0	1.0	2.02(20)
O4	0.1945(4)	0.0	0.1947(10)	1.0	2.02(20)
O5	1/4	1/4	1/4	1.0	2.02(20)
O6	0.1543(6)	0.2729(8)	1/2	1.0	2.02(20)
O7	0.1023(3)	0.2568(6)	0.1936(8)	1.0	2.02(20)
O8	0.3303(3)	0.0879(2)	0.2584(13)	1.0	2.02(20)
W1	0.1114(1)	1/2	1/2	0.148(20)	13.22(30)
W2	0.0	0.3509(1)	1/2	0.305(25)	19.10(10)
W3	0.0	0.1270(1)	1/2	0.767(10)	15.27(50)

Table D

Bond distances (Å)	Ga-L
T1-O1	1.666(8)
T1-O2	1.668(3)
T1-O4 [x2]	1.630(4)
<T1-O>	1.650
T2-O3	1.639(6)
T2-O4	1.765(6)
T2-O5	1.846(1)
T2-O6	1.641(5)
<T2-O>	1.722
T-O-T angles (°)	
T1-O1-T1	112.6(5)
T1-O2-T1	147.5(8)
T2-O3-T2	140.0(6)
T1-O4-T2	138.2(4)
T2-O5-T2	115.4(3)
T2-O6-T2	146.1(6)
<T-O-T>	133.3

Table E

Bond distances (Å)	Na-MOR	Ga-MOR
T1-O1	1.647(2)	1.659(4)
T1-O3	1.647(2)	1.658(4)
T1-O6	1.666(2)	1.667(4)
T1-O7	1.657(2)	1.664(4)
<T1-O>	1.654	1.662
T2-O2	1.644(2)	1.651(4)
T2-O3	1.649(2)	1.656(4)
T2-O5	1.667(2)	1.662(3)
T2-O8	1.642(2)	1.647(3)
<T2-O>	1.650	1.654
T3-O1 [x2]	1.659(1)	1.658(2)
T3-O4	1.654(2)	1.653(4)
T3-O9	1.656(2)	1.665(4)
<T3-O>	1.657	1.658
T4-O2 [x2]	1.656(1)	1.657(2)
T4-O4	1.656(2)	1.653(4)
T4-O10	1.664(2)	1.660(4)
<T4-O>	1.656	1.657
T-O-T angles (°)		

T1-O1-T3	134.9(4)	129.9(6)
T2-O2-T4	136.2(2)	135.3(5)
T1-O3-T2	143.5(3)	139.0(5)
T3-O4-T4	178.1(8)	171.5(1)
T2-O5-T2	137.7(4)	143.2(7)
T1-O6-T1	139.6(5)	140.4(8)
T1-O7-T1	131.3(5)	138.9(8)
T2-O8-T2	180.0	180.0
T3-O9-T3	165.5(1)	151.9(1)
T4-O10-T4	133.5(6)	129.0(1)
<T-O-T>	148.0	145.9

Table F

Bond distances (Å)	**NH4-FER Martucci et al.,(2014)**	**Ga-FER**
T1-O3 [x2]	1.609(1)	1.653(2)
T1-O4 [x2]	1.608(1)	1.649(2)
<T1-O>	1.607	1.651
T2-O1	1.606(1)	1.658(2)
T2-O3	1.608(1)	1.651(3)
T2-O7 [x2]	1.608(1)	1.653(2)
<T2-O>	1.607	1.654
T3-O2	1.615(1)	1.656(2)
T3-O4	1.608(1)	1.650(3)
T3-O8 [x2]	1.609(1)	1.655(2)
<T3-O>	1.609	1.653
T4-O5	1.613(1)	1.612(1)
T4-O6	1.605(1)	1.639(2)
T4-O7	1.610(1)	1.645(2)
T4-O8	1.605(1)	1.644(2)
<T4-O>	1.607	1.635
	T-O-T angles (°)	
T2-O1-T2	174.12(1)	152.9(1)
T3-O2-T3	151.74(1)	140.4(7)
T1-O3-T2	152.31(1)	143.9(4)
T1-O4-T3	157.70(1)	144.1(9)
T4-O5-T4	180.0	180.0
T4-O6-T4	139.96(1)	143.0(7)
T2-O7-T4	149.77(1)	134.6(6)
T3-O8-T4	143.71(1)	136.6(4)
T-O-T	151.7	146.9